sid.inpe.br/mtc-m21c/2020/08.06.23.10-TDI

STUDY ON MEDIUMSCALE TRAVELING IONOSPHERIC DISTURBANCES OBSERVED IN THE SOUTH AMERICAN EQUATORIAL REGION

Patrick Essien

Doctorate Thesis of the Graduate Course in Space Geophysics/Atmospheric Sciences, guided by Drs. Hisao Takahashi and Cosme Alexandre Oliveira Barros Figueiredo, approved in August 27, 2020.

URL of the original document:
<http://urlib.net/8JMKD3MGP3W34R/432JP4S>

INPE
São José dos Campos
2020

PUBLISHED BY:

Instituto Nacional de Pesquisas Espaciais - INPE
Gabinete do Diretor (GBDIR)
Serviço de Informação e Documentação (SESID)
CEP 12.227-010
São José dos Campos - SP - Brasil
Tel.:(012) 3208-6923/7348
E-mail: pubtc@inpe.br

DIGITAL LIBRARY:
Dr. Gerald Jean Francis Banon
Clayton Martins Pereira - Serviço de Informação e Documentação (SESID)
DOCUMENT REVIEW:
Simone Angélica Del Ducca Barbedo - Serviço de Informação e Documentação (SESID)
André Luis Dias Fernandes - Serviço de Informação e Documentação (SESID)
ELECTRONIC EDITING:
Ivone Martins - Serviço de Informação e Documentação (SESID)
Cauê Silva Fróes - Serviço de Informação e Documentação (SESID)

sid.inpe.br/mtc-m21c/2020/08.06.23.10-TDI

STUDY ON MEDIUMSCALE TRAVELING IONOSPHERIC DISTURBANCES OBSERVED IN THE SOUTH AMERICAN EQUATORIAL REGION

Patrick Essien

Doctorate Thesis of the Graduate Course in Space Geophysics/Atmospheric Sciences, guided by Drs. Hisao Takahashi and Cosme Alexandre Oliveira Barros Figueiredo, approved in August 27, 2020.

URL of the original document:
<http://urlib.net/8JMKD3MGP3W34R/432JP4S>

INPE
São José dos Campos
2020

Cataloging in Publication Data

Essien, Patrick.

Es77s Study on mediumscale traveling ionospheric disturbances observed in the South American Equatorial region / Patrick Essien. – São José dos Campos : INPE, 2020.

xxvi + 169 p. ; (sid.inpe.br/mtc-m21c/2020/08.06.23.10-TDI)

Thesis (Doctorate in Space Geophysics/Atmospheric Sciences) – Instituto Nacional de Pesquisas Espaciais, São José dos Campos, 2020.

Guiding : Drs. Hisao Takahashi and Cosme Alexandre Oliveira Barros Figueiredo.

1. Medium-scale traveling ionospheric disturbances. 2. Equatorial ionosphere. 3. Detrending TEC map. 4. Secondary and tertiary gravity waves. 5. Intertropical convergence zone. I.Title.

CDU 551.510.535

Aluno (a): ***Patrick Essien***

"ESTUDO SOBRE DISTURBIOS IONOSFERICOS ITINERANTES DE MÉDIA ESCALA NA REGIÃO EQUATORIAL DA AMÉRICA DO SUL"

Aprovado (a) pela Banca Examinadora em cumprimento ao requisito exigido para obtenção do Título de *Doutor(a)* em

Geofísica Espacial/Ciências Atmosféricas

Dr. Alexandre Alvares Pimenta

Alexandre Alvares Pimenta

Presidente / INPE / SJCampos - SP

(X) Participação por Video - Conferência

(X) Aprovado ( ) Reprovado

Dr. Hisao Takahashi

Alexandre Alvares Pimenta

Orientador(a) / INPE / SJCampos - SP

(X) Participação por Video - Conferência

(X) Aprovado ( ) Reprovado

Dr. Cosme Alexandre Oliveira Barros Figueiredo

Alexandre Alvares Pimenta

Orientador(a) / INPE / São José dos Campos - SP

(X) Participação por Video - Conferência

(X) Aprovado ( ) Reprovado

Dr. Jonas Rodrigues de Souza

Alexandre Alvares Pimenta

Membro da Banca / INPE / SJCampos - SP

(X) Participação por Video - Conferência

(X) Aprovado ( ) Reprovado

Dr. Akeem Babatunde Rabiu

Alexandre Alvares Pimenta

Convidado(a) / CARNASRDA / Nigéria - NGR

(X) Participação por Video - Conferência

(X) Aprovado ( ) Reprovado

Este trabalho foi aprovado por:

(X) maioria simples

( ) unanimidade

São José dos Campos, 27 de agosto de 2020

Aprovado (a) pela Banca Examinadora em cumprimento ao requisito exigido para obtenção do Título de *Doutor(a)* em

Geofísica Espacial/Ciências Atmosféricas

Dr. Igo Paulino da Silva

Alexandre Alvares Pimenta

Convidado(a) / UFCG / Campina Grande - PB

(X) Participação por Video - Conferência

( ) Aprovado (X) Reprovado

Este trabalho foi aprovado por:

(X) maioria simples

( ) unanimidade

São José dos Campos, 27 de agosto de 2020

"I would rather die trying to live my dream than to live a longer life filled with regret".

Anonymous

I dedicate this thesis to my inspiration and the main brain behind my Ph.D journey, ***Dr. Mrs. Nana Ama Browne Klutse****, my best friend* ***Smart Essel*** *and my mentor, uncle and father,* ***Late Prof. Abeeku Brew-Hammond***

ACKNOWLEDGEMENTS

My greatest appreciation goes to my advisors; Prof. Hisao Takahashi and Dr. Cosme Alexandre Oliveira Barros Figueiredo for their professionalism, motivation, support, patience, dedication and leadership to the course of my dream as a scientist. I thank Dr. Cristiano Max Wrasse for his guidance, love, motivation and leadership right from the first day of my Ph.D studies till this final day. Last but not the least, I am very grateful to all the Professors of INPE; Prof. Inez Batista, Prof. Eurico, Prof. Jose H. Sobral, and Dr. D. Alisson among others, for their generosity with knowledge.

I thank Prof. Babatunde Rabiu and Dr. Jonah Olusegun for their recommendation for my master's program in Brazil in the year 2014. I thank Dr. Mrs. Nana Ama Brown Klutse for her support right from my first degree in the University of Cape Coast through to my PhD level at the National Institute for Space Research (INPE). I am grateful to the Late Prof. Abeeku Brew-Hammond for sponsoring my first degree education and showing me fatherly love till he was called by his maker in the course of my academic journey.

I thank Dr Igo Paulino, who requested me as a student from Africa, Prof Ricardo A. Buriti and Prof A. Medeiros who guided me in all my endeavors during my masterâs program in Federal University of Campina Grande (UFCG).

I am thankful to my lovely and virtuous wife Mrs. Rebecca Essien and my lovely daughter Miss Ekua Kuntuwah Essien, for their patience and support in pursuance of this dream. I would like express my profound gratitude to my mother, Miss Rose Tawiah, for her endless love and support and my late father, Mr Thomas Kuta Essien for his disciplinary education. Thanks be to my siblings, Rev. Fr. Capt. Anthony K. Essien, Angelina K. Essien, Mrs Catherine Essien Otoo and Vincent K. Essien; and to my nephews and nieces, Lawyer Nicholas Appiah, Dominic Ebo Arhin, Benedicta Osei, Hannah Appiah, Emmanuel K. Essien; and finally, thanks to my cousin Albert Aidoo, Lt. Tabitha Simons-Dadzie and the entire family for all their support.

I thank Dr. Maria Virginia Alves who admitted me into the Ph.D program and to the Postgraduate Council in Space Geophysics for availability of financial and computational resources that are essential for carrying out this research. I also thank all colleagues and friends including Smart Essel, Dr Esmeralda Romero Hernandez, Mr. Clement Abaidoo, among others, whose conviviality will make the memories of this journey a longing one.

I thank all the institutes that own the GNSS (this is the first time it is being referred to so we need to refer to it in full) receivers network over South America: RBMC (Brazilian Institute of Geography and Statistics, Brazil), RAMSAC (National Geographic Institute, Argentina), CORS (National Geodetic Survey, USA), IGS (International GNSS Service) and UNAVCO (National Science Foundation, USA and National Atmospheric and Space Administration, USA), for making available the RINEXs files, substantial for obtaining the results. I am grateful to the Brazilian Space Climate Study and Monitoring program (EMBRACE) for making RINEX files available. I am grateful to the Center for Weather Forecasting and Climate Studies (CPTEC) for providing images from the 'Geostationary Operational Environmental Satellite' (GOES) 13 and 16.

I appreciate the financial support and institutional framework of the "Conselho Nacional de Desenvolvimento Cientifico e Tecnologico" (CNPq), project no. 141044/2017-9 of the "Coordenacao de Aperfeicoamento de Pessoal de Nivel Superior" (CAPES), for the PhD scholarship, and the National Institute of Space Research (INPE).

I also thank the American Geophysical Union (AGU) for the Max Hammond Student Travel Grant Award for good abstract to participate in the 2019 AGU Fall Meeting in San Francisco, CA, U.S.A. I thank the Committee on Space Research (COSPAR) for granting me the opportunity to participate in Capacity Building Workshop on Space Weather in 2018 at INPE and awarding my group for best presentation.

I would like to acknowledge the defense board for the time and contribution to the success of this thesis. Finally, I thank the entire Brazilian populace for hosting and taking care of me with their taxes till this dream comes to fruition reality.

ABSTRACT

Using data collected by GNSS (GPS and GLONASS specifically) dual frequency receivers network, detrended TEC maps were generated to identify and characterize the medium-scale traveling ionospheric disturbances (MSTIDs) over the South American equatorial region (latitude: 0° to 15°S and longitude: 30° to 55°W) during solar cycle 24 (from January 2014 to December 2019). Among 742 MSTIDs that were observed, 712 of them representing ∼96% were observed during geomagnetic quiet condition and 30 events indication 4% were observed during geomagnetic disturbed condition. The observed MSTIDs show strong positive correlation with the solar activity. The positive correlation might have been caused by gravity waves dissipation due to high viscosity in the thermosphere as a result of low and high thermospheric temperature during solar minimum and maximum respectively. The predominant daytime MSTIDs representing 70% of the total observation occurred in winter with the secondary peak in equinox, while the evening time MSTIDs which is 28% of the entire events occurred in summer and equinox, while the remaining 2% of the MSTIDs were observed during nighttime. The local time dependency of the MSTIDs was attributed to the mechanisms generating them and/or the medium at which they propagated while the seasonal variation could be as results of wind filtering and dissipation effect during winter and summer. The horizontal wavelengths of the MSTIDs were concentrated between 300 and 1400 km, with the mean value of 667±131 km. The observed periods were ranging from 20 to 60 min with the mean value of 36±7 min. The observed horizontal phase speeds were distributed around 100 to 700 m/s, with the corresponding mean of 301±75 m/s. The MSTIDs in winter solstice and equinoctial months preferentially propagated northeastward and northwestward. Meanwhile, during summer solstice they propagated in all directions. The anisotropy of the propagation direction might be due to several reasons: the wind and dissipative filtering effects, ion drag effects, the primary source region and the presence of the secondary or tertiary gravity waves in the thermosphere. Atmospheric gravity waves from strong convective sources originated from the equatorial and Amazon region might be the primary precursor of the northeastward and northwestward propagating MSTIDs during summer solstice and autumn equinox. Nevertheless, strong cold front emanating from low latitude might have been the primary source for the northeastward and northwestward MSTIDs during winter solstice and spring equinox. In all the seasons, we noted that the MSTIDs propagating southeastward were probably excited by the likely gravity waves that was generated by the intertropical convergence zone (ITCZ).

Palavras-chave: Medium-scale traveling ionospheric disturbances. Equatorial ionosphere. Detrending TEC map. Secondary and tertiary gravity waves. Intertropical convergence zone.

ESTUDO DE DISTÚRBIOS IONOSFÉRICOS PROPAGANTES DE MÉDIA-ESCALA OBSERVADOS NO REGIÃO EQUATORIAL DA AMÉRICA DO SUL

RESUMO

Usando dados coletados pela rede de receptores GNSS de dupla frequência (especificamente GPS e GLONASS), obtêm-se mapas de TEC perturbado com o objetivo de identificar e caracterizar os MSTIDs (sigla em inglês para Medium-Scale Traveling Ionospheric Disturbances) na região equatorial da América do Sul (latitude: 0° to 15°S and longitude: 30 to 30°W) durante o ciclo solar 24 (Janeiro de 2014 e dezembro de 2019). Entre os 742 MSTIDs observados, 712 deles, representando ∼96%, foram observados durante a condição geomanéticas calmas e 30 eventos, 4% durante períodos geomagneticamente perturbadas. Os MSTIDs observados mostram uma forte correlação positiva com a atividade solar. Essa correlação pode ter sido causada pela dissipação das ondas de gravidade devido à alta viscosidade na termosfera, e como resultado da baixa e alta temperatura termosférica durante mínima e máxima solar, respectivamente. Os MSTIDs ocorrem predominante durante o dia, 70% da observação total, com pico no inverno e pico secundário no equinócio, enquanto que os MSTIDs noturnos, 28% de todos os eventos, ocorrem no verão e no equinócio, enquanto os 2% restantes dos MSTIDs foram observados durante a noite. A dependência do hora local dos MSTIDs foi atribuída aos mecanismos que os geraram e/ou ao meio em que se propagam. A variação sazonal pode ser resultado dos efeitos de filtragem das ondas através do vento e dissipação, durante o inverno e o verão. Os comprimentos de onda horizontais dos MSTIDs variam entre 300 e 1400 km, com valor médio de 667±131 km. Os períodos observados variam de 20 a 60 min, com valor médio de 36±7 min. As velocidades de fase horizontal observadas foram observados entre 100 e 700 m/s, com a média de 301±75 m/s. Os MSTIDs durante os solstício de inverno e nos meses de equinócio se propagam preferencialmente para noroeste , norte e nordeste. Enquanto isso, durante o solstício de verão, eles se propagavam em todas as direções. A anisotropia da direção da propagação pode ser devida aos efeitos de filtragem do vento, efeitos dissipativos, efeitos de arrasto de íons, além da região de fonte primária e por fim, a presença das ondas de gravidade secundária ou terciária na termosfera. As fontes de convecção troposférica originadas da região equatorial e amazônica podem ser o precursor primário dos MSTIDs que se propagam para nordeste e noroeste durante o solstício de verão e o equinócio de outono. Por outro lado, uma frente fria que emana de altas latitudes pode ser sido a principal fonte para os MSTIDs que se propagam para nordeste e noroeste durante o solstício de inverno e o equinócio da primavera. Em todas as estações, observamos que os MSTIDs que se propagam para o sudeste provavelmente são originadas por ondas de gravidade geradas pela Zona de Convergência Intertropical (ZCIT).

Keywords: distúrbios ionosféricos propagantes de média-escala. ionosfera equatorial. Mapa de TEC de "detrend". Ondas de gravidade secundárias e terciárias. Zona de convergência intertropical.

LIST OF FIGURES

LIST OF TABLES

CONTENTS

1 INTRODUCTION

1.1 Introduction

Medium-scale traveling ionospheric disturbances (MSTIDs) are plasma density fluctuations that propagate as waves through the ionosphere at a wide range of velocities and frequencies. These wave-like perturbations of the ionospheric plasma have horizontal phase velocities of hundreds of meters per second (m/s), periods of less than 1 hour, and wavelengths of several hundred to few thousands of kilometers (SQUAT; SCHLEGEL, 1996; TSUGAWA et al., 2007; OTSUKA et al., 2013). They vary with latitude, longitude, local time, season, and solar activities. They were first postulated to be the ionospheric manifestation of gravity waves from the neutral atmosphere by Hines (1960), however, the advent of Global Navigation Satellite System (GNSS) receivers, all-sky imagers, ionosondes, incoherent scatter radars, and HF Doppler systems including space weather probes and models among others have helped to better understand the origins of MSTIDs.

MSTIDs constitute a specific type of space weather and geophysical phenomenon that can be solar driven or driven by other processes from auroral sources at the high latitude thermosphere to the solar terminator and storms, tropospheric convection, hurricanes and tornado in the troposphere (KOTAKE et al., 2007; HERNANDEZ-PAJARES et al., 2006). Independently of the source, the negative effects arising from MSTIDs at ionospheric altitudes are very important and need to be addressed. The main concern of the scientific community is to be able to have direct and timely information of MSTID events and hence, be able to mitigate the effects in the affected operations. Meanwhile, due to the high occurrence rate of MSTIDs in daily bases and the variety of their characteristics regarding the velocity, wavelength, period, propagation direction and amplitude, their identification and tracking are very complicated and has not been fully achieved in operational service mode yet.

Nevertheless, the characterization of MSTIDs in South American equatorial region into wavelength, phase velocity, propagation direction, source region and period of propagation among others are not known. Meanwhile, MSTIDs and their effects on radial waves speak to the need for a better understanding of their morphology and climatology, and ultimately the need to predict their behavior more accurately in the future. Before such improvements are achieved, more measurements of MSTIDs are needed in which South American equatorial region is not an exception. So far there is no useful F-region MSTID climatological study for the South American equatorial region at the moment that could be used to predict MSTID periods, amplitudes, speeds and directions at a given location. Therefore, any operational requirement for MSTID information means the MSTID characteristics have to be measured at the required location. Because of the variability of MSTIDs, their occurrence even on a statistical basis are unable to be predicted. This variability arises from the multiple sources of gravity waves in both the troposphere and thermosphere, and the variability of the medium (background winds and temperature) through which they propagate (as state in second paragraph).

The Ionosphere is an important domain in the Earth's atmosphere due to its ability to modify the properties of radio waves propagation that passes through (ABDU, 2016). It consequently provides the means as well as the constraints for sustaining radio-based communication and navigation systems in the globe. The nature of this ionic layer has a significant impact on a variety of space-based application systems of our technology-based modern life. Therefore, it is very important for the scientific community to understand the variability of the ionosphere in order to develop models to study the ionospheric weather. This goal remains a highly challenging task because of the major drivers of the variability arising from sources not limited to neutral atmospheric forcing from below but also geomagnetic storms, and solar activities from the above (KUBOTA et al., 2000).

The equatorial ionosphere possesses distinguish features from the other latitudes due to the low inclination of geomagnetic field lines and the relatively larger fraction of the incident solar ionizing radiation that characterizes the region. This region in question can be characterized with the highest values of the peak-electron density with the most pronounced amplitude and phase scintillation effects. The combined effects of the high radiation level from the sun, and electric and magnetic fields of the earth results in rising of the plasma along the magnetic field lines. This leads to a phenomenon known as Equatorial Ionization Anomaly (EIA) when the rising plasma loses its momentum and energy and gravity and pressure gradient act on it. Narayanan et al. (2014) reported that the EIA constrains the MSTIDs that are propagating from the middle latitudes to disappear when reaching the low latitudes. Shiokawa et al. (2002) also suggested that crest region of EIA restricts the equatorward propagation of MSTIDs.

In the equatorial region of South America, there have been a few MSTIDs studies such as the first ever measurements by Röttger (1977) using HF-ground-backscatter in Peru: In the western longitudes of South America, Makela et al. (2010) also used optical methods to study nighttime TIDs. Moreover, MacDougall et al. (2011)

studied day and nighttime MSTIDs using one year measurement made by ionosonde, however, it was limited to small area over northeast of Brazil (about 10° south of the magnetic and geographic equators). Paulino et al. (2016) recently studied the nocturnal MSTIDs propagating over Cariri (36°W, 7.4°S). Jonah et al. (2017) also studied the characteristics of geomagnetic conjugate MSTIDs but was limited to daytime summer MSTIDs that were generated at the conjugate hemispheres. However, the characterization of MSTIDs over South America equatorial latitude has not been done yet.

In the low latitude ionosphere over South America, few studies on MSTIDs have been done by Jonah et al. (2016) and Figueiredo et al. (2018a) using GPS detrending TEC (dTEC) maps but were mostly daytime. Moreover, nocturnal MSTIDs have been extensively observed as 'dark bands' at the atomic oxygen red line airglow emission (OI 630.0 nm) by all-sky-imagers (PIMENTA et al., 2008; CANDIDO et al., 2008; AMORIM et al., 2011; MACHADO, 2017; FIGUEIREDO et al., 2018b) over the low latitude of South America. Furthermore, in the mid-latitude over the northern hemisphere, observation of MSTIDs using global position system (GPS) detrending TEC maps have been explored extensively (TSUGAWA et al., 2004; TSUGAWA et al., 2007; OTSUKA et al., 2004; OTSUKA et al., 2013) probably due to the dense distribution of the GPS receivers at the region. In the equatorial region over Asia, Shiokawa et al. (2006) studied nocturnal MSTIDs in Indonesia at geomagnetic latitude −10.4°. Husin et al. (2011) studied day and nighttime MSTIDs in Malaysia equatorial region (around 3° north of the geographic equator or about 6° south of the magnetic equator) using GPS TEC measurements. Fukushima et al. (2012) also studied nighttime MSTIDs at Kototabang, Indonesia (geographic longitude: 100.3°E, geographic latitude: 0.2°S and geomagnetic latitude: 10.6°S). Among others, Chou et al. (2018) also used simulation such as SAMI3 to study the lowâlatitude nighttime MSTIDs triggered by the typhoonâinduced concentric gravity waves (CGWs).

There are various features of the ionosphere, among others plasma bubbles and equatorial electrojet that are unique to the equatorial ionosphere. Sieradzki e Paziewski (2016) reported that TEC fluctuations caused by MSTIDs in the equatorial ionosphere is one of the main unresolved problems degrading ambiguity resolution and affect the reliability of the position and navigation of GNSS and related applications. Therefore, the need to study the MSTIDs should be vital to the scientific community. The equatorial region over South America has not been fully explored as far as MSTIDs are concerned, probably due to less number of GNSS receivers, and other ionospheric instruments in the region. Krall et al. (2011) simulated plasma bubble seeding using the effect of MSTIDs during the post-sunset hours. Takahashi et al. (2018) also reported that MSTIDs as a possible candidate to generate equatorial plasma bubbles.

1.1.1 Motivation of the research

The motivation of this work is neither limited to what have not been done in the South American equatorial region or what have been done in other latitude. Instead, we attest the fact that, MSTIDs constitute a specific type of space weather phenomenon that can sometimes be solar driven or mostly be driven by other processes acting below the ionosphere. The urgent concern is to be able to have direct and timely information of ionospheric perturbation due to MSTIDs, and hence be able to mitigate the effects in the affected operations. It is for this reason that enough studies have to be done in the ionospheres over different geographic/geomagnetic latitude to unravel the mystery of their occurrence rate, time dependence, characteristics, seasonal variations, source regions, generation mechanisms and the effect they impose on technology.

South American equatorial ionosphere is among the regions where high spatial variations of the ionospheric plasma density among others can be found. There is a particular interest in MSTIDs in this region because of their implied role (MILLER, 1997) in the triggering of plasma bubbles and associated strong Spread F irregularities that can cause dropouts and Scintillation of GPS based systems (KINTNER et al., 2007). Yet, there have been few systematic measurements of day and nighttime MSTID in the region.

The inability to study MSTIDs in the South American equatorial region, could be probably due to the availability of instruments, their low occurrence rate and the prominent variability of their characteristics regarding their wavelength, period, phase velocity, propagation direction, and amplitude, thus making their identification and tracking very complicated (CANDIDO et al., 2008). Nevertheless, if the above-mentioned phenomenon is well studied, it will still improve the understanding regarding the physical processes of its formation, source regions and then identify the necessary drivers. This will help to reduce the impact they have on space-based navigation systems such as GNSS among others, and other ground-based radio related instruments in the region (CROWLEY; AZEEM, 2018). Therefore, mitigation strategies can then be designed for the technologies affected by MSTIDs and in close collaboration with operators of these technologies, to demonstrate the added value of the proposed mitigation techniques. Another relevant point is that long-term study on MSTIDs during daytime have not been done especially, using GNNS receivers.

For that matter, the motivation of this research is to investigate the occurrence, characteristics and the source regions of the MSTIDs in the South American equatorial region. In order to fully achieved this, the spatial and temporal resolution of the GNSS (GPS and Global Orbiting Navigation Satellite System (GLONASS)) TEC perturbation maps have to be improved to identify and analyze the TEC perturbations in the region.

1.1.2 Research questions

In this regard, the following research questions will resolve all the loopholes if answers are provided to them.

a) What is the long term variability of the MSTIDs in relation to the solar cycle?

b) What is the local time dependence of the MSTIDs in the area under investigation?

c) Do the equatorial MSTIDs have different characteristics from those observed in other latitudes e.g. Figueiredo et al. (2018a), Otsuka et al. (2011), MacDougall et al. (2011) and Kotake et al. (2006)?

d) What are the source regions and generation mechanisms of the MSTIDs in the region?

1.1.3 Objectives of the Research

The overarching aim of this research work is to develop a methodology that will characterize day-to-day MSTIDs over the South American equatorial region during solar cycle 24 (2014 to 2019) using GPS and GLONASS TEC perturbation maps. In order to achieve such objective, this work will be guided by the following specific objectives:

- Study the statistical analysis of the MSTIDs during the solar maximum activity phase (January 2014 to December 2015), descending phase (January 2016 to December 2017) and minimum phase (January 2018 to December 2019) of the solar cycle 24.

- Characterize the MSTIDs by horizontal wavelength, period, horizontal phase velocity, propagation direction and amplitude

- Investigate the seasonal variability of the MSTIDs.

- Comparative study of the MSTID characteristics between the equatorial (present work) and low to mid latitude among others Figueiredo et al. (2018a), Otsuka et al. (2011), MacDougall et al. (2011) and Kotake et al. (2006).

- Investigate the source locations and generation mechanisms.

1.2 Structure of the Research

In order to achieve the above-mentioned aim and objectives, this thesis will follow the order below.

- In other to provide the basic understanding about ionosphere and theoretical basis within which phenomena will be discussed in chapter 2 presents the Earth's ionosphere and its electrodynamics processes; the mathematical description of the MSTIDs. This will be presented from the linear theory of gravity waves in the presence of the plasma. In addition, the historic review of global observation of MSTIDs will be presented.

- The instrumentation and methodology will be presented in chapter 3. The description of the instruments will encompass GPS and GLONASS. The methodology will be used to calculate the detrending TEC and consequently generate the detrending TEC maps. Finally, chapter 3 will calculate the parameters of the MSTIDs using spectral analysis.

- chapter 4 presents the results on the statistical analysis of the occurrences and characteristics of the MSTID observed during solar cycle 24. It furthers elaborate the time dependence, seasonality and the long term solar cycle dependence of the observed MSTIDs.

- chapter 5 presents the interpretation and discussion of the result presented in chapter 4. It will first and foremost, discuss the characteristics and statistical occurrences rate of MSTIDs. The anisotropy of the wavelength, period, phase velocity and azimuth will be discussed and compare to the previous works in the equatorial, low and midlatitude. The variation of the time dependence of MSTIDs will be looked into and the annual and seasonal variation of the occurrence rate of the observed MSTIDs and their solar cycle dependence will be discussed thoroughly. The variability of background winds and temperature effects on the propagation of MSTIDs will also be considered.

- chapter 6 will present the possible primary source regions of the MSTIDs over the South American equatorial region. Effort will be thrown into discussing the possible mechanisms where gravity waves produce these MSTIDs. Pertinent to the present work, three possible sources for the MSTIDs will be discussed: upward propagating and filtered meteorological atmospheric gravity waves (AGWs) as well as secondary and tertiary gravity waves.
- chapter 7 will present the conclusion of the present research and recommendation for future work.

2 MEDIUM-SCALE TRAVELING IONOSPHERIC DISTURBANCES: THE THEORY AND HISTORICAL REVIEW

The purpose of chapter 2 is to present the Earth's ionosphere and its electrodynamic process; the background of TIDs and the mathematical description of MSTIDs. The mathematical model of TIDs is presented from the linear theory of gravity waves in the presence of the ionospheric plasma. In addition, a historical review of global observation of MSTIDs will be elaborated.

The atmosphere which is a spheroidal gaseous envelope surrounding the earth is generally held around the planet in approximately hydrostatic equilibrium by the gravitation force of the planet. Small oscillations such as gravity waves can take place in this equilibrium state and propagate into the ionospheric level as traveling ionospheric disturbances (TIDs). The bulk of atmosphere is electrically neutral, however, above 50 km the constituents are ionized. The region where ionization is so important is called ionosphere.

2.1 The Earth's ionosphere

The existence of the ionosphere was first inferred by Marconi through the trans-Atlantic radio wave propagation experiment in 1901. In 1902, Kennelly and Heaviside further hypothesized the existence of ionized layer around the earth that could guide the electromagnetic waves to greater distances and was named Heaviside layer (named after the physicist Oliver Heaviside). In 1926, Robert Watson-Watt proposed the term ionosphere to replace Heaviside layer. Appleton and his associates set up experiments to measure the height of the ionized layer and its properties, which won Appleton Nobel Prize in physics in 1926. This really provided much knowledge about the ionosphere until the age of rockets and satellites began in the 1940 and 1950's.

Though tremendous amount of research works have been devoted to studies of the ionosphere, nevertheless, for more than a century after its discovery, the Earth's ionosphere remains a poorly explored region. Still, scientific community is unable to predict the ionospheric behavior precisely, either during geomagnetic storms, or during geomagnetically quiet time conditions. The knowledge of the structure and dynamics of the ionospheric plasma at each moment of time is vital for various scientific applications and services, such as telecommunication via radio signals, point positioning based on global navigation satellite systems (GNSS). The ionosphere is where free electrons exist in enough density to have an appreciable effect on the propagation of electromagnetic waves (RISHBETH; GARRIOTT, 1969; BANKS et al., 1974; KELLY, 1989; HARGREAVES, 1992; RISHBETH et al., 2009). This ionic layer lies at the altitude between 50 to 1000 km above the surface of the Earth and overlaps the mesosphere, thermosphere, and exosphere. The ionized layer is formed as a result of the process called photoionization of neutral atoms and molecules by solar X-ray, extreme ultraviolet (EUV) radiation and the precipitation of energetic charged particles at higher latitudes. Furthermore, cosmic rays also cause some minor ionization primarily at lower ionosphere (60-90 km) (NICOLET; AIKIN, 1960; WEBBER, 1962). The rate of ionization depends on the intensity of the ionizing radiation, atmospheric density, composition, and ionization cross sections of the atmospheric constituents. The electrodynamic nature of the ionosphere has latitudinal dependence. For the purpose of this thesis, the discussion will be limited to the equatorial ionosphere.

2.1.1 The dynamics of equatorial ionosphere

A variety of chemical and dynamical processes in the ionosphere result in the redistribution of ionization which leads to the formation of distinct peaks and layers denoted by D, E, F1 and F2 as shown in Figure 2.1. The three dominant constituents in the ionosphere are N_2, O_2 and O that are ionized by solar radiation to produce N_2^+, O_2^+, N^+, O^+ and NO^+ (RISHBETH; GARRIOTT, 1969; RICHMOND et al., 1992).

Figure 2.1 - A temperature profile of the Earth's ionosphere.

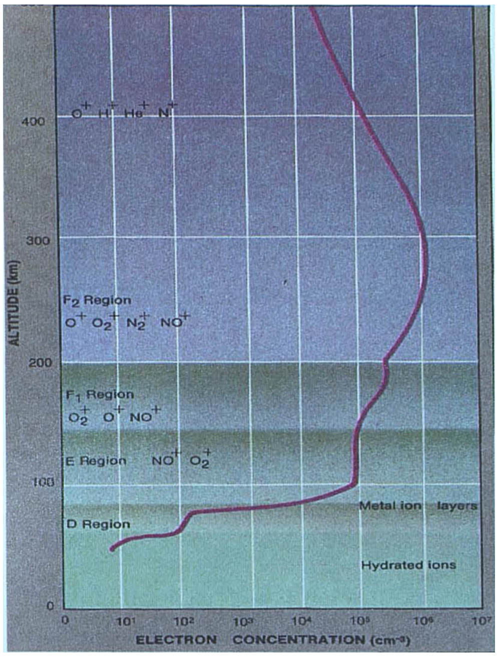

Source: Heelis (2004).

The D-region is located between the altitude of 60-90 km which corresponds to a sparse layer of polyatomic ion such as NO^+ and O_2^-. Solar L-alpha (121.6 nm) radiation seems to be the most important for ionizing NO, solar X-rays (<0.8 nm) for ionizing N_2, O_2, and Ar, solar ultraviolet (UV) radiation (λ < 111.8 nm) for ionizing unstable O_2, and galactic cosmic rays for ionizing all the constituents in D-layer (MEIRA, 1971).

The E-region is located around 90-120 km above the Earth's surface and moderately dense layer of principal molecular ions such as NO^+ and O_2^+ as shown in Figure 2.1. The ionization in the E-region is mainly caused by X-rays between 8 and 10.4 nm as well as the UV radiation from 80 nm to L-beta (102.6 nm). This layer exhibits the Chapman model behaviour with daily maximum at local noon, seasonal maximum in summer, and highly solar cycle dependence (MEIRA, 1971). Metallic ions such as Fe^+, Mg^+, Na^+ and Si^+ have also been discovered to form a thin layer called sporadic E within the E-region. The source of these metallic ions are the ablation of meteors that become ionized by photoionization or exchange of charges with ions present in the ionosphere. The metallic ions have a lifetime much longer than the molecular ions of E-region, therefore, the sporadic-E persist during the night once is formed (RISHBETH; GARRIOTT, 1969; MEIRA, 1971; HEELIS, 2004).

The F-region is a major segment of the terrestrial ionosphere and the most important from the point of view of radio communications and Global Navigation Satellite Systems (GNSS). It lies between the 140 and 600 km with altitudes extending to the upper limits of the ionosphere (MEIRA, 1971) depending on the season, latitude and rate of ionization. The F-region, corresponds to a dense layer consisting mainly of O^+, O_2^+, NO^+, and N_2^+ ions as shown in Figure 2.1. As a result of the complex physical processes involved in its formation, solar radiation causes the F-region to split into two separate layers, called F1 and F2.

Figure 2.2 depicts a typical electron density profile showing the various ionospheric layers for day and night (RISHBETH; GARRIOTT, 1969; HEELIS, 2004). The regions below and above the F2 peak are called the bottom-side and topside ionosphere respectively. The F1 layer is the layer with maximum electron density which occurs at midday and exhibits dependence on solar zenith angle and sunspot numbers. Accordingly, the F1 layer is more pronounced in summer than in winter season, however, it always disappears during the night: The main source of ionization is extreme ultraviolet (EUV) solar radiation in the wavelengths $\lambda \approx$ 58.4 and *30.4* nm (RISHBETH; GARRIOTT, 1969; MEIRA, 1971).

Figure 2.2 - A typical electron density profile of the Earth's ionosphere.

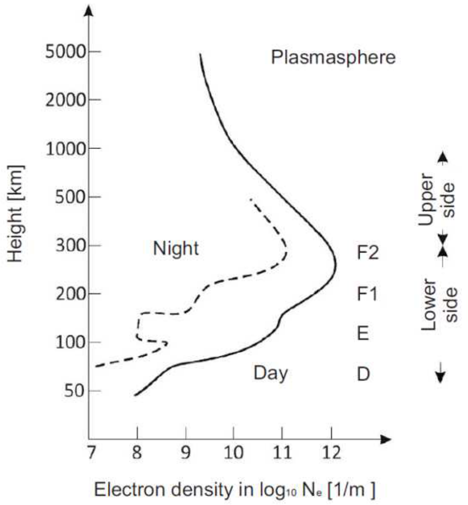

Source: Komjathy (1997).

The existence of F2 region during day and night makes it unique and an interesting research zone for scientific studies. In this region, the ratio of collision to gyrofrequency for both ions and electrons are very large, so the ion and electron velocities perpendicular to geomagnetic field ($\mathbf{B}$) are very nearly equal to each other. This means that the plasma flow velocity can be uniquely defined and related to the electric field.

The thermospheric wind system produced by the pressure inequalities in the solar EUV heating is the main driving force for the F-region dynamo. According to Rishbeth (1971), the idea of F-region having its own dynamo after sunset is due to the fact that the E-region conductivity becomes too small, thus the plasma in the F-region forms a layer with a well defined lower boundary as shown in the configuration Figure 2.3.

From Figure 2.3, the F-region plasma has a constant finite Pedersen conductivity inside the slab and zero outside, and a constant zonal wind (u) within the slab. The vertical polarization electric fields develop at the F-region, giving rise to a zonal drift ($\mathbf{V}_D = \mathbf{E} \times \mathbf{B}/B^2$) of the plasma, which is in the same direction and magnitude as that of the neutral wind during nighttime (RISHBETH, 1971; HEELIS, 2004). The magnitude of the electric fields which builds up as a result of these charges is such that

Figure 2.3 - Electrodynamics of the equatorial F-region in which the density and conductivity profiles subject to a constant zonal eastward neutral wind.

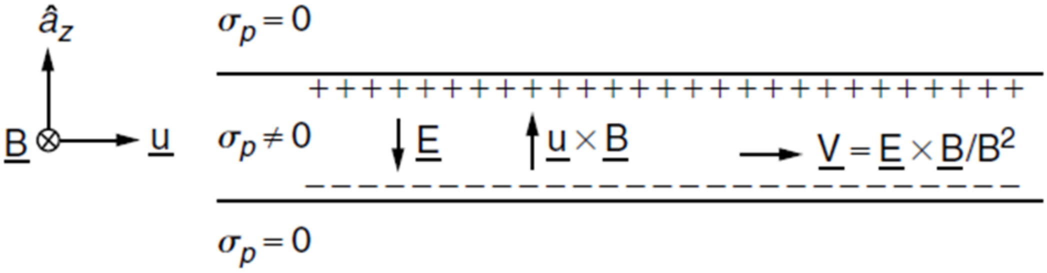

Source: Kelley (2009).

$$J_z = \sigma_p E_z + \sigma_p uB = 0 \tag{2.1}$$

This means that, $E_z = -u \times B = -uB$. Thus, the perfect F-region dynamo can be generalized as,

$$\mathbf{E}+\mathbf{U} \ \times \ \mathbf{B} = 0 \tag{2.2}$$

This implies that during nighttime, the electromagnetic force on the plasma vanishes and the thermospheric wind blows freely without ion drag. However, during daytime the process changes due to the integrated E-region conductivity which is comparable to or more than the magnetic field line integrated F-region conductivity. Hence, the F-region field cannot build up, and the daytime ion drag remains high (HEELIS et al., 1974). The magnitude of the electric field is essentially determined by the winds in the E-region and the ionospheric conductivity during the day.

$$E_z = -\frac{(u(z)B)\Sigma_P^F(z)}{\Sigma_P^F(z) + 2\Sigma_P^E(z)} \tag{2.3}$$

The model in Equation 2.3 can be used to explain the general diurnal variation in the vertical electric field that maps E- to F-region. During the nighttime, Σ_P^E becomes very small and thus $\mathbf{Ez} \approx -\mathbf{U} \times \mathbf{B}$ in regions where Σ_P^F smaller, for instance, near the F-region plasma density peak. On the order hand, during the daytime, the E-region conductivity is comparable to or larger than the magnetic field line-integrated

F-region conductivity (Σ_P^F). For large Σ_P^E the E-region controls the electrodynamics of the ionosphere. The dynamo in the E-region is driven by daytime tidal winds, which are smaller than the thermospheric winds in the F-region, explains the diurnal variation in the F-region zonal plasma drifts. At night the conductivity of the E-region becomes low, and the high zonal winds at several hundred kilometers altitude determine the vertical electric field and thus the horizontal plasma flow. For Σ_P^F and Σ_P^E the electric field will be almost equal to $\mathbf{U} \times \mathbf{B}$. The eastward plasma velocity nearly matches the neutral wind speed. During the day, however, the F-region dynamo loses control of the electrodynamics, and the resulting electric fields are determined by winds in the E-region. Since these winds tend to be weaker, the plasma drift is smaller during the day.

Furthermore, the equatorial ionosphere sometimes exhibits the presence of an additional layer known as the F3 layer between 500 km and 700 km altitude, depending on the meridional wind. This layer was first called the G-layer, however, when it was discovered that the layer had no distinct neutral species within it with also no new ionization processes occurring but arose essentially due to the dynamics of the F-layer at low-latitudes, Balan et al. (1997) named it F3.

2.2 Traveling Ionospheric Disturbances (TIDs)

One of the most important dynamic properties of the Earth's atmosphere is its ability to withstand oscillatory movements such as gravity waves, planetary waves, tidal waves and acoustic waves. The impact of these atmospheric waves on ionospheric plasma and variability has been realized for decades. These waves have the ability to carry energy and momentum from one point to another as well as modifying the local thermodynamic state of the atmosphere (**??**). In 1960, Hines (1960) pioneering work first proposed gravity waves as the cause of irregular motions in the thermosphere and ionosphere. This irregular motion is called Traveling Ionospheric Disturbances (TIDs) which is seen as the fluctuations on electron density in the ionosphere.

TIDs can be classified into three groups according to their characteristics such as amplitude, wavelength, velocity, period and source among others (HUNSUCKER, 1982; **??**): They are Large-Scale Traveling Ionoshperic Disturbances (LSTIDs), Medium-Scale Traveling Ionospheric Disturbances (MSTIDs) and Small-Scale Traveling Ionospheric Disturbance (SSTIDs) as shown in Table 2.1: LSTIDs are excited by high latitude processes in the auroral regions usually associated with geomagnetic storms. They are characterized by long horizontal wavelengths and high speeds and can travel long distances as far as equatorial region. For instance, in the midlatitude

Tsugawa et al. (2004) reported that LSTIDs are observed when the geomagnetic index, $kp >\sim 4$. AndFigueiredo et al. (2017), studied LSTIDs over South American sector during 17 and 18 March 2015 Saint Patrick geomagnetic storm. The SSTIDs, which have not been studied extensively, have wavelengths of less than 100 km and periods of few minutes. For the purpose of the present thesis, the discussion of TIDs will be limited to MSTIDs.

Table 2.1 - Types and characteristics of TIDs (NW, NE, SH and NH are Northwest, Northeast, Southern and Northern hemispheres respectively).

Type	Period	Wavelength (km)	Velocity (m/s)	Source region	Propagation direction
LSTIDs	30 min to several hours	λ>1000	300 to 1000	High latitudes	Equatorward
MSTIDs	15 min to 1 hour	$\lambda \leq 1500$	100 to 300	High and mid-latitudes	In all directions but mostly they propagate; from SE to NW in SH and NE to SW in NH
SSTIDs	few minutes	$\lambda \leq 100$	$\lambda \leq 200$	Not known	Not known

Adopted: Figueiredo et al. (2017) PhD thesis

MSTIDs have horizontal wavelength less than 1500 km, amplitude of less than 10% of TEC and velocities ranging from 100 to 500 m/s with a corresponding period of 10 to 40 min. region. Mostly, daytime MSTIDs occur in winter and tend to propagate southeastward and northeastward in the northern and southern hemispheres respectively Their propagation direction depends on the time of the day, season as well as the latitudes and the hemisphere of the source region (TSUGAWA et al., 2007; OTSUKA et al., 2013). Meanwhile, the nighttime MSTIDs occur during the summer months and propagate southwestward in the northern hemisphere and northeastward (OTSUKA et al., 2013) in the southern hemisphere (PIMENTA et al., 2008). The dawn and dusk MSTIDs occur frequently in summer and propagate eastward and north-northwestward respectively (OTSUKA et al., 2011). At midlatitude this produces approximately eastward propagating TIDs after sunrise, and approximately westward propagating waves after sunset (MACDOUGALL et al., 2009; MACDOUGALL et al., 2011). The daytime MSTIDs are not associated with F region irregularities, however, the nighttime is characterized with F-region irregularities (OGAWA et al., 2009).

MSTIDs were known to be the ionospheric manifestation of gravity waves from the neutral atmosphere (HINES, 1960), however, the advent of Global Positioning System (GPS) detrending TEC maps and airglow observations had also shown that nighttime MSTIDs are related to polarization electric fields in the mid latitude ionosphere (SHIOKAWA et al., 2003; TSUGAWA et al., 2007; PIMENTA et al., 2008; OTSUKA et al., 2013). Meanwhile, there is no enough proof yet that the nighttime MSTIDs from midlatitude propagate to the equatorial region (MAKELA et al., 2010), therefore, the concept of gravity waves is relevant to the dynamic procedures that occur in the atmosphere/ionosphere leading to MSTIDs.

2.2.1 Atmospheric gravity waves

Atmospheric gravity waves (AGWs) are periodic movement of air parcels that are generated in the troposphere by convective systems or by airflow over mountains which propagate vertically and horizontally, contributing to the atmospheric processes ranging from the transport of momentum and energy from their source to the sink, the mixing of the atmospheric constituents dynamics and coupling of neutral atmosphere and ionosphere (HINES, 1960; HOOKE, 1968; MEDVEDEV et al., 2015; ESSIEN et al., 2018). Another reason for the importance of AGW studies related to their practical applications is that energy and momentum fluxes transported by gravity waves from the lower to the upper atmosphere/ionosphere are comparable or even larger than those coming from the solar wind or other sources (FRANCIS, 1975; EBEL, 1984; FRITTS et al., 1990; KIM; MAHRT, 1992; ALEXANDER; PFISTER, 1995). Most complete survey of the observations of medium-scale gravity waves that are capable of propagating into ionosphere over Brazilian equatorial region has been presented by Essien et al. (2018).

The basic equations governing the idealized model of gravity waves in the neutral atmosphere are considered stationary, monochromatic with temperature and density. Thus, neutral atmospheric oscillations are characterized by three principles; conservation of momentum, mass and energy which are explained in Figueiredo et al. (2017), Fritts e Alexander (2003).

2.2.2 Gravity wave dissipative dispersion relation and amplitude decay in time

Inasmuch as MSTID is concerned, the AGWs dissipative dispersion and polarization relations, the amplitude decay rate in time, as well as the procedure to determine the gravity waves perturbations as a function of altitude are relevant using Vadas e

Becker (2017) analogy.

The thermosphere begins at the turbopause, which is located at an altitude of z$\sim$107 km and extends up to z$\sim$500-600 km in the Earth's atmosphere, depending on the latitude. This layer is characterized by a rapidly increasing kinematic viscosity with altitude, $v = \mu/\bar{\rho}$ where μ is the molecular viscosity and $\bar{\rho}$ is the background neutral density (HINES, 1960). Molecular viscosity resulting from collisions between neutral molecules. As the thermosphere becomes more rarefied with increasing altitude, molecular collisions are less frequent, so the velocity amplitude and direction of the molecules associated with a gravity waves are not transmitted effectively, thereby damping the gravity waves (PITTEWAY; HINES, 1963; HICKEY; COLE, 1988; VADAS, 2007; VADAS; BECKER, 2017; WALTERSCHEID; HICKEY, 2011; HEALE et al., 2014; FRITTS; ALEXANDER, 2003).

The gravity waves dispersion relation shown in Equation 2.4 is derived using the Wentzel-Kramers-Brillouin (WKB) approximation (VADAS; BECKER, 2017)

$$m^2 = \frac{k_H^2 N_B^2}{\omega_{lr}^2\left(1+\delta_+ + \delta^2/Pr\right)}\left[1+\frac{v^2}{4\omega_{lr}^2}\left(\mathbf{k}^2 - \frac{1}{4H^2}\right)^2 \frac{\left(1-Pr^{-1}\right)^2}{\left(1+\delta_+/2\right)^2}\right]^{-1} - k_H^2 - \frac{1}{4H^2} \tag{2.4}$$

where ω_{lr}^2 is the real part of the complex intrinsic frequency; k, l and m are the zonal, meridional, and vertical wave numbers, respectively; $k_H = \sqrt{k^2 + l^2}$ is the horizontal wave number; $\mathbf{k^2} = k_H^2 + m^2$; N_B is the buoyancy frequency; $H = -\bar{\rho}\left(d\bar{\rho}/dz\right)^{-1}$ is the neutral density scale height; $\kappa = v/Pr$ is the thermal diffusivity; Pr is the Prandtl number; $\delta = vm/H\omega_{lr}$; and $\delta_+ = \delta(1 + Pr^{-1})$. The zonal, meridional, and vertical wavelengths are $\lambda_x = 2\pi/l$, $\lambda_y = 2\pi/l$, and $\lambda_z = 2\pi/m$, respectively, and the horizontal wavelength is $H_H = 2\pi/k_H$.

For an upward propagating gravity waves, δ is negative since $m < 0$. This dispersion relation is anelastic and includes molecular viscosity and thermal conduction, the main mechanisms for damping high-frequency gravity waves in the thermosphere (VADAS; BECKER, 2017). It neglects ion drag, which is appropriate for gravity waves having periods less than one to several hours (GOSSARD; HOOKE, 1975) and neglects wave-induced diffusion, which is appropriate for gravity waves having periods less than an hour (GENIO et al., 1979). It also neglects the Coriolis force, which is appropriate for gravity waves having periods less than a few hours (VADAS; BECKER, 2017).

Relating the gravity waves intrinsic frequency to its observed frequency, $\omega_r = 2\pi/\tau_r$, via

$$\omega_r = \omega_{lr} + kU + lV = \omega_{lr} + k_H U_H \tag{2.5}$$

where U and V are the background zonal and meridional winds, respectively, U_H is the projection of the background neutral wind along the propagation direction of the gravity waves, and τ_r is the period of the observed gravity wave.

$$U_H = (kU + lV)/k_H \tag{2.6}$$

When dissipation is negligible (i.e., $v = \delta = 0$), Equation 2.4 reduces to the familiar gravity waves anelastic dispersion relation (GOSSARD; HOOKE, 1975; MARKS; ECKERMANN, 1995).

$$\omega_{lr}^2 \simeq \frac{k_H^2 N_B^2}{m^2 + k_H^2 + \frac{1}{4H^2}} \tag{2.7}$$

Considering the dissipation of a gravity waves packet explicitly in time and implicitly in z (rather than explicitly in z and independent of time, which results in a steady state gravity waves solution), it assumed a complex intrinsic frequency ω_l (rather than a complex vertical wave number m). Thus, the ansatz utilized to derive Equation 2.4 is as follows:

$$\omega_l = \omega_{lr} + i\omega_{li} \tag{2.8}$$

where ω_{li} is the inverse decay rate in time of a gravity waves. Because a gravity waves amplitude is proportional to $\exp(-i\omega_{li}) = \exp(\omega_{li}t)\exp(\omega_{lr}t)$, a gravity waves decays explicitly in time here rather than explicitly in altitude. This ansatz results in an inverse decay rate in time of (VADAS; FRITTS, 2005). Note that ω_{li} varies significantly along a gravity waves raypath.

$$\omega_{li} = \frac{v}{2}\left(\mathbf{k^2} - \frac{1}{4H^2}\right)\frac{[1 + (1 + 2\delta)/Pr]}{(1 + \delta_+/2)} \tag{2.9}$$

2.2.3 Grace wave dissipative polarization relations

As a linear gravity wave dissipates in the thermosphere, the amplitudes and phases between the various perturbation components such as velocity, temperature, and density change (VADAS; FRITTS, 2005; VADAS; NICOLLS, 2012; VADAS; BECKER, 2017). The equations which describe these changes are called the gravity wave polarization relations (VADAS; BECKER, 2017). These expressions differ from the usual gravity waves dispersion relations in Vadas (2013), Fritts e Alexander (2003). They included gravity waves dissipation from kinematic viscosity and thermal diffusivity.

For the purpose of deriving the gravity waves polarization relations, the background temperature $T = \bar{T}$ is set to be constant (i.e., isothermal): (Afterward, these relations can be applied to a fluid with a slowly varying background:) This results in a background neutral density which varies exponentially with altitude: $\tilde{\rho} = \tilde{\rho}_0 \exp(-z/H)$, where $\tilde{\rho}_0$ is the background density at $z = 0$ and over lines denote mean values (HINES, 1960; VADAS; BECKER, 2017). The density-scaled perturbations are thus defined as

$$\begin{aligned}
\tilde{u} &= e^{-z/2H}u^{'} \\
\tilde{v} &= e^{-z/2H}v^{'} \\
\tilde{w} &= e^{-z/2H}w^{'} \\
\tilde{u_H} &= e^{-z/2H}u_H^{'} \\
\tilde{\rho} &= e^{-z/2H}\rho^{'} \\
\tilde{T} &= e^{-z/2H}T^{'}
\end{aligned} \tag{2.10}$$

where tildes $''\sim''$ represent the density-scaled variables, $u^{'} = \sqrt{(u')^2 + (v')^2}$ is the gravity waves horizontal velocity perturbation (positive by definition) and all the primes denote perturbations, which can be expressed as,

$$\begin{aligned}
u^{'} &= \frac{k}{k_H}u_H^{'} \\
v^{'} &= \frac{l}{k_H}u_H^{'}
\end{aligned} \tag{2.11}$$

Here the gravity waves perturbation variables are the zonal, meridional, and vertical velocities $u^{'}$, $v^{'}$, and $w^{'}$, respectively, the density $\rho^{'}$, and the temperature $T^{'}$. The fluid equations are linearized and then write each perturbation component in Equation 2.10 as, for example, and $\tilde{u}_0$, $\tilde{u}_0$ among others are the amplitudes of the gravity waves at (x, y, z, t).

$$\tilde{u} = \tilde{u}_0^{'} \exp[i(kx + ly + mz - \omega t)] \tag{2.12}$$

where ω and ω_l are the complex frequency and intrinsic frequency respectively and $\tilde{u}_0$, $\tilde{u}_0$ among others are the amplitudes of the gravity wave at (x, y, z, t).

$$\omega_l = \omega - kU - lV \tag{2.13}$$

The dissipative anelastic gravity wave polarization relations interrelating these perturbations are (VADAS; FRITTS, 2005; VADAS; NICOLLS, 2009; VADAS; NICOLLS, 2012):

$$\frac{\tilde{w}}{\tilde{u_{H_0}}} = -\frac{k_H}{m^2 + \frac{1}{4H^2}}\left[1 - \frac{\mathbf{k^2} + \frac{1}{4H^2}(\omega_l - i\alpha v)}{2mHk_H^2N_B^2}\left[\left(\frac{2}{\gamma} - 1\right)\omega_l - \frac{i\alpha v}{Pr}\right]\right] \tag{2.14}$$

$$\frac{\tilde{T}}{\tilde{w}_0} \simeq \frac{(\gamma - 1)\tilde{T}}{HD}\left(im - \frac{1}{2H}\right) \tag{2.15}$$

$$\frac{\tilde{\rho}}{\tilde{w}_0} \simeq \frac{(\gamma - 1)\tilde{\rho}}{HD}\left(im - \frac{1}{2H}\right) \tag{2.16}$$

$$\frac{\tilde{u}_0}{\tilde{u_{H_0}}} = \frac{k}{k_H} \tag{2.17}$$

$$\frac{\tilde{v}_0}{\tilde{u_{H_0}}} = \frac{l}{k_H} \tag{2.18}$$

where

$$\alpha \equiv -\mathbf{b} + \frac{1}{4H^2} + \frac{im}{H} \tag{2.19}$$

$$D = \left[i\omega_l \left(\gamma im + \frac{1}{H} - \frac{\gamma}{2H} \right) + \frac{\gamma \alpha v}{Pr} \left(im + \frac{1}{2H} \right) \right] \tag{2.20}$$

$\gamma - 1 = R/C_v$ and C_v is the mean specific heat at constant volume, $R = (8314/X_{MW})m^2 s^{-2} K^{-1}$, and X_{MW} is the mean molecular weight of a molecule in the fluid (in gâmol). Note that the right-hand sides of Equation 2.14 to Equation 2.20 only depend on the parameters of a gravity waves (such as (k, l, m) and ω_{lr}) and on the background parameters (such as H and N_B), and not on the gravity waves amplitude. In general, the ratios $\tilde{w}_0/\tilde{u}_{H0}$, $\tilde{T}_0/\tilde{w}_0$, $\tilde{\rho}_0/\tilde{u}_0$, $\tilde{u}_0/\tilde{u}_{H0}$, and $\tilde{v}_0/\tilde{u}_{H0}$ are complex and thus can be written as a $exp(ib)$, where a is the ratio of the amplitudes and b is the phase difference between the components. Equation 2.10 and Equation 2.12 are then used to extract the perturbation amplitude and phases. For example, using equations Equation 2.10, Equation 2.12, and Equation 2.16, the ratio of the density perturbation to the vertical velocity perturbation is

$$\frac{\rho'}{w'} = \left(\frac{\bar{\rho}}{\rho_0} \right) \left(\frac{\tilde{\rho}}{\tilde{\rho}_0} \right) = -\frac{(\gamma - 1)\tilde{\rho}}{HD} \left(im - \frac{1}{2H} \right) \tag{2.21}$$

The perturbation quantities of a gravity waves are determined along its ray path, and the initial momentum flux of a gravity waves at $x = x_i$ and $t = t_i$ is $\overline{u'w'}(\mathbf{x}, t)$. The momentum flux of this gravity waves at a later time t and location $\mathbf{x}$ along its ray path is (VADAS; NICOLLS, 2009) is as expressed as:

$$\overline{u'_H w'}(\mathbf{x}, t) = \overline{u'_H w'}(\mathbf{x}, t) \frac{\rho(\bar{z_i})}{\rho(z)} \exp \left(-2 \int_{t_i}^{t} |w_{li}| \, dt' \right) \tag{2.22}$$

An absolute value around ω_{li} is put to ensure that the gravity wave dissipates even if $\mathbf{k}^2 < 1$â$4H^2$ and where the integral of $|\omega_{li}|$ is performed along the ray path. The horizontal and vertical velocity, temperature, and density perturbations along the ray path are then

$$w' = \sqrt{\left| \frac{\tilde{w_0}}{\tilde{u_{H0}}} \right| \overline{u'_H w'}} \tag{2.23}$$

$$u'_H = \left(\frac{\tilde{w_0}}{\tilde{u_{H0}}} \right)^{-1} w' \tag{2.24}$$

$$u'_H = \left(\frac{\tilde{u}_0}{\tilde{u_{H0}}}\right) u'_H \tag{2.25}$$

$$v'_H = \left(\frac{\tilde{v}_0}{\tilde{u_{H0}}}\right) u'_H \tag{2.26}$$

$$\rho' = \frac{\bar{\rho}}{\bar{\rho}_0}\left(\frac{\tilde{\rho}}{\tilde{w}_0}\right) w' \tag{2.27}$$

where the phases are defined relative to the phase of w', and Equation 2.27 is obtained from Equation 2.21. Here, $({}_0/\tilde{u_{H0}}), (\tilde{v}_0/\tilde{u_{H0}}), (\tilde{w}_0/\tilde{u_{H0}}), (\tilde{T}_0/\tilde{w}_0), and({}_0/\tilde{w}_0)$ are calculated from Equation 2.14 to Equation 2.18, and

$$\left|\frac{\tilde{w}_0}{\tilde{u_{H_0}}}\right| = \sqrt{\left(\frac{\tilde{w}_0}{\tilde{u_{H_0}}}\right)\left(\frac{\tilde{w}_0}{\tilde{u_{H_0}}}\right)^{\star}} \tag{2.28}$$

where the complex conjugate are denoted with "asterisk". General, u', v', w'_H, T' and ρ' are complex numbers and hence, have nonzero phases relative w'. In the present work, Equation 2.23 to Equation 2.23 do not take into account the decrease of a gravity waves amplitude due to the geometric spreading of a wave packet in time, which is proportional to $1/z^2$. This is likely adequate here, since mostly the gravity waves that propagate into the ionosphere are medium to large scale, and their momentum fluxes are only computed from $z_i = 220$ km to $z \sim 385$ km.

2.2.4 TID created by a gravity wave

Here, the review the mechanism by which a gravity wave creates a TID as well as the expression for a gravity wave momentum flux at the observation altitude in terms of the TID properties and the Earth's magnetic field orientation are considered.

The thermosphere is generally considered to begin just above the turbopause at $z \sim 107$ km, while the ionosphere is located above $z \geq 90$ km. As a gravity wave propagates within the neutral thermosphere, the neutral molecules in the gravity wave collide with the ions. The neutral wind perturbations associated with a gravity wave push and pull the plasma along the Earthâs magnetic field lines through ion drag, thereby creating a TID (KLOSTERMEYER, 1972; YEH; LIU, 1974; KIRCHENGAST, ; SQUAT; SCHLEGEL, 1996; VADAS; BECKER, 2017). This plasma disturbance is not self-sustaining but relies on the gravity wave for its maintenance (VADAS; BECKER, 2017).

From Appendix A in Nicolls et al. (2014), the ion velocity perturbations induced by a gravity wave is therefore, reviewed here. Then compute the vertical displacement of the ions created by a gravity waves. Considering the F region of the ionosphere, whereby a single ion, O^+, dominates (approximately $z > 200$ km) [(BANKS; KOCKARTS, 1973). (Other ions important in the D and E regions of the ionosphere, N_2^+ , O_2^+ , and NO_+, can be taken into account via the inclusion of chemical reactions) (BANKS; KOCKARTS, 1973; YU et al., 2017). If a gravity wave propagates with an azimuth of ψ (clockwise from north), then

$$k = k_H \sin\psi l = k_H \cos\psi \tag{2.29}$$

The corresponding wind velocity vector of this gravity wave can be written as follows:

$$u' = (u'_0\hat{i} + v'_0\hat{j} + w'_0\hat{k})exp(i\phi) \tag{2.30}$$

where u'_0, v'_0, and w'_0, are the zonal, meridional, and vertical velocity amplitudes, respectively; Ì$\hat{i}$, Ì$\hat{j}$, and $\hat{k}$ are the unit vectors in the geographic zonal (positive eastward), meridional (positive northward), and vertical (positive upward) directions, respectively; and ω is the phase of the gravity wave:

$$\phi = kx + ly + mz - \omega_r t \tag{2.31}$$

Note that u'_0 and v'_0 are in general complex in order to capture the phase difference between u'_0 and w'_0 and between v'_0 and w'_0.

Due to the neutral-ion collisions, and an ion can only easily move along the Earth's magnetic field, the induced ion velocity perturbation is approximately equal to the projection of the gravity waves velocity vector along the magnetic field. The unit vector along the magnetic field is

$$\hat{\mathbf{B}} = cosIsinD\hat{i} + cosIcosD\hat{j} - sinI\hat{k} \tag{2.32}$$

where I is the dip or inclination angle and D is the magnetic declination angle (or the angle between magnetic and geographic north). Here$I$ is defined positive down by convention in order to be consistent with the International Geomagnetic Reference Field (IGRF) model, whereas it was oppositely defined in (NICOLLS et al., 2014). For example, in the Southern (northern) Hemisphere $\hat{B}$ points upward (downward) although $I < 0$ ($I > 0$) in the IGRF model. Thus, the results of (NICOLLS et al., 2014) can be applied here with the substitution $I \rightarrow -I$). The ion velocity perturbation induced by a gravity waves is then given by

$$v_i' = v_{i0}' exp(i\phi)\hat{\mathbf{B}} \tag{2.33}$$

Here v_{i0}' is the ion velocity amplitude and is determined from equations Equation 2.30 and Equation 2.32:

$$v_{i0}' = (\mathbf{u}' \cdot \hat{\mathbf{B}})/exp(i\phi) = cosI(u_0' sinD + w_0' cosD) - w_0' sinI \tag{2.34}$$

The vertical component of the induced ion velocity is

$$w_i' = w_{i0}' exp(i\phi) \tag{2.35}$$

Using equations Equation 2.32 and Equation 2.33,

$$w_i' = v_i' \cdot k = -v_{i0}' sinI exp(i\phi) \tag{2.36}$$

Therefore, the amplitude of the TIDs vertical velocity is

$$w_{i0}' = v_{i0}' sinI \tag{2.37}$$

The vertical displacement of the ions during one quarter of a gravity wave period is then

$$h_i = \int_0^{\tau_r/4} |w_i'| \, dt = \left| \frac{e^{i(kx+ly+mz)} w_{i0}'}{w_r} exp(-i\omega_r t) \right|_0^{\tau_r/4} = \frac{|v_{i0}' sinI| \, \tau_r}{2\pi} \tag{2.38}$$

Where h_i is the height of the wave amplitude at the radio reflection height and since τ_r is measured, the ion velocity amplitude, v'_{i0} can be determined from Equation 2.38.

2.3 Observation of MSTIDs

MSTIDs have been studied since 1940s using variety of techniques such as ionosondes (RÖTTGER, 1977; MORGAN et al., 1978; MACDOUGALL et al., 2009; MACDOUGALL et al., 2011; AMORIM et al., 2011), satellite (EVANS; WAND, 1983; EVANS et al., 1983; JACOBSON et al., 1995), incoherent scatter radar (BEHNKE, 1979; KIRCHENGAST,), all-sky-imager (SOBRAL et al., 2001; CANDIDO et al., 2008; PIMENTA et al., 2008; PAULINO et al., 2016) and Global Positioning System (GPS) receivers network (SAITO et al., 1998; TSUGAWA et al., 2007; OTSUKA et al., 2013; JONAH et al., 2016; FIGUEIREDO et al., 2017; FIGUEIREDO et al., 2018a) among others. This section will exclusively focus on the global observation of MSTIDs.

2.3.1 Observation of MSTIDs in Low and Equatorial Region

In the equatorial ionosphere (±15°), we will discuss the work done by Röttger (1977) in Congolese and Peruvian regions using HF-ground-backscatter, MacDougall et al. (2011) work on day and nighttime MSTIDs in northeast of Brazil also using ionosonde,Husin et al. (2011) work in the Malaysian region using GPS detrending TEC maps, Jonah et al. (2017) work on conjugate daytime MSTIDs also using GPS dTEC maps and Paulino et al. (2016) nighttime MSTIDs using all-sky images among others.

In the South America low latitude (between 15°S and 30°S), the first nighttime MSTID observations was reported by Sobral et al. (2001) using the All-Sky imager in Cachoeira Paulista, Brazil. Pimenta et al. (2008) extensively observed 5 years nighttime dark band purported to be MSTIDs using all-sky imaging systems in the Brazilian low latitude sector. Candido et al. (2008) observed nighttime MSTIDs at the same site, intensifying what Pimenta et al. (2008) studied by 15 months. They also reported that Perkins instability is main mechanism to explain the direction of propagation and origin of nighttime MSTIDs over southeast of Brazil. Amorim et al. (2011) also conducted a statistical study between 1990 and 2008, using six years of the data used by Pimenta et al. (2008) and Candido et al. (2008) as well as the ion probe data to obtain $h'F$ and foF2 values which presented spread F associated with the observed MSTIDs. Figueiredo et al. (2018a) recently studied day and nighttime MSTID over south-southeast of Brazil using GPS detrending TEC map.

Röttger (1977) used HF-ground-backscatter to investigate the characteristics of MSTIDs over the equatorial zones of Africa and South America. The backscatter ionograms were recorded in Tsumeb/Southern Africa, transmitting to the north at the area of $\sim 5° - 10°$S geographic latitude. The mean phase velocity, period and horizontal wavelength of the MSTIDs obtained from the African equatorial region were 110 m/s, 20 min and 130 km respectively, and they propagated meridional out of the equatorial region over Africa. On the other hand, the results from Huancayo, Peru, yielded the mean horizontal velocity of 210 m/s, period between 30 min and the mean horizontal wavelength of 150 km, and they propagated southward away from the tropical rainforest. They found out that the diurnal variation of the occurrence of MSTIDs were maxima during the morning and the afternoon/evening hours. The seasonal variation of the MSTIDs indicated that during summer in southern hemisphere(October-February) only a small number of events were observed around noon, however, the diurnal maximum in summer showed up in the evening hours. Meanwhile, the morning and late afternoon maxima were most pronounced during the equinoxes and southern winter (May-August) as shown in Figure 2.4. Each vertical line is the mean of three days of evaluation. Local time in the probed ionospheric area near the Tsumeb territory is approximately $UT + 1h$. In both regions, significant correlation of the TID occurrence and tropical rainfall activity was investigated to prove that the observed MSTIDs were caused by gravity waves excited by penetrative cumulus convection in the intertropical convergence zone.

Figure 2.4 - TID occurrence in the equatorial zone of Africa, deduced from backscatter records (11.345.3 MHz). The indications C, E denote that no evaluation was possible due to equipment failure or due to too low critical frequency.

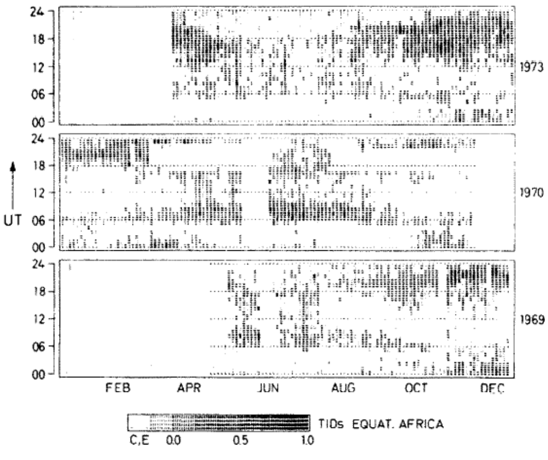

Source: Röttger (1977).

In the equatorial region of Brazil around latitude 10° south of the magnetic and geographic equators, MacDougall et al. (2011) measured the motion of day MSTIDs for one year (January to December 2010), using spaced fixed frequency radio transmitters. They reported that most of the MSTIDs propagated to southeast direction (i. e. 150° clockwise from north). However, there were few that propagated northeastward during local winter months (April to September) and this occurred normally during the afternoon and evening hours as shown in the upper panel of Figure 2.5. They postulated that the possible source of the MSTIDs that propagated southeastward could be the Inter-Tropical Convergence Zone (ITCZ) which is located south in December solstice and north in June solstice (CITEAU et al., 1986; WALISER; GAUTIER, 1993; TSUNODA, 2010). They proposed that for further evidence to establish the connection between the ITCZ and TIDs, further continuous measurements should be done at the same location. They reported that the source location of the northeast propagating MSTIDs were not compatible with any of the possible source patterns in the study area, so they suggested that further source possibility for the northward propagating MSTIDs might be the known MSTIDs that are generated by powerful weather disturbances near the Antarctic continent (GALUSHKO et al., 2007). The propagation speeds of the observed MSTIDs were typically between 150 and 300 m/s in all months as shown in the lower panel of Figure 2.5. Meanwhile, the nighttime MSTIDs were rare whenever there was strong sporadic-E and spread F occurrences.

Figure 2.5 - The propagation direction Azimuth and speed of the TID measured from March 2010 to February 2011 at northeast of Brazil.

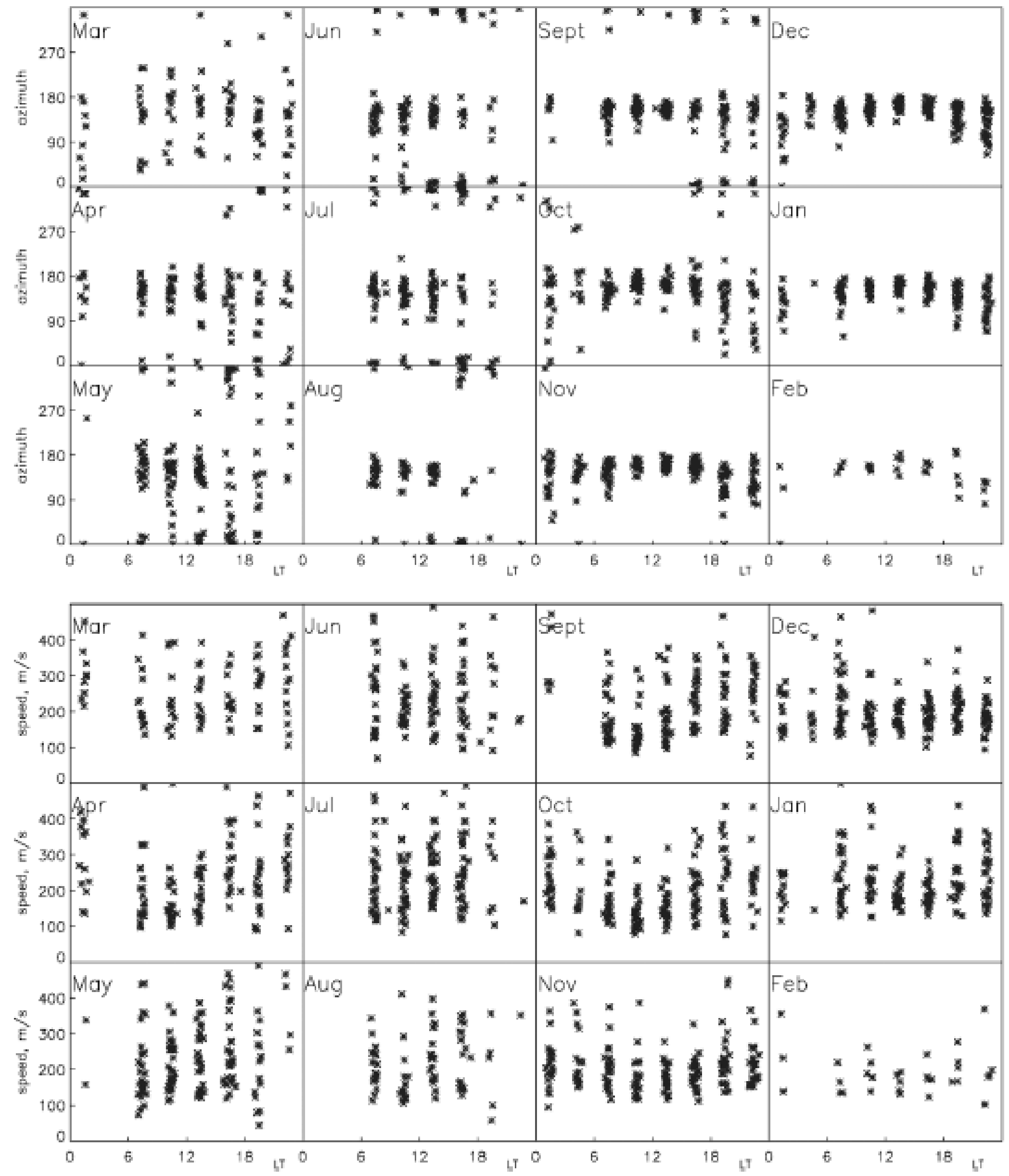

Source: MacDougall et al. (2011).

In the Malaysian equatorial latitude (3° south and 12° north of the geographical equator), Husin et al. (2011) observed time variations of TEC caused by MSTIDs during geomagnetic quiet time in September 2007, using GPS MyRTKnet network over Peninsular Malaysia. They associated the two dimensional map of the vTEC fluctuation (detrended TEC) variations with the occurrence of MSTIDs. The analysis of the cross correlation of the detrended TEC data yielded MSTID velocities around 100 ± 50 m/s in daytime and 60 ± 30 m/s during nighttime with the probability of occurrence of 17.6% and 13.7% respectively. Figure 2.6 shows the vTEC perturbation obtained using Ionospheric Piercing Point (IPP) trajectories during four intervals of 30 min (i.e., 0000-0030 UT, 0030-0100 UT, 0100-0130 UT and 0130-0200 UT): It is evident that the MSTIDs over the map is propagating equatorward and westward, and they reported that all the MSTID oscillations during the period of the study predominately followed the same directions. They suggested that the propagation direction might be influenced by the background thermospheric wind around an altitude of $\sim 400km$.

Figure 2.6 - MSTIDs oscillations on Malaysian map based on 6th September 2007 during the following observation periods: (a) 0000-0030 UT, (b) 0030-0100 UT, (c) 0100-0130 UT and (d) 0130-0200 UT.

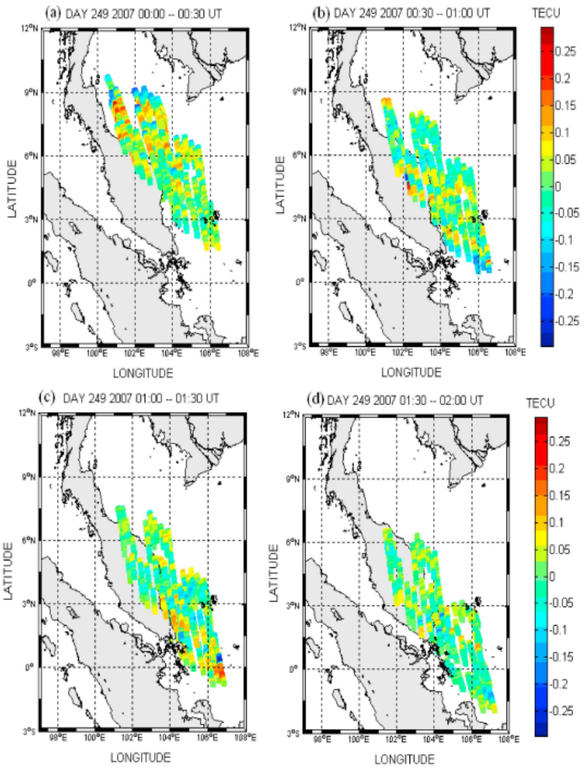

Source: Husin et al. (2011).

Jonah et al. (2017) also observed the characteristics of geomagnetically conjugate daytime MSTIDs over the South America sector using detrended TEC derived from GPS receivers over the Brazilian. They selected the geographic grid of latitude 1°N to 14°S and longitude 60°W to 50°W for the study, and used the cross-correlation method between two latitudes and longitudes in time to observe the propagation of the MSTID waves. Figure 2.7 presents example of TEC disturbances derived during quiet geomagnetic conditions ($Kp \leq 3$) on 17 December 2014 during 12-17 UT. The upper panel represents the TEC polynomial fit $\triangle TEC$ as function of universal time which depicts the temporal variations of the TEC disturbance extracted in the latitude. In this case, each line plot represents the latitudinal oscillation for each 0.5° latitude. Whereas the lower panel denotes the corresponding cross-correlation maps in latitude as function of universal time which shows MSTID events oscillate in time with period of 20 to 35 min at both southern and northern regions. According to them, the MSTIDs were well developed at both hemispheres and their peak amplitudes varied from one hemisphere to another. Therefore, they suggested that the MSTIDs were generated in one Hemisphere by gravity wave-induced electric fields, and mirrored along the magnetic field lines to the conjugate hemisphere.

Figure 2.7 - (top) The TEC disturbance in latitude. Each line represents latitude/longitude as indicated in the legend. (bottom) MSTID propagation derived from the cross-correlation coefficients in latitude.

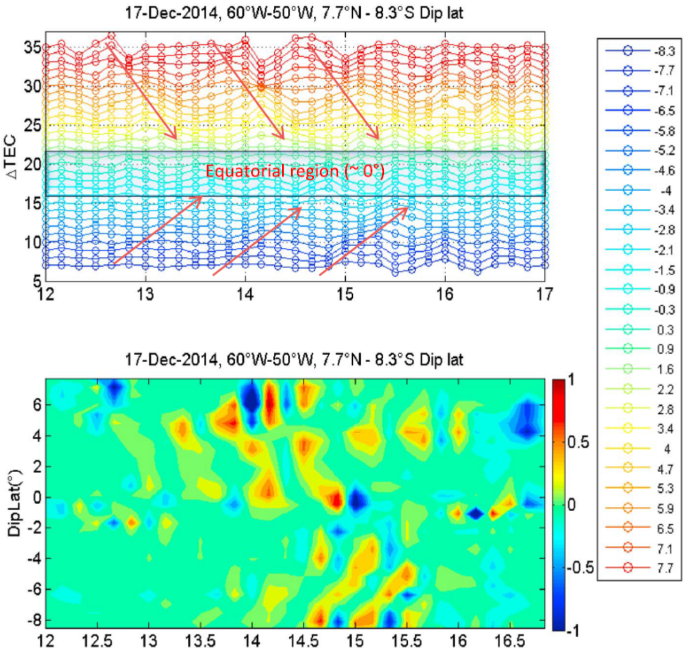

Source: Jonah et al. (2017).

Paulino et al. (2016) studied nighttime periodic wave structures so called be MSTIDs in the thermosphere over Brazilian equatorial region from September 2000 to November 2010 using OI630.0 nm airglow images at Cariri (geographic coordinates: 36.5°W, 7.4°S; geomagnetic coordinates based on IGRF model to 2015: 35.8° W, 0.48 N). In total, they characterized 98 waves. The period, horizontal wavelength and phase speed observed were ranged from; 10 to 35 min, 100 to 200 km, and 30 to 180 m/s respectively. Figure 2.8 shows a typical example of a periodic wave observed on 20 September 2006 that was propagating from southeast to northwest. Most of the observed waves appeared during magnetically quiet nights, and the occurrence of those waves followed the solar activity. On the other hand, most of the waves observed did not present a phase front parallel to the northeast-southwest direction, which is predicted by the Perkins instability process. They suggested that the observed waves have different generation mechanisms from the Perkins instability, which is the source mechanism for the nighttime MSTIDs generated in the midlatitude lower thermosphere.

Figure 2.8 - Sequence of unwarped images showing a gravity wave propagating to the northwest observed on 20 September 2006. Darkened grooves in the center of the images represent the Milky Way and the white arrows are pointed in the propagation direction of the wave.

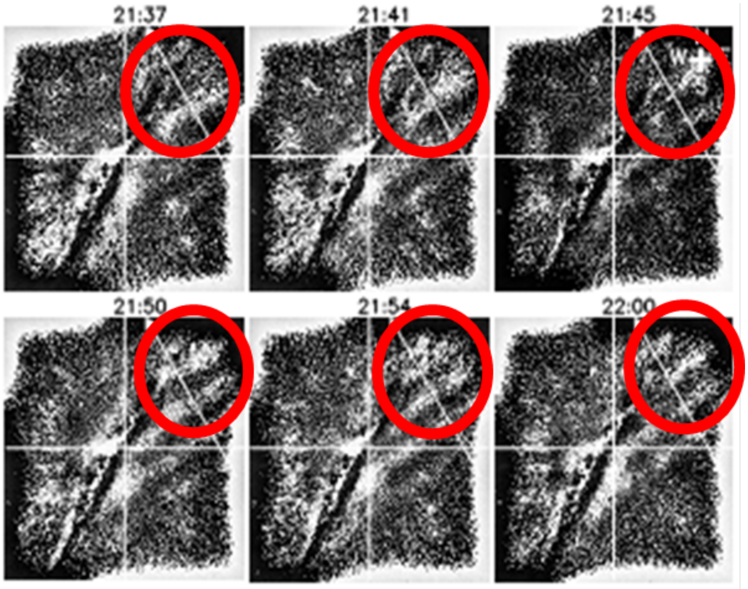

Source: Paulino et al. (2016).

Takahashi et al. (2018) studied the occurrences of equatorial plasma bubbles (EPBs) and MSTIDs using GPS TEC map, ionograms, and 630 nm all-sky airglow images observed over the South American continent during the period of 2014-2015. According to them, they observed a close relationship between the inter-bubble distance and the horizontal wavelength of the MSTIDs which followed by EPBs occurred primarily in the afternoon to evening period under strong tropospheric convective activities. They suggested based on the relationship that MSTIDs could be one of the seeding sources of EPBs. They proposed that many MSTIDs likely had their origin in atmospheric gravity waves generated in tropospheric convection and the ITCZ.

In the low latitude region over Brazilian sector, Pimenta et al. (2008) used two ground-based all-sky imaging systems to detect some moving dark band structures in the OI 630.0 nm night-glow emission purported to be MSTIDs. These measurements were made on 30-31 August 1995, 18-19 July 1998, and 13-14 July 1999 at Cachoeira Paulista (22.7°S, 45°W, magnetic declination 20°W). They reported that the dark band structures observed stretched across the entire image and propagated from southeast to northwest with propagation velocity between 50 and 200 m/s as shown in Figure 2.9. They suggested that the observed dark band structures were probably formed in the midlatitude region and propagated into the field of view of the imaging system situated in the low latitude region of Brazil. They also used Digisonde observations to register abrupt increases in both the F-layer peak height (hmF2) and minimum virtual height ($h'F$) on 19 July 1998 and 13 July 1999 when the low-intensity band passed over Cachoeira Paulista. They pointed out that the nighttime MSTID events were not related to geomagnetic disturbed conditions since the period was with $Kp < 2$. They also reported that the nighttime MSTIDs were more frequent during low solar activity and rising phase.

Figure 2.9 - Dark band structure observed by the airglow OI 630 nm emission on 13 July 1999 from 2147 to 2355 LT at Cachoeira Paulista using all-sky imager.

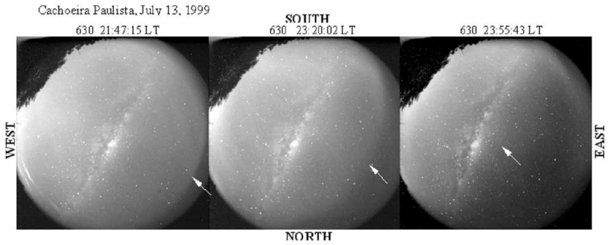

Source: Pimenta et al. (2008).

In the low latitude region over South America (south-southeast of Brazil), Figueiredo et al. (2018a) studied day and nighttime MSTIDs from December 2012 to February 2016 using GPS TEC perturbation maps and keograms. Out of 826 MSTIDs observed, most of them were found during the daytime around 11 to 15 local time in winter (June-August) and near to dusk solar terminator (17-19 local time) in the other seasons. According to them, the highest occurred in the winter months (44%), followed by the equinoxes (42%), and summer solstice (14%). Figure 2.10 shows an example of dTEC map on 10 August 2014, between 17:00 and 18:00 UT propagating northeastward (where from red and blue denote crest and trough respectively). The mean horizontal wavelength, period, and horizontal phase velocity were 445 ± 107 km, 23±4 min and 322±81 m/s, respectively. They found out that during the winter, the waves propagated to north-northeast, while in the other seasons they propagated to other directions. The anisotropy observed in the MSTID propagation direction were attributed to the source region of the gravity wave in the troposphere. They also suggested that atmospheric gravity waves in the thermosphere, mesosphere, and troposphere could be the possible precursor of the MSTIDs. According to them, the source region might had influenced the propagation direction of the MSTIDs. However, they suggested that ray tracing could be the possible method understand the source region of the MSTIDs observed (VADAS, 2007; VADAS; CROWLEY, 2010). They also recommended to investigate MSTIDs in the equatorial region to find out if they act as a precursor of plasma bubble generation or not.

Figure 2.10 - dTEC map on 10 August 2014, between 17:00 and 18:00 UT propagating northeastward over south-southeast of Brazil (where from red and blue denote crest and trough respectively).

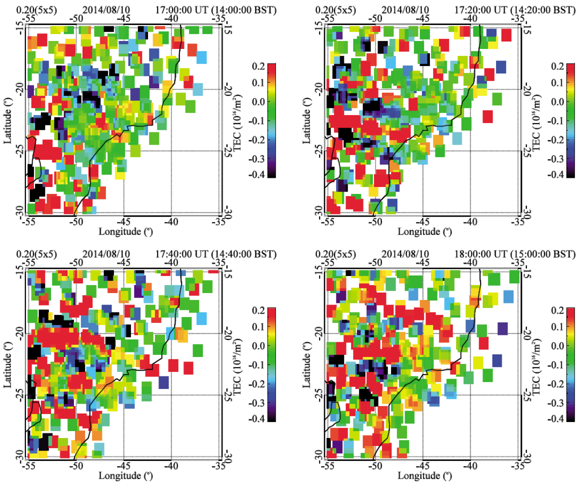

Source: Figueiredo et al. (2018a).

2.3.2 Observation of MSTIDs in Mid and High latitude

In the mid-latitude ionosphere, traveling ionospheric disturbances (TIDs), have been observed by using various techniques. Among others, this section will discuss, the work done by Saito et al. (1998), Saito et al. (2001), Tsugawa et al. (2007), Kotake et al. (2006) and Otsuka et al. (2013), in which all of them used GPS TEC perturbation maps to study MSTIDs over the midlatitude.

Saito et al. (1998) is the pioneer of the two-dimensional GPS TEC perturbation maps when they first used the technique to study the TIDs over Japan. Figure 2.11(a)-(d) shows the first ever two-dimensional nighttime TEC perturbations maps covering longitude 128°E to 146°E and latitude 32°N to 46°N that was composed to separate spatial and temporal variations of TIDs. At 21:40:00 JST several bandlike structures of high and low TEC values elongated from north-northwest to south-southeast are seen. In Figure 2.14(a), the difference between the maximum and minimum perturbation of TEC around 136°E and 134°E respectively is $0.8 \times 10^{16} el/m^2$. During the next 40 minutes, the TID structures kept traveling to southwestward as their amplitude changes gradually. They recommended TEC perturbation mapping as a strong tool to investigate the ionospheric structures such as TIDs.

Figure 2.11 - Two-dimensional maps of GPS TEC perturbations over Japan at (a) 21:40:00, (b) 21:50:00, (c) 22:00:00 and (d) 22:10:00 on July 03, 1997 in JST. One pixel is 0.15° latitude × 0.15° longitude.

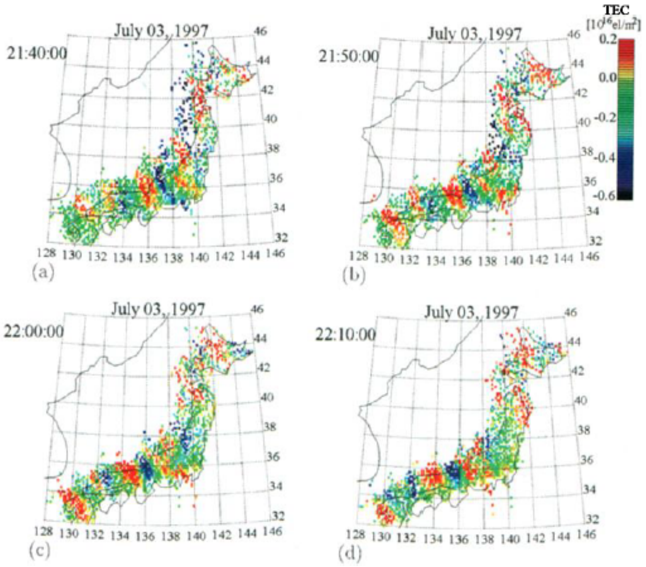

Source: Saito et al. (1998).

Also, Saito et al. (2001) observed nighttime TIDs at midlatitudes in May, 1998 and August, 1999 using all-sky CCD cameras and a GPS receiver network observed a wide area of the ionosphere over Japan. Figure 2.12 shows a typical example of GPS TEC perturbation map and Structures of 630 nm band airglow were detected on May 22, 1998 by all-sky imager over Japan. From Figure 2.12a, the wave fronts of TEC stretching from the northwest to the southeast. The wavelength was longer in the northern part of Japan than in the southern part whereas the amplitude was more intense in the southern part. At 00:00 on May 22, 1998 JST, the wavelengths in the southwestern part of Japan were 160km, 240km, 320km and 400km, and those in the northeastern were 320km and 500km. The peak to peak amplitudes of TEC variations around 00:00 was 1.59 TECU over Shigaraki and 0.32 over Moshiri. The cluster of all-sky CCD cameras observed wavefront structures of the airglow that were similar to the TEC structures. The composite map of the airglow around 23:20 on May 22, 1998 JST is presented in Figure 2.12b. The structures of airglow shows significant coincidence with the GPS TEC perturbation structures.

Figure 2.12 - Two-dimensional distribution of total electron content at 23:20:00 (a) and 630nm band airglow between 23:17:34 and 23:21:39 (b) on May 22, 1998 (JST).

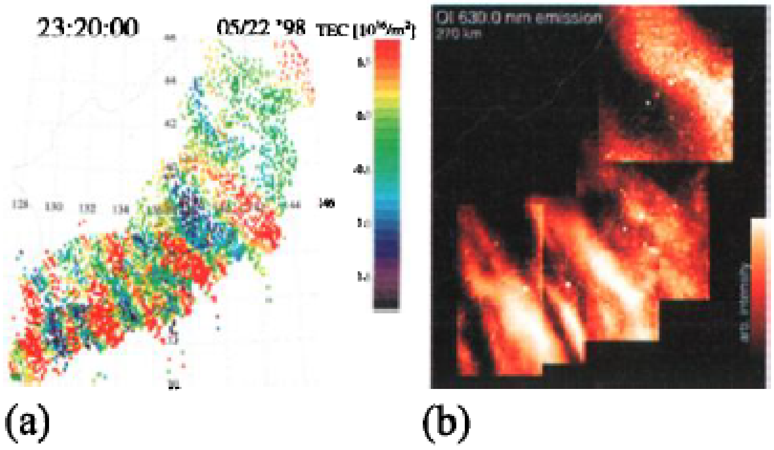

Source: Saito et al. (2001).

In the midlatiude, Tsugawa et al. (2007) detected day and nighttime MSTIDs with the dense and wide dTEC maps over North America using multiple GPS receiver networks. Figure 2.13 shows an example of time sequence of two-dimensional maps of TEC perturbation between 03:30 UT (21:30 CST) and 06:10 UT (00:10 CST) on July

20, 2006 with a 20 minutes interval. The Kp index during this day was between 0 and 1, indicating geomagnetic quiet time. From Figure 2.13b, clear wavelike structures with the wavelengths of 200-500 km and the wavefront stretching in NW-SE direction gradually appear around 03:50 UT in 70-90°W and 30-45°N, and in 110-120°W and 30-40°N with peak-to-peak amplitudes larger than ∼0.5 TECU. Figure 2.13b, c, d, and e clearly show that the wave-like structures were propagating in a southwestward direction from 03:50-04:50 UT (1 hour). Therefore, their propagation velocity were 100-150 m/s.

Figure 2.13 - Time sequence of two-dimensional maps of TEC perturbation, detrended with one-hour window, in the nighttime between (a) 03:30 UT (21:30 CST) and (i) 06:10 UT (00:10 CST) on July 20, 2006, with a 20 min interval.

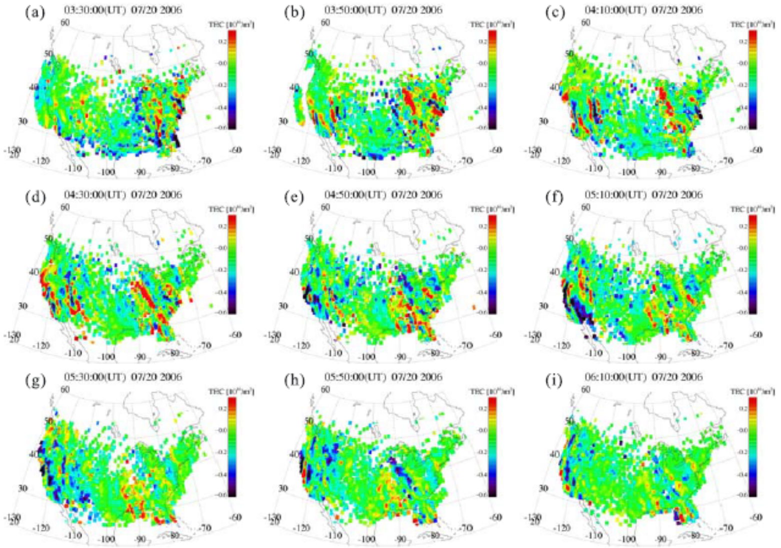

Source: Tsugawa et al. (2007).

Also, Figure 2.14 shows the Time sequence of two-dimensional maps of TEC perturbation between 19:20 UT (13:20 CST) and 22:00 UT (16:00 CST) on November 28, 2006. On this day, the Kp index was between 1 and 2+, still indicating geomagnetic quiet time. From Figure 2.14a, b, c, d, e, and f consecutive wavelike structures with the wavefront stretching in NE-SW direction were seen in the entire field of observation between 19:20-21:00 UT propagating southeastward at the velocity of 100-200 m/s. They had wavelengths around 300-1000 km, wavefront and peak-to-peak amplitudes larger than ∼2,000 km and ∼0.5 TECU, respectively. They also observed southwestward propagating MSTIDs in the late afternoon between 21:20

and 22:00 UT (15:20 and 16:00 CST) as shown in Figure 2.14g, h, and i. However, they had a comparable wavelength and velocity, but relatively small peak-to-peak amplitude to the former southeastward propagating MSTIDs. They concluded that the two MSTIDs propagating in the different directions are superimposed on each other around mid- to late afternoon.

Figure 2.14 - Time sequence of two dimensional maps of TEC perturbation, detrended with one hour window, in daytime between (a) 19:20 UT (13:20 CST) and (i) 22:00 UT (16:00 CST) on November 28, 2006.

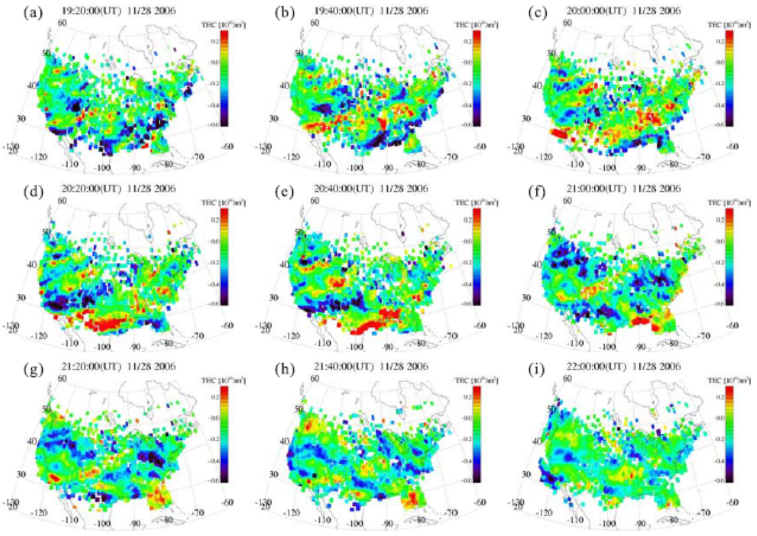

Source: Tsugawa et al. (2007).

In the midlatitude over the Europe too, Otsuka et al. (2013), used TEC obtained from more than 800 GPS receivers networks to revealed two-dimensional structures of MSTIDs. Figure 2.15 shows local time and seasonal variations of the MSTID occurrence rate for higher and lower latitudes in Europe, respectively. It was inferred from their observation that, the occurrence rate of MSTIDs was high during daytime around 10:00-13:00UT in winter at the higher latitudes, and at the lower latitudes, daytime was around 08:00-16:00 and nighttime was between 02:00-05:00 UT in winter. In summer, they realized a secondary peak around 20:00-22:00 UT at the lower latitudes. According to them, the maximum occurrence rate at lower latitudes is approximately 50% whereas that of the higher latitudes is not visible. However, they found out that the maximum occurrence rate in monthly and hourly bin exceeds 70% at lower latitudes, whereas it was approximately 45% at higher latitudes.

Figure 2.15 - The Local time and seasonal variations in MSTID occurrence rate at (left) higher latitudes (> 55° N) and (right) lower latitudes (< 55° N) of Europe in 2008.

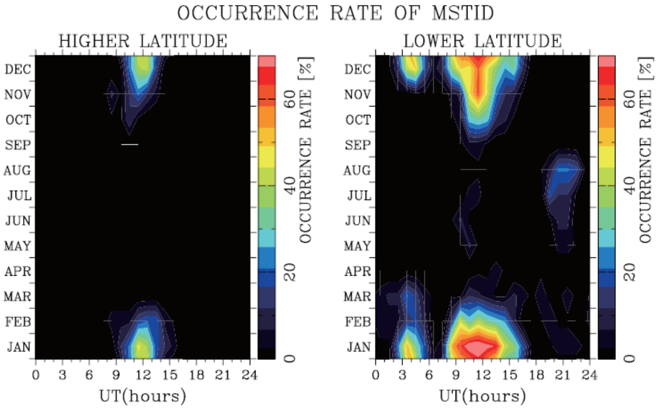

Source: Otsuka et al. (2013).

Figure 2.16a and b also shows the examples of daytime and nighttime TEC perturbation maps of MSTIDs. From Figure 2.16a, it is obvious that wave structures of the TEC perturbations with phase fronts were aligned in the east-west direction during daytime, and in the NW-SE direction during nighttime. Since most of the daytime MSTIDs propagate southward, they speculated that it could be caused by atmospheric gravity waves in the thermosphere. They also reported that the nighttime MSTIDs propagating southwestward were consistent with the theory of polarization electric fields. Therefore, they proposed that polarization electric fields might play an important role in generating those MSTIDs.

Figure 2.16 - Two-dimensional maps of TEC perturbations observed with GPS networks in Europe (a) at 12:30UT on 9 January 2008, and (b) at 22:40 UT on 17 August 2008.

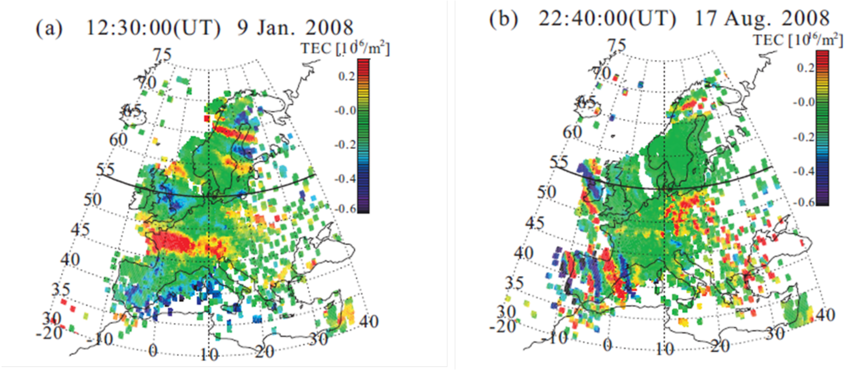

Source: Otsuka et al. (2013).

Kotake et al. (2006) also investigated TEC perturbations associated with MSTIDs almost globally. Figure 2.17 shows the local time and seasonal variations of MSTIDs activity over Japan, Europe, Eastern U.S, Western U.S, Australia, and South America regions in 1998, 2000, and 2001. They found that MSTIDs activity during daytime was different from that of the nighttime with respect to seasonal, solar activity, longitudinal, and latitudinal dependence. Daytime MSTID activities were high in winter in all the six regions. However, seasonal variation of nighttime MSTID was coupled with its longitudinal variation. In the Japanese and Australian longitudinal sector, they realized that nighttime MSTIDs were most active near the June solstice, whereas it was most active near the December solstice in the European longitudinal sector. Nighttime MSTIDs activity at the Japanese and Australian longitudinal sector showed negative correlation with solar activity, whereas solar activity dependence was not seen in daytime MSTID activities. They suggested that the mechanisms causing the MSTIDs could be different between daytime and nighttime.

Figure 2.17 - Local time and seasonal variations of MSTIDs activity in (a) 1998, (b) 2000, and (c) 2001 over (1) Japan, (2) Europe, (3) Eastern U.S., (4) Western U.S., (5) Australia, and (6) South America, respectively.

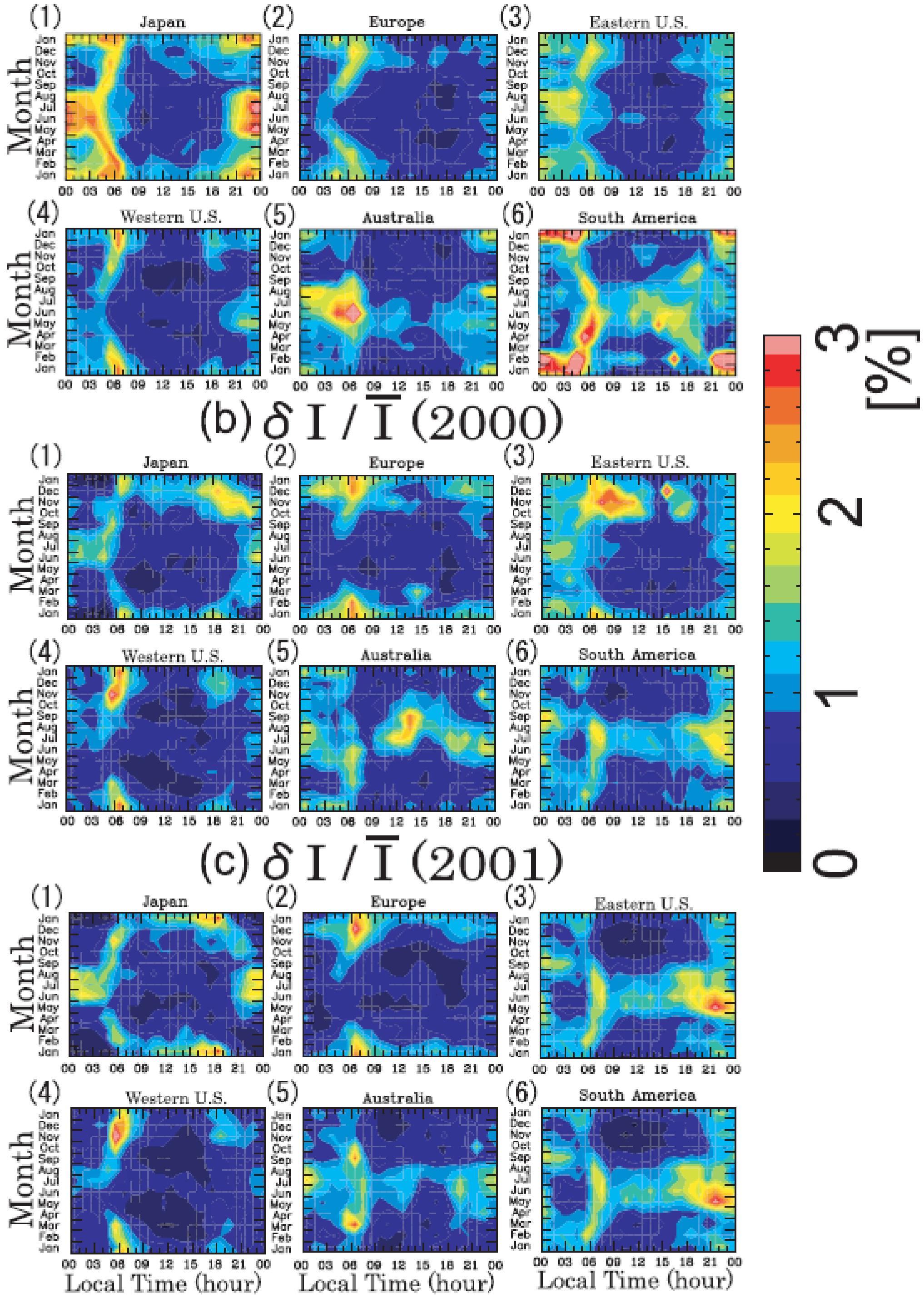

Source: Kotake et al. (2006).

In the high latitude, Negale (2018) used the Poker Flat Incoherent Scatter Radar (PFISR) in central Alaska (69°N, 147°W) to obtained continuous electron density measurements from 2012 to 2013 and analyzed to quantify the properties of over 650 high latitude MSTIDs. Figure 2.18a shows the derived relative electron density perturbations for the MSTID event for the zenith-pointing beam. The constant phase lines of the MSTID slope downward in time, indicative of upward energy propagation for gravity waves which is consistent with a lower atmospheric gravity waves source. Figure 2.18b shows the relative electron densities are band-passed filtered to further enhance the phase structures. The seasonal day/night distributions of MSTIDs at high northern latitudes yielded mean values of the horizontal wavelength, horizontal phase speed and period are 446 km, 187 m/s, and 41 min respectively. According to them, the MSTIDs measurements revealed predominantly eastward during summer, while winter was southward. Their results suggested a cyclic change in the seasonal horizontal propagation directions that was found to be consistent with critical level wind and dissipative filtering.

Figure 2.18 - Derived relative electron density perturbations and (b) band-passed perturbations used in the medium-scale traveling ionospheric disturbance analysis for the case on 18 May 2011 for the zenith-pointing beam.

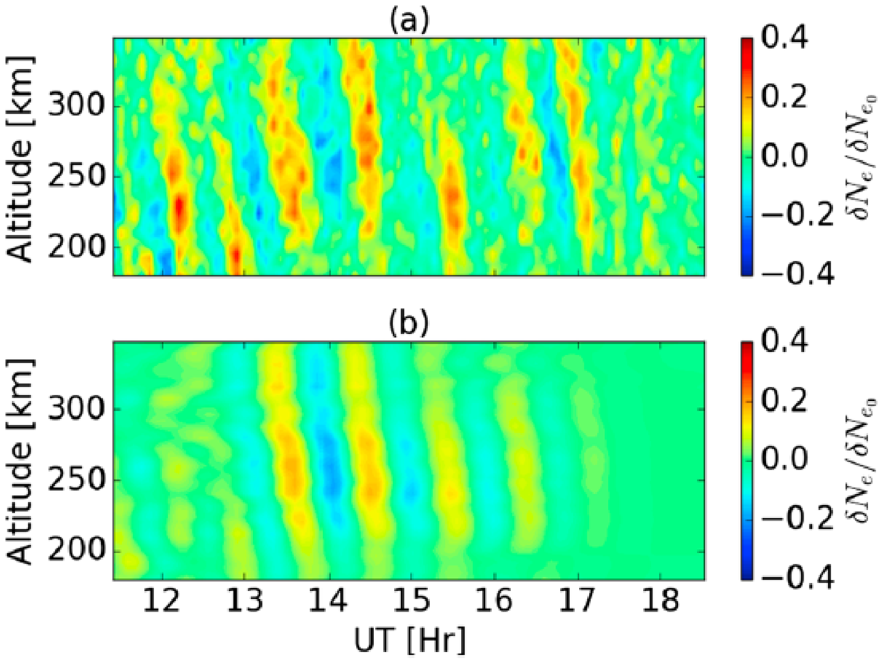

Source: Negale (2018).

2.3.3 Ionospheric irregularities related to ITCZ

Some previous works suggest that ITCZ is responsible for the MSTIDs that propagate south, southwest and southeastward in South America equatorial and low latitude region (MACDOUGALL et al., 2011; FIGUEIREDO et al., 2018a). In this scenario, gravity waves are assumed to be generated by mesoscale convective systems (MCSs) in the troposphere and propagate up to the F region, where they seed perturbations; TIDs, Plasma bubbles or ESF in the ionosphere: These MCSs are usually found within the inter-tropical convergence zone, and even ESF morphology is assumed to be controlled by the seasonal migration of the ITCZ (SU et al., 2014; TSUNODA, 2010). According to Tsunoda (2010), for the gravity wave to seed the RT instability, it should appear close to the location where the RT instability is initiated at the dip equator. However, when the generated irregularity rises with the geomagnetic flux tube, it can be observed at different latitudes depending on the location of the flux tube.

Tsunoda (2010) presented the tangible link between lower atmospheric disturbances and ESF. They showed for the first time, that gravity waves and magnetic field alignment (GWBA) occurs most often during solstice, when the ITCZ is collocated with the magnetic dip equator. They also showed that occurrences of ESF during the solstices are likely produced by enhanced seeding by supporting with the following hypothesis, that perturbations in the neutral gas, produced by gravity waves, elicit a response in plasma density only when there is alignment in the phase fronts of gravity waves with magnetic field lines (HUANG; KELLEY, 1996). According to them, when the solar terminator magnetic field alignment (STBA) and GWBA hypotheses are combined, then a complete description of ESF morphology, which seems to account for its major features, would be arrived. A highly reflective cloud detected at visible and infrared wavelengths from satellites were used to identify ITCZ and data from ground track of the C/NOFS satellite was also used for the ESF.

As shown in Figure 2.19a, each curve represents averaged behavior over three months, the letters indicate months of the year. In summary, they found the most noticeable anomalies in the South American and African sectors as shown in the NDJ and ASO curve respectively. Figure 2.19b shows the sum of the monthly curves; it has two maxima, a shoulder, and two minima. The maximum is situated over Africa, while the smaller maximum is situated over Micronesia, in the western Pacific region. The shoulder brackets South America and the eastern Pacific region. The probability of ESF occurrence during any season over Africa is comparable to that over South America during the December solstice. This implies that the large sum is a consequence of an almost perpetual presence of ESF over Africa. In contrast, the deepest minimum, which brackets Vietnam and the Philippines, appears to be produced by a virtual absence of ESF in that sector throughout the year. The other minimum, located to the east of Christmas Island, in the eastern Pacific region, is not as deep because there is some enhancement in ESF activity during the fall equinox.

Figure 2.19 - (a) The curves for ESF probability, for different month-sets of the year, are superposed to allow comparison of seasonal behavior at different longitudes. (b) A curve showing the sum of the curves in Figure 1a. (c) Global map showing locations of interest to this proposal, indicated by black circles, as well as other stations located near the magnetic dip equator, indicated by squares. A possible ground track of the C/NOFS satellite is also shown. (d) Plots showing the latitudinal migration of the ITCZ as a function of month of year, for four different locations

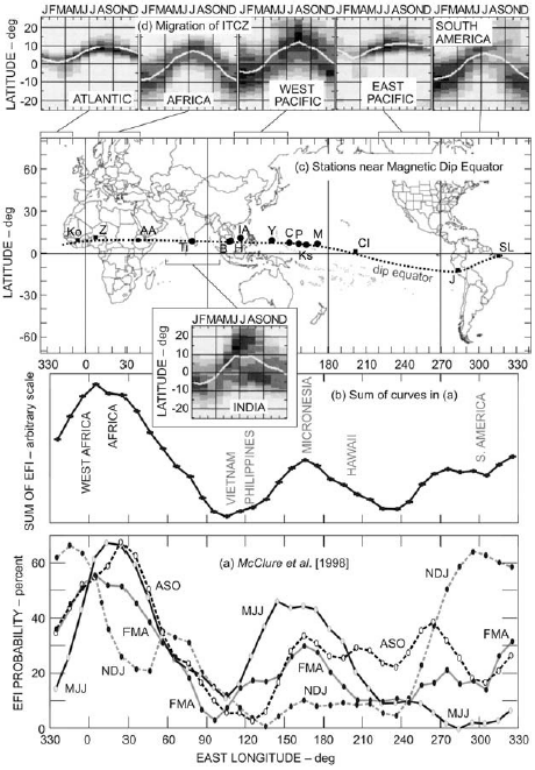

Source: Waliser e Gautier (1993).

Also, Su et al. (2014) studied the seeding mechanism of ionospheric irregularity occurrences by carrying out a correlation study between the global monthly/latitudinal (m/l) distributions of irregularity occurrences and the deep atmospheric convective clouds in the ITCZ indicated by the outgoing longwave radiation (OLR) measurements. ROCSAT satellite was used for the observation of the ionospheric density irregularities and atmospheric convective clouds in the ITCZ was used as the proxy of gravity wave occurrences. They selected seven longitudinal sectors; African, Indian, West Pacific, Central Pacific, East Pacific, South American, and Atlantic sectors for the study. Figure 2.20 shows the global seasonal/longitudinal (s/l) distributions of density irregularity occurrences observed by ROCSAT-1 from 1999 to 2004 at the upper panels of each season; March equinox, June solstice, September equinox, and December solstice, and the lower panels are the corresponding OLR measured in the ITCZ during the same period. A gravity wave was assumed to exist in the deep convective clouds. From the figure, the white dotted line is drawn along the geographic equator in the plot of OLR observations to highlight the seasonal variation in the latitudinal migration of OLR occurrences between hemispheres, which is to contrast the irregularity distribution seen in the upper panel for the same season. There was a topographic overlap of high occurrence patterns in the December solstice and in the equinoxes only in the South American and African sectors, respectively. Therefore, they concluded that good correlations exist only in the South American sector and to some extent in the African sector.

Figure 2.20 - The global seasonal/longitudinal distributions of density irregularity occurrences observed by ROCSAT-1 from 1999 to 2004 are plotted in the upper panels of each season - March equinox, June solstice, September equinox, and December solstice. The lower panels are the OLR measured in the ITCZ from NOAA 14 and 16 during the same period.

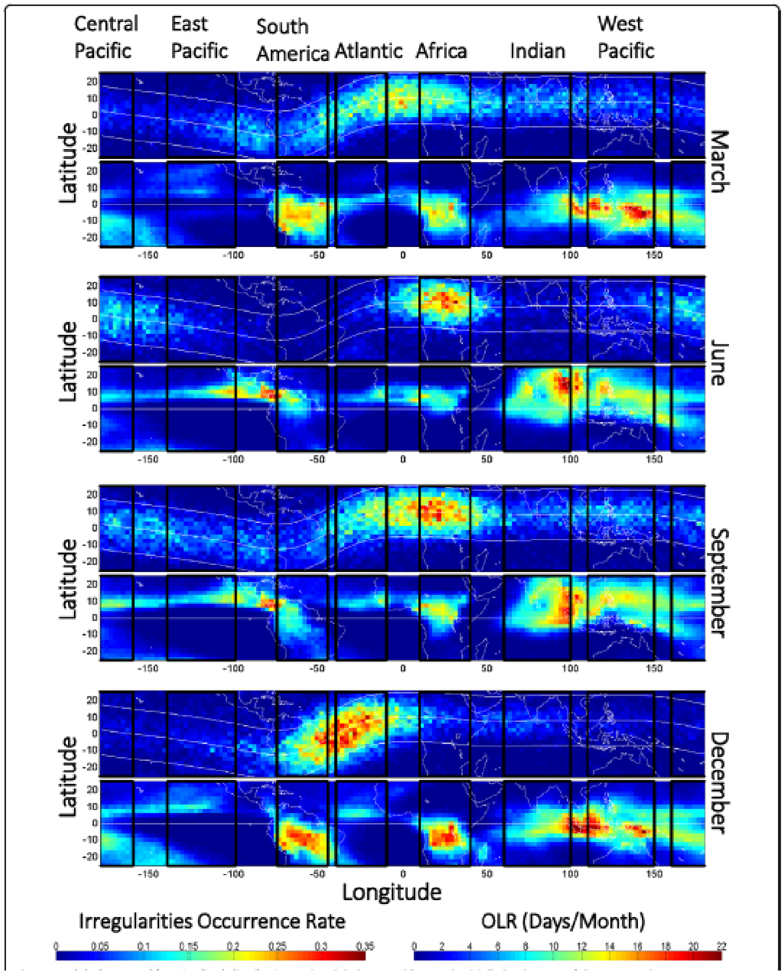

Source: Su et al. (2014).

2.4 Summary of the MSTID Observation

Though tremendous amount of research works have been devoted to studies of the ionosphere, nevertheless, for more than a century after its discovery, the Earth's ionosphere still remains not fully explored region. Still, scientific community is unable to predict the ionospheric behavior precisely, either during geomagnetic storms, or during geomagnetically quiet time conditions. The knowledge of the structure and dynamics of the ionospheric plasma at each moment of time is vital for various scientific applications and services, such as telecommunication via radio signals, point positioning based on global navigation satellite systems (GNSS). MSTIDs are among the ionospheric disturbances not well known especially the daytime MSTIDs in the South American equatorial region.

So far, many reviews have been presented to spell out major studies on global MSTIDs, however, the climatology and morphology of daytime MSTIDs in the equatorial region is totally missing. Therefore, this present is studying the statistical analysis of the occurrence rate and characteristics of the MSTIDs in the South American equatorial region using GNSS TEC perturbation maps. In addition, the long term solar cycle dependence of MSTIDs is still not well understood, hence the present work will fully explored that and go ahead to look in the time dependence of MSTIDs as well.

In general, TIDs and their effects on radio systems speak to the need for a better understanding of their morphology and climatology, and ultimately the need to predict their behavior more accurately. Before such a climatology can be done, more measurements of TIDs are needed. At the moment, there is no useful daytime MSTID climatology and characteristics in the South American equatorial region that could be used to predict TID periods, amplitudes, speeds and directions at a given location. Therefore, any operational requirement for TID information means the TID characteristics have to be measured at the required location not limited to equatorial region over South America.

3 INSTRUMENTATION AND METHODOLOGY OF THE RESEARCH

3.1 Introduction

The purpose of this chapter is to present the instrumentation and the methodology used in this thesis. The instrumentation will focus on Global Navigation Satellite System (GNSS) and their respective ground receivers network in South America region. It further elaborates the method of calculating TEC and dTEC, generating dTEC maps, creating keograms and characterization of the dTEC oscillation using spectral analysis by applying the fast Fourier transform (FFT).

3.2 Global Navigation Satellite System (GNSS)

GNSS is a system of satellites in constellation that provide geo-spatial positioning with global coverage and allow electronic receivers on the surface of the earth to determine their location (longitude, latitude, and altitude/elevation) using time signals transmitted along a line of sight by radio waves from satellites. In summary GNSS provides positioning, navigation, and timing services on a global or regional basis. Currently, four GNSS systems are in operation; Global Positioning System (GPS) from United States of America, the GLONASS (Globalnaya Navigazionnaya Sputnikovaya Sistema) which is owned and operated by Russian Federation, the European Space Agency's Galileo and Chineseâs BEIDOU. Each of these systems employs a constellation of orbiting satellites working in conjunction with a network of ground stations. For the purpose of this research, the discussion will be limited to GPS and GLONASS due to the fact that there are adequate number of receivers of the aforementioned navigation systems in the South American equatorial region to develop dTEC maps with good resolution.

The GNSS receivers network in the South America region comprises of "Rede Brasileira de Monitoramento Continuo" (RBMC) which belongs to "Instituto Brasileiro de Geografia e Estatistica (IBGE)"', "Rede Argentina de Monitoreo Satelital Continuo" (RAMSAC), Low Latitude Ionospheric Sensor Network (LISN), and International GNSS Service (IGS) are shown in Table 3.1. Combination of all the four networks together provide more than 236 GNSS receivers in the whole South American region. Among them, 83 of the GNSS receivers in located in the equatorial region in which are more useful for the present work.

Figure 3.1 shows the distribution of the GNSS ground-based receivers network on

Table 3.1 - GNSS receivers network in South America.

Network	Total number of receivers	number of receivers in the Equatorial region
RMBC	149	76
Ramsac	33	0
LISN	32	3
IGS	30	4
Total	244	83

the South America map. The dot (RMBC, RAMSAC, LISN and IGS are represented by red, blue, violet and green, respectively) shows the latitudinal and longitudinal position of the receivers in this present work. From the map, the study area indicated by red rectangle, covers latitude 0° to 15°S and longitude 30° to 55° west equivalent to a distance 1667 km by 2778.0 km respectively, covering a total area of 4630926 km^2 (Converter: https://www.nhc.noaa.gov/gccalc.shtml). The study area was selected to investigate about the MSTID behavior and their possible source regions.

Figure 3.1 - Distribution of the GNSS ground receivers network. RMBC, RAMSAC, LISN and IGS are represented by red, blue, violet and green respectively.

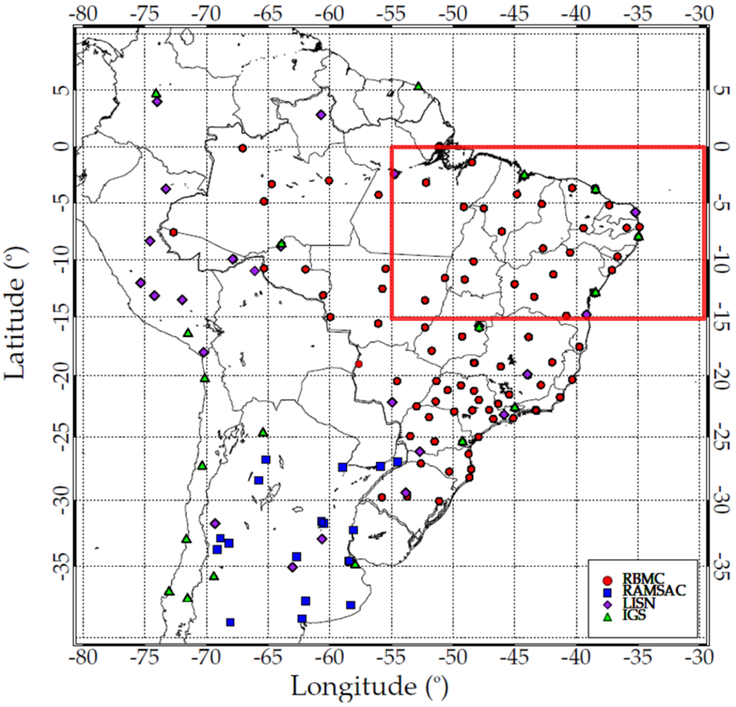

3.2.1 Global Positioning System (GPS)

GPS satellites transmit positioning signals on two L-band frequencies. Ranging is carried out by measuring the time required for a signal to propagate from a GPS satellite to the ground base station. GPS system consists of space, control and user segment. The space segment currently consists of 32 operational satellites in six orbital planes. They operate in circular orbits at a height of about 20,200 km inclined at an angle of 55° with the corresponding orbit period of about 12 sidereal hours. The control segment consists of five monitoring stations passively tracking all satellites in view to accumulate data. The information is processed at the master control station to estimate the satellite orbital position, clock error, and other navigation data parameters such as the health of each satellite. This information is transmitted to each satellite via Ground Antennas. The user segment consists of antennas and receivers providing positioning, velocity and precise timing (LEE, 1988; RAI, 2012).

The two L-band frequencies on which the GPS satellites transmit with their corresponding wavelength are shown in Table 3.2. The pseudorange and the carrier phase are the two basic observables. Two pseudorandom noise codes (PRN) are modulated onto the carrier signals, the Coarse/Acquisition (C/A)-code and the P-code (precision code). The C/A-code is modulated on the L1 carrier only and the P-code is modulated onto both L1 and L2 carriers. A low bit rate navigation message is modulated onto both L1 and L2 carriers (COUNTERMEASURES. . . , ; GREWAL et al., 2007; WANG et al., 2008). There is also an L5 signal (1176 MHz) which is the third GPS signal, designed to meet demanding requirements for safety-of-life transportation and other high-performance applications. L5 is broadcast in a radio band reserved exclusively for aviation safety services. It features higher power, greater bandwidth, and an advanced signal design. However, the L5 signal is not relevant for the present work, hence, it's absence from Table 3.2.

Table 3.2 - Frequencies and their respective wavelengths for GPS.

L-Band	Frequency (Hz)	Wavelength (cm)
L1	$f_1 = 1575.42$	$\lambda_1 = 19.05$
L2	$f_2 = 1227.60$	$\lambda_2 = 24.45$

Users of single frequency receivers have access to lower accuracy C/A code which is provided in the GPS Standard Positioning Service (SPS), the level of service authorized for civilian users. The Precise Positioning Service (PPS) provides access to both C/A code and encrypted P-code and is designed for military users. The SPS incorporates denial of full accuracy (Selective Availability or SA) which can be accomplished by intentionally degrading the broadcast orbit ephemeris and dithering the satellite clock. Operationally, the current SA approach uses the delta-process (LANGLEY, 1996; KOMJATHY, 1997; WITCHAYANGKOON, 2000).

With the use of relative or differential techniques, error sources such as satellite position errors, satellite clock errors, tropospheric and ionospheric delays that are common to simultaneously observing receivers, one with a well determined position, can be eliminated or greatly reduced. Depending on the sophistication of the algorithm, code differential techniques can routinely achieve accuracies at the level between 1 to 10 meters (KOMJATHY, 1997). For high precision geodetic applications, carrier phase observations are used. Depending on the level of sophistication of the post processing software, a few parts in 109 precision can be achieved over baseline lengths of thousands of kilometers (HAGER et al., 1991; KOMJATHY, 1997; WITCHAYANGKOON, 2000; BOND et al., 2007).

GPS uses a spectrum multiple access called code modulation multiple access (CDMA) techniques for the transmission of the signals. In CDMA, signals are sent at the same time in the same frequency band (L1 and L2).

3.2.2 Globalnaya Navigazionnaya Sputnikovaya Sistema (GLONASS)

GLONASS is the Russian equivalent of GPS with 24 satellites in constellation including three spares. The GLONASS satellites are arranged in three orbital planes with each orbital plane contains 8 equally spaced satellites. Two carrier signals in the L-band are broadcast and modulated by binary codes and a navigation message. The GLONASS satellites transmit in two frequency bands; between 1602.0 and 1615.5 MHz (Ll) and between 1246.0 and 1256.5 MHz (L2). The carrier frequencies (f1 and f2) on which a satellite broadcasts are defined as, (HOFMANN-WELLENHOF et al., 2007).

$$\begin{aligned} f1 &= 1602.0 + 0.5625k \\ f2 &= 1246.0 + 0.4375k \end{aligned} \tag{3.1}$$

Here, k is the frequency channel numbers shown in Table 3.3.

Table 3.3 - Slot number and their respective channel number for the GLONASS (https://www.glonass-iac.ru/en/GLONASS/ Accessed: 04 May, 2020).

Slot Number	Reference Channel
1,5	01
2,6	-4
3,7	05
4,8	06
9,13	-2
10,14	-7
11,15	0
12,16	-1
17,21	04
18,22	-3
19,23	03
20,24	02

Unlike GPS, GLONASS uses frequency modulation multiple access (FDMA) technique, where every two antipodal satellites are assigned with the same carrier frequencies as shown in Table 3.3. The main advantage of FDMA over CDMA is the guarantees signal separation since each signal is transmitted in a different frequency. Also, a narrow band interference source that disrupts only one FDMA signal would disrupt all CDMA signals simultaneously. Furthermore, FDMA eliminates the need to consider the interference effect between multiple signal codes. However, the use of multiple frequencies does introduce the possibility for hardware delays that are different for each channel (HURSKAINEN et al., 2008; HUMPHREYS et al., 2008). Nevertheless, this requires a higher complexity and cost regarding antenna and receiver design, related to the implementation of the different band-pass filters and calibration.

3.3 Method of calculating detrending TEC (dTEC)

3.3.1 The Ionospheric Effects on the Propagation of Electromagnetic Waves

When radio waves emitted from GNSS pass through the ionosphere, there are two effects: the trajectory of the beam is refracted and the signal delays (MARKOVIĆ, 2014). This phenomenon is cause by the free electrons in the ionosphere, due to refraction, which is defined by Snell's law (PARAZZOLI et al., 2003; REPP et al., 2004). However, the behavior of the waves in the ionosphere cannot be described with Snell's law only. Thus, in order to be able to adequately describe the behavior of radio waves passing through the ionosphere, it is assumed that the ionosphere is only partially ionized, spherically stratified plasma with a broad spectrum of unevenly spaced irregularities, which extends along the uneven magnetic field, which is distorted in itself due to the disorder that arises as a result of the occurrence of solar winds (IVANOV-KHOLODNY; MIKHAILOV, 2012; MARKOVIĆ, 2014).

In the case of the ionosphere, the refractive index is a complex quantity, which Edward Appleton has described in his magnetic-ionospheric theory. Appleton demonstrated first that when going through the magnetized plasma, a plane polarized wave splits into two circularly polarized waves rotating in opposite directions. Hartree then suggested that the Lorentz polarization should be applied in the theorem, so the formula for calculating the complex refractive index was named Appleton-Hartree formula. This formula refers to an electrically neutral environment with equal number of electrons and positive ions, which extends along a constant magnetic field: Where the effect of the positive ions on the wave is negligible. Letting a plane electromagnetic waves travel along the x-axis of orthogonal coordinate system as shown in Figure 3.2, and a uniform external magnetic field lie in x-y-z plane forming an angle of Θ with the direction of wave propagation.

Figure 3.2 - The orthogonal coordinate system.

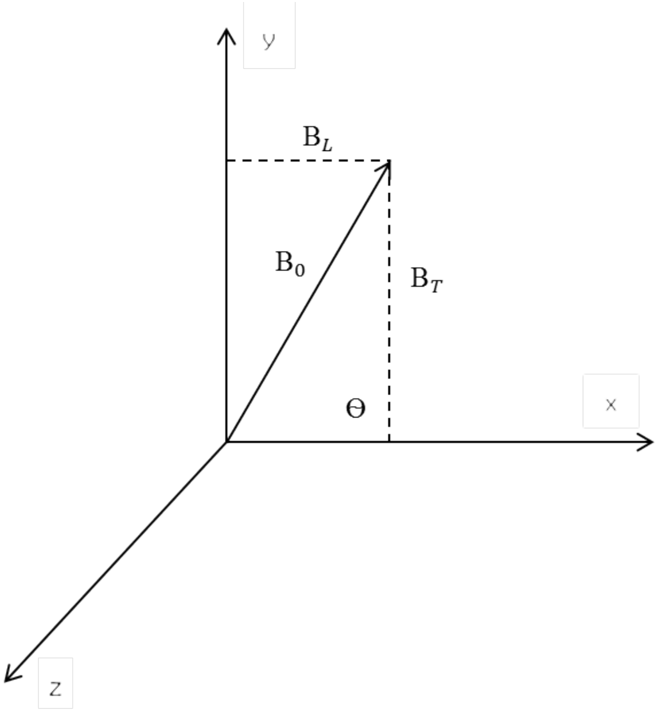

The complex index of refraction given by Appleton-Hartree is:

$$n^2 = 1 - \frac{X}{1 - iZ - \frac{Y_T^2}{2(1-X-iZ)} \pm \sqrt{\frac{Y_T^4}{4(1-X-iZ)} + Y_2^2}} \tag{3.2}$$

where n is the complex refractive index $(\mu - i\chi)$, with real part μ and imaginary part χ.

where, $X = \frac{f_N^2}{f^2}, \quad Y = \frac{f_H}{f}, \quad Y_L = \frac{f_L}{f}, \quad Y_T = \frac{f_T}{f}, \quad and \quad Z = \frac{f_c}{f}$

Here,

- $f[Hz]$ is the carrier frequency
- f_N [Hz] is the frequency of the plasma
- $f_H[Hz]$ - gyro frequency of free electrons
- $f_L[Hz]$ - longitudinal gyro frequency
- $f_T[Hz]$ is the transverse gyro frequency
- $f_c[Hz]$ is the frequency of collisions between electrons and heavy particles
- Θ is the angle between the signal and the vector magnetic field

In this case, Equation 3.2 can be developed into endless series, for instance, when collisions ($Z \approx 0$) and the influence of magnetic fields ($\Theta \approx 0$) are neglected, then only the first two terms remain as,

$$n = 1 - \frac{1}{2}\frac{f_N^2}{f^2} \tag{3.3}$$

Given, that for each point f_N^2=80.6 $\cdot$ $N \ Hz^2$ (where N is the electron density in electron/m^3), then the refractive index can be calculated as:

$$n_p = 1 - 40.3\frac{N}{f^2} \tag{3.4}$$

$$n_g = 1 + 40.3\frac{N}{f^2} \tag{3.5}$$

where n_p and n_g are phase and group refractive index respectively.

After integrating Equation 3.4 or Equation 3.5 along the line of sight of the radio signal path result in ionospheric delay (Δ^{iono}) which is an error caused by signal propagation through the ionosphere. This error is known as ionospheric signal delay which is proportional to slant TEC and inversely proportional to square of the frequency. Since the frequencies of GNSS signal are known, it follows that ionosphere signal delay is the only function of the slant TEC as shown in Figure 3.3.

$$\Delta^{iono} = \frac{40.3}{f^2} TEC \tag{3.6}$$

Figure 3.3 - The total electron content from the satellite to the receiver on the Earth's surface.

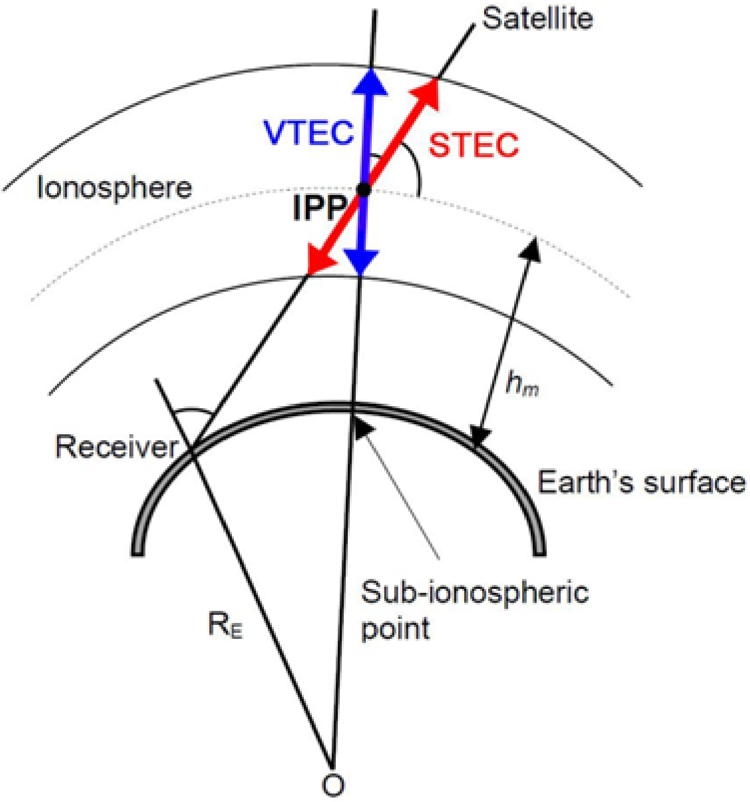

Source: ROB (2014).

The slant TEC (STEC) which is the line integral of electron density along the signal path between the receiver and a satellite given in the TEC units ($1\ TECU = 10^{16}$ $1/m^2$), which can be expressed as (MANNUCCI et al., 1998),

$$TEC = \frac{1}{40.3}\frac{f_i^2 f_j^2}{(f_i^2 - f_j^2)}[(L_1 - L_2) - (\lambda_1 N_1 - \lambda_1 N_1) + br + bs] \tag{3.7}$$

where L_1 and L_2 are the carrier phase values of the signal (converted to distance units). GNSS data include carrier phase and group delays (P-code pseudoranges) of dual frequency GNSS signals every 30 seconds in a file format called RINEX (Receiver Independent Exchange Format) and Hatanaka; $\lambda_1 N_1$ and $\lambda_2 N_2$ are integer cycle ambiguities, and b_r and b_s are satellite and receiver instrumental biases. The f_i and f_j corresponds to the frequencies of GPS and GLONASS. Due to the ambiguity in the carrier phase measurements, the level of the TEC is unknown. Meanwhile, the level is adjusted to the slant TEC derived from the pseudoranges for each satellite-receiver pair. TEC obtained by the above procedure still contains biases inherent in satellite and receiver hardware. Moreover, the ambiguities as well as the biases of both the satellite and receiver ought to be estimated to obtain the absolute value of TEC (KOTAKE et al., 2006; TSUGAWA et al., 2007). However, this study is not interested in the absolute TEC, but instead focusing on the perturbation components of TEC caused by MSTIDs. Besides, the STEC is calculated by the average of the L1 and L2 signals, so all the constant terms become zero.

To obtained the vertical TEC (vTEC), the Zenith angle ψ of the signal path through the ionospheric piercing point (IPP) in the F2 region has to be estimated as,

$$\psi = \frac{\pi}{2} - El - sin^{-1}\left(\frac{R_e}{R_e - 300} \times cos(El)\right) \tag{3.8}$$

where R_e is the radius of the Earth, El is the elevation angle which can be estimated from ephemeris file called Sp3 (Standard parameter 3) that gives the final orbital position (XYZ coordinates) of the satellite for both GPS and GLONASS in every 30 min. In this case, interpolation is necessary to synchronized the time of the XYZ coordinates with that of TEC. GPS broadcast ephemeris are linked to the position of the satellite antenna phase center in the World Geodetic Service-84 (WGS-84) reference frame. WGS-84 is a unified terrestrial reference system for position and vector referencing of GPS. Whereas GLONASS broadcast ephemeris are given in the Parametry Zemli 1990 (Parameters of the Earth 1990) (PZ-90) reference frame. Therefore, transformation of the XYZ coordinates from PZ-90 to the WGS-90 is necessary. Thus, the matrix transformation in Equation 3.10 (BOUCHER; ALTAMIMI, 2001; CAI; GAO, 2009; GORAL; SKORUPA, 2012) can be used.

$$\begin{pmatrix} x \\ y \\ z \end{pmatrix}_{WGS84} = \begin{pmatrix} x \\ y \\ z \end{pmatrix}_{PZ-90} + \begin{pmatrix} T_1 \\ T_2 \\ T_3 \end{pmatrix} + \begin{pmatrix} D & -R_3 & R_2 \\ R_3 & D & -R_1 \\ -R_2 & R_1 & D \end{pmatrix} \begin{pmatrix} x \\ y \\ z \end{pmatrix}_{PZ-90} \tag{3.9}$$

where T_1, T_2,and T_3 are 3 translation parameters, D is a scale factor, and R_1, R_2 and R_3 are three rotation angles which are constant values as shown in Table 3.4.

Table 3.4 - The transformation parameters of GNSS reference frame.

T_1	T_2 (cm)	T_3	D (ppb)	R_1	R_1 (mas)	R_1
7	0	-77	-3	-19	-4	353

where mas is milli-arcseconds (radians) and ppb is parts per billion (1ppb=10^{-9}).

Now, the vertical vTEC can be obtained by the product of the slant TEC and cosine of the zenith angle

$$vTEC = TEC \times cos(\psi) \tag{3.10}$$

With regard to these available information, the detrending TEC (dTEC) is can be calculated by subtracting one hourly moving average ($vTEC(t \pm 30min)$ from the time sequence of vTEC(t). These methods of deriving the two-dimensional TEC perturbation maps have been used by Saito et al. (1998), Kotake et al. (2006), Tsugawa et al. (2007), Otsuka et al. (2013), Figueiredo et al. (2018a).

$$dTEC(t) = vTEC(t) - < vTEC(t \pm 30min) > \tag{3.11}$$

Figure 3.4 shows the TEC with its running average (upper panel) and the dTEC (lower panel) GPS PRN 32. The data derived from paths with low elevation angle are uncertain because of errors on conversion from slant to vertical TEC include cycle slips. Therefore, data from elevation angles lower than ±30° are not included in this procedure (TSUGAWA et al., 2007). The upper panel shows the STEC profile (black) and the corresponding one hour running average (±30 min) TEC (red) while the lower panel is the TEC perturbation cause by MSTIDs which can be seen at the amplitude greater than 0.1 TECU (KOTAKE et al., 2007; TSUGAWA et al., 2007; OTSUKA et al., 2013; FIGUEIREDO et al., 2018a) as shown in Figure 3.4. The maximum MSTID oscillations are seen between 9:00 UT and 12:05 UT, and 13:00 and 15:00 UT. In the present study, the TEC values elevation angles greater than 30° are considered to minimize errors due to cycle slips and slant factor.

Figure 3.4 - STEC (upper panel) with El>30° and the corresponding dTEC (lower panel).

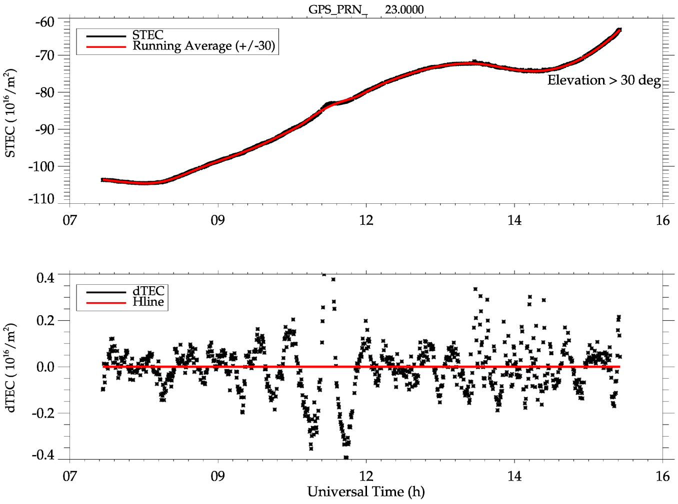

3.3.2 Generation of two-dimensional dTEC maps

Generating of dTEC maps required the longitude and latitude of ionospheric piercing point (IPP) position, which can be estimated from the following model (OTSUKA et al., 2002; BASU et al., 2001; PROL et al., 2017).

$$\phi_{ipp} = sin^{-1} \left[sin\left(\phi_r\right) cos(\psi) + cos(\phi_r) sin(\psi) cos(Az) \right] \tag{3.12}$$

$$\lambda_{ipp} = \lambda_r + sin^{-1} \left[\frac{sin(\psi) sin(Az)}{cos(\phi_{ipp})} \right] \tag{3.13}$$

where λ_r and ϕ_r are longitude and latitude of the receiver respectively.

Figure 3.5 GPS (upper panel) and GLONASS (lower panel) trajectories at IPP for all the PRNs at the respective latitudinal and longitudinal IPP for Elevation angle greater than 30° over Sao Luis (2.36°S, 44.13°W) on 10th August, 2014. These describe the signal path through ionosphere interpolated on the South American map.

Figure 3.5 - GPS (upper panel) and GLONASS (lower panel) trajectories at IPP for all the PRNs at the respective longitudinal and latitudinal IPP for Elevation angle greater than 30° over Sao Luis (2.36°S, 44.13°W) on 10th August, 2014.

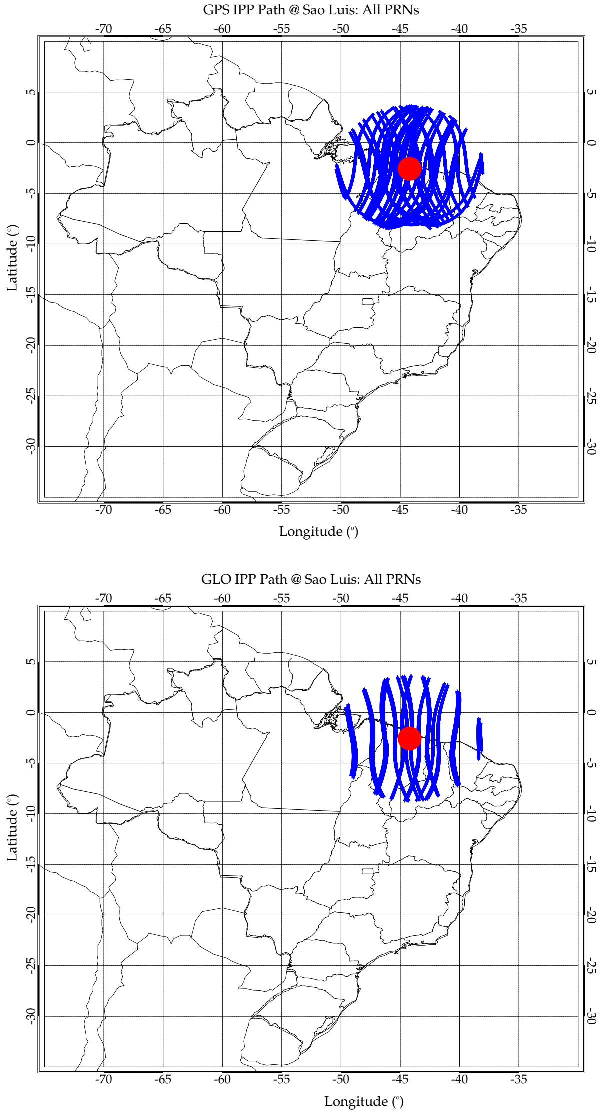

Having the information about the dTEC, longitude and latitude at the IPP position, two-dimensional maps of the TEC perturbations within the area of 30° − 55°W and

0° − 15°W N were derived with a temporal resolution of 1 min and a spatial resolution of 0.25° × 0.25° in longitude and latitude. Figure 3.6 shows an example of two-dimensional maps of TEC perturbations during the passage of MSTIDs over South America on June 30th, 2015 at 16:45:00 Universal time (UT= 13:45:00 local time (LT)). From the dTEC map, the MSTID oscillations can be identified with red and blue denoting crest and trough respectively. On this day, MSTIDs oscillations with wavefront elongated from the northwest to the southeast were observed propagating northeastward between, at 15:00 UT and 18:00 UT (12:00 LT to 15:00 LT).

Figure 3.6 - dTEC maps with 1 min resolution over South America equatorial region June 30, 2014 at 16:45:00 Universal time (UT) (13:45:00 local time (LT)).

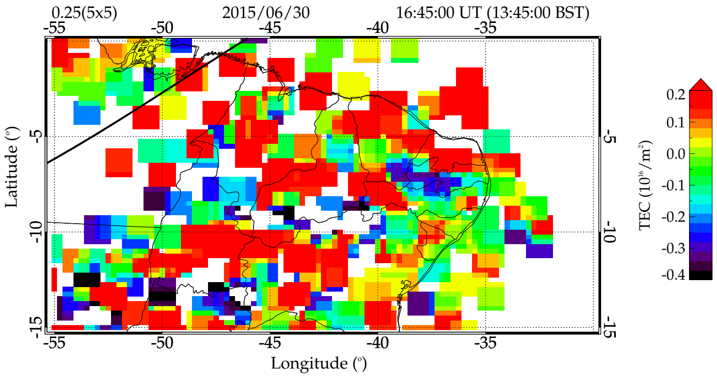

3.4 Method of Creating Keograms

Keograms shows the time variation of longitudinal (zonal) and latitudinal (meridional) components of series of images, in the present case, dTEC maps. This has been used in many research works not limited to Sobral et al. (2001), Saito et al. (2007), Taylor et al. (2009), Paulino et al. (2011), Narayanan et al. (2014), Figueiredo et al. (2018a), Essien et al. (2018). This technique helps in identifying the oscillations in dTEC maps, since it is possible to observe the behavior over 24 hours in one single frame.

In other to characterize the MSTIDs into wavelength, propagation direction, period, velocity and amplitude, keograms are created from series of the series of dTEC maps (FIGUEIREDO et al., 2018a) by taking latitudinal and longitudinal slice of each dTEC map. For example, a cut was made at latitude −12.5°S and longitude −45.0°W in every 1 min of the series of dTEC maps generated from 30th June 2015 as shown

Figure 3.7.

Figure 3.7 - Series of dTEC maps on June 30th, 2015 selected for the keogram process.

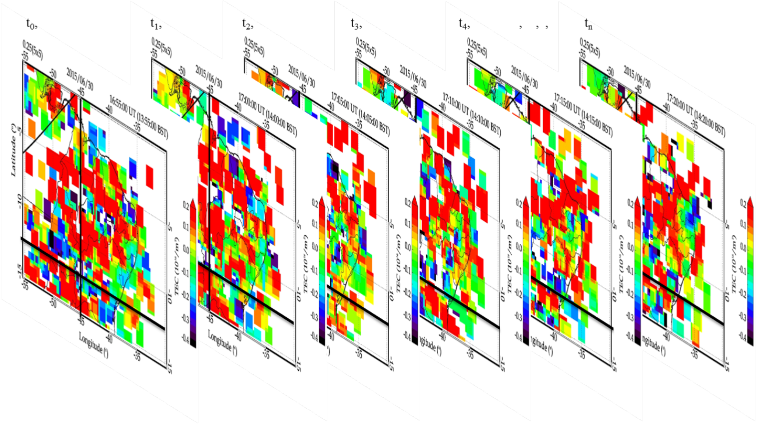

The keogram from the series of dTEC map is shown in Figure 3.8, where the abscissa determines the interval of time and the ordinate determines the corresponding distance in geographic coordinates. From the keogram, the MSTID oscillations can be identified with positive (red) and negative (blue) dTEC lines denoting crest and trough respectively. The black dashed lines indicate the dawn and dusk solar terminator.

Figure 3.8 - Keograms created from dTEC maps on June 30th, 2015; longitudinal (top) and latitudinal (bottom). The black dashed lines indicate the dawn and dusk solar terminator.

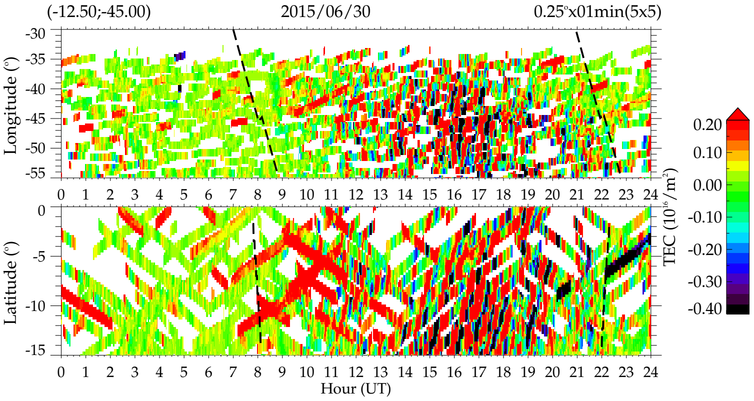

The flow chart shown in Figure 3.9 demonstrates the complete processes involving in the processing of the data to the generating of dTEC maps and creating of keograms.

Figure 3.9 - Flow chat to illustrate the method of genrating 2D dTEC maps and creating keograms.

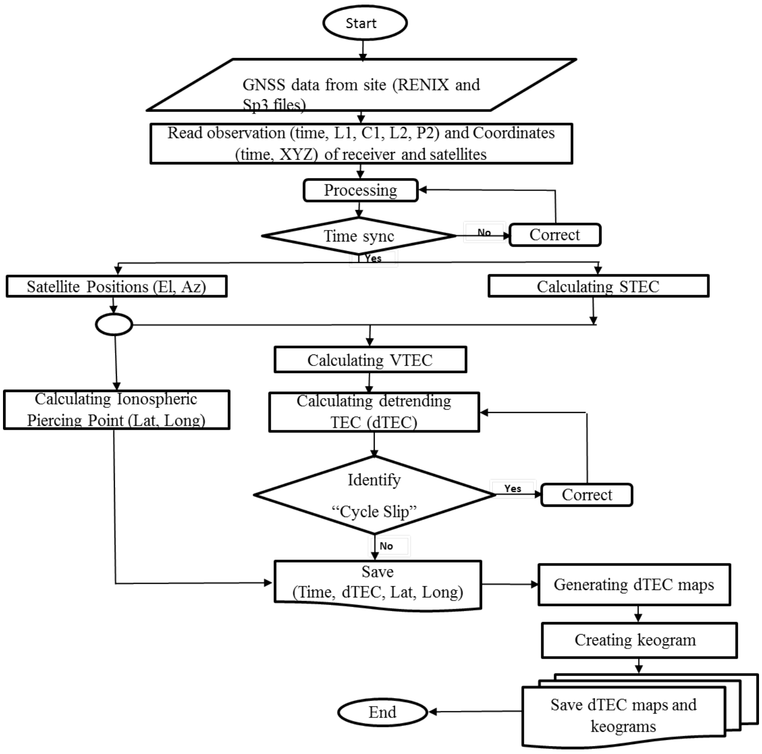

3.4.1 dTEC keogram analysis

This method of analysis has been developed to calculate the wavelength, period, direction of propagation, amplitude and phase velocity. It employs the spectral analysis, using discrete Fourier transform. This procedure had already been used by Figueiredo et al. (2018a) to characterized the MSTIDs over the low latitude of South America region.

In order to analyze the parameters, the areas of the MSTID oscillations are first selected from the longitudinal and latitudinal keogram as indicated by the white box shown in Figure 3.10.

Figure 3.10 - Spectral analysis of Keogram produced on 30th June, 2015 zoomed between 10 to 24 hours. Example of one of the areas to be analyzed are selected in white boxes in the longitude and latitude keograms.

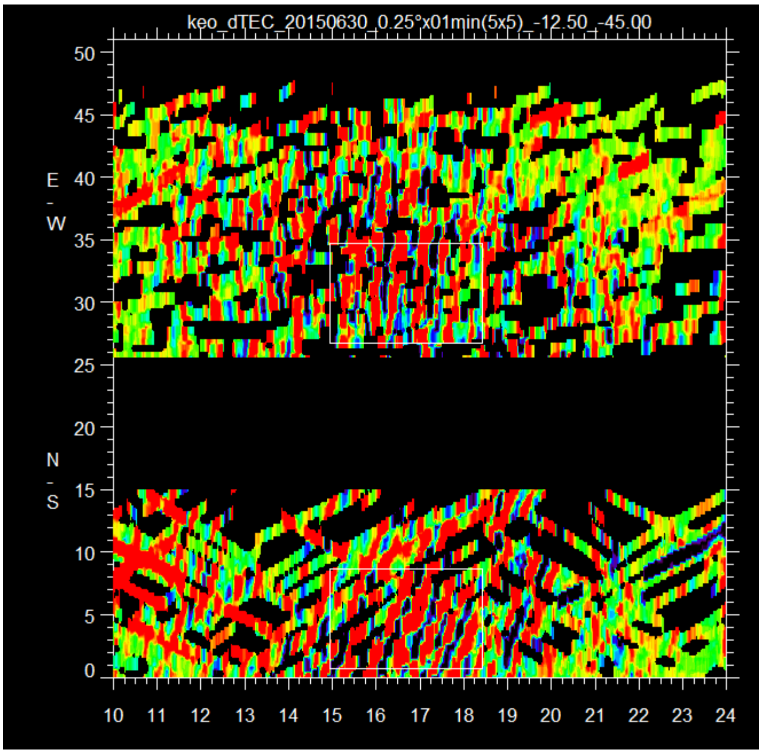

The following criteria are used in identifying and analyze the MSTID oscillations.

- The amplitude of dTEC oscillation should be more than 0.1 TECU.
- It is requested that the areas to be analyzed are equal in both zonal and meridional components of the keogram
- The time interval for the oscillation(s) should be at least 30 min.
- The oscillation should have at least two wavefront and propagates on the maps, when assume that the propagation direction is perpendicular to the wavefront of the MSTID.
- The Wavefront should be greater than 3° in latitude and longitude on the keograms.
- The inclination of the MSTID in the latitudinal and longitudinal components determines the direction of propagation.

- Propagation direction must be perpendicular to the front of the TID, and the variation azimuth starts from the geographic North (0°) and clockwise.
- The wave phases selected in a particular component should be moving in the direction.
- The horizontal wavelength should be at most 1,500 km.

After selecting the required MSTID oscillations in both latitudinal and longitudinal frames (as shown in the white boxes), the discrete Fourier transform is apply to the selected set of time series to calculate the frequency (Equation 3.14).

$$F(\omega) = \sum_{n=0}^{N-1} f(t) e^{\frac{-2\pi\omega n i}{N}} \tag{3.14}$$

where $F(\omega)$ is the transform of the Fourier function $f(t)$, $n = 0, ..., N-1$ is the frequency index, and N is the number of points in time series in selected regions.

Then, the cross spectrum is calculated using Equation 3.15:

$$C(\omega) = F_S(\omega) F^*_{S+1}(\omega), \tag{3.15}$$

Here, $C(\omega)$ is the cross spectrum between two time series and $F_S(\omega)$ and $F^*_{S+1}(\omega)$ represent the Fourier transform of the series $f_S(t)$ and $f_{S+1}(t)$, respectively. $F^*_{S+1}(\omega)$ is the complex conjugate of $F_S(\omega)$. The one-dimensional cross power spectrum is defined by the quadratic modulus, $|C^2|$. If the number of time series selected is S, the resulting cross power spectrum will be the average of $S-1$ cross power spectrum computed.

Thus, the amplitude of the cross power spectrum is expressed by $2\sqrt{|C^2|}$ with the phase of the spectrum being defined as,

$$\Delta\psi = tan^{-1} \frac{Im(C(\omega))}{Re(C(\omega))}, -\pi \leq \psi \leq \pi \tag{3.16}$$

For the frequency ω, in which the amplitude is maximum, the phase of the cross spectrum is the phase difference caused by the wave propagation between these time series. With the frequency known the period can be estimated as,

a) Period (min)

$$\tau = \frac{1}{|f(\omega)|}; \tag{3.17}$$

b) Then, the wavelength (km) for the zonal and meridional components ($\lambda_{(NS,EW)}$):

$$\lambda_{NS,EW} = \frac{\Delta d}{\Delta\psi/360^\circ} \tag{3.18}$$

in which Δd represents the distance between the time series.

c) Consequently, the horizontal wavelength (km) can be calculate as,

$$\lambda_H = \frac{\lambda_{NS}\lambda_{EW}}{\sqrt{\lambda_{NS}^2 + \lambda_{EW}^2}} \tag{3.19}$$

d) Finally, the horizontal phase velocity, C_H (m/s), and phase of propagation direction, ϕ, can be obtained by

$$C_H = \frac{\lambda_H}{\tau} \tag{3.20}$$

$$\phi = \cos^{-1}\left(\frac{\lambda_H}{\lambda_{NS}}\right) \tag{3.21}$$

Apart from calculating the ϕ, there are other visualization techniques that are necessary to be done in order to testify whether the propagation direction calculated are correct. The information in Table 3.5 can be used to identify the propagation direction of the MSTID and is the interpretation to the simulation made by (FIGUEIREDO et al., 2017) to estimate the approximately propagation direction of MSTIDs using keograms visualization. Here, the "incre" indicates an increase of the profile phase, "decr" is decreasing from the phase profile and "const" is the constant profile phase.

The block diagram shown in Figure 3.11 summarizes the keogram analysis described above.

Table 3.5 - Propagation direction of MSTID obtained from the keograms visualization. "incre" indicates an increase of the profile phase, " decr" decreasing from the phase profile and "const" is the constant profile phase.

Phase	N	NE	E	SE	S	SW	W	NW	Stationary
Latitude	incr	incr	const	decr	decr	decr	const	incr	const
Longitude	const	incr	incr	incr	const	decr	decr	decr	const

Source: Paulino et al. (2011).

Figure 3.11 - Block diagram illustrating the process of keogram analysis and the respective equations.

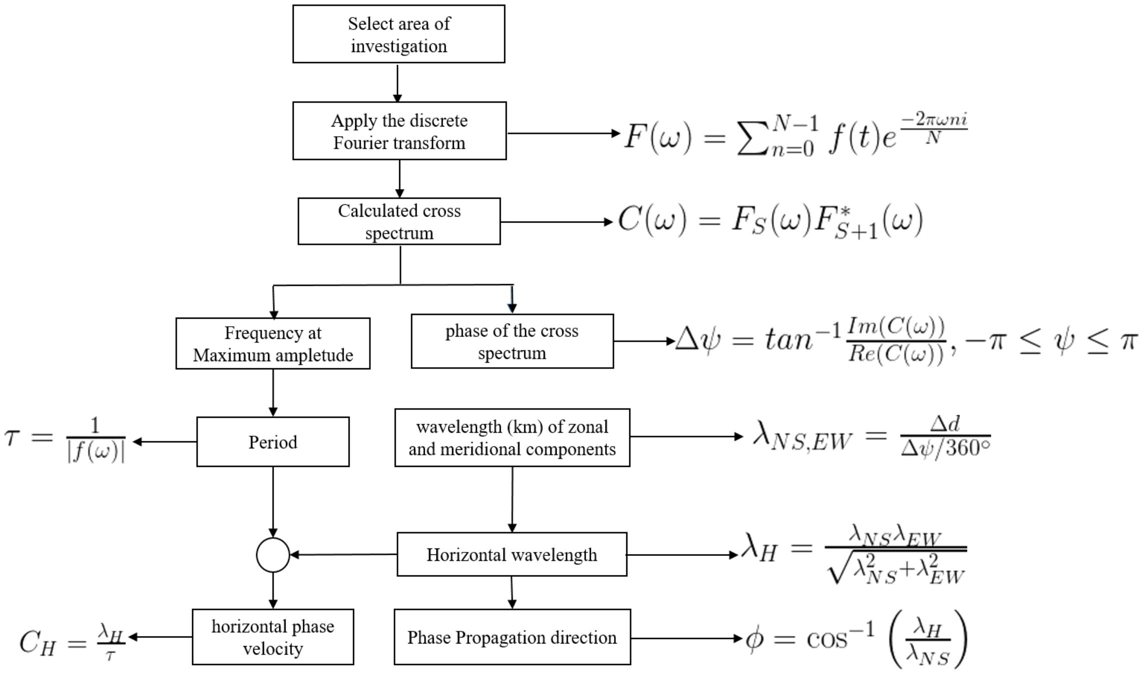

3.4.2 The outcome of spectral analysis of dTEC keograms

The results of the spectral analysis for the dTEC keogram in Figure 3.10 are shown in Figure 3.12; wavelength (λ_H) of 552.0 km; period (τ) of 29.9 minutes; horizontal phase velocity (C_H) of 308.1 m/s and propagation direction (ϕ) is 8.1° which implies almost northward. The left and right columns show the analysis of the zonal section and meridional respectively. The upper panel are the longitudinal (RHS) and latitudinal (LHS) keograms selected in Figure 3.10 as indicated by the white boxes. The middle panel shows the amplitudes and the lower panel shows the phase difference of the waves. The red dashed lines represent the level of significance, which is 95%.

Figure 3.12 - Result from the spectral analysis for the keogram in Figure 3.10. The upper panels are the result from the longitudinal (RHS) and latitudinal (LHS) keograms in Figure 3.10, indicated by west east (E-W) and north south (N-S), the second panel shows the amplitudes calculated by spectral analysis; the dashed line in red represents the level of significance which is 95%. The lower panels are the phase differences of the analyzed spectrum.

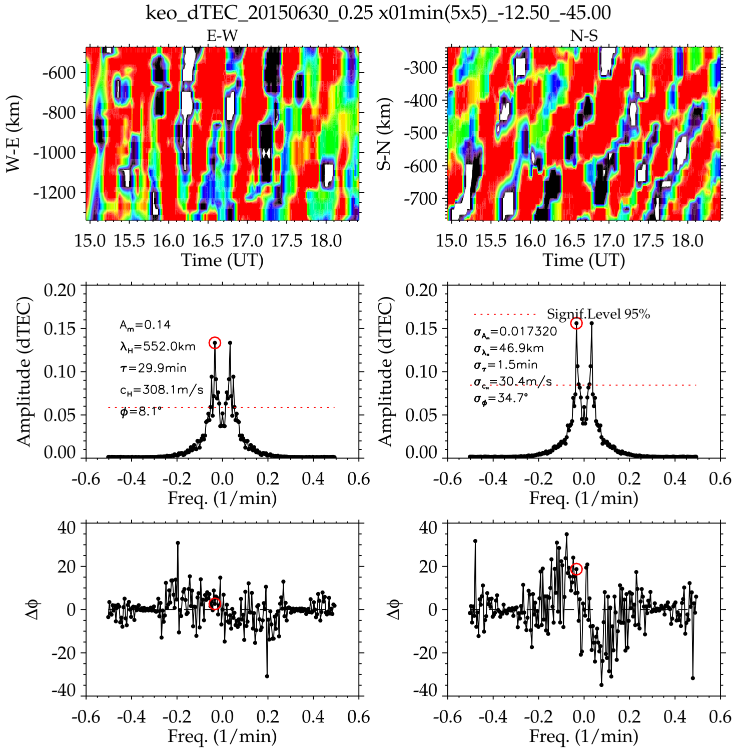

It is important to emphasize the need to interpolate the selected dTEC values. The reason is that the networks of GNSS receivers are not dense enough for the production of keograms with continuous spatial coverage. The region selected in rectangles present a discontinuity in the data, due to the adopted spatial resolution.

3.5 The uncertainty and significance level ot the spectral analysis

It is fundamental importance to know the uncertainty in the calculations of spectral analysis and its propagation to the other parameters such as (λ_H, τ, C_H and ϕ). The propagation of uncertainty in the spectral analysis is not trivial until it is not considered as an uncertainty produced by the Fourier transform. In the present study, an uncertainty of 5% was considered in the estimation of the period of propagation as a consequence of the level of significance estimated at 95% as shown in the spectral analysis result in Figure 3.12. Equations 3.12-3.15 from Bevington et al. (1993)

(page 41) were adopted to estimate the propagation of uncertainties.

An analysis was performed, in which waves with wavelengths of 100 to 1500 km were simulated, with a 50 km step; periods of 10 to 120 min, with a 10 min rate; and propagation directions from 0 to 600 m/s, with a pitch of 30 m/s. In the calculations of λ_H and C_H shows uncertainties less than 10%, with the corresponding uncertainty of propagation direction less than 5%.

To determine the significance levels for each Fourier spectrum, one must first and foremost chooses an appropriate background spectrum. For many geophysical phenomena, an appropriate background spectrum is white noise which is distributed consistently across all frequencies of the Fourier spectrum, or red noise, characterized by a noise that is distributed as follows: increases energy with decreasing frequency (TORRENCE; COMPO, 1998).

To estimate the normalized Fourier spectrum for red or white noise, Equation 3.22 is used Torrence e Compo (1998), which is assumed as the coefficient of the auto-correlation ωn= 0, ..., N / 2 is the frequency index; Note that for white noise, zero is used. On the other hand, the value of red noise is between 0 and 1, estimated from models that use auto-correlation.

$$P_\omega = \frac{(1-\alpha^2)}{1+\alpha^2-2\alpha cos(2\pi\omega/N)} \tag{3.22}$$

The Fourier power spectrum of the time series is normalized by the variance (σ^2/N), and the spectra calculated in the present work use white noise with a 95% significance level. Thus, to use the level of significance, the null hypothesis must be defined. The null hypothesis is the amplitude of the mean spectrum that is above the white noise amplitude with a certain level of confidence; which is 95% for the current study. An example is shown in the middle panel of Figure 3.12, the 4 peaks in the mean spectrum amplitude above red dotted lines. From the definition of the null hypothesis, we can assume that the oscillation presents a period with a confidence level of 95%.

The significance level is defined by the multiplication of the calculated mean spectrum (P_ω) By the variance of the mean temporal series (σ^2) with the 95% percentile of the distribution of χ_2 to two degrees of freedom (χ_2^2) (TORRENCE; COMPO, 1998). In that the distribution of χ_2 to 2 degrees of freedom relative to the Fourier power spectrum as,

$$\frac{N\left|F(\omega)\right|^2}{\sigma^2} \Rightarrow \frac{1}{2}P_\omega\chi_2^2 \tag{3.23}$$

It uses the concepts of variance defined by Torrence e Compo (1998), and thus, the theoretical Fourier spectrum becomes $\omega^2 P_\omega$, conforming to the normalized spectrum.

4 RESULTS: STATISTICAL ANNALYSIS OF MSTID CHARACTERISTICS OBSERVED OVER SOUTH AMERICAN EQUATORIAL REGION DURING SOLAR CYCLE 24

4.1 Introduction

In chapter 4, the outcome of the statistical analysis of the characteristics occurrence rate of the day-to-day variability of the MSTIDs observed over South American equatorial ionosphere using GPS and GLONASS will be presented. It will first and foremost, focus on the result from the characterization (horizontal wavelength, period, phase speed) of the present equatorial MSTIDs. It will futher present the monthly and annual occurrences of the MSTIDs during the solar maximum phase (January 2014 to December 2015), descending phase (January 2016 to December 2017) and minimum phase (January 2018 to December 2019) of the solar cycle 24. Finally, conclusion will be drawn based on the statistical distribution and the characteristics derived from the results.

Over the equatorial region of South America a few works on MSTIDs had been carried out (PAULINO et al., 2016; JONAH et al., 2016) and (MACDOUGALL et al., 2011). They reported and discussed the propagation velocity, period and possible source mechanisms. So far, no thorough work has been done on the long term and seasonal variations of MSTIDs occurrence rate and characteristics in relation to the solar cycle phases over the equatorial region of South American and beyond. Therefore, the present work will throw more light on the characteristics and occurrences of MSTIDs observed by GPS and GLONASS during solar cycle 24 over South American equatorial region (0°-15°S, 30°-55°W).

4.2 Characteristics of MSTIDs over South American equatorial region

The TEC data obtained with the GLONASS and GPS receivers in South America from January 2014 to December 2019 were processed, dTEC (also called TEC perturbation) calculated and interpolated on the map at their corresponding longitude and latitude of the IPP positions. In total, 13140 keograms were created from the sequences of TEC perturbation maps as described in section 3.4. This implies that 6 different keograms were created for each day throughout the observation period. This was done in order to characterize the possible MSTID structure. Using the FFT cross spectrum analysis, the characteristics of 742 MSTIDs were calculated from January 2014 to December 2019. In order to investigate the seasonal variations of the MSTIDs characteristics and their local time dependence, the 6-year dataset was divided into all seasons, equinoxes (March-May and September-November), summer (December-February) and winter (June-August). The MSTIDs events are characterized by their usual horizontal wavelength, period, horizontal phase velocity and propagation direction.

4.2.1 Horizontal wavelength of the MSTIDs

Using Equation 3.18, the wavelengths of all the MSTIDs captured on the keograms were calculated. Figure 4.1 shows the distribution of the number of MSTID occurrence as a function of the horizontal wavelength of the MSTIDs observed (at the left hand side (left column)) from January 2014 to December 2019 in (a) all seasons, (b) equinoxes, (c) summer, and (d) winter. The horizontal wavelengths are divided into 100 km bins and the solid black line represent the Gaussian fit of the distribution. In order to investigate the local time dependence of the horizontal wavelength, the data were divided into 200 km bins, and plotted against the corresponding time of occurrence at the right hand side (right column). Most of the horizontal wavelengths in (a), (b) and (d) are between 500 and 800 km and occurred during daytime and evening time, although there are few nighttime events during equinox. In summer, the majority of the events are distributed between 500 and 900 km and occurred during dusk and nighttime with few daytime events. The corresponding mean values are for (a), (b) (c) and (d) are 667 ± 131, 705 ± 120, 719 ± 163 and 628 ± 114 km respectively.

Figure 4.1 - The horizontal wavelength distribution (left column) and the time variation (right column) of the MSTIDs observed between December 2012 and February 2016 for (a) all seasons, (b) equinoxes, (c) summer, and (d) winter. The solid black line is a Gaussian fit (left column).

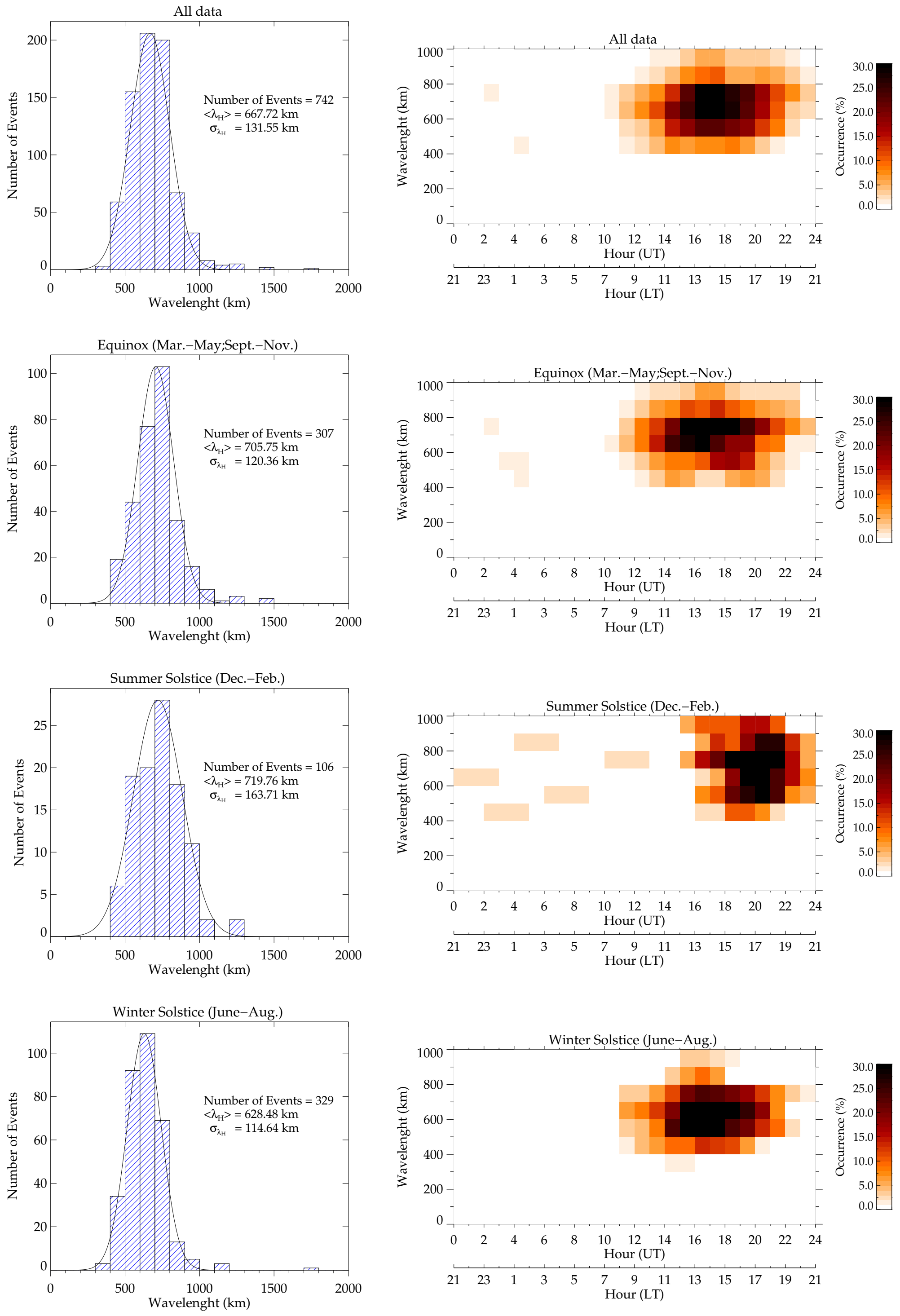

4.2.2 Period of MSTIDs

The corresponding periods of the MSTIDs were calculated using Equation 3.16. The left column of Figure 4.2 shows the number of events as a function of MSTID period for (a) all seasons, (b) equinoxes, (c) summer, and (d) winter. The periods are divided into 5 min bins and solid black line represent the Gaussian fit of the distribution. The periods for (a), (b), (c), and (d) are ranging from 20 and 60 min with mean value of 36 ± 7 , 37 ± 7, 39 ± 7 and 34 ± 6 min respectively. In all season and equinoxes, the maximum period is concentrated around 30 to 45 min while summer and winter are 35 to 45 min and 30 to 40 min respectively. The respective time dependence of the periods of the MSTIDs for (a), (b), (c) and (d) are shown at right column. The periods of the daytime and evening time MSTIDs are widely distributed for (a), (b), (c), and (d) compare to nighttime MSTIDs. Meanwhile, it is difficult to compare the day and dusk to nighttime due to the limited number of events.

Figure 4.2 - Distribution of the observed period (left column)) and the time variation (right column)) of the MSTIDs observed between December 2012 and February 2016 for (a) all seasons, (b) equinoxes, (c) summer, and (d) winter. The solid black line is a Gaussian fit.

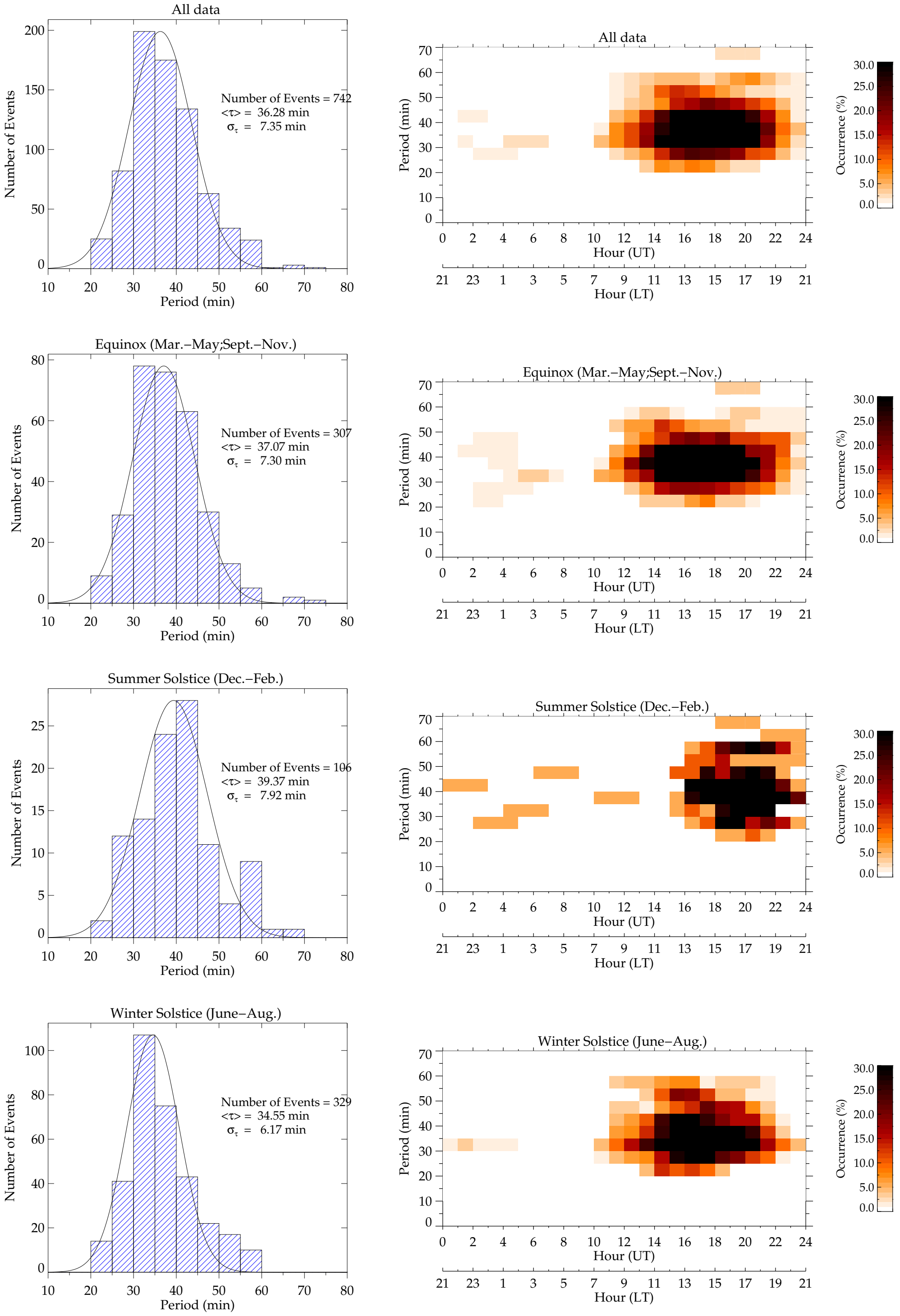

4.2.3 Horizontal phase velocity of the MSTIDs

The phase velocities of the respective MSTIDs observed from January 2014 to December 2019 over South American equatorial region were calculated using Equation 3.19. The left column of Figure 4.3 presents the horizontal phase velocity of the MSTIDs for (a) all seasons, (b) equinoxes, (c) summer, and (d) winter. They are divided into 200 m/s bins and the solid black line is a Gaussian fit for the distribution. It is clear that the MSTIDs phase velocities peak at 200 to 400 m/s for all seasons, equinox, summer and winter components. The mean distribution of the horizontal phase velocity for (a), (b), (c), and (d) are 301 ± 60, 309 ± 78, 317 ± 85 and 291 ± 66 m/s, respectively. The summer mean is higher as compare to winter, and equinox. The RHS of Figure 4.3 shows the time dependence of the horizontal phase velocity of MSTIDs observed for (a), (b), (c), and (d). They are also divided into 200 m/s bin, and the horizontal phase velocities are plotted as a function of the local/universal time. The phase velocities are distributed between 100 and 600 m/s in the summer daytime and evening hours, and 300 to 600 m/s in the summer nighttime. The dominants winter daytime and dusk MSTIDs are distributed between 100 to 500 m/s. Meanwhile, the daytime and dusk MSTIDs during equinoxes are widely distributed between 100 and 700 m/s with nighttime peaked around 100 to 400 m/s. The high values of horizontal phase velocities occurred during daytime MSTIDs, which implies that present the phase velocity is found to be slightly faster in daytime than evening and nighttime.

Figure 4.3 - The horizontal phase velocity distribution and time variation of the observed medium-scale traveling ionospheric disturbances for (a) all seasons, (b) equinoxes, (c) summer, and (d) winter. The solid black line is a Gaussian fit.

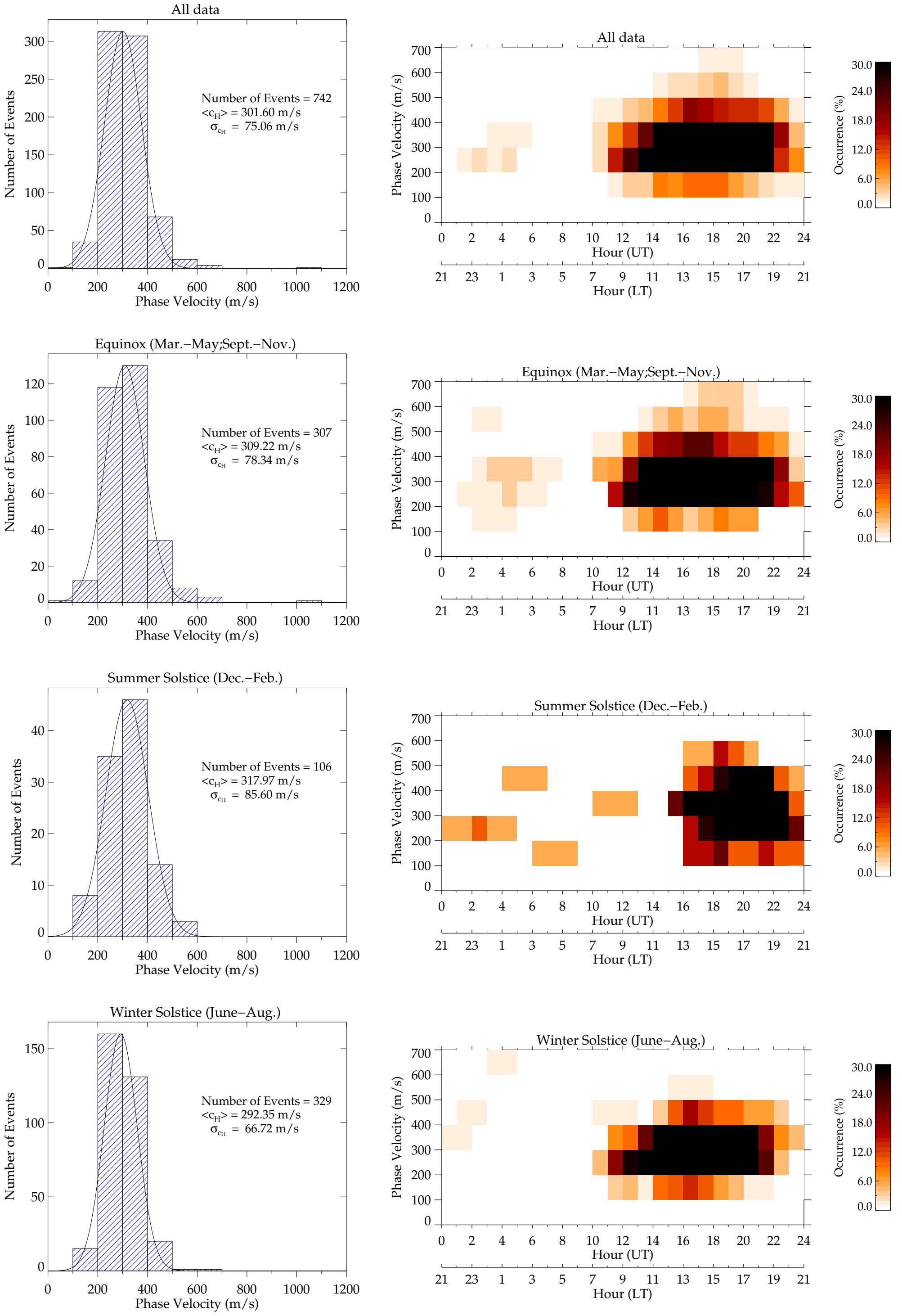

4.2.4 Propagation direction of the MSTIDs

The propagation direction of the MSTIDs observed as a function of phase velocity from January 2014 to December 2019 for (a) all seasons, (b) equinoxes, (c) summer, and (d) winter are shown in the left column of Figure 4.4. The propagation direction was defined as the angle clockwise from geographical north. The data was classified into 30° bins and calculated the occurrence rate in each azimuthal bin. The red arrows indicate the nighttime MSTIDs events while that of the blue are daytime and evening time. In (a) and (b), the MSTID activities propagated predominantly north-northeast, north-northwest and south-southeast directions while few are propagating westward. There is a significant different between summer and winter events in their propagation directions. That is, in summer, the propagation directions are preferentially south-southeastward and westward while in winter is predominantly north-northeast and north-northwest directions with few southeastward.

The left column of Figure 4.4 shows the azimuth of the MSTID propagation direction as a function of local time for (a), (b), (c), and (d). The occurrence rate was defined as the ratio of the period for the entire MSTIDs observation interval. In summer, $\sim 50\%$ of the daytime and evening time MSTID propagation direction are concentrated in south-southeast direction (120° to 180°); another $\sim 30\%$ daytime and evening time MSTID also propagating in the north-northwestward (300° to 360°); also about $\sim 15\%$ of them propagate in the westward (140° to 300°) direction. The few nighttime events captured did not show any preferential propagation direction. In the equinoxes, $\sim 90\%$ of the daytime and dusk MSTIDs occurred propagated to north-northeastward, north-northeastward and south-southeastward. In winter, $\sim 90\%$ of the daytime and evening time MSTIDs are preferentially north-northeastward and north-northeastward with $\sim 10\%$ propagating in the south-southeast direction.

Figure 4.4 - The propagation direction and time variation of the observed medium-scale traveling ionospheric disturbances for (a) all seasons, (b) equinoxes, (c) summer, and (d) winter. The red arrows indicate the nighttime MSTIDs events while that of the blue are daytime and dusk.

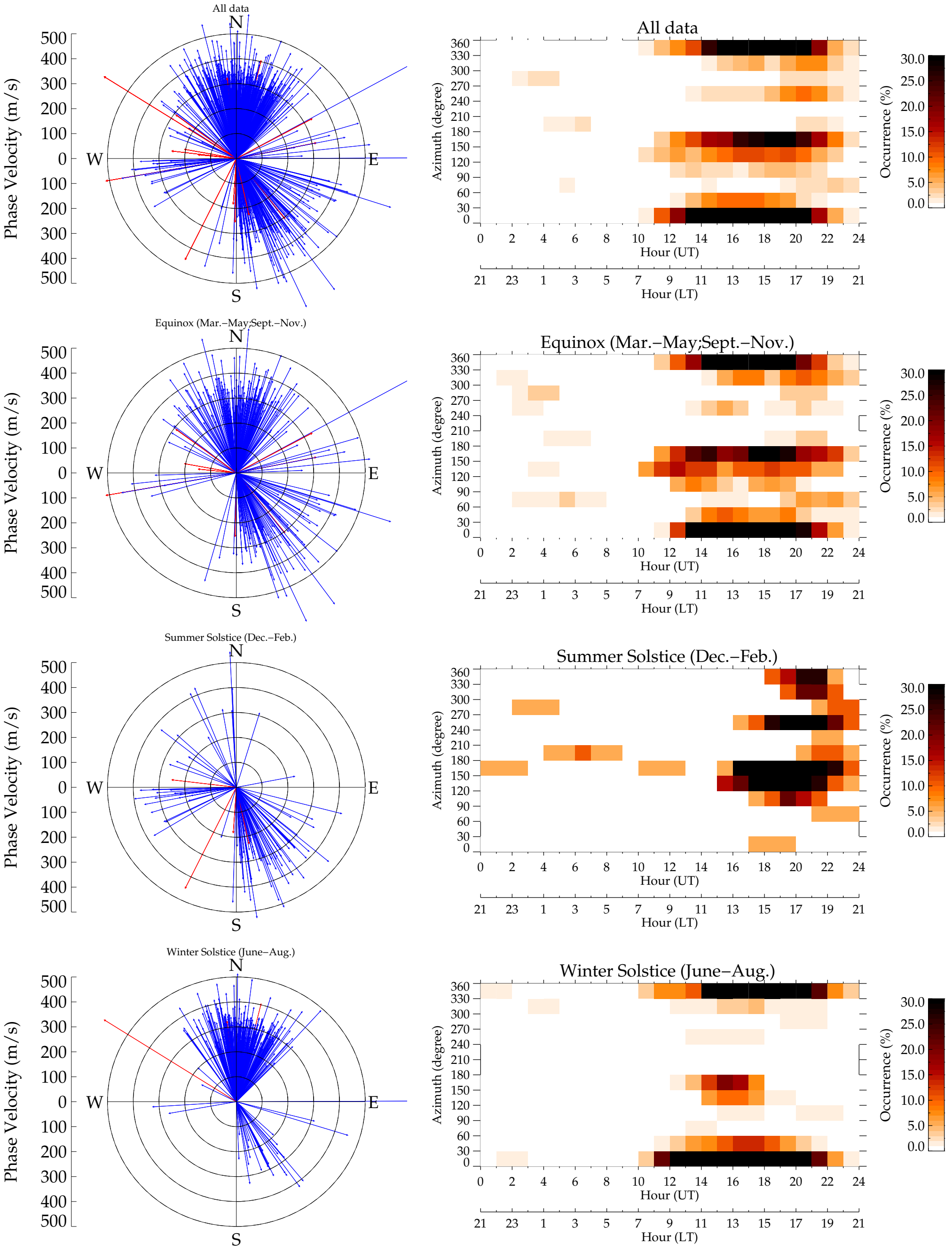

4.3 The evolution of the observed MSTID characteristics during solar cycle 24

In other to investigate the evolution of the characteristics of the MSTIDs observed during solar cycle 24, we plotted the horizontal wavelengths, periods, phase velocities and azimuths from 2014 to 2019.

For instance, Figure 4.5 shows the wavelengths of MSTIDs observed from January 2014 to December 2019 over South American equatorial region. Most of the wavelength in 2014, 2015, 2016 and 2017 propagated around 500-800 km with the mean of 654 ± 110, 634 ± 120 , 675 ± 61 and 709 ± 122 km respectively, while those of 2018 and 2019 range between 400-800 and 500-1000 km with the mean of 660 ± 153 and 755 ± 166 km respectively. The mean wavelengths of the MSTIDs observed increase with solar activities. In the solar maximum and descending phases, the wavelengths ranges are widely spread as compare to the minimum solar phase epoch. The corresponding mean values of the wavelengths are tabulated in Table 4.1.

Figure 4.5 - The evolution of wavelength of MSTID observed from January 2014 to December 2019 over South American equatorial region.

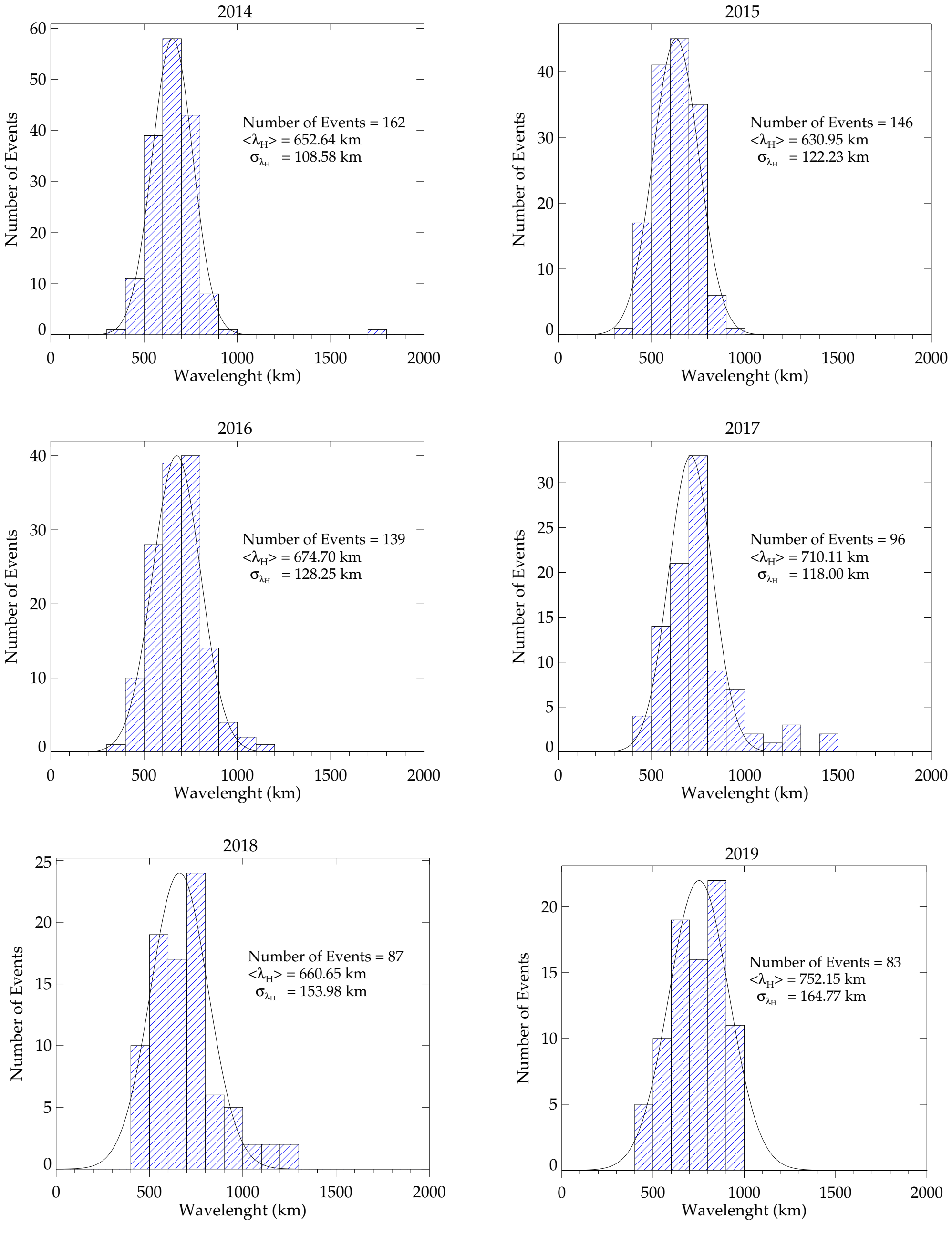

Table 4.1 - The annual mean distribution of period, horizontal wavelength, phase speed and the number of events of the MSTIDs events observed during solar cycle 24.

Parameter	Wavelength (km)	Period (min)	Phase Velocity (m/s)
2014	654 ± 110	35 ± 7	292 ± 73
2015	634 ± 120	35 ± 6	292 ± 62
2016	674 ± 128	35 ± 5	312 ± 67
2017	709 ± 122	37 ± 7	310 ± 85
2018	660 ± 154	36 ± 9	307 ± 85
2019	752 ± 165	38 ± 9	306 ± 86

As shown in Figure 4.6, majority of the periods in 2014, 2015, 2016, 2017, 2018 and 2019 propagated around 30-45 min with the mean of 35 ± 7, 35 ± 6, 35 ± 5, 37 ± 7, 36 ± 9 and 38 ± 9 min respectively. The mean periods of the observed MSTIDs indicate clear correlation with solar activities as increasing with decreasing solar flux. The corresponding mean values of the periods are tabulated in Table 4.1.

Figure 4.6 - The evolution of period of MSTID observed from January 2014 to December 2019 over South American equatorial region.

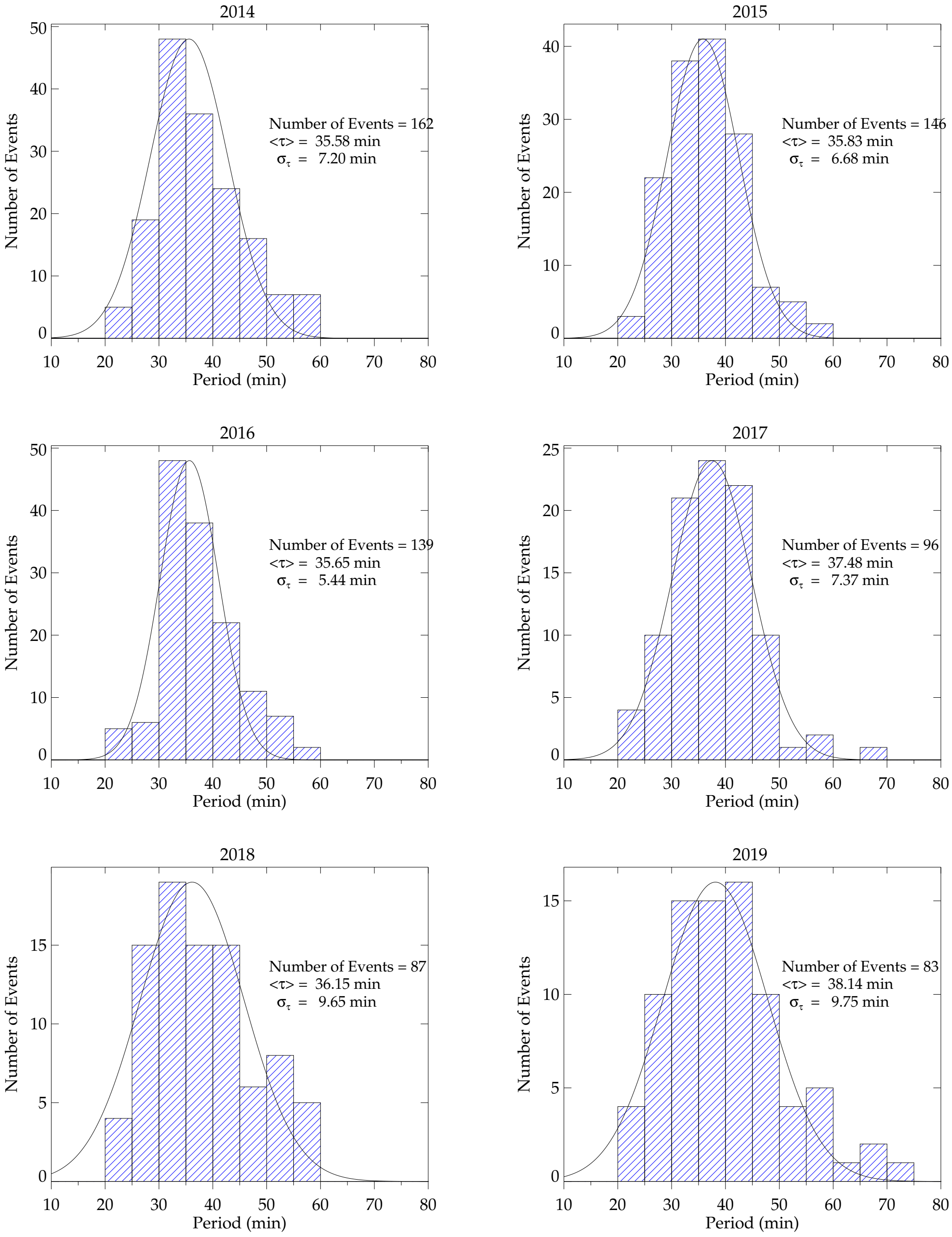

The maximum phase velocities of the MSTID events observed in 2014, 2015, 2016, 2017, 2018 and 2019 propagated around 200-400 m/s with the mean values of 292 ± 73, 292 ± 6, 312 ± 66, 310 ± 8, 307 ± 8, and 307 ± 7 m/s, respectively as shown Figure 4.7. The mean horizontal phase velocities of the observed MSTIDs indicate clear correlation with solar flux. The corresponding mean values of the phase velocities are tabulated in Table 4.1.

Figure 4.7 - The evolution of phase velocity of MSTID events observed from January 2014 to December 2019 over South American equatorial region.

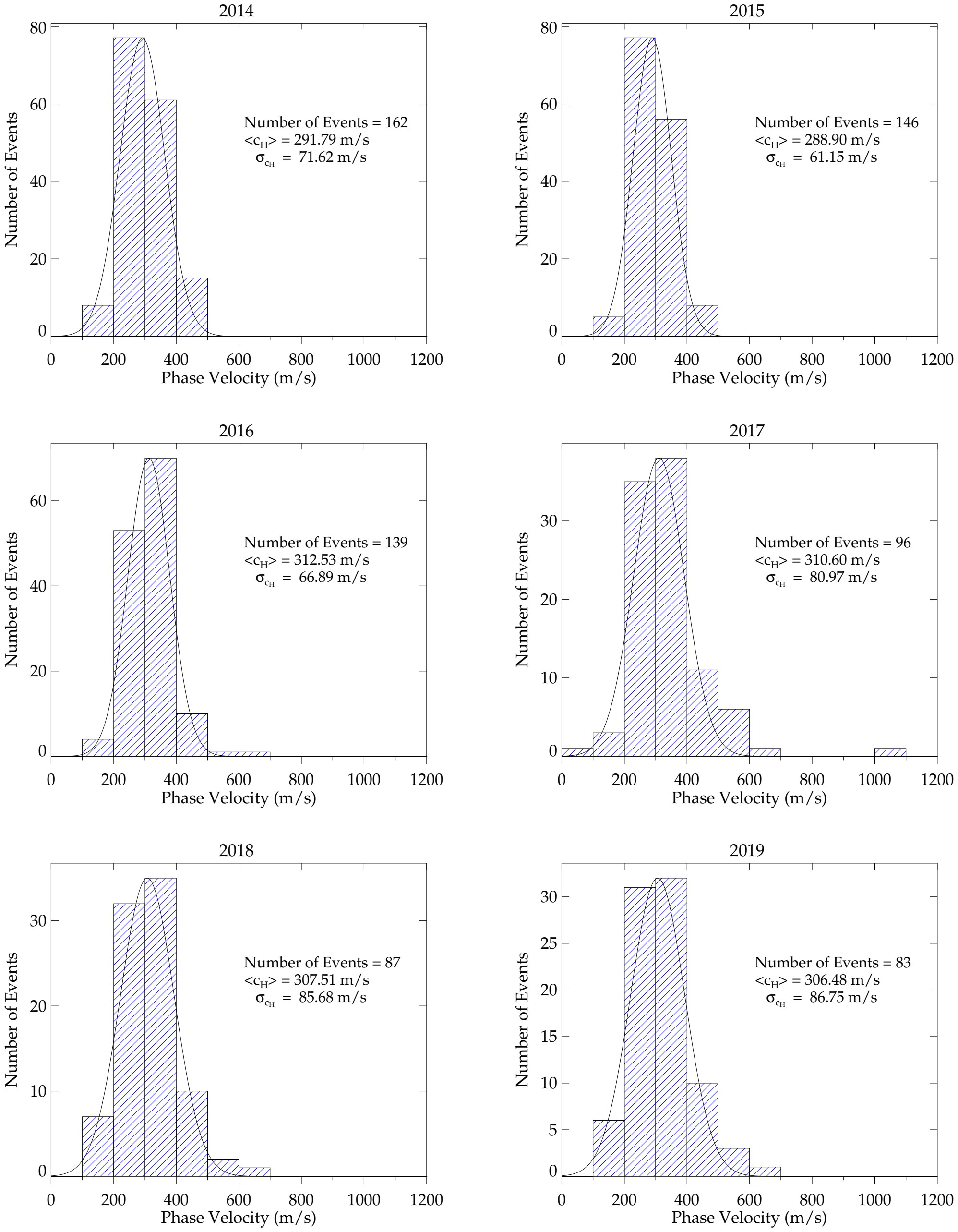

To analyze the anisotropy of the azimuth, the propagation direction of the MSTIDs are plotted as a function of the phase velocity as shown in Figure 4.8. Actually, all the years shows same azimuthal preference to north-northeastward and north-northwestward, south-southeastward and few to westward. There are more nighttime events in 2016 than the other years as indicated by the red color.

Figure 4.8 - The propagation direction of the MSTIDs observed from January 2014 to December 2019 over South American equatorial region.

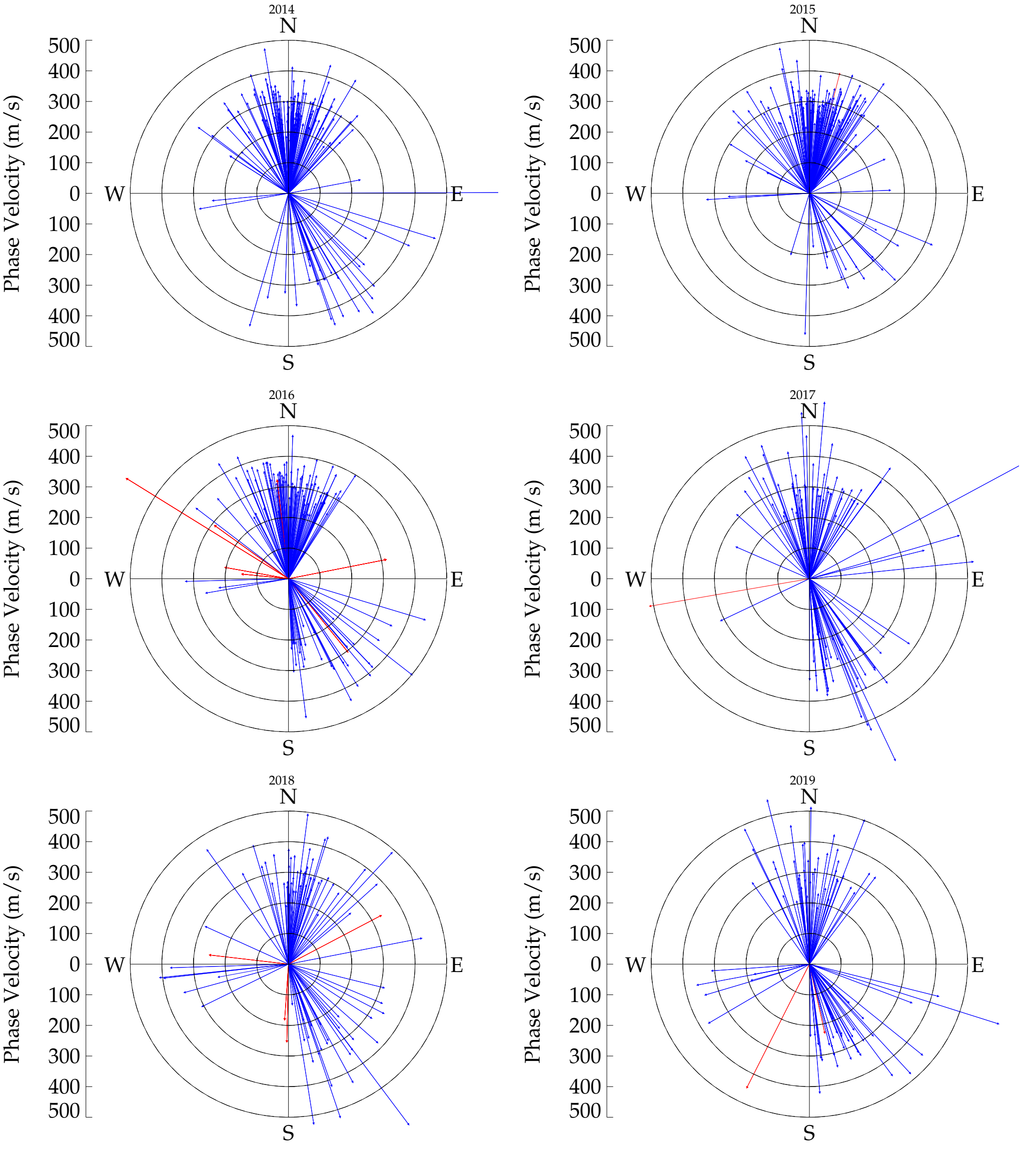

4.4 The occurrences rate of MSTIDs over South American equatorial region during geomagnetically quiet and disturbed conditions

Day-to-day visual assessment of the TEC perturbation keograms were done to record the number of MSTIDs that propagated during the period of study. The selected number of MSTIDs were analyzed using FFT cross spectrum described in subsection 3.4.2 to confirm their existence and then characterized them into wavelength, phase velocity, period and propagation direction.

After thorough assessment, the total number of MSTID events registered within the six years of observation were 742 for both geomagnetically quiet and disturbed condition. A total of 30 MSTIDs events were recorded during geomagnetic disturbed time. The climatological MSTIDs observed are 712 which account for $\sim 96\%$ of the total number of wave activities observed in the South American equatorial region from January 2014 to December 2019. Table 4.2 shows the statistical distribution of the number of MSTID events observed during geomagnetically quiet and disturbed conditions.

Table 4.2 - The number of MSTIDs observed during geomagnetically quiet and disturbed conditions from 2014 to 2019

Year	Geomagnetically Quiet time	Geomagnetically disturbed time	Total MSTID
2014	162	2	164
2015	146	12	158
2016	139	2	141
2017	96	14	110
2018	86	2	88
2019	83	0	83

The Dst (Disturbance Storm Time) is the H-component perturbation on equatorial magnetometers (BOROVSKY; SHPRITS, 2017; MAYAUD, 1980) which is a historical definition of a magnetic storm that goes back to von Humbolt in the early 1800's (MALIN; BARRACLOUGH, 1991). The creation of the Dst index was initiated by Bartels who advocated for the development of an index for monitoring the equatorial ring current (BOROVSKY; SHPRITS, 2017; KERTZ, 1964; MAYAUD, 1980; SUGIURA, 1963). The Dst index represents the longitudinally averaged part of the external field measured at the geomagnetic dipole equator at the surface of the Earth (SUGIURA, 1963; BOROVSKY; SHPRITS, 2017) and is provided by the World Data Center for

Geomagnetism, Kyoto. The most often used definition of a geomagnetic storm is an event wherein the minimum of the Dst index goes below a critical value, for example,-50 nT or -100 nT (SUGIURA; CHAPMAN, 1961). Hence, the present work classified MSTID as geomagnetically storm related events when the Dst$\leq$-50 nT.

4.4.1 Solar cycle dependence of the MSTID occurrence rate

The ionosphere is part of the upper atmosphere where free electrons occur in sufficient density to have an appreciable influence on the propagation of radio frequency electromagnetic waves. The ionization depends primarily on the Sun and its activity. Ionospheric structures and peak densities in the ionosphere vary greatly with time (sunspot cycle, seasonally, and diurnally), with geographical location (polar, auroral zones, mid, low latitudes and equatorial regions), and with certain solar-related ionospheric disturbances.

The sunspot cycle is an important periodicity of solar variability that indicates the extent of closed magnetic field structure on the sun, hence, determining the solar activity. The solar radio flux at 10.7 cm (2800 MHz) which is often called the F10.7 index is an excellent indicator of the solar radiation, and one of the longest running records of solar activity. Unlike many solar indices, the F10.7 flux can easily be measured reliably on a day-to-day basis from the Earth's surface, in all types of weather. The “solar flux units (SFU)” can vary from below 50 to above 300 over the course of a solar cycle. Therefore, F10.7 index has proven very valuable in the study of space weather since is a long record, which provides climatology of solar activity. The F10.7 radio emissions originates from the chromosphere and corona of the sun, and tracks other important emissions such as Extreme Ultra-Violet (EUV) emissions that affect the ionosphere through photoionization process.

The recent ended solar cycle is the 24th since 1755, when the extensive recording of solar sunspot activity began. Figure 4.9 shows the profile of the complete cycle 24. It began in December 2008 with a smoothed minimum sunspot number of 2.2 and reached maximum in April 2014. The maximum phase continued through 2015 and assumed descending phase in 2016 and 2017. In 2018 and 2019, it attained a minimum phase with low solar activities. The green points represent the daily F10.7 indices and the blue is the six months corresponding running averaged.

Figure 4.9 - The entire Solar cycle 24 in green and the Six month running averages of the daily mean values in blue.

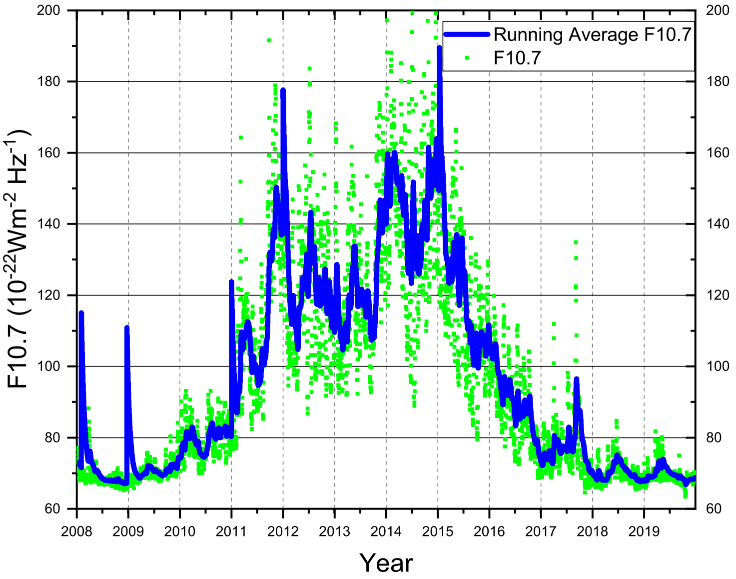

The present study covers the half period of solar cycle 24 epoch, therefore, in order to investigate the possible effect of solar activity on the occurrence rate of MSTIDs events. The statistical analysis of the occurrence rate of the MSTIDs observed during the solar cycle 24 is plotted as a function of month and year as shown in Figure 4.10. The most significant difference between the geomagnetic quiet and disturbed condition is seen in September 2017 MSTID events where the total MSTID events for both geomagnetic quiet and disturbed condition were 24, but considering the days with only geomagnetically quiet condition, it becomes 13 MSTID events. These differences are due to the sequences of geomagnetic storm that occurred between 6-10 and 25-26 September.

The typical examples of MSTIDs observed during the geomagnetic disturbed condition were 2015 March 18-19 (St. Patrick's Day storm), 2017 September 6-12, and 2018 August 20-26 among others. This result is interesting, because there have been many studies investigating the relationship between the occurrence of MSTIDs with such geophysical activity (CHIMONAS, 1970; CROWLEY et al., 1987; FRANCIS, 1974; FRANCIS, 1975; HE et al., 2004; MACDOUGALL et al., 2011; GROCOTT et al., 2013; FRISSELL et al., 2014; FRISSELL et al., 2016). For instance, Frissell et al. (2016) investigated whether or not space weather had an effect on MSTID occurrence. They concluded that the AE and SYM-H indices did not correlate with MSTID occurrence. The new availability 4% MSTID measurements in the equatorial latitude of South America as presented herein during high Dst indices, has therefore, opened the door to new correlative investigations. However, the present study will focus on the MSTIDs that propagated during the geomagnetically quiet condition since that account for only 96% of the total events.

From Figure 4.10, in 2014 and 2015 which denote the maximum solar phase, 165 and 156 MSTID events respectively, were observed with majority occurring during the winter solstice (June, July and August). In 2016, in the solar declining phase, a total of 141 MSTID events were recorded with high occurrence rate in the winter months as well. This is similar to what Figueiredo et al. (2017) observed over south-southeastern region of Brazil. Although, the number of MSTIDs activities continued decreasing to 110 in 2017; but unlike the previous years, most activities in September equinox followed by the usual winter majority. In the 2018 and 2019, the minimum solar phases, 88 and 83 MSTID events were recorded respectively, but they do not show the usual winter predominance. Therefore, the six-year statistical analysis reveals positive MSTID occurrence rate dependency with the solar activity.

Figure 4.10 - The occurrence rate of MSTIDs over South America equatorial region during solar cycle 2, for both geomagnetic quiet and disturbed conditions.

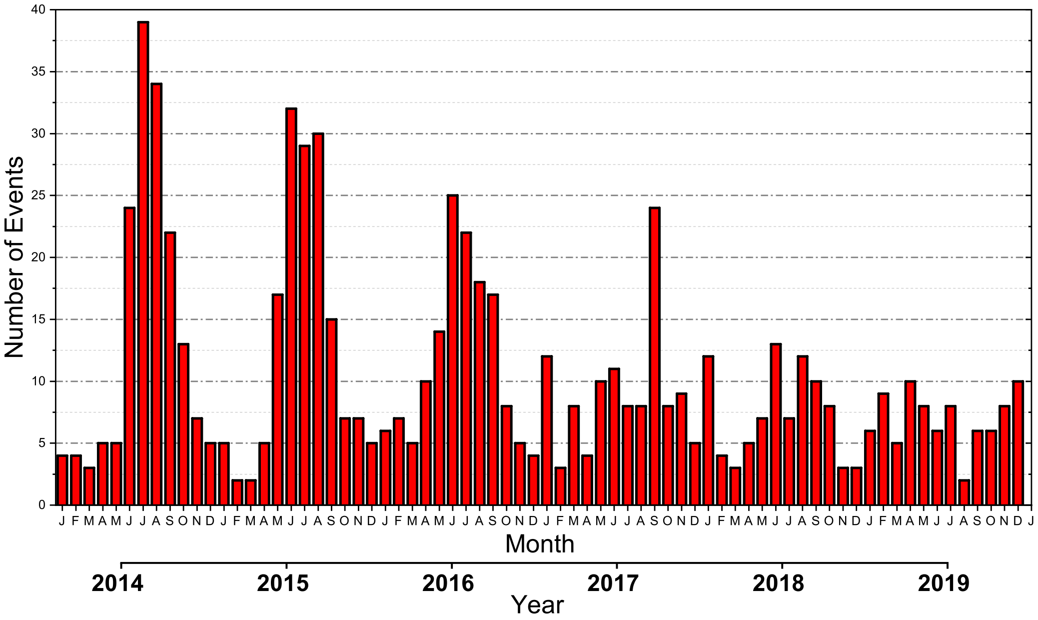

There is an annual variations in the statistical analysis of the MSTID events. For example, from the maximum solar phase, the MSTIDs occurrence rate decrease rapidly through the descending phase to the minimum solar phase. Meanwhile, the seasonal variation exhibited by MSTID occurrence rate peaks around the winter solstice months in all the years with the exception of the minimum solar phase where the usual winter preference are not clear. On the other hand, the summer events seems to increase from the solar maximum to minimum. The common lack of MSTID activity is noticeable in summer months, especially during maximum solar phase, which can be a potential interest for applications where MSTID is a significant. The occurrence pattern during equinoxes from 2014-2016 are quite similar as well as 2017-2019. Therefore, we report that in the South American equatorial region, there is a clear positive solar activity dependence of the annual MSTIDs occurrence rate. The significant of the solar cycle influence on the MSTIDs dependence will be discussed in the chapter 5

In summary, Table 4.3 show the occurrence rate of MSTIDs and the corresponding percentage from 2014 to 2019. For instance during solar maximum phase, 2014 and 2015 the observed MSTID occurrence rates are 164 and 158 with corresponding percentage of ∼ 22.1% and ∼ 21.0%. During descending solar phase we recorded 141 and 110 MSTID events in 2016 and 2017 with corresponding percentage of ∼ 19% and ∼ 14.8%. In 2018 and 2019 solar minimum phase, we obtained 88 and 83 activities representing ∼ 11.9% and ∼ 11.2% respectively.

Table 4.3 - The annual occurrence rate of MSTIDs and the corresponding percentage from 2014 to 2019

Year	Solar cycle phase	MSTID events	Percentage
2014	Maximum	164	22.1
2015	Maximum	158	21.0
2016	Descending	141	19.0
2017	Descending	110	14.8
2018	Minimum	88	11.9
2019	Minimum	83	11.2

4.4.2 Time dependence of MSTIDs occurrence rate

The occurrence rate of MSTIDs has been reported to be dependent on local time by many authors (KOTAKE et al., 2007; TSUGAWA et al., 2007; OTSUKA et al., 2013; FIGUEIREDO et al., 2018a). However, in the South American equatorial region the local time dependency of MSTIDs are not known. Thus, this section will investigate the monthly/seasonal time dependence of MSTIDs occurrence rate during the six years of observation. The yearly interval was divided into four seasons; winter (June-August), summer (December-February), and spring equinox (September-November) and autumnal equinox (March-May). Figure 4.11 shows the time dependence of the MSTID occurrence rate in monthly and hourly bins for the six years data combined (January 2014 to December 2019). The occurrence rate is defined as the ratio of the time duration of the MSTIDs to the monthly and hourly observation intervals. The months are represented by their initials and the dawn and dusk solar terminator are shown at the altitude of 100 km (dotted lines) and 300 km (broken line).

Figure 4.11 - Time dependence of rate of occurrence of MSTID observed from January 2014 to December 2019 over South American equatorial region. The months are represented by their initials and the dawn and dusk solar terminator are shown at the altitude of 100 km (dotted lines) and 300 km (broken line).

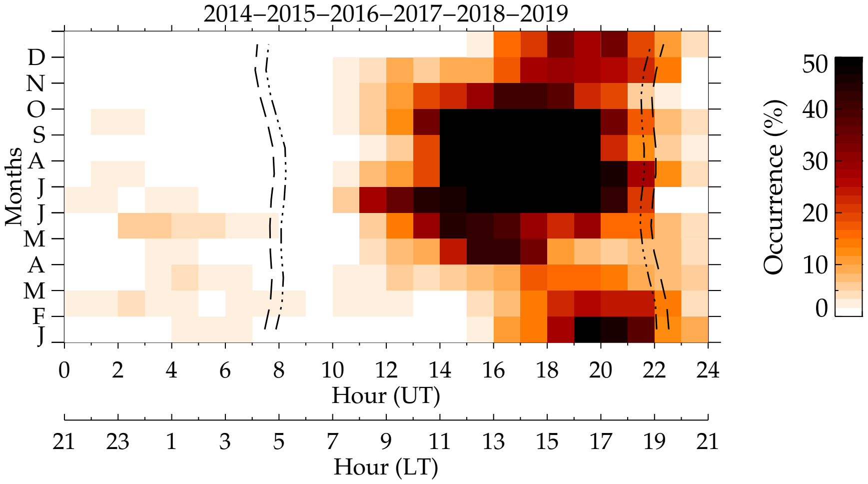

It is obvious from Figure 4.11 that the MSTID occurrence rate strongly depends on the local time. The occurrence rate can be classified into three as daytime, evening time and nighttime. The daytime (7:00-17:00 LT) which mostly occur during winter with secondary peak in equinox whereas the evening time (17:00-20:00 LT) occur in winter and summer with minor peak in equinox while the few nighttime (21:00-4:00) events do not show any clear seasonality. The occurrence rate in daytime is ~70% of the total number of MSTIDs observed, while evening time MSTIDs is ~28% and the nighttime account for only ~2% of the total MSTIDs observed. The local time occurrence of MSTID near the dawn terminator side in the present work is rare.

Moreover, Figure 4.12 shows the evolution of the time dependence of MSTIDs from 2014 to 2019. The nighttime MSTIDs were rare during solar maximum but frequently occurred in summer and equinox descending and minimum solar phase. The daytime MSTIDs occurred mostly during winter maximum solar phase and decreases with the solar activities.

Figure 4.12 - Time dependence of rate of occurrence of MSTID observed from January 2014 to December 2019 over South American equatorial region. The months are represented by their initials and the dawn and dusk solar terminator are shown at the altitude of 100 km (dotted lines) and 300 km (broken line).

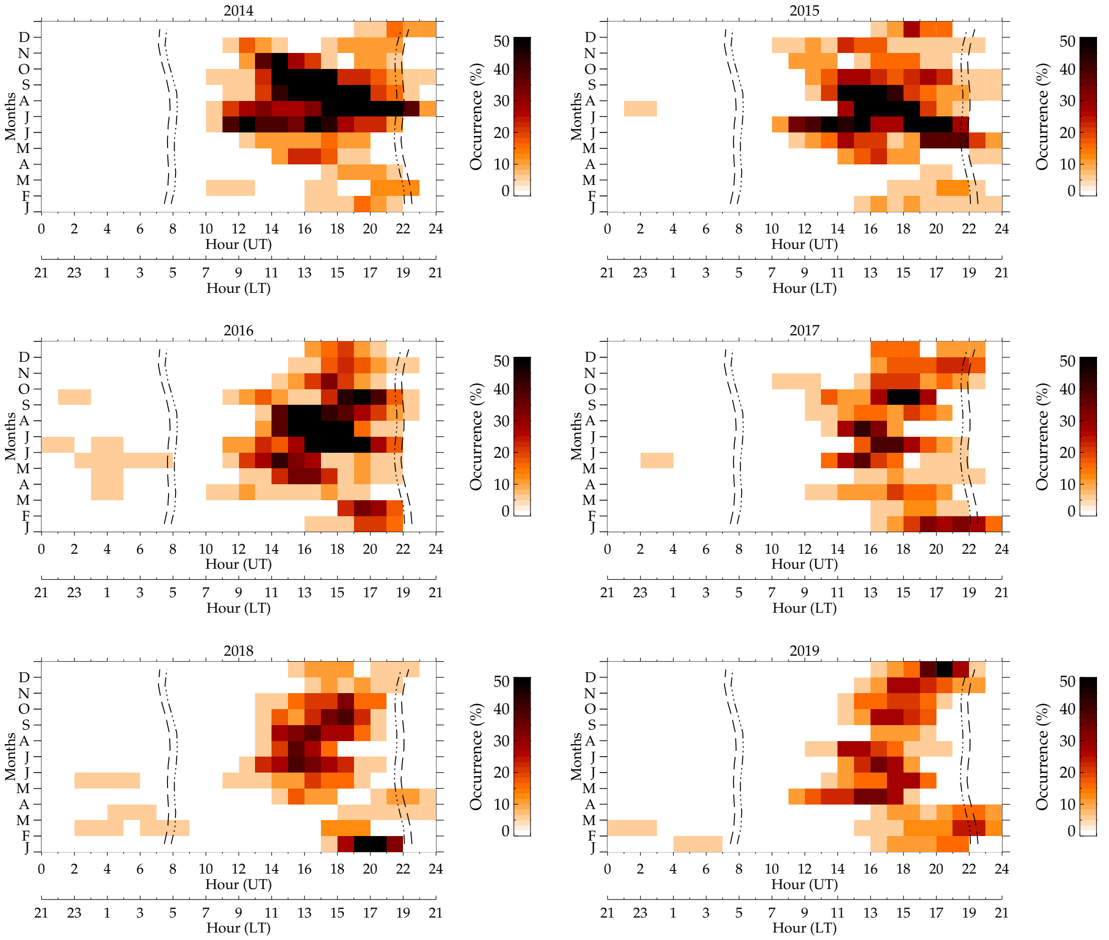

4.5 Summary of the results

Using the GNSS detrending TEC maps and keograms we studied the occurrence rates and characteristics of MSTIDs in the South America equatorial region during solar cycle 24. The outcome of the statistical analysis and the characteristics are as follows;

- The horizontal wavelengths for all seasons, equinoxes and winter are peaked between 500 and 800 km with mean values of 667 ± 131, 705 ± 120 and 628 ± 114 km respectively, while summer events are distributed between 500 to 900 km with mean value of 719 ± 163. The wavelength in 2014, 2015, 2016 and 2017 propagated around 500-800 km with the mean of 654 ± 110, 634 ± 120 , 675 ± 61 and 709 ± 122 km while those of 2018 and 2019 range between 400-800 and 500-1000 km with the mean of 660 ± 153 and 755 ± 166 km respectively.

- The periods for all seasons, equinoxes, summer, and winter are ranging from 20 and 60 min with mean value of 36 ± 7 , 37 ± 7 , 39 ± 7 and 34 ± 6 min respectively. The periods of the daytime and dusk MSTIDs are widely distributed compare to nighttime MSTIDs. Periods in 2014, 2015, 2016, 2017, 2018 and 2019 propagated around 30-45 min with the mean of 35 ± 7, 35 ± 6, 35 ± 5, 37 ± 7, 36 ± 9 and 38 ± 9 min respectively.

- The MSTIDs phase velocities peak at 200 to 400 m/s for all seasons, equinoxes, summer and winter components with the mean values of 301 ± 60, 309 ± 78, 317 ± 85 and 291 ± 66 m/s, respectively. The maximum phase velocities of the MSTID events observed in 2014, 2015, 2016, 2017, 2018 and 2019 propagated around 200-400 m/s with the mean values of 292 ± 73, 292 ± 6, 312 ± 66, 310 ± 8, 307 ± 8, and 307 ± 7 m/s, respectively.

- The MSTID activities in equinoxes and winter propagated predominantly north-northeast, north-northwest and south-southeast directions while in summer they propagation directions are preferentially south-southeastward. In addition, a few MSTID events propagated in westward during summer and equinox

- The annual occurrence rate of MSTIDs for 2014, 2015, 2016, 2017, 2018 and 2019 are 164, 158, 141, 110, 88 and 83 representing $\sim 22.1\%$, $\sim 21.0\%$, $\sim 19\%$, $\sim 14.8\%$, $\sim 11.9\%$ and $\sim 11.2\%$ respectively.

- A total of 742 MSTIDs events were observed during geomagnetically quiet and geomagnetically disturbed condition with 30 of them observed during geomagnetically disturbed condition representing 4% respectively. Among them 307, 106 and 329 were observed in equinoxes, summer, and winter.
- Most of the MSTIDs were observed during winter daytime (7:00-17:00 LT) with minor peak in equinoxes; evening time (17:00-20:00 LT) MSTIDs were frequent in equinox and the few nighttime (21:00-4:00) events were seen in summer.

5 DISCUSSION I: OCCURRENCE RATE AND CHARACTERISTICS OF MSTIDs OVER SOUTH AMERICAN EQUATORIAL REGION DURING SOLAR CYCLE 24

5.1 Introduction

Using GPS and GLONASS data obtained over South America equatorial region (between longitude: 30° to 55°W and latitude: 0°-15°N) from January 2014-December 2019, the characteristics and statistical occurrences rate of MSTIDs were investigated to reveal the annual and seasonal variation of the MSTID occurrence rate, horizontal wavelength, period, phase velocity and propagation direction as well as their time and solar cycle dependence. This Chapter presents the interpretation and discussion of the result presented in chapter 4. First and foremost, the anisotropy of the wavelength, period, phase velocity and azimuth will be discussed and compare to the previous works in the equatorial, low and midlatitude. Since the MSTIDs in the present work occurred during daytime, dusk hours and nighttime, the variation of the time dependence of MSTIDs will be looked into. The annual and seasonal variation of the occurrence rate of the observed MSTIDs and their solar cycle dependence will be discussed thoroughly. The variability of background winds and temperature effects on the propagation of MSTIDs will also be considered.

5.2 Characteristics of MSTIDs over South American equatorial latitude

TIDs are classified based on their horizontal wavelengths, periods, phase velocities and propagation directions, hence, the present equatorial MSTIDs characteristics are equal importance. In total, 748 MSTIDs were analyzed and their aforementioned characteristics calculated as presented in section 4.2 in chapter 4. The horizontal wavelength observed in the present work ranges between 300 and 1300 km and most of them are concentrated between 500 and 800 km with the mean value of 667 ± 131 km. The present experiment yielded MSTIDs with periods between 20 and 60 min and the maximum peak around 30 to 50 min with the mean values of 37 ± 7. One of the key parameters that determines the survival of waves in the atmosphere/ionosphere is the phase velocity. The horizontal phase velocities observed in the present work are between 100 and 700 m/s with majority of having values between 200 and 400 m/s, with the mean of 301 ± 75 m/s.

5.2.1 Horizontal wavelength, period and phase speed of equatorial MSTIDs and the possible presence of secondary gravity waves in the thermosphere

Previously, Figueiredo et al. (2018a) used GPS dTEC maps to study MSTIDs and observed the horizontal wavelength, period and phase speed between 200 and 1000 km, 15 and 35 min, 100 to 600 m/s with the mean values of 445 ± 106 km, 23 ± 3 min and 322 ± 80 m/s respectively in the southeast of Brazil (15° to 30°S). In the midlatitude over California, Kotake et al. (2007) as well used GPS dTEC maps to obtain MSTIDs with the horizontal wavelength, period and phase velocity ranging between 100 and 450 km, 20 to 60 min, 50 to 200 m/s respectively; while using densely spaced GPS receivers in Japan, Otsuka et al. (2011) used same dTEC maps to observe MSTIDs with horizontal wavelength, period and phase velocity ranging from 100 to 600 km, 15 to 60 min and 50 to 300 m/s respectively. In the low-latitude region over China, Chen et al. (2019) used the Hong Kong Continuously Operating Reference Stations network to record MSTIDs with the horizontal wavelength, phase speed and period in the spring, autumn and winter daytime (from 10:00 to 17:00 LT) between 250 and 450 km, 140 and 240 m/s and 20 and 50 min, while these data and between 200 and 450 km, and 220 m/s and 30 and 45 min in the spring and summer nighttime (from 22:00 to 03:00 LT) respectively.

Generally, the horizontal wavelengths and phase velocities in the present equatorial MSTIDs are much longer and faster than the previous works done by Chen et al. (2019), Figueiredo et al. (2018a) and Kotake et al. (2007), Otsuka et al. (2011) in the low and midlatitude respectively. Although, the aforementioned works used the same 1 hour running average principle as well as the same GNSS dTEC map technique, yet their periods are lesser than the MSTIDs in the present work. Therefore, the differences could be as a result of the variations in latitudinal and longitudinal ionospheric dynamics and their responses to gravity waves or the mechanisms that generated them (KOTAKE et al., 2007; OTSUKA et al., 2011). Moreover, some of the phase velocities of the present equatorial MSTIDs are faster than the sound speed below the turbopause. Probably, these present equatorial MSTIDs were likely induced by the secondary or tertiary gravity waves created in the thermosphere from the dissipation of primary gravity waves that were excited from deep convection in the troposphere (VADAS; CROWLEY, 2010).

Using forward ray tracing model, Vadas e Fritts (2006) calculated the body forces which resulted from the saturation and dissipation of the gravity waves excited by

Tropical Storm Noel at 04:32 UT on 30 October 2007. They concurrently analyzed 59 TIDs located at the bottomside of the F layer at 230-290 km, observed by the TIDDBIT ionospheric sounder. The TIDs had periods of 15 to 90 min, horizontal wavelengths of 100 to 3000 km, and horizontal phase speeds of 140 to 650 m/s. They reported that the observed TIDs were likely secondary gravity waves excited by thermospheric body forces with 40% of their phase speeds faster than 280m/s. They noted that those secondary gravity waves spectrum peaked at ∼100-300 km and ∼100-300 m/s. Most of the horizontal wavelengths and phase velocities of the present equatorial MSTIDs are consistent with Vadas e Fritts (2006) ray tracing model analysis.

Vadas e Becker (2019) investigated the effects on the mesosphere and thermosphere from a strong mountain wave (MW) event over the wintertime Southern Andes using a gravity wave resolving global circulation model (GCM). They reported that the MWs broke and attenuated at altitude of 50-80 km, thereby, creating local body forces that generated large-scale secondary gravity waves having concentric ring structure with horizontal wavelengths between 500 and 2000 km, horizontal phase speeds from 70 to 100 m/s, and periods of 3 to 10 hr. These secondary gravity waves were said to dissipate in the upper mesosphere and thermosphere and further created local body forces having horizontal wavelength of 180 to 800 km, depending on the constructive/destructive interference between wave packets and the overall sizes of the wave packets. They found out that the largest body force at 80-130 km altitude had an amplitude of ∼2,400 m/s/day, and was located ∼1,000 km east of the Southern Andes. This force excites medium- and large-scale tertiary gravity waves having concentric ring structure, with horizontal wavelengths decrease with radius from the centers of the rings. They further realized that near the Southern Andes, these tertiary gravity waves had phase speed of 120-160 m/s, horizontal wavelength between 350 to 2,000 km, and period of 4 to 9 hr. Some of the larger-horizontal wavelength of tertiary gravity waves propagated to as far as the west coast of Africa with large phase speeds of 420 m/s.

In the equatorial region over Brazil, Paulino et al. (2016) used all-sky imager to observe nighttime MSTIDs over northeast of Brazil with horizontal wavelength, period and phase velocity ranging from 100 to 220 km, 5 to 45 min and 30 to 120 m/s with the mean values of 144 ± 24 km, 21 ± 10 min and 109 ± 37 m/s respectively. In the same region, MacDougall et al. (2011) also used ionosonde to observe the MSTIDs horizontal phase velocities between 150 and 300 m/s. The relatively short horizontal wavelength, period and phase velocity of the previous nighttime events in the northeast of Brazil compare to the present work could be as a result of instrumental limitations and techniques for analyzing the data since they were conducted with different instrument with different time resolutions. The field of view of all-sky imager is 1500 km with typically time resolution of 90 s for the OI 577.7 nm, and OI 630.0 nm emissions (CLEMESHA et al., 2001; TAYLOR, 2001). Thus, they are limited to horizontal wavelength of 600 to 700 km (MAKELA et al., 2010). The ionosonde is only capable of observing the base of the ionosphere with limited time resolution of 10 min covering the frequency range from 0.5 to 30 MHz (BATISTA et al., 1990; MACDOUGALL et al., 2011). Meanwhile, the GNSS time resolution is 15 and 30 seconds for the TEC data with at least four satellite observing at a time.

To investigate the seasonal variability of the MSTID characteristics, we grouped the MSTID parameters into the summer, winter, and equinox (combining spring and fall) as shown in Figure 4.1 to Figure 4.3. We found out that the summer mean of horizontal wavelength, period and phase speed are higher than that of winter. This could be attributed to the high dissipative and filtering rate in summer due to high meridional and zonal wind (FISHER et al., 2015; MAKELA et al., 2013). Thus, only MSTID events with longer horizontal wavelength and faster phase speeds consequently survived the thermospheric dissipation. Furthermore, Vadas (2007) reported that gravity waves with horizontal wavelength of 400 km can dissipate at the highest altitudes if they are launched from 120 km altitudes while gravity waves with horizontal wavelength of 600 km can penetrate to higher altitudes especially during active solar conditions. This implies that higher penetration altitudes are achievable for gravity waves propagating in hotter summer thermosphere (VADAS, 2007). This might be the reason for the high mean values for the equatorial MSTID characteristics since the solar activity affect equatorial thermosphere directly during summer.

5.3 Propagation direction of equatorial MSTIDs

The propagation direction of the present MSTIDs are divided into 4 main groups; north-northeastward, north-northwestward, south-southeastward and westward with waves propagating within ±30° due west as shown in Figure 4.4. To further investigate the seasonal variability of the anisotropy in the propagation direction we grouped them into winter, equinox and summer based on their corresponding azimuthal value. The winter and equinox MSTIDs predominantly propagated to north-northeastward, north-northwestward and south-southeastward. In addition, few number of MSTIDs propagating westward. Moreover, the summer azimuthal orientation is more prevalent to southeastward, westward and northwestward. MacDougall et al. (2011) had already reported that the dominant azimuth of the MSTIDs in the local winter months was southeast direction with few propagating northward which are consistent with the present work even though the study times are different between the two works. Importantly, the seasonal measurements of summer and winter suggest a consistent cyclic picture with predominantly north-northeastward propagation during the winter months, transitioning to south-southeastward during the summer periods.

The propagation direction for equinox in the present work is similar to that of Figueiredo et al. (2018a) at the low latitude though the period of study are not exactly the same. Meanwhile, the propagation direction during summer in the present work demonstrates the sparseness of MSTIDs propagating in the north-northeast direction compare to Figueiredo et al. (2018a) whose summer MSTIDs propagated in all directions as shown in Figure 5.1. Moreover, in winter, there are strong link between the Figueiredo et al. (2018a) and the present work except that the former shows sparseness in the south-southeast direction. The MSTIDs that propagate in south-southeastward in the South American region have already been reported to be the gravity waves that are generated by ITCZ which lies at the north of the study area during winter and migrates southward during summer (RÖTTGER, 1977; MACDOUGALL et al., 2011). The main difference between the present work and that of Figueiredo et al. (2018a) is the south-southeastward propagating MSTIDs of the former.

Figure 5.1 - Comparison of MSTID propagation direction between the present work (left column) and Figueiredo et al. (2018a) right column.

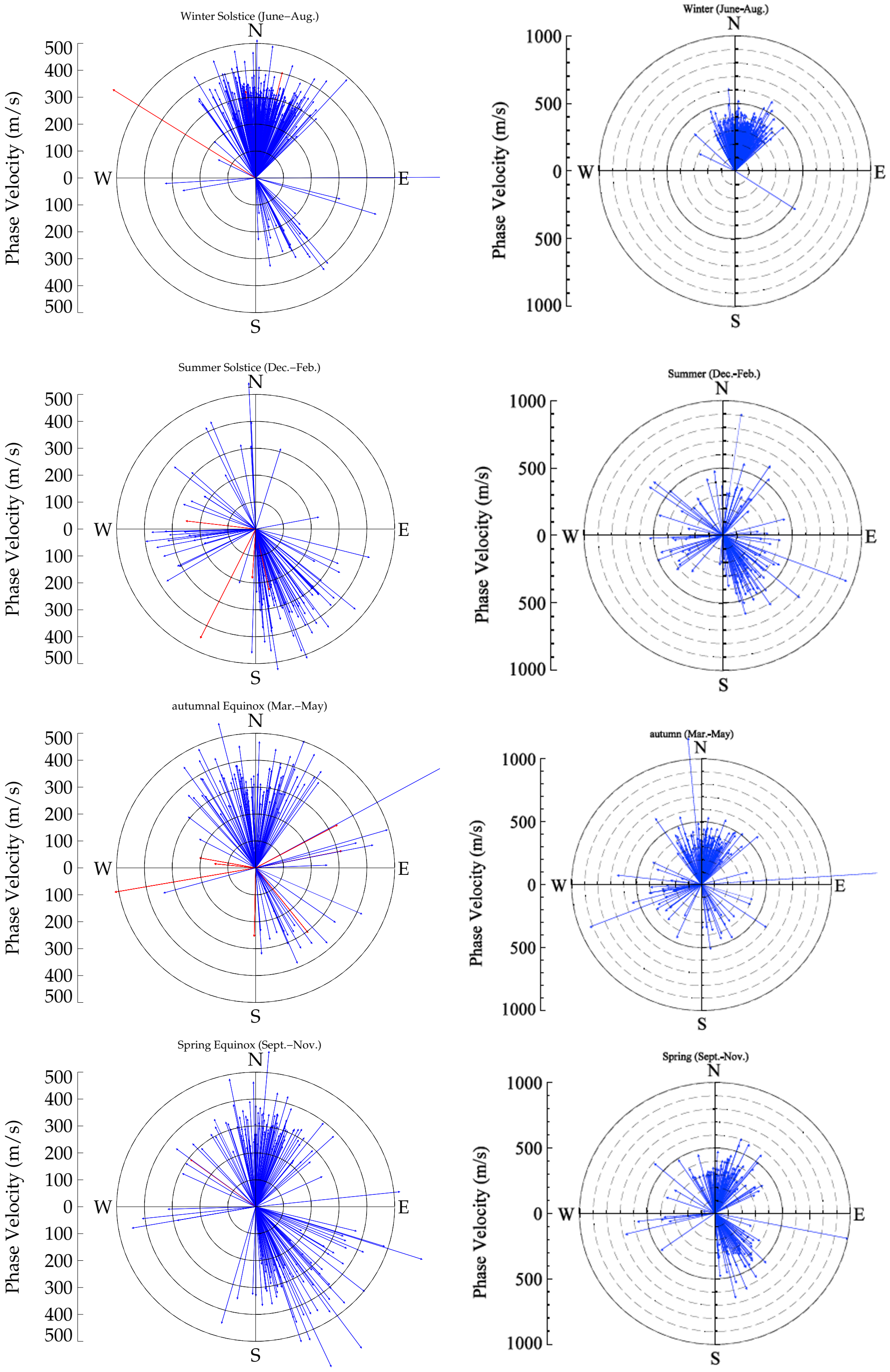

Source: Figueiredo et al. (2018a) (right column).

On the other hand, in winter and equinox, both the present work and that of Figueiredo et al. (2018a) have similar propagation direction. The most interesting and proving connection between the two studies is the fact that during winter the MSTIDs propagated preferentially to the north-northeastward and north-northwestward. Although the two works were not conducted in exactly same years, it is still possible that the winter MSTIDs could have been generated from gravity waves from common hotspot or similar source location for their origin. Some of the north-northeastward MSTIDs could be excited by the secondary and tertiary gravity in the thermosphere (VADAS; BECKER, 2019). The north-northwestward MSTIDs could also be those MSTIDs that propagating along the magnetic field lines. Although, we recommend for ray-tracing for both works to unravel the mystery of their sources, it is still clear from the propagation directions that they have similar sources in winter and equinoxes both are consistent with (VADAS; BECKER, 2019) secondary and tertiary waves.

There are three main factors, which could explain the anisotropy of the characteristics of the MSTIDs in this present work. First and foremost, the wind and dissipative filtering effects in which the background wind causes the gravity waves to dissipative in the mesosphere or thermosphere. Secondly, the ion drag effects which favors gravity waves propagating equatorward along the magnetic field lines due to the less ion-neutral collision which gives rise to the ions in the F region gyrate along the geomagnetic field lines. Finally, the source region of the gravity waves in the neutral atmosphere which will be discussed in chapter 6.

5.3.1 Wind and dissipative filtering effects on the propagation direction of equatorial MSTIDs

It is known that the signatures of gravity waves in the ionospheric plasma are TIDs seen as fluctuations of the ionospheric electron density. These electron density perturbations are caused by atmospheric via ion-neutral collisions (HINES, 1960; HOOKE, 1968; SQUAT; SCHLEGEL, 1996). Thus, it is known that MSTIDs and the underlying gravity waves play a critical role in driving the day-to-day variability of the ionosphere. According to Vadas e Crowley (2010) and Vadas e Becker (2017), the theoretical understanding of upward gravity propagation in the atmosphere suggests that while small-scale gravity waves are confined to below the stratopause, the medium and large scale AGWs have appropriate characteristic amplitudes and phase velocities to penetrate into the mesopause and ionosphere. Essien et al. (2018) observed small- and medium-scale gravity waves in the MLT over Brazilian equatorial latitude and reported that the medium-scale gravity is less susceptible to wind filtering compare to small-scale due to the high phase velocities of the later.

To investigate the critical level wind and dissipative filtering of atmospheric gravity waves the phase velocity, horizontal wavelength and propagation directions among others are considered. The critical level wind filtering mechanism is well known to affect the spectrum and directionality of the gravity waves as they propagate upward (NEGALE, 2018; ESSIEN et al., 2018). Especially, when the phase velocity of the gravity waves is equal to or less than that of the wind speed in the direction of the wave, then the wave is absorbed into the mean flow (BOOKER; BRETHERTON, 1967; CROWLEY et al., 1987; MACDOUGALL et al., 2009; VADAS, 2007; WALDOCK; JONES, 1984; ESSIEN et al., 2018). However, if the gravity wave is propagating against the wind, then it is favored as long as its intrinsic period is longer than the buoyancy period. In addition, the dissipative filtering mechanism can take place in the thermosphere when viscosity is stronger. In this case, the gravity propagating against the wind with larger vertical wavelengths are less affected by the molecular viscosity of the thermosphere compare to those propagating in the same direction with the wind with smaller vertical wavelengths (NEGALE, 2018).

In the northeast of Brazil Barros et al. (2018), Figueiredo et al. (2017), Fisher et al. (2015), and Makela et al. (2013) observed the nighttime thermospheric neutral wind magnitude by Fabry-Perot interferometer reported that the velocities not greater than 150 m/s. Moreover, Drob et al. (2015) used the monthly average of the Horizontal Wind Model (HWM14) and also reported the diurnal thermospheric neutral wind not exceeding 160 m/s on quiet days. Also, Essien et al. (2018) applied the critical level theory of atmospheric gravity waves to investigate the effects of wind filtering on medium-scale gravity waves (MSGWs) propagation directions. They also found out that the wind in the equatorial region was weak, yet the MSGWs with phase speed less or equal to 70 m/s were still susceptible to wind filtering effects. Paulino et al. (2018), reported that fast waves could skip turning and critical levels and propagate into the thermosphere/ionosphere. According to them, the strength and direction of the wind vector in the thermosphere is the main cause for the anisotropy in the propagation direction of the periodic waves they observed, even if the sources of these waves are assumed isotropic.

In the case of the present study, wind filtering mechanism in the neutral atmosphere cannot fully justify the anisotropy in the characteristics since $\sim 90\%$ and $\sim 60\%$ of the MSTIDs have horizontal wavelengths and phase velocities exceed 500 km and

300 m/s respectively. These velocities are greater than the wind velocities observed by Barros et al. (2018), Figueiredo et al. (2017), Fisher et al. (2015), and Makela et al. (2013) by FPI in the Brazilian equatorial region as well as the HWM-14 analysis done by (ESSIEN et al., 2018). Probably, those MSTIDs with low phase velocities would have been filtered out by the background wind while the rest survived due to their higher parameters.

Furthermore, based on theoretical evidence, diffusive separation is also an important dissipative mechanism for gravity waves in the lower thermosphere, which increases with wave period and decreases with wavelength (COLE; HICKEY, 1981). They gave a typical example that a wave with a period 60 min and horizontal wavelength 400 km will lose 60% of its energy when it propagate between the 140 and 240 km level, whereas in the same altitude a wave of period 20 min and the same wavelength will lose only about 10% of its original energy. The above theoretical discovery could buttress why short period waves below 20 min were not capture, probably they lost their energy and dissipated therefore, could not get to an altitude of 300-350 km where this MSTIDs were observed. In the present work, we recorded the mean value for all season as 36 ± 7 min with the range between 20 to 60 min which survived the dissipation in the lower thermosphere (VADAS; CROWLEY, 2010).

5.4 Local time dependency of MSTID occurrence

From the statistical analysis of the occurrence rate of the observed equatorial MSTIDs, we categorized them into their time of occurrence: the daytime that frequently occurred between 7:00-17:00 LT, evening hours between 17:00-20:00 LT and nighttime between 21:00-4:00LT as shown in Figure 4.11. However, throughout the 6-year observation, we observed only 15 nighttime MSTID events among a total of 742 which represent 2% of the total observation. The mechanisms producing MSTIDs in the daytime, evening and nighttime might be different. Due to the limited number of the nighttime events in the present work, we will henceforth focus on the daytime and evening hours events.

To highlight a few previous works; Röttger (1977) reported that in the southern summer only a small number of TIDs were observed over Peruvian equatorial region around noon while the diurnal maximum in summer was observed around evening hours. Kotake et al. (2007) also reported on the statistical characteristics of the MSTIDs over Southern California observed with densely spaced GPS receivers, and found that the occurrence rate of nighttime MSTIDs peaked in summer; the daytime MSTIDs peaked in winter while the dusk events frequently occurred during equinoxes and summer as shown in Figure 5.2 (a). Otsuka et al. (2012), also investigated the statistical characteristics of the MSTIDs observed over Japan and found that they are different at daytime, nighttime, and dawn and dusk. The observed characteristics were summarized into occurrence rate of daytime, which was high in winter and equinoxes whereas nighttime, dawn and dusk MSTIDs peaked in summer as shown in Figure 5.2 (b). These statistical findings are consistent with the local time dependence of the present work with the exception of the dawn time MSTIDs, which is rare in the present work.

Figure 5.2 - Local time and seasonal variations in MSTID occurrence rate over (a) Japan in 2002 and (b) Southern California in 2002.

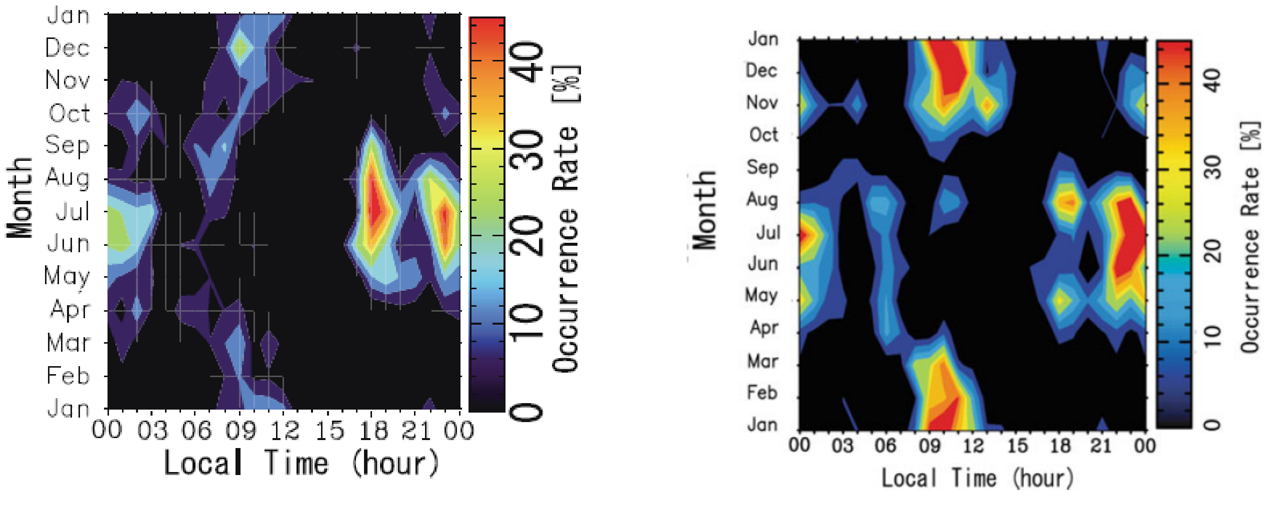

(a) (b)

Source: (a) Kotake et al. (2007) and (b) Otsuka et al. (2011).

In the northeast of Brazil, MacDougall et al. (2011) analyzed one year MSTIDs data and discovered more events in daytime and dusk with few during nighttime which are in agreement with the present work, probably, due to the fact that both experiments were conducted at the same latitude. Ding et al. (2011) also observed a total of 793 MSTIDs during using dense GPS receiver array in Central China around 1500 LT and 0100 LT. According to them, the daytime MSTIDs were characterized by a major occurrence maximum around the winter solstice. In low latitude over Brazil 15°S to 30°W), Figueiredo et al. (2018a) observed 826 MSTID events from December 2012 to February 2016 and found that the maximum peak in daytime winter solstice, and secondary peak in the daytime equinoxes as shown in Figure 5.3. From the above statistical analysis about the local time dependency of MSTID occurrence, there is a clear evidence that the occurrence rate of the daytime events in winter and equinoxes are consistent with the present work as shown in Figure 4.11.

Figure 5.3 - Seasonal variation of medium-scale traveling ionospheric disturbance occurrence rate with the function of local time in south-southeast of Brazil. Data from December 2012 to February 2016 are averaged. The black dashed and dash-dotted lines represent the solar terminator at 300 and 100 km altitude, respectively.

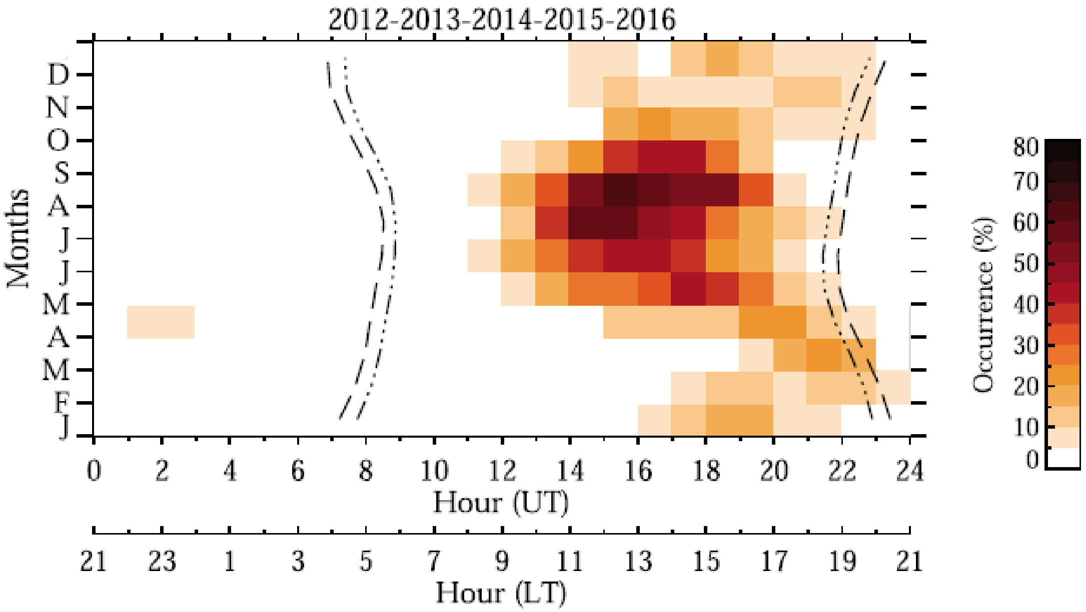

Source: Figueiredo et al. (2018a).

The local time dependence of these equatorial MSTIDs could be attributed to the variability of mechanisms causing them (MILLER, 1997; KELLEY; MILLER, 1997). This variability could arise from the multiple sources of gravity waves in both the troposphere and thermosphere, as well the medium (background winds and temperature) through which they propagate. The proceeding subsections discuss the local time dependence of the equatorial MSTIDs in relation to the occurrence rate and propagation direction.

5.4.1 Daytime equatorial MSTIDs

The daytime MSTIDs over South American equatorial region frequently occur in winter with secondary peak in equinoxes which is consistent with that of Bristow e

Greenwald (1996), Kotake et al. (2006), Otsuka et al. (2012), Otsuka et al. (2013), Figueiredo et al. (2018a), Chen et al. (2019). The horizontal wavelengths, periods and phase velocities of the observed MSTIDs are between 400 and 1000 km, 20 and 60 min and 100 and 700 m/s respectively. The daytime preferentially propagate north-northeastward, north-northwestward and south-southeastward. We noted from Figure 4.1 that the seasonal measurements of daytime MSTIDs propagated predominantly north-northeastward during the winter months and transitioning to south-southeastward during the summer periods.

As usual, MSTIDs have been known to be the manifestation of atmospheric gravity waves (HINES, 1960; HOOKE, 1968) at ionospheric height. In the F region, the ion mobility along the geomagnetic field is high, and the velocity of the ion and neutral motion along the geomagnetic field is caused by gravity waves Hooke (1968). However, the collision frequencies of the electrons and ions are relatively insignificant, therefore, the ion motion across the B is restricted because the ion gyro-frequency is much higher than the ion-neutral collision frequency. Therefore, the ions gyrate along the magnetic field rather than drifting with the neutral wind (KELLEY; MILLER, 1997; OTSUKA et al., 2011). This ion mobility causes directivity in the response of the electron density variations to the neutral motion due to the gravity waves Kotake et al. (2006), Otsuka et al. (2011). Since neutral particle oscillation parallel to B is larger for gravity waves propagating equatorward than for those propagating to other directions, according to this theory, gravity waves propagating equatorward could have greater amplitude, hence, advantage compare to those propagating away from the equator (HOOKE, 1968).

The directivity of ion mobility causes the north-northwestward propagation direction in the response of the plasma density variations to the neutral motion due to the gravity waves. In order to verify these equatorward directivity in the present work, we use the MSTID observed on the June 30th, 2014 around 13:50:00 UT (10:50:00 LT). It is clear that on this day the MSTID that was observed in the South American equatorial region might have originated from low latitude as shown by the dTEC map in Figure 5.4 (first row). The oblique line at the left corner (Longitude 45°W, Latitude 10°S) of the map is the geomagnetic equator which is highly tilted in the South American region. The second row of Figure 5.4 shows South American map with geomagnetic field lines perpendicular to the magnetic equator. It is obvious that the propagation direction of these MSTIDs is northwestward (as indicated by the arrows) which are aligned along the magnetic field lines. In the South American continents, the magnetic field lines have high declination (between 15° and 20°W) in the Brazilian sector as shown in Figure 5.4, therefore it is expected that the daytime gravity waves propagating northwestward would experience the least amount of ion drag and thus, the most prominent in ionospheric observations as mentioned by Kelley e Miller (1997).

Figure 5.4 - MSTIDs observed on the June 30th, 2014 propagating to northwestward (first row) and South American map demostrating the geomagnetic field lines (second row)

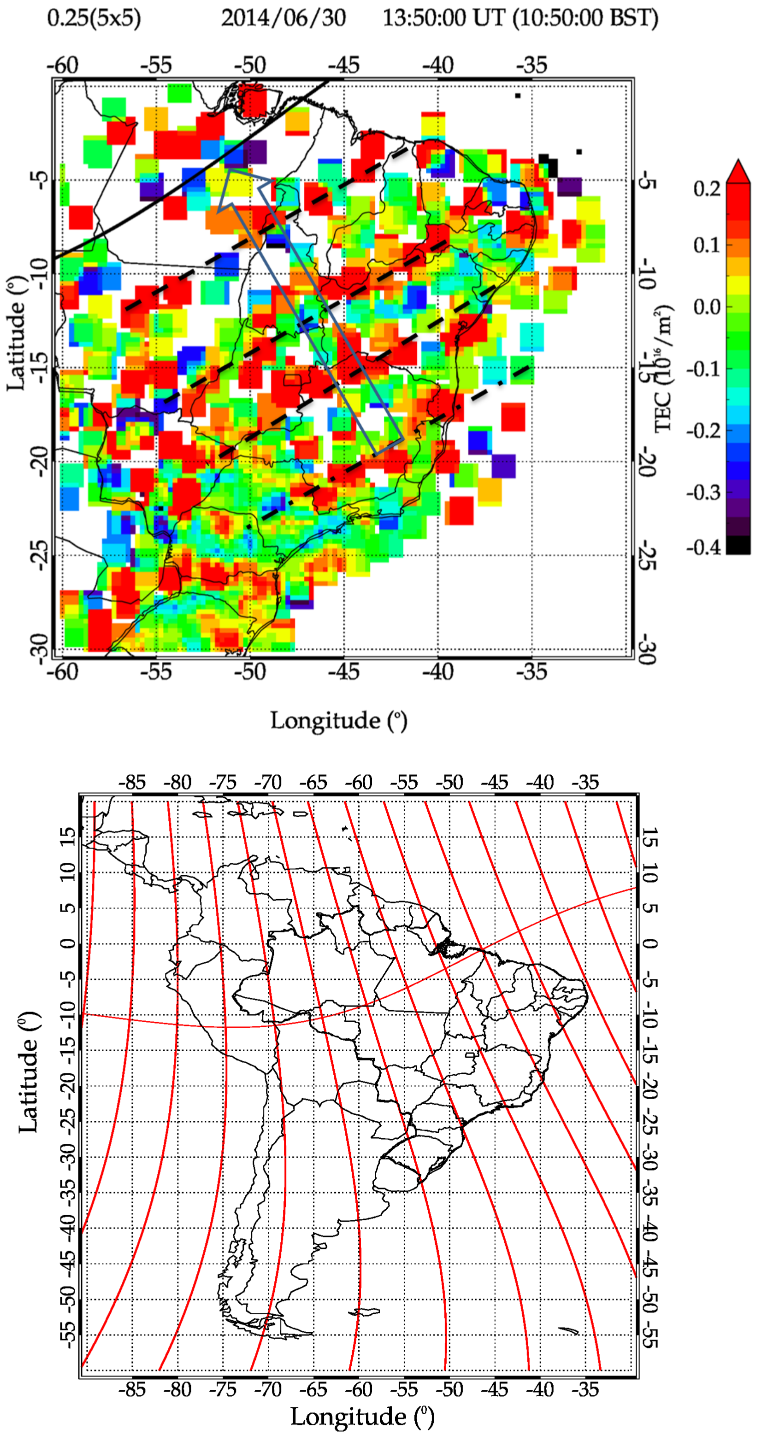

In addition, some of the daytime MSTIDs propagating to north-northeastward could be excited by medium- and large-scale daytime secondary and tertiary waves which are likely Mountain waves with concentric ring structures from the Southern Andes (VADAS; BECKER, 2019). According them, these waves have wavelength increasing with radius from the centers of the rings and they propagate northeastward over the Brazil. We show here, an example of concentric like MSTID propagating from the east of Southern Andes to the northeast of Brazil on 1st July, 2014 at 15:03:00 UT (12:30:00 LT), as shown in Figure 5.5. The possible center (indicated with a blue star) of this MSTIDs is located at latitude 35°S and longitude 50°W. The circles are just to reinforce the clarity of the concentric structures of the MSTID and the blue short dashes arrow denotes the propagation direction. The primary source region of this MSTID is shown and discussed in Figure 6.6.

Figure 5.5 - MSTIDs observed on the July 1st, 2014 at 15:03:00 UT (12:30:00 LT) propagating to north-northeastward. The possible center (indicated with a blue star) of this MSTIDs is located at latitude 35°S and longitude 50°W. The circles are just to reinforce the clarity of the concentric structure of the MSITD and the blue short dashes arrow denotes the propagation direction.

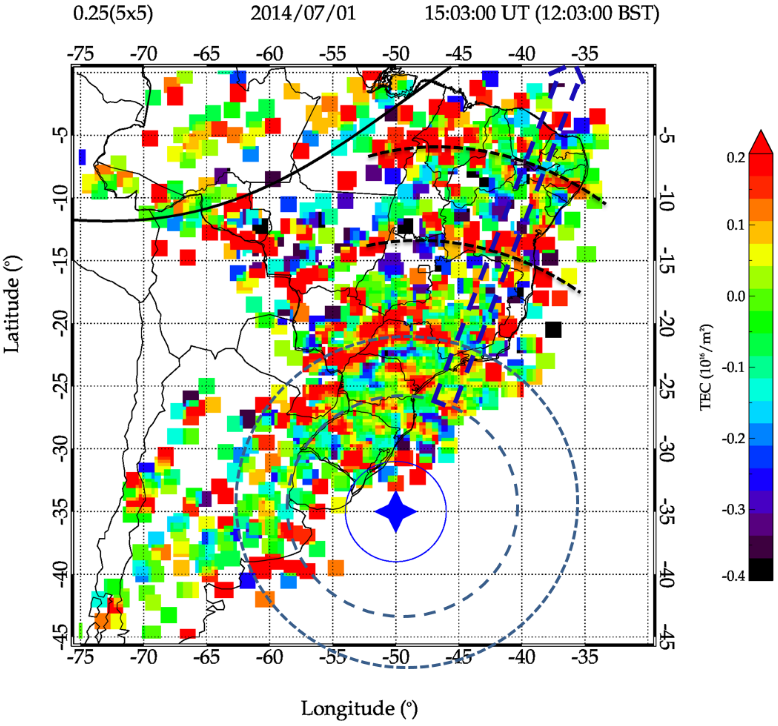

The two case studies could be the possible reason for daytime MSTIDs propagating to north-northeastward and north-northwestward (equatorward) accounting for the more than 70% of the total MSTIDs observed in the present work. In addition, they could be the possible observational evidence of MSTIDs propagating from the low and mid latitude to the equator.

Meanwhile, the south-southeastward daytime MSTIDs in the present work propagating away from the equator are likely excited active gravity waves generated by ITCZ (RÖTTGER, 1977; MACDOUGALL et al., 2011). These cannot be explained by the linear theory between plasma density perturbations, and neutral wind oscillations caused by gravity waves as well as the ion drag force dumps neutral particle oscillation due to the gravity waves, neither could it explain by the MWs analogy that breaks and generate secondary and tertiary waves (VADAS; BECKER, 2019) since there is no mountains north of the study area. The possible primary source of these south-southeastward MSTIDs will be discussed in chapter 6.

5.4.2 Evening hours equatorial MSTIDs

Evening hours MSTIDs (which occurred 17:00-20:00 LT) over South American equatorial region occur frequently in summer with a secondary peak in equinox as shown in Figure 4.11. The preferential propagation directions of the MSTIDs observed during the evening hours are south-southeastward, north-northwestward and westward in both summer and equinox. Moreover, in equinox, there are some MSTIDs propagating to north-northeastward. The seasonality of propagation direction of the present work is consistent with that of (FIGUEIREDO et al., 2018a) over Southeast of Brazil, with the exception of the absence of north-northeastward summer MSTIDs in the present work. Nevertheless, the seasonality of evening time MSTIDs in the present work is entirely different from the that of Kotake et al. (2007) and Otsuka et al. (2012) over Southern California and Japan respectively. With regard to the horizontal wavelengths, periods and phase velocities of the evening time MSTIDs, they are between 500 and 900 km, 25 and 60 min and 100 and 500 m/s respectively. Again, these horizontal wavelengths and phase velocities of the evening time MSTIDs in the present work are longer and higher respectively, than the aforementioned works. This has been explained in subsection 5.2.1.

As described under the daytime MSTIDs, equatorward (north-northwestward) propagating gravity waves could cause a larger amplitude of TEC perturbations than gravity waves propagating in other directions (HOOKE, 1970; OTSUKA et al., 2011). This is because the amplitude of the electron density perturbation, which is proportional to the neutral wind velocity in the direction parallel to the geomagnetic, field lines. (OTSUKA et al., 2011) explained that gravity waves with a large amplitude of neutral wind perturbations could be needed to produce the evening time MSTIDs. Therefore, the north-northwestward events in equinox could be aligned with this scenario too. In addition, the south-southeastward MSTIDs are still suspected to be caused by ITCZ, which lies at the north of the present study area.

In order to further explain the westward and eastward dusk MSTIDs, (OTSUKA et al., 2011) considered the neutral winds in the thermosphere which is driven by the pressure gradient of the neutral atmosphere, the neutral winds below from the day side to the night side, and then westward at dawn and eastward at dusk. These neutral winds in the Earth's thermosphere are driven primarily by pressure gradients resulting from temperature differences of the neutral atmosphere. This is a key feature of the E-region dynamo which generate the zonal electric field that drives a vertical $\mathbf{E}\times\mathbf{B}$ drift of F-region plasma at the equator, which controls the distribution of plasma density. The neutral winds blow from the day side to the night side leading to upward plasma drift during the day and downward drift at night, hence, eastward at dusk. The zonal (westward) component of the horizontal propagation velocity of the observed evening time MSTIDs propagate contrary to the neutral winds. This relationship between the MSTID propagation direction and background neutral winds suggests that the wind filtering mechanism could be operating effectively (COWLING et al., 1971; WALDOCK; JONES, 1984; OTSUKA et al., 2011). However, in the situation where the horizontal phase velocity of the gravity waves is close to the background neutral wind velocity, then the waves can be absorbed by the critical level (BRETHERTON, 1966). This could account for the absence of eastward propagating MSTIDs during evening and even daytime. Meanwhile, the favored azimuth of the MSTIDs propagation could counter the background wind. Consequently, the preferred azimuth of the MSTIDs propagation direction could be westward at dusk (OTSUKA et al., 2011).

Afraimovich et al. (2009) reported that the evening time MSTIDs over Japan appear 1.5-3 hours before the sunset solar terminator and when it passes over Australia. Also, Forbes et al. (2008), Liu et al. (2009) observed terminator waves of neutral density, wind and plasma temperature in the morning and evening by CHAMP satellite. MacDougall e Jayachandran (2011) studied gravity waves generated by the sunrise terminator and reported that the propagation direction of solar terminator sources TIDs was approximately eastward in early morning and rotated clockwise throughout the day to approximately southward around sunset time. Kotake et al. (2007) as well suggested that sunset solar terminator might have excited such westward and eastward dusk MSTIDs. The terminator sources MSTIDs in the present work will be discussed in chapter 6.

5.5 Seasonal dependency of equatorial MSTIDs occurrence rate

The seasonal variation of MSTIDs has been reported in almost every single study of MSTIDs research that have been conducted, be it evening, night or daytime. The seasonal occurrence rate of MSTIDs had already been reported in low (CHEN et al., 2019; FIGUEIREDO et al., 2018a) and mid latitudes (KOTAKE et al., 2007; TSUGAWA et al., 2007; OTSUKA et al., 2011; OTSUKA et al., 2013). All the aforementioned authors found out that MSTIDs were predominantly observed during daytime winter with second peak during equinoxes. The nighttime MSTID events frequently occurred in the mid latitude during summer is almost absent in the present work which is consistent (FIGUEIREDO et al., 2018a). Probably, the mechanism that causes the nighttime is not situated in the low and equatorial region. Moreover, the variation of seasonal occurrence rate in the present work is consistent with the day and evening time MSTIDs observed in Southern California, Japan, Europe, China and southeast of Brazil by Kotake et al. (2007), Otsuka et al. (2011), Otsuka et al. (2013), Chen et al. (2019) and Figueiredo et al. (2018a) respectively. However, in the equatorial region, this is the first time occurrence rate of daytime MSTIDs experiment has been conducted using long term GNSS dTEC map. Thus, the section will thoroughly discuss the seasonal variation of MSTIDs occurrence rate in the equatorial region of South American during the six-year observation. Therefore, the seasonal variation of the present MSTID occurrence rate maximizes at daytime winter since more than 70% of the events occurred during the day. For example, from the statistical analysis of the occurrence rate of MSTID events; a total of 307, 106 and 329 were observed in equinoxes, summer, and winter respectively.

First and foremost, we will discuss the factors that could influence the seasonal variation of the occurrence rate of the present MSTIDs observed in the South America equatorial region. Among others, the primary, secondary and tertiary source are important factors since without them the presence of gravity waves in the ionospheric height is almost impossible. For example, in winter and fall, there is a strong cold front emanating from the mid and high latitude which likely excited the north-northeastward and north-northwestward MSTIDs observed in southeast of Brazil Figueiredo et al. (2018a). Miyoshi et al. (2014) used general circulation model (GCM) to study seasonal variations of upward gravity wave propagation during the summer and winter solstices in South America. They reported that the energy of the gravity waves at 120 km altitude was slightly high but much higher at 300 km altitude during winter while in summer the gravity waves lacked the ability to propagate vertically upward: This implies that the high frequency gravity waves with high energy generated in the troposphere are also capable of propagating to the thermosphere to induce wave structures in the upper atmosphere especially during winter. They suggested that the zonal wind filtering effect between 100 and 200 km altitude in 20°S is the mechanism that normally blocks the vertical propagation of the gravity waves. It is possible that the MSTIDs in the present work were excited secondary and tertiary gravity waves in the thermosphere from the likely dissipated primary gravity waves from deep convection sources in the troposphere. Vadas e Crowley (2010) also reported that the body forces which generate these secondary gravity waves often occur within 3-10 degrees in latitude/longitude from the location of the deep convective plumes which is approximately horizontal distance between 330 to 1300 km.

Meanwhile, the gravity waves being generated by the deep convective sources in the South American equatorial region, predominant in summer and spring equinox seem to be filtered out but the winds or probably consumed by thermospheric viscosity. However, chapter 6 has been dedicated to the primary sources of the present equatorial MSTID. Therefore, we will focus on the medium at which the gravity waves propagate to the ionospheric height. In this case, the background wind and the temperature of the medium are paramount to this study. Bristow e Greenwald (1996) studied the climatology of the MSTIDs observed with the Super Dual Auroral Radar Network (Super-DARN) at high latitudes, and reported that the vertical gradient of the neutral temperature in the thermosphere is less abrupt in winter than in summer, which implies that more gravity waves can penetrate into the ionosphere during winter, however, in summer, they are more reflected near the mesopause. Crowley e Azeem (2018) also reported that thermospheric gravity waves are selectively filtered by the kinematic dissipation and only the high frequency, long vertical wavelength components penetrate to the highest altitudes. On the other hand, Fisher et al. (2015) studied thermospheric winds and temperatures using high-resolution Fabry-Perot interferometer measurements of the 630.0 nm airglow emission spectral line at northeastern Brazil August 2009 to August 2014. They however, reported that while the temperature climatology shows the expected solar cycle dependence, the neutral winds are most heavily dominated by seasonal change. Therefore, it will be better to analyze the seasonal variation of the MSTIDs occurrence rate in the South American equatorial region by considering the wind filtering of gravity waves analogy.

In other to investigate the background wind effect on the present MSTIDs, we present the meridional (left hand side) and zonal (right hand side) winds monthly averaged between August 2009 and August 2014 over the Brazilian equatorial and low region from the combined FPIs, as shown in 5.6 (FISHER et al., 2015). They reported that the typical meridional wind flow (positive northward) at low latitudes is observed with summer to winter hemispherical flow that peaks at $\sim 50m/s$. The flow from the summer to winter hemisphere peaks at around 21 solar local time (SLT) which is slightly faster in the local summer months than local winter months. During the equinox, the meridional winds show two equatorward maxima (23 SLT and 04 SLT) with a null near 01 SLT. Similarly, the zonal wind flow (positive eastward) is in line with previous results from same region with large eastward winds that slowly decrease toward zero at the end of the night (MAKELA et al., 2013). The peak eastward wind, occurring an hour or two after local sunset, ranges from 150 m/s in local summer to 75 m/s in local winter. The similarity between these two wind components is the day-to-day variability of the winds, displayed as error bars. This could be filtering most of the gravity waves with shorter wavelength and slow speed in summer.

Figure 5.6 - Monthly averages of the meridional (left hand side) and zonal (right hand side) thermospheric wind over northeast Brazil plotted against solar local time (SLT). The positive values are northward and eastward respectively.

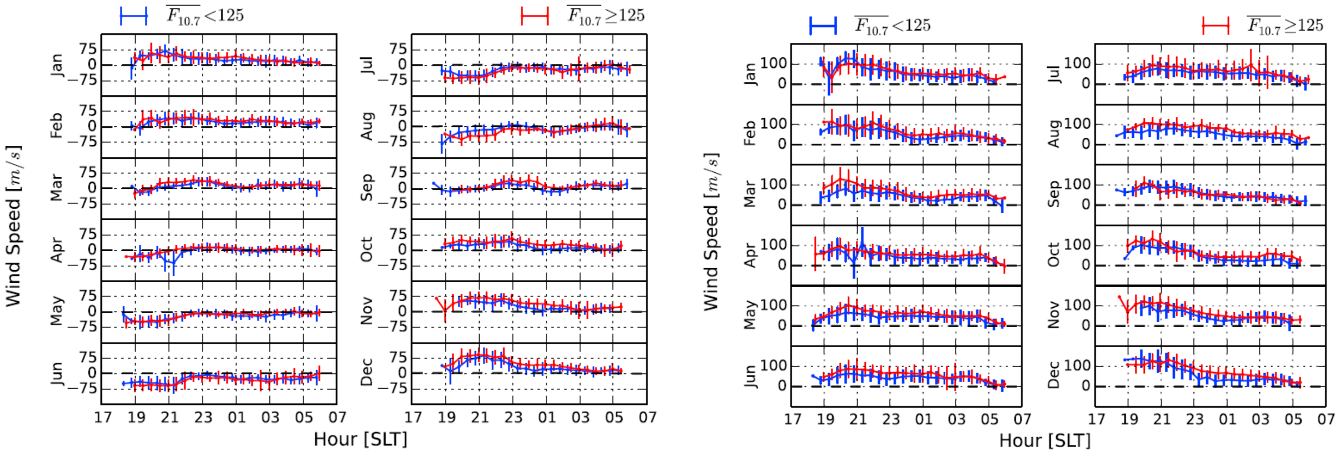

Source: Fisher et al. (2015).

In summer, the velocity of the neutral wind is higher than winter (FISHER et al., 2015; MAKELA et al., 2013), hence, the vertical wave number may consequently be large which implies short vertical wavelength (VADAS; FRITTS, 2006): In this regard, the gravity waves might have been filtered out by critical level or dissipate due to high thermospheric viscosity. As a result, a few gravity waves might have propagated into the ionosphere as MSTIDs. On the other hand, in winter, the neutral wind velocity is slow (FISHER et al., 2015; MAKELA et al., 2013), and less than any of the phase velocities of the present MSTID which could result in small vertical wave number. In this case, the gravity waves could propagate into the thermosphere/ionosphere without critical level effect or dissipative filtering (VADAS; FRITTS, 2006). This could be the possible reason for the high occurrence rate of MSTID events in winter daytime and low summer daytime events in the present work. Thus, the seasonal variation of the observed background wind (FISHER et al., 2015; MAKELA et al., 2013) may address the pertinent question about why the daytime MSTIDs almost disappear in summer and appear in winter in the present work.

5.6 Long term (solar cycle) variability of equatorial MSTIDs

The six-year present study of MSTIDs during solar maximum (2014-2015), descending (2016-2017) and minimum (2018-2019) yielded a total of 742 events with 43.3%, 33.7% and 23.0% respectively. The aforementioned statistics attest that more MSTID events were observed during solar maximum compare to minimum phase. The number of MSTID events obtained during solar descending phase is the intermediary between the minimum and maximum phase events. Once again, the annual variation of the present work is limited to daytime. The important question is the connection between the solar activities and MSTIDs, that is whether they have any direct relationship or not. The climatology of the MSTIDs have been extensively studied, though the daytime occurrence rate in the South American equatorial region and its dependence on solar cycle has not been established yet.

Kotake et al. (2006) first studied MSTIDs across the globe during solar descending (1998) and maximum phase (2000 and 2001). According to them, the daytime events were different from that of the nighttime with respect to seasonal, solar activity, longitudinal, and latitudinal dependence. Their nighttime MSTIDs activity at the Japanese and Australian longitudinal sector shows negative correlation with solar activity whereas solar activity dependence was not seen in daytime MSTIDs activity. Hernandez-Pajares et al. (2012) also studied MSTIDs over California, New Zealand, Alaska and Hawaii during solar maximum conditions most of the MSTID climatological trends were modulated by the solar cycle intensity, especially, in the case of local fall/winter daytime equatorward MSTIDs. Though the inverse dependence of the occurrence of nighttime MSTID in relation to solar activity had previously been reported by Bowman (1990), Garcia et al. (2000), Shiokawa et al. (2003), Pimenta et al. (2008) and Candido et al. (2008) in the mid and low latitude, yet the 11-year nighttime MSTIDs of Paulino et al. (2016) using OI630.0 nm airglow images at Cariri (36.5°W, 7.4°S) did not show any correlate with solar activities.

In order to investigate the possible effect of solar activity on the occurrence rate of MSTIDs events, the solar flux F10.7 cm and the total MSTID events are plotted together as a function of month and year as shown in Figure 5.7. The monthly occurrence rate of MSTIDs during geomagnetically quiet condition is indicated with red histogram, the green represent the solar cycle numbers while the blue line is the respective eighty-one day running average. The present equatorial MSTIDs show strong positive correlation with the solar activity. Probably, this is an indication of the conspicuous differences of day and nighttime MSTIDs that exist over the ionospheres of different latitudes and longitudes over the globe. This also implies the solar cycle dependency of MSTIDs differs in day and nighttime, since the dark bands observed by all-sky imager have inverse correlation. Therefore, the present 6-year study being the first to investigate long term solar activity dependence on MSTID in the Brazilian equatorial region cannot be underestimated. Meanwhile the most important question about this is the connection between the solar activities and MSTIDs.

The earliest observations of TIDs were conducted by Munro (1948), Munro (1950), Munro (1958) which coupled with the radar observations of drifting meteor trails Greenhow (1958), led Hines (1960) to hypothesize that TIDs were simply the manifestations of neutral internal gravity waves in the ionospheric plasma, which is a generally accepted result today. For instance, medium-scale gravity waves are known to transport energy and momentum throughout the atmospheric layers resulting in a coupling between these layers (VADAS et al., 2009; TAYLOR et al., 2009; ESSIEN et al., 2018). Vincent (2015) reported that medium-scale gravity waves in the thermosphere with high frequency and long vertical wavelength components penetrate into the highest altitudes. They also mentioned that there was a strong solar cycle effect on gravity waves propagation into the thermosphere. They concluded that gravity waves could propagate to higher altitudes during high sunspot activity than minimum conditions. Crowley e Azeem (2018) further reported that gravity waves could propagate to higher altitudes during high sunspot activity conditions than during solar minimum conditions. This implies that there is a strong solar cycle effect on gravity wave propagation into the thermosphere.

Figure 5.7 - Solar Cycle 24 dependence on the occurrence rate of MSTIDs over South America equatorial region during geomagnetically quiet conditions. The monthly occurrence rate of MSTIDs is indicated with red histogram; the green represent the solar cycle numbers while the blue is the respective eighty-one day average.

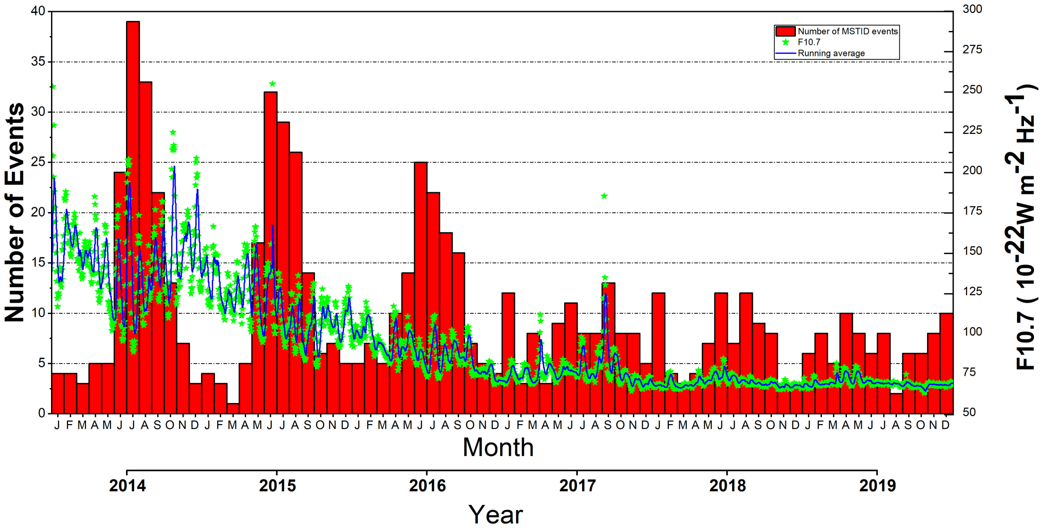

The sources and mechanisms that generate gravity waves in the troposphere could be a major factor to the variation in the occurrence rate of MSTIDs between solar maximum and minimum phase. Another factor that could be a possible contributor is the gravity waves propagation characteristics in relation to the background wind and thermospheric temperature. The temperature determines thermospheric viscosity, which is highly dense during solar minimum and consequently impedes the propagation of gravity waves due to high dissipative rate. Cole e Hickey (1981) reported that the dissipation rates due to thermospheric viscosity and thermal conduction are inversely proportional to the neutral gas density. This dissipation rate depends on the temperature structure of the thermosphere, which consequently affects the wave group velocity. That is, a hotter thermosphere refracts the wave energy up at more oblique angles and thus increases the dissipation rate. Therefore, the fact still remains that gravity wave dissipation depends strongly on local time and solar activity, as well as magnetic activity (COLE; HICKEY, 1981). The aforementioned factors might have caused the decreasing rate of MSTIDs from January 2014 (Solar maximum) to December 2019 (Solar minimum).

Investigated the important role tropospheric cloud convection plays in the thermosphere using deep convection and ray trace models, Vadas e Fritts (2006) realized that in the absence of dissipation, the vertical wavelength of gravity wave increases by $\sqrt{\bar{T}/\bar{T_0}}$ or greater if its intrinsic frequency is close to the smaller thermospheric buoyancy frequency $N = \sqrt{\bar{T}/\bar{T_0}}N_0$, where $\bar{T}$ and $\bar{T_0}$ are the asymptotic temperatures in the thermosphere and lower atmosphere, respectively. However, they mentioned that in the presence of dissipation, vertical wavelength increases in the thermosphere during active solar conditions, which is more applicable during solar maximum. Meanwhile, during extreme solar minimum, there is negligible forcing above an altitude of 230 km, which extends up to 360 km during active solar conditions. With regard to the MSTIDs in the present work, this analogy could be the possible factor for the high number of MSTIDs during solar maximum phase compare to minimum phase.

In order to investigate the themospheric temperature in relation with the dissipation of gravity waves in the thermosphere, we plotted altitude as a function of temperature using values from NRLMSIS-00 model as shown in Figure 5.8. Each line represents the profiles of average neutral temperature for a particular year as indicated in the plot. While the thermospheric temperature during solar minimum is $\sim$ 650 K, that of maximum phase is $\sim$ 950 K. It is clear that the temperature variation between solar maximum and minimum in the thermosphere is wide enough to influence the dissipative difference between the solar phases. Rishbeth (1972) reported that the basic structure of thermospheric neutral winds above about 150 km altitude is formed by atmospheric expansion due to solar heating on the dayside, creating a pressure bulge with a temperature maximum developing near 14:00 LT. This establish the fact that there is high viscosity in the thermosphere, which leads to high dissipation of gravity waves during low solar activity.

Figure 5.8 - Thermospheric neutral temperature profiles from 2014 to 2019 by NRLMSIS-00 model atmosphere.

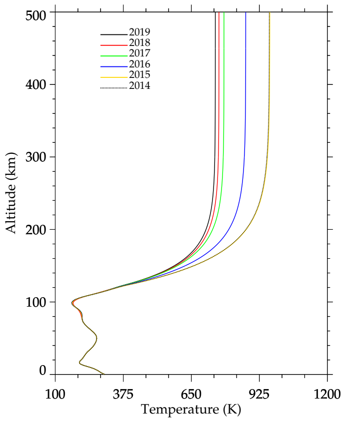

In the equatorial region over Brazil, Makela et al. (2013) used ground-based Fabry-Perot interferometers to measure thermospheric temperatures between solar cycles 23 and 24 through the maximum of cycle 24. They reported that the increase in the temperatures associated with the increase in solar flux was seen in the progression of temperature from 2009 through 2012 which is consistent with the results of Fisher et al. (2015) in the same study area. For instance, the average early evening (19 LT) temperatures observed in September increase from 739 K in 2009 F10.7 1/4 71:2 to 950 K in 2011 F10.7 1/41. This trend was seen in the neutral temperature against the solar flux for several local time. With these real observational thermospheric temperature data during solar maximum and minimum phase from Makela et al. (2013), Fisher et al. (2015), we could establish the connection between the solar activities and the gravity waves dissipation due to thermospheric viscosity as the precursor of the wide variation of the occurrence rate of the present MSTIDs.

It is well known that the Earth's ionosphere responds in a complex manner to geophysical conditions like solar flux among others with a lot of variability. Hence, various ionospheric parameters such as electron/ion density, TEC, electron and ion temperatures behave partially regular and irregular resulting in daily, seasonal, annual, latitudinal variations (KAWAMURA et al., 2002; SHARMA et al., 2012; AGGARWAL et al., 2007; AGGARWAL et al., 2009). From the thermospheric viscosity analogy discussed above using modeled and observational temperature data, gravity waves could dissipate due to high viscosity in the thermosphere, which is frequent during solar minimum. Therefore, during solar minimum only gravity wave with longer vertical wavelength and higher phase velocity can exist or survive to induced TIDs at high altitudes in the thermosphere, which led to the current positive correlation of equatorial MSTIDs occurrence rate during solar cycle 24.

In the present work, the mean phase velocities are higher in the solar descending and minimum phase compare to the maximum phase as shown in Figure 4.12. Although, some MSTID speeds are above the supersonic speed, it is still possible that the high viscosity condition in the thermosphere during the solar descending and minimum phase filtered out most of the gravity waves events with low speed. Richmond (1978) reported that the gravity waves vertical wavelength in the thermosphere is larger than in the lower atmosphere, which is more applicable when the sun is active. This minimizes the dissipation rate of gravity waves in the thermosphere during high solar activities, thereby, propagating into the ionospheres as TIDs. This could explain the positive correlation of the MSTIDs occurrence rate and solar cycle 24.

5.7 Summary

We have thoroughly discussed the characteristics and statistical occurrences rate of MSTIDs observed over South America equatorial region (between longitude: 30° to 55°W and latitude: 0° to 15°N) from January 2014 to December 2019 using TEC perturbation maps and keograms. We particularly discussed the horizontal wavelength, Period and Phase Speed of MSTIDs, the local time dependency of MSTID occurrence, seasonal dependency of equatorial MSTIDs, long term (solar cycle) variability of equatorial MSTIDs and the propagation direction of equatorial MSTIDs.

- The six-year observation of MSTIDs shows strong positive correlation with the solar activity. We observed 322, 251 and 171 MSTID events during solar maximum (2014-2015), descending (2016-2017) and minimum (2018-2019) which represent 43.3%, 33.7% and 23.0%. We realized that gravity waves dissipate due to high viscosity in the thermosphere as a result of low thermospheric temperature which frequently occur during solar minimum.
- The seasonal statistics of the MSTID occurrence rate are 307, 106 and 329 events for equinoxes, summer, and winter respectively. The neutral wind velocity observed by Fisher et al. (2015) and Makela et al. (2013) are high in summer and low in winter. Consequently, there is high wind filtering in summer than winter which explains the seasonal variation of MSTIDs. This account for why the MSTIDs almost disappear in summer and mostly appear in winter. The summer mean horizontal wavelength,

period and phase speed are larger than that of winter. This is might be due to the fact that, only MSTIDs events with long horizontal wavelength and fast phase speeds survived the critical level and dissipative filtering during summer.

- We also found out that the MSTIDs were highly dependence on the local time; the daytime and evening account for ∼70% and ∼28% of the total observation while the nighttime account for only ∼2%. The daytime MSTIDs occurred frequently in winter with the secondary peak in equinox, while the evening time MSTIDs occurred in summer and equinox. The dependency of the MSTIDs on the local time was attributed to the mechanisms causing them and the medium at which they propagated.
- There is strong link between the MSTIDs propagating to north-northeastward and north-northwestward of the Figueiredo et al. (2018a) and the present work especially, during winter and equinox. Also, MSTIDs observed by MacDougall et al. (2011) and the present have the same propagation directions. The present and the aforementioned works have high occurrence rate in winter daytime and secondary peak in equinox and a few events in summer. Among them, only the present work considered a detailed statistical analysis of MSTIDs and the solar cycle. Concerning the characteristics, the present equatorial MSTIDs have long wavelengths (300 - 1300 km m/s) and high phase velocities (100 - 700 m/s) compare to the former. They were likely induced by the secondary or tertiary gravity waves created in the thermosphere from the dissipation of primary gravity waves that were excited from deep convection in the troposphere (VADAS; CROWLEY, 2010).
- There are three preferential propagation direction of the present MSTIDs; north-northeastward, north-northwestward and south-southeastward. Moreover, in equinox and summer evening time, a few MSTIDs propagating westward. The anisotropy of the propagation direction is due to the wind and dissipative filtering effects, ion drag effects that favors MSTIDs propagating equatorward along the magnetic field lines and the presence of the secondary or tertiary gravity waves in the thermosphere.

6 DISCUSSION II: POSSIBLE SOURCE REGION AND MECHANISM OF THE MSTIDs OVER SOUTH AMERICAN EQUATORIAL REGION

6.1 Introduction

Knowing and understanding the sources of MSTIDs is of utmost importance for unraveling the complexities of the thermosphere/ionosphere coupling system as well as the prediction of the climatology of MSTIDs in the future. Yet, the question of the primary sources of MSTIDs over the South American equatorial ionosphere is unanswered. For science to provide answers to these questions, a lot of day-to-day and seasonal source analysis have to be done in the aforementioned region to ascertain fully understanding about the subject matter. For that matter, this chapter presents the possible primary source regions of the MSTIDs over the South American equatorial region. Effort will be thrown into discussing the possible mechanisms whereby gravity waves produce these MSTIDs. Pertinent to the present work, the possible sources for the equatorial MSTIDs will be limited to the upward propagating and filtered meteorological atmospheric gravity waves (AGWs) as well as secondary and tertiary gravity waves. The correlation of most MSTIDs propagation directions in the present work (as shown in Figure 4.4) points to some meteorological sources of the MSTID exciting gravity waves.

6.2 Possible source regions of the Equatorial MSTIDs

The Earth's ionosphere is largely impacted by the solar and magnetic activities as well as perturbed from below by geophysical phenomena such as severe tropospheric weather events, earthquakes, tsunamis, volcanic eruptions and man-made events such as explosions, rocket and missile launches and mini blasts among others (ASTAFYEVA, 2019). The disturbances from the below arrive in the ionosphere as gravity waves (internal or acoustic) leading to TIDs and other disturbances such as plasma bubbles among others in the case of equatorial region. The upward propagation of gravity waves triggers the increase in amplitude significantly due to the exponential decrease of the atmospheric density with altitude. The gravity waves generated in the neutral atmosphere may consequently give rise to significant disturbances in the upper atmosphere and ionosphere, which can be detected by ionospheric sounding tools, such as, Global Navigation Satellite System (GNSS) receivers, ionosondes, airglow and cameras among others.

The study of TID commenced by the early days of long-distance radio transmission, variations and interruptions over-the-horizon transmissions (CROWLEY; AZEEM, 2018). In the pioneer paper published by Hines (1960), he proposed that TIDs are cause by the upward propagating gravity wave disturbances originating from the neutral atmosphere (e.g., troposphere). The gravity wave-MSTID transfer function depends on the characteristics such as period, phase velocity, horizontal wavelength, wavenumber, amplitude and propagation direction of the wave in question, in addition to the conditions in the neutral atmosphere and ionosphere (HOOKE, 1968; GEORGES; HOOKE, 1970). Thus, the call for the investigation into the origin of the present equatorial MSTIDs from the neutral atmosphere and other geophysical sources in relate to the statistical behaviour is of equal importance to science.

Several authors have suggested that the possible source regions for equatorial and low latitude MSTIDs are associated with the gravity waves in the thermosphere that are originated from the tropospheric deep convection (PAULINO et al., 2016; FIGUEIREDO et al., 2018a) and ITCZ (RÖTTGER, 1977; MACDOUGALL et al., 2011) among others. In the mid latitude, day and nighttime MSTIDs have been reported to be generated via atmospheric gravity waves propagating in the F-layer bottom height Otsuka et al. (2013) and Perkins instability Otsuka et al. (2011), Kotake et al. (2007), Kelley et al. (2000) while the high latitude, MSTIDs haven been attributed to the geomagnetic storms and polar electroject (LIU et al., 2020). For the purpose, the present work will discuss the potential equatorial sources of MSTIDs specifically, in South America.

With regard to the present equatorial MSTIDs in the South American region, the propagation directions change with seasons as shown in Figure 4.4. The anisotropy observed in the propagation direction could be due to a non-uniform distribution of sources of gravity waves that triggered them. The source region with respect to the propagation direction is an important factor to unearth the mystery of the MSTID sources in the South American equatorial region. Therefore, based on the propagation directions we investigate some likely source mechanisms of the gravity waves exciting the present equatorial MSTIDs such as meteorological sources like in-situ tropospheric deep convection, intertropical convergence zone (ITCZ), and the supersonic motion of solar terminator, as well as secondary and tertiary gravity waves sources. Consequently, the relative importance of various gravity waves sources, their spatial and temporal variability, and their statistical influences on the larger-scale atmospheric flow are virtually unknown at present. The next section will deliberately explain the aforementioned potential primary sources of the equatorial MSTIDs.

6.3 Tropospherical convection and Frontal Systems

It has been well known and understood for decades that tropospheric deep convection can excite gravity waves that can propagate into the ionosphere as perturbation in the plasma density popularly known as TIDs (HINES, 1960; RÖTTGER, 1977; KELLEY et al., 2000; KOTAKE et al., 2007; OTSUKA et al., 2011; MACDOUGALL et al., 2011; CROWLEY; AZEEM, 2018). Nevertheless, there are still considerable controversy about the connection of the primary source regions and generation mechanisms of equatorial MSTIDs. According to Fritts e Alexander (2003), gravity waves generated by convection are not characterized by a single prominent phase speed or frequency as is the case for topographic waves: Instead, convection can generate waves throughout the full range of phase speeds, wave frequencies, and vertical and horizontal scales. They reported that the low-frequency waves, in particular, might be observed in the middle atmosphere at large horizontal distances from the convective source, making correlation with clouds or other indicators of convection more difficult. However, in the tropical region far from topography and regions of baroclinic instability, the occurrence of inertia-gravity waves has been linked to convection as the source (PFISTER et al., 1986; TSUDA et al., 1994; KAROLY et al., 1996; SHIMIZU; TSUDA, 1997; WADA et al., 1999; VINCENT; ALEXANDER, 2000). This convection in the troposphere involves a time-varying thermal forcing associated with latent heat release that can interact with overlying stable layers and shear in complex ways that are not fully understood (FRITTS; ALEXANDER, 2003).

In the midlatitude of England (Leicester: 52.53°N, 1.13°W), Waldock e Jones (1987) observed MSTIDs through the Doppler shift in HF (High Frequency) signal. They analyzed the sources using the trajectory plotter model and identified that most of them originated from the troposphere within a radius of 1500 km from the observation point. They suggested that the source could probably be jet streams. Alexander e Vincent (2000) reported that the seasonal and inter-annual variability in gravity waves observed at Cocos Island was likely due to deep convection. Using a ray tracing model Vadas (2007) explored gravity waves properties that resulted from a wide range of temperatures, calculated the dissipation altitudes, horizontal distances traveled, times taken, and maximum horizontal wavelengths prior to dissipation for a wide range of upward-propagating gravity waves that originate in the lower atmosphere. Grimsdell et al. (2010) also reported that thunderstorms trigger a broad spectrum of gravity waves via latent heat release and interactions with the mean flow.

In the Brazilian equatorial region, MacDougall et al. (2011) observed that winter MSTIDs spread to the north-northeast. However, they did not identify a possible source responsible for the oscillations in the aforementioned direction. In the equatorial and low latitude over South America, Essien et al. (2018) studied the possible sources of SSGWs and MSGWs in the troposphere over Brazilian equatorial region using the 11 years of daily mean of outgoing longwave radiation (OLR) data obtained from the National Oceanic and Atmospheric Administration (NOAA) as a proxy for tropospherical deep convection regions. They realized strong convective regions emanating from Amazon rainforest during fall equinox and summer solstice that were the possible source mechanism for the gravity waves they observed. However, in spring and winter the deep convection in the equator region were rare, therefore, they concluded that deep convective within the vicinity did not play any important role in the waves observed at Cariri. Most importantly, Figueiredo et al. (2018a) used cloud top brightness temperature (CTBT) data observed by Geostationary Operational Environmental Satellite 13 and 16 (GOES 13and 16) to study the possible sources of the MSTIDs observed in the southeast of Brazil from December 2012 to February 2016. They reported that the atmospheric gravity waves in the thermosphere, mesosphere and troposphere could play an important role in generating the MSTIDs.

The present work is investigating the potential primary sources of the MSTIDs observed over South American equatorial latitude. In order to achieve this, we adopt the parameter used to measure the intensity of the convection cloud; cloud top brightness temperature data from GOES 13 and 16, with spatial resolution of 4×4 km which is available in binary files by the scientific cooperation between GOES 13 and Center for Weather Forecasting and Climate Studies in Brazil. The temperatures between 208° and 233° K (-65°C and -40°C) were selected to be with associate cumulonimbus or deep convective clouds (FIGUEIREDO et al., 2018a; INOUE et al., 2008). In the present study, we consider cloud top brightness temperature with -55° and -45°C as upper limit temperatures. In all the analysis, we considered six hours of deep convective source before the time of occurrence of the observed MSTIDs as Vadas (2007) said that gravity waves with wavelengths shorter than 500 km take around 1 to 3 hours to propagate from the troposphere to the thermosphere. Vadas (2007) further reported that gravity waves generated from tropospherical deep convection have much larger amplitudes, and therefore account for most of the vertical transport of energy and momentum from the troposphere to the middle atmosphere. Fukushima et al. (2012) reported that most MSTID events observed in the equatorial and low latitude regions were related to tropospheric convection.

In order to investigate the potential primary sources of the observed MSTID in the present work, we consider day-to-day analysis of the observed MSTID and the cloud top brightness temperature front that are susceptible to trigger the gravity waves which manifested as the observed MSTID. Figure 6.1 shows the structures of cloud top brightness temperature front on South American map (left column) with red arrows indicate the propagation directions of the MSTIDs observed on 30th June and 8th November, 2015 and 1st October, 2017. In order to relate the MSTID oscillations observed to the possible primary sources, we include the TEC perturbation maps (right column). For example, on 30th June 2015, it is obvious that the MSTID is propagating north-northwestward with horizontal wavelength of 552.0 km, period of 29.9 min and phase speed 308.1 m/s. The possible source region for this direction is located over the low latitude around 20° to 25° south and 50° to 60° west. Also, on 8th November 2015, the MSTID is propagating north-northwestward with horizontal wavelength of 635.7 km, period of 35.0 min and phase speed 322.7 m/s and the source region is located within the equatorial region around 10° to 15° south and 45° to 50° west. Finally, on 1st October, 2017 MSTID oscillation is propagating south-eastward and the source region is located around 7° to 12° south and 55° to 60° W over the Amazon region. The MSTID on this day is propagating southeastward with respective horizontal wavelength of 647.9 km, period of 35.0 min and phase speed 308.5 m/s

The distance between the possible source region and the where the MSTIDs was observed on 30th June 2015 is ∼1150 km (That is each degree in latitude and longitude is approximately 115 km at 300 km altitude, therefore, ∼10° is equivalent to ∼1150). However, Waldock e Jones (1987) reported that gravity waves generated in the troposphere are capable of traveling within a radius of 1500 km before ascending vertically into the ionosphere as fluctuation on the plasma density. Vadas (2007) used ray tracing model to investigate gravity waves source region and propagation properties. They reported that small- and medium-scale gravity waves can travel horizontal wavelength of less than 500 km, phase speed of 100 m/s and the period of less than 60 min can propagate less than 2000 km horizontally from the ground prior to dissipating at 150 to 250 km altitude. Also Freund e Jacka (1979) and Taylor e Hapgood (1988) reported that in the absence of background winds, gravity waves of a period of $\leq$1 h would be expected to propagate from the source region to OH heights within a ground range of 800 km. According to Takahashi et al. (2018) the propagation direction of the gravity wave depends on the source region and the background winds in the lower atmosphere.

Figure 6.1 - Cloud top brightness temperature (CTBT) below -50°C (left column) and the possible corresponding MSTID (right column) on 30th June and 08 November 2015, and 1st October, 2017. The red arrows on cloud top brightness temperature map indicate the propagation directions of the MSTID observed on the aforementioned days. The possible sources and propagation directions are also indicate on dTEC map with blue star and arrow.

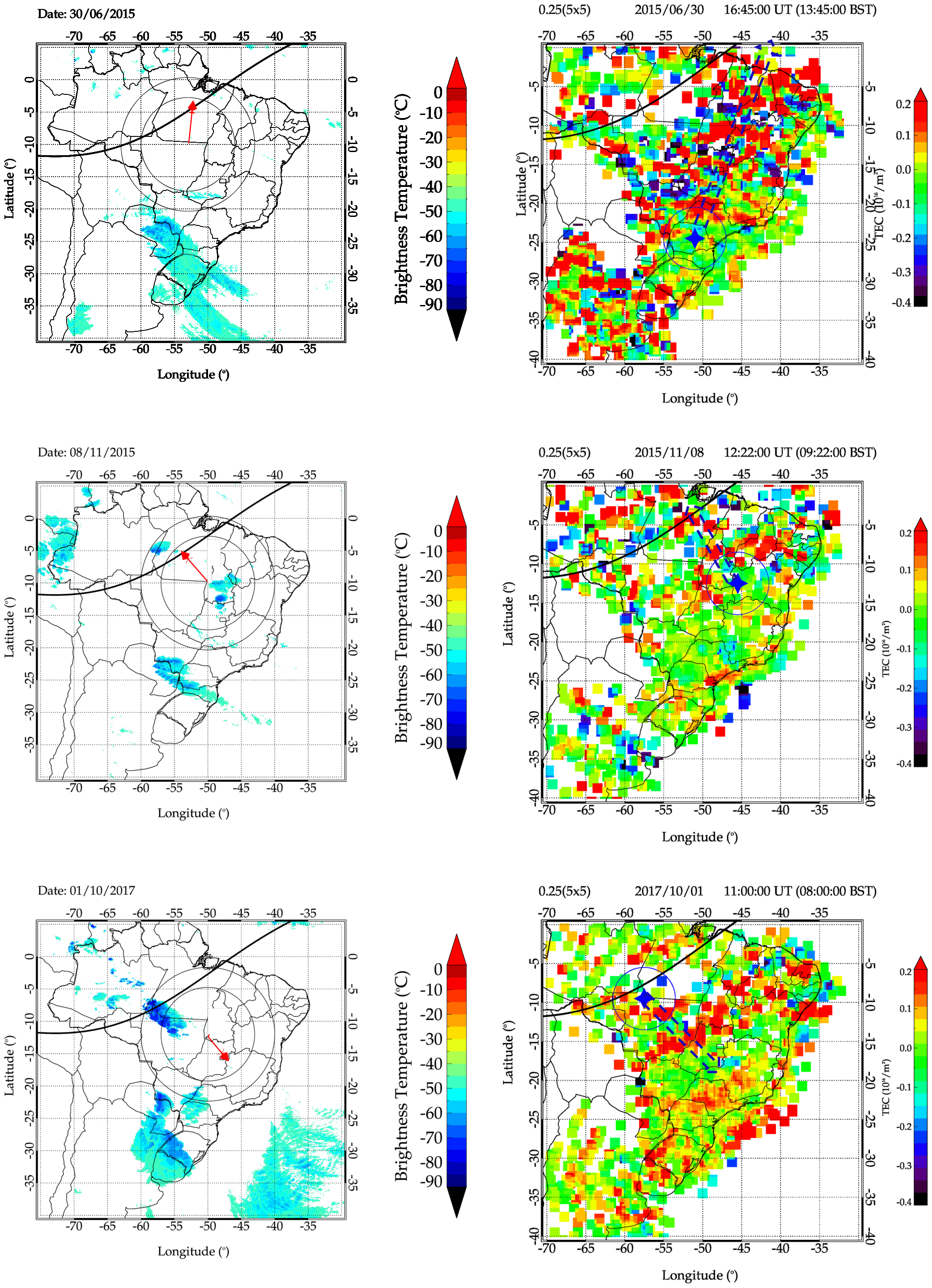

In order to investigate the seasonal variation of the sources regions of the observed equatorial MSTIDs, we plotted convection map for only the days MSTIDs were observed in a particular season as well as the corresponding propagation directions of the MSTIDs observed on those days. Figure 6.2 shows cloud top brightness temperature maps over South America for (a) summer, (b) autumn, (c) winter, and (d) spring. The red arrows indicate the propagation directions of the MSTIDs observed in the particular season. In summer, spring and autumn, there are deep convective cells associated with cumulus nimbus clouds within the South American equatorial region that are capable of generating gravity waves and propagate into the ionosphere. However, the propagation direction of the MSTIDs do not correlate with the sources in the troposphere. However, in the winter, convection clouds are located in the low latitude (20°) emanating from the midlatitude, which is the south of the area of the present study.

Figure 6.2 - Cloud top brightness temperature maps with temperatures below ~55°C overplotted between January 2014 and December 2019. The red arrows indicate the propagation direction of medium-scale traveling ionospheric disturbances observed in (a) summer, (b) autumn, (c) winter, and (d) spring. The selected time zones for the seasons were 6 hours before the MSTIDs were observed.

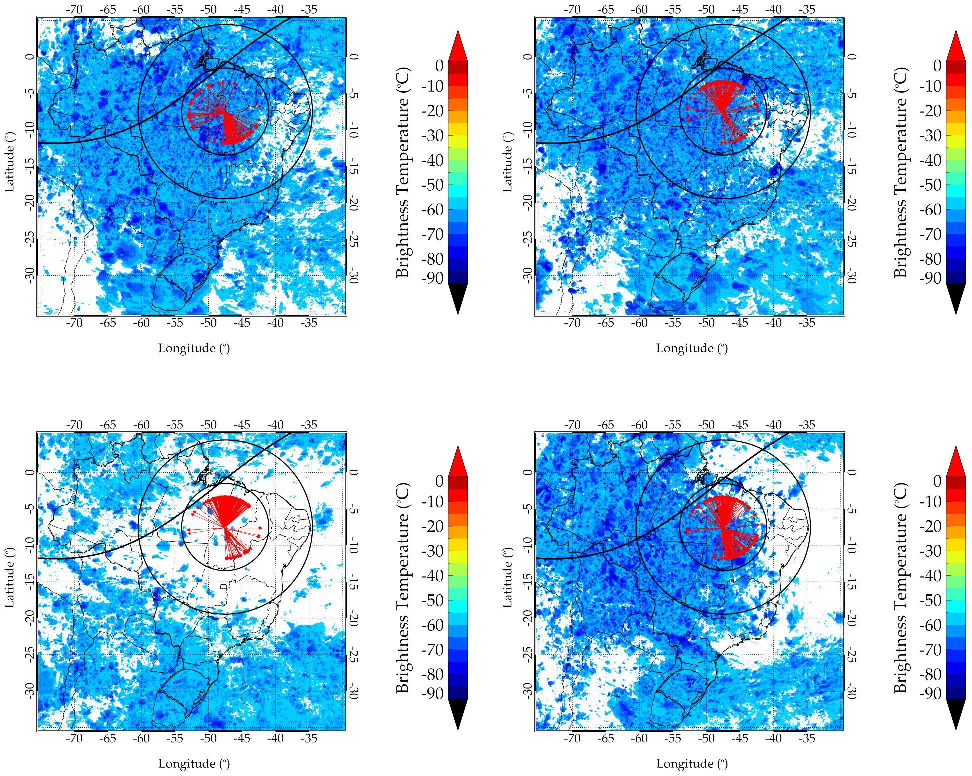

According to Zhang (2004), the deep convection activities in the south of Brazil during the winter are highly related to the jet stream associated with cold fronts. This cold front in winter correlate well with the propagation direction of the present equatorial MSTIDs, particularly those propagating to northward. Therefore, it is possible that the primary sources of the winter equatorial MSTIDs are from the low and midlatiude region. Hoffmann et al. (2013) reported that in the wintertime, the winds do not typically reverse the sign until the mesosphere and, thus, the waves can propagate up to these altitudes and obtain larger amplitudes before being filtered. From the area of the observation of the present MSTIDs to the location of the cold front in the low latitude is between ∼1000 to ∼1500 km, which is consistent with (VADAS, 2007) model.

Meanwhile, the source regions in summer, autumn and spring are not consistent with the MSTIDs propagation direction, therefore, it could be possible that they are non-primary gravity waves, which propagated into the ionospheric plasma density as MSTIDs. Heale et al. (2020) reported that in summer time, winds switch between east and westward directions in the middle atmosphere, thus, gravity waves tend to get filtered in the stratosphere. Probably, the primary wave generated by the sources of the present MSTIDs encountered critical level, hence, were absorbed into the mean flow or dissipate. According to them, the dissipation exerts a body force on the mean flow at packet form, which generates spectra of non-primary waves with larger scales and longer periods than the primary wave. Therefore, it must be noted that, the important physics in the north-northeastward and north-northwestward MSTIDs cannot be described by only tropospheric sources. We therefore, suspect that secondary or tertiary gravity waves could be the possible source for most of these equatorial MSTIDs observed.

Nevertheless, the MSTIDs that are propagating south-southeastward could not be explained by a mere deep convective sources since they do not correlate. Hence, we will explore ITCZ as the possible option since it lies at the north of the study area.

6.4 Intertropical convergence zone (ITCZ)

The ITCZ is characterized by low atmospheric pressures due to the upward movement induced by the trade winds from the Northern and Southern Hemisphere convergence which results in high atmospheric pressure in the upper troposphere (GIRESSE, 2007). The ITCZ is a permanent low-pressure feature lies in the equatorial trough where surface trade winds laden with heat and moisture converge to form a zone of increased convection, cloudiness, and precipitation (WALISER; JIANG, 2015): The latent heat released in the ITCZ is critical to the atmospheric energy budget and ITCZ cloudiness provides an important contribution to the planetary albedo: The position, structure, and migration of ITCZ influence ocean/atmosphere and land/atmosphere interactions on a global scale. The resulting circulation that forms with air converging near the surface around the equator and diverging above is known as the Hadley Cell (MADDEN R. A, 2015). Throughout the year, the ITCZ follows the migration of the sun's overhead position typically with a delay of around 1-2 months. As the ocean heats up more slowly than land, the ITCZ tends to move further north and south over land areas than that over water. In winter, the ITCZ lies well to the north of the equator and migrates to the south in summer (WALISER; JIANG, 2015). In South America region, the winter and summer positions can go as far as 15°N and 5°S over the continent.

Therefore, the ITCZ provides a useful framework to study the primary source region of the gravity waves that might propagated to the ionospheric level as MSTIDs. This section will investigate the MSTIDs in the present work propagating to south-southeast direction and the ITCZ, which is suspected to be the possible primary source.

6.4.1 Data processing and characterization of synoptic systems

First and foremost, images from GOES 13 from the Center for Forecasting and Climate Studies (CPTEC: INPE; http://satelite.cptec.inpe.br/acervo/) of the National Institute for Space Research, in the infrared (IR) and water vapor channel, with a horizontal resolution of $0.42.5°x0.42.5°$ for every 30 min were obtained to realize the features of ITCZ. The typical example of these images observed by GOES 13 in South American are shown in first panel of Figure 6.3; The position of ITCZ is indicated with red box, though there are other features such as frontal systems (FS) and Bolivia High (BH) at the southeast and central part of South American continent. All these features are common in the low and equatorial latitude of South America.

Figure 6.3 - GOES 13 Satellite images on the IR channel on 1st January, 2017 at 12:00UTC and 12:30UTC at the first row, average daily OLR fields and horizontal wind current lines at 1000 hPa (a), wind convergence at 1000 hPa and wind current lines at 200 hPa on 1st of January 2017 at the second row and the average daily vertical profiles between 1000-200 hPa of ascending humidity and vertical wind current lines at the third row.

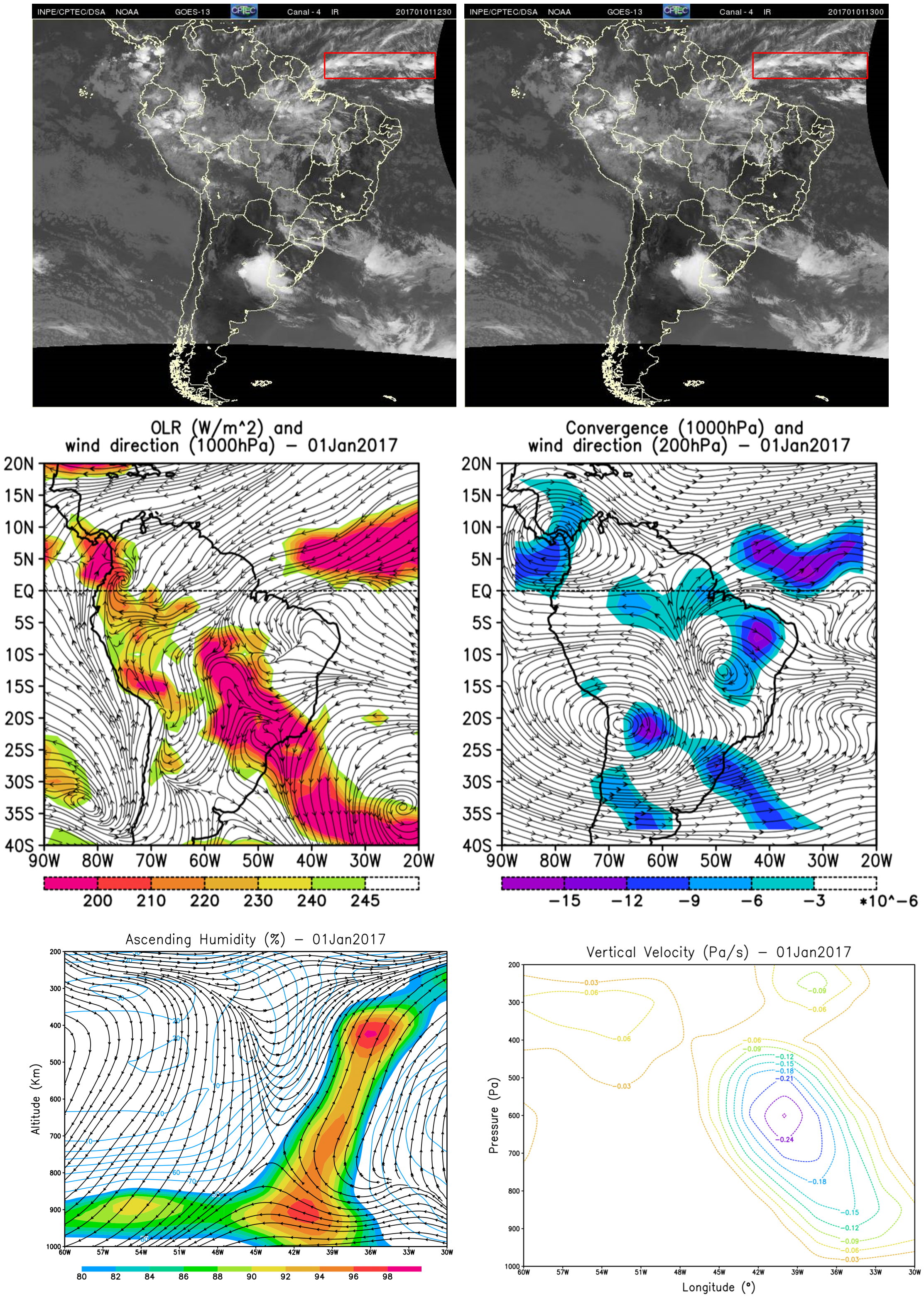

In order to study the ITCZ position, we obtained the Outgoing Longwave Radiation (OLR), zonal (u (m/s)), meridional (v(m/s)) and the vertical (omega (Pa/s)) components of wind variables from the National Oceanic and Atmospheric Administration (NCEP) reanalysis data. These data were used to generate daily average fields between latitude: 20°N-40°S and longitude: 90°-20°W as shown in Figure 6.3 second and third rows. The fields comprise of current lines (shown in **??**) at the pressure levels of 1000, 925, 800, 700, 500, 300 and 200 hPa and the divergence of the wind (shown in **??**) at 1/s at the pressure level of 1000 hPa and the average filtered OLR field (OLR <245 W/m^2). The zonal (u) and meridional (v) wind components at 1000 hPa pressure and OLR filtered average field (245 W/m^2) correspond to longitude (x) and latitude (y) coordinates. The fields composed of filtered OLR are used to obtain information related to the convective cloud (KOUSKY, 1988). The remaining fields are used for the identification of the main large-scale systems (synoptic scale) responsible for the convective activity over South America; these are the ITCZ, the High Levels Cyclonic Vortex (HLCV), Bolivia High, South Atlantic Convergence Zone (SACZ) and transients like frontal systems. The vertical cross-sections that confirm the performance of the ITCZ, built at fixed lengths of 30° - 60°W and variable latitude according to the position of the ITCZ.

$$\delta = \frac{dx}{u} + \frac{dx}{v} \tag{6.1}$$

Where δ is wind divergence, u and v the zonal and meridional horizontal wind components respectively, and x and y are the latitude and longitude coordinates.

In the present work, ITCZ was identified as the current fields lines at the convergence of winds at pressure levels of 1000 hPa (LHS: left hand side) around latitude ~2.5° and the divergence (RHS: right hand side) at tropopause at the pressure of 200 hPa. We then validated the ITCZ position with satellite image from GOES 13 (shown at the first row), through clusters of convective clouds in the equatorial latitudes. Bolivia High (BH) and HLCV were also identified by anticyclonic and cyclonic circulation, respectively, in the fields of horizontal wind current lines at the tropopause (GUTMAN; SCHWERDTFEGER, 1965; VIRJI, 1981; LENTERS; COOK, 1997; VUILLE, 1999). The frontal systems were identified by the joint analysis of aerodynamic convergence in the wind fields at 850 hPa level and cloudiness characteristics of the system in the satellite images on the IR channel (ZVEREV, 1968). The frontal systems that remained permanent forming a band of cloudiness in the northwest-southeast direction in the satellite images, in parallel with the convergence of the winds in the fields of current lines at low levels were also identified as the SACZ (QUADRO, 1994; KODAMA, 1992).

Also, the vertical profiles which confirm the performance of the ITCZ over the tropical Atlantic Ocean between longitudes 30° and 51°W are shown in third row of Figure 6.3. The ascending humidity profile shows values up to ~80% in the most intense region where ITCZ operates over the ocean and above 90% over the continental. In the case of Figure 6.3 it is highly humid between longitude 45° and 30°W at the low pressure level and extended to tropopause as shown in third row. The upward vertical movements from the atmospheric layers close to the surface to the high levels is also shown by the current lines with vertical velocity above 0.2 Pa/s. The negative sign is an indication of ascending profile.

6.4.2 Day-to-day variations of ITCZ as the possible source of equatorial MSTIDs

Figure 6.4 shows the average situation of the performance of the synoptic scale systems responsible for the convective activity over South America on 5th of January 2016, 1st of January 2017 and 29th of January 2017. On these day, the ITCZ is located between ~ 0° and ~ 5°N latitudinal over the tropical Atlantic band, visible by the convergence of the winds at low (shown in the right column), however, over the continent, the position of the ITCZ is not clear due to the mountain ranges. Meanwhile, the performance of BH as a result of superficial warming over the central part of South America, and frontal systems over the southeastern region enabled the occurrence of convective activity over these regions (HOREL et al., 1989). The predominance of the performance of these systems during the day can be observed in the satellite images on the IR channel as shown in Figure 6.3 where the frontal systems moved in the northeast direction coupling to BH during most of the day, forming a convection corridor at northwest-southeast.

Figure 6.4 - The observed MSTID over South America on 5th of January 2016, 1st of January 2017 and 29th of January 2017 (left column) and the corresponding ITCZ position (right column). The red arrow shows the propagation direction of the observed MSTID.

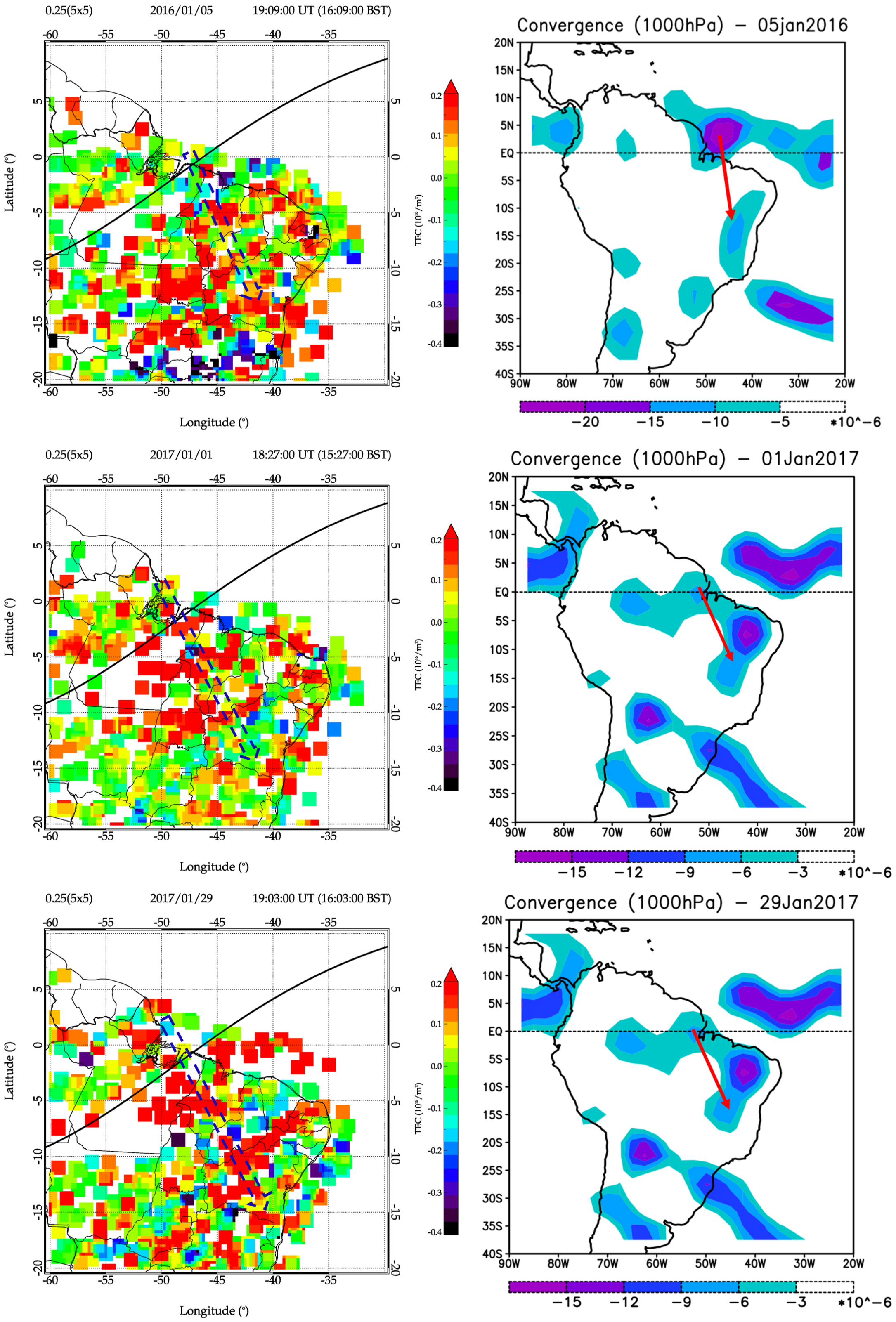

In order to relate the ITCZ as the possible primary of the MSTID on the aforementioned days, we include the corresponding observed MSTIDs (right column) indicating the propagation directions with the blue arrow and the source region with the blue star on the South American map. The characteristics of the MSTIDs were calculated, for instance on 5th of January 2016 the oscillation were observed at 16: 16LT with horizontal wavelength of 922.8 km, period of 52.0 min and phase velocity of 295.8 m/s. On 1st of January 2017, we also observed MSTID oscillations at 15:27 LT with horizontal wavelength of 757.3 km, period of 37.7 min and phase velocity of 335.1 m/s. Finally, we observed another MSTIDs with horizontal wavelength of 751.0 km, period of 40.0 min and phase velocity of 312.9 m/s 29th of January 2017 at 16:03 LT. We suspect that the gravity waves generated by ITCZ could also break and secondary waves generated if the phase velocity of the wind is not high enough.

The propagation direction of the aforementioned MSTIDs correlate with the corresponding ITCZ position as shown in Figure 6.4. On these days, we found that MSTID propagating to south-southeastward towards the low latitude. As shown at the right column, the source positions of the MSTDs are over the north as indicated by the blue star. This implies that the propagation direction is still a strong factor to trace or determine the possible sources. Hence, the ITCZ positioning is still the preferred candidate for the possible primary source of the observed MSTIDs propagating south-southeastward. This and many days (not shown here) are consistence with the results of MacDougall et al. (2011) and Röttger (1977).

Since the early theories of Hines (1960), Hines e Reddy (1967), tropospheric phenomena, such as weather systems and the orographic lifting of air masses, have long been suspected as sources of atmospheric gravity waves. Due to the amplitude growth with increasing altitude, which offsets the decreasing atmospheric density, these waves of tropospheric origin are expected to contribute significantly to the wave energy present in the mesosphere (HINES, 1960; GOSSARD, 1962) and beyond. Additionally, gravity waves are assumed to be generated by mesoscale convective systems in the troposphere and propagate up to the F region as MSTIDs. These mesoscale convective systems are usually found within the ITCZ and even ESF morphology is assumed to be controlled by the seasonal migration of gravity waves generated by ITCZ (TSUNODA, 2010; SU et al., 2014).

During ALOHA-93 campaign, Gardner (1995) presented aircraft-borne Michelson Interferometer measurements of OH Meinel band rotational temperature and integrated band radiance observed during a trans-equatorial flight over the ITCZ. The aircraft motion afforded the opportunity to examine the horizontal wave number spectra of the gravity-wave induced fluctuations in the mesospheric OH temperature and radiance (QIAN et al., 1995; GARDNER, 1995) and both showed the presence of gravity waves confined to regions near the equator. According to them, the spatial variation of the wavelength of these waves would suggest a source associated with the convective instabilities of the ITCZ and imply that the ITCZ may play an important role in mesospheric circulation through its generation of gravity waves. In the Peruvian equatorial region, Röttger (1977) found a significant correlation with rainfall activity and occurrence of MSTIDs. They conclusion that penetrative cumulus convection in the ITCZ was the most likely generation mechanism of the gravity waves exciting the observed TIDs. In the northeast of Brazil, MacDougall et al. (2011) reported that the possible source for the southeastward TIDs is the ITCZ.

6.4.3 Seasonal variations of ITCZ as the possible source of equatorial MSTIDs

In other to analyze the seasonal variability of the MSTIDs propagation direction and ITCZ as the possible primary sources, we compiled the seasonal average position of the ITCZ for the days we observed MSTIDs propagating south-southeastward, and plotted alongside the seasonal variation of the propagation directions of the MSTIDs observed during the 6-year study, as shown in Figure 6.4.3. In summer and fall/autumn, the average position of the ITCZ are located on latitude ∼0°, meanwhile during the winter it is located at ∼10° while ITCZ position in the spring is located at ∼5°. The possible source region of the south-southeastward MSTIDs being far from the area of study during winter could explain why we observed few events propagating to the said direction. It also explains why south-southeastward MSTIDs are rare in low latitude (FIGUEIREDO et al., 2018a). Moreover, in summer, we have majority of the MSTID activity propagating to south-southeast direction, possibly as a result of the primary source location being located within the study area.

Also, the deep convictive field shows an intense convection signal over the South American equatorial region during summer and autumn/fall as a result of surface warming, and BH at ∼5°S. Meanwhile, during spring the convective activity is weak in the equatorial region, but intense in the southeast and subtropical latitudes between 25° and 40°S). In winter, the convective activity in the equatorial region is rare, however, there is a strong cold front emanating from the midlatitude into the low latitude (this can be seen during equinox as well) and these frontal systems are the possible primary sources for the north-northeastward and north-northwestward observed MSTIDs.

Figure 6.5 - Seasonal average position of the ITCZ (left column) and propagation direction of the observed MSTIDs (right column).

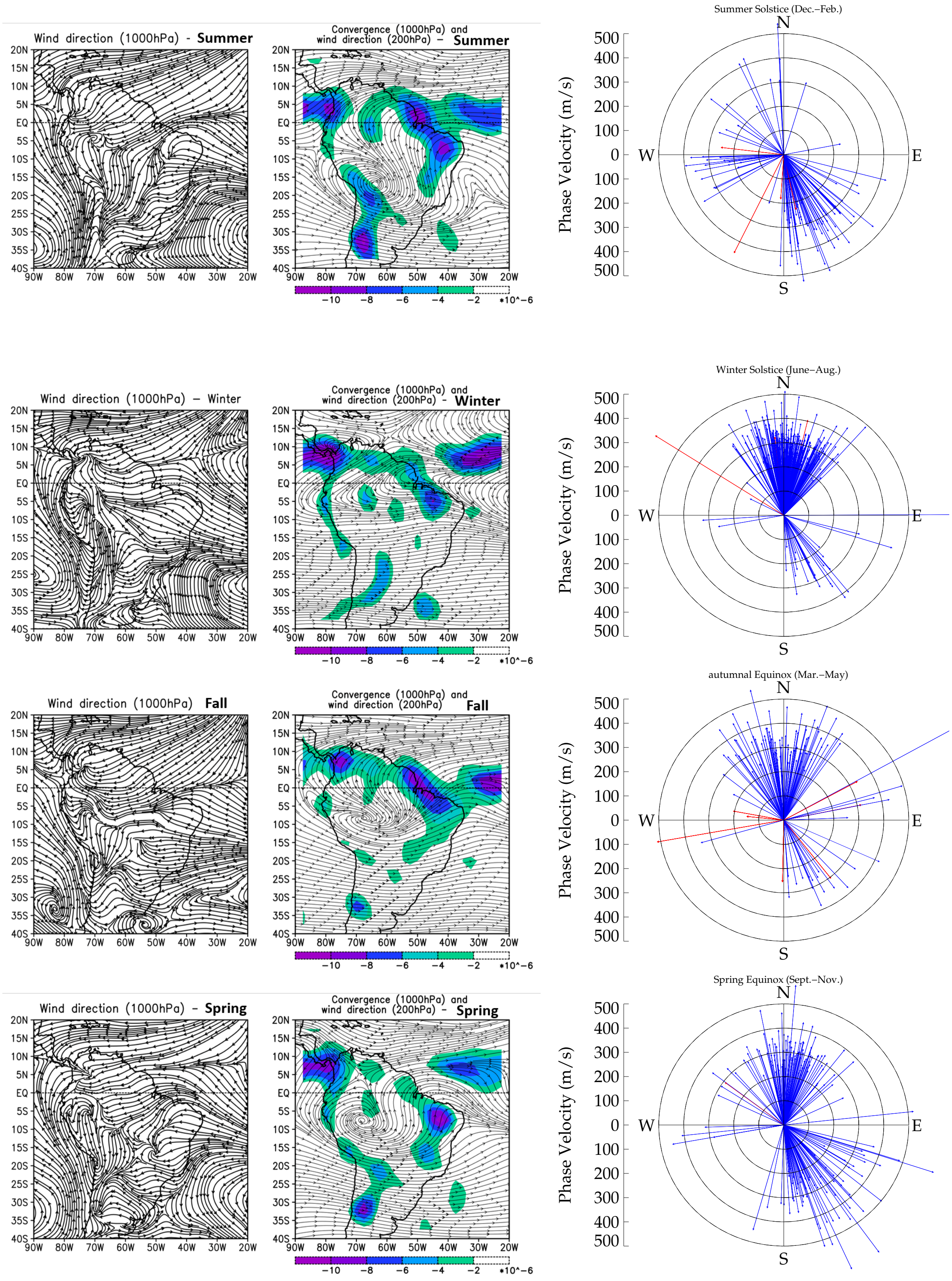

Most of the MSTIDs propagating south-southeastward have high phase velocity equivalent to the phase speed of secondary and tertiary waves as shown in the Figure 6.4.3. Therefore, we suspect that some of the MSTIDs in the present work might have been excited by secondary and tertiary gravity waves that were generated from the ITCZ in the troposphere.

6.5 Secondary and tertiary sources of the Equatorial MSTID

Secondary gravity waves are generated from primary wave breaking while tertiary gravity waves are generated as a result of secondary wave breaking. The wave breaking creates turbulence and generates secondary or tertiary waves (BACMEISTER; SCHOEBERL, 1989; BOSSERT et al., 2017; EHARD et al., 2016; HEALE et al., 2017; VADAS, 2013; VADAS et al., 2018; VADAS; BECKER, 2019). These waves are recognized to have potentially significant effects at higher altitudes such as thermosphere/ionosphere. From the ray tracing model, Vadas e Fritts (2006) reported that thermospheric body forces likely generate medium and large-scale secondary gravity waves which may be a new source of MSTIDs and LSTIDs which occur during geomagnetically quiet and active conditions. They also reported the possibility of tidal winds acting like a filter for secondary wave spectra reaching the thermosphere (VADAS et al., 2003; VADAS et al., 2018; VADAS; BECKER, 2019). However, the secondary and tertiary waves analogy still remain theoretical since they have not been any observational evidence. Meanwhile, most of the characteristics of the present equatorial MSTIDs shows evidence of been excited by the secondary and tertiary waves since their propagation directions do not correlate with their corresponding primary sources and also the fact that their wavelength and phase velocities are higher beyond the scope of convectively generated gravity from the troposphere.

Vadas e Fritts (2006) used forward ray tracing to calculate the body forces which resulted from the saturation and dissipation of the gravity waves excited by Tropical Storm Noel at 04:32 UT on 30 October 2007. They simultaneously analyzed 59 TIDs located at the bottomside of the F layer at 230-290 km, observed by the TIDDBIT ionospheric sounder. The TIDs had periods of 15 to 90 min, horizontal wavelengths of 100 to 3000 km, and horizontal phase speeds of 140 to 650 m/s. They reported that the observed TIDs were likely secondary gravity waves excited by thermospheric body forces with 40% of their phase speeds faster than 280m/s. The reason being that none of the TIDs was identified as primary gravity waves excited directly by Tropical Storm Noel, which precluded a tropospheric source and suggested mesospheric and thermospheric sources instead. They also compare the gravity waves locations with the regions of convective overshoot, mesospheric body forces, and thermospheric body forces, and discovered that 11 of the selected gravity waves with phase speed <205 m/s likely reflected near the tropopause prior to detection. Most of the horizontal wavelengths and phase velocities of the present equatorial MSTIDs are between 500 and 800 km, and 200 and 400 m/s respectively, hence, they are likely secondary gravity waves from the mesosphere or thermosphere.

In the case of South American continent, Vadas e Becker (2019) used a gravity wave resolving global circulation model (GCM) to investigate the effects on the mesosphere and thermosphere from a strong mountain wave (MW) event over the Southern Andes during winter. They reported that the MWs broke and attenuated at altitude of 50-80 km, thereby, creating local body forces that generated large-scale secondary gravity waves having concentric ring structure with horizontal wavelengths between 500 and 2000 km, horizontal phase speeds from 70 to 100 m/s, and periods of 3 to 10 hr and can consequently break and generate tertiary gravity waves. Most of the horizontal wavelengths and phase velocities of the present equatorial MSTIDs are between 500 and 800 km, and 200 and 400 m/s respectively. We also observed few MSTIDs with wavelength as far as 100-1400 as well as phase speed between 500 to 700 m/s. These characteristics are consistent with the parameters of the secondary and tertiary medium- and large-scale gravity waves calculated using GCM (VADAS; BECKER, 2019). However, the period are inconsistent with the secondary and tertiary gravity waves periods due to the fact that the present MSTIDs were calculated using 1-hour running average. The phase velocities in the present work and that of Figueiredo et al. (2018a) from the low latitude (southeast of Brazil) are not too different, probably, they might have been excited by the likely same secondary and tertiary gravity waves from the mesosphere or thermosphere that were generated by the MWs from Southern Andes (VADAS; BECKER, 2019).

We show an observational evidence of such MSTIDs with concentric ring structures propagating from the east of Southern Andes to the northeast of South American equatorial region on 1st July, 2014 at 15:03:00 UT (12:30:00 LT), as shown in Figure 6.6 LHS. The possible center (indicated with a blue star) of this MSTIDs is located at latitude 35°S and longitude50°W. This MSTID propagated at a wavelength of 534.1 km, period of 35.7 min, phase velocity of 249.6 ms and propagating north-northeastward. The circles are just to reinforce the clarity of the concentric structure of the MSITD and the blue short dashes arrow denotes the propagation direction. The RHS shows the deep convection map observed by GOES 13. The potential primary sources of the MSTID on this day are located around Southern

Andes: specifically, latitude ~40°S and longitude ~67°W. The red arrow indicated the propagation direction the MSTID observed. It is obvious that the propagation direction of the MSTID and the source region are not correlated, besides, the distance from the point source to the point of observation is ~5750 km. This means that, the primary gravity waves generated at this source broke and generated a secondary (is also possible the secondary wave broke and tertiary wave generated) wave that excited the MSTID we observed in the equatorial region. The characteristics of the present work is the typical observational evidence of the TIDs excited by secondary and tertiary medium- and large-scale gravity waves that Vadas e Becker (2019) calculated.

Figure 6.6 - MSTIDs observed on the July 1st, 2014 at 15:03:00 UT (12:30:00 LT) propagating to north-northeastward (left column). The possible center (indicated with a blue star) of this MSTIDs is located around latitude 35°-50°S and longitude 65°-70°W. The circles are just to reinforce the clarity of the concentric structure of the MSITD and the blue short dashes arrow denotes the propagation direction. Cloud top brightness temperature (CTBT) below -50°C (right column) on 1st July, 2014. The red arrows on cloud top brightness temperature map indicate the propagation direction of the MSTID observed on the aforementioned days

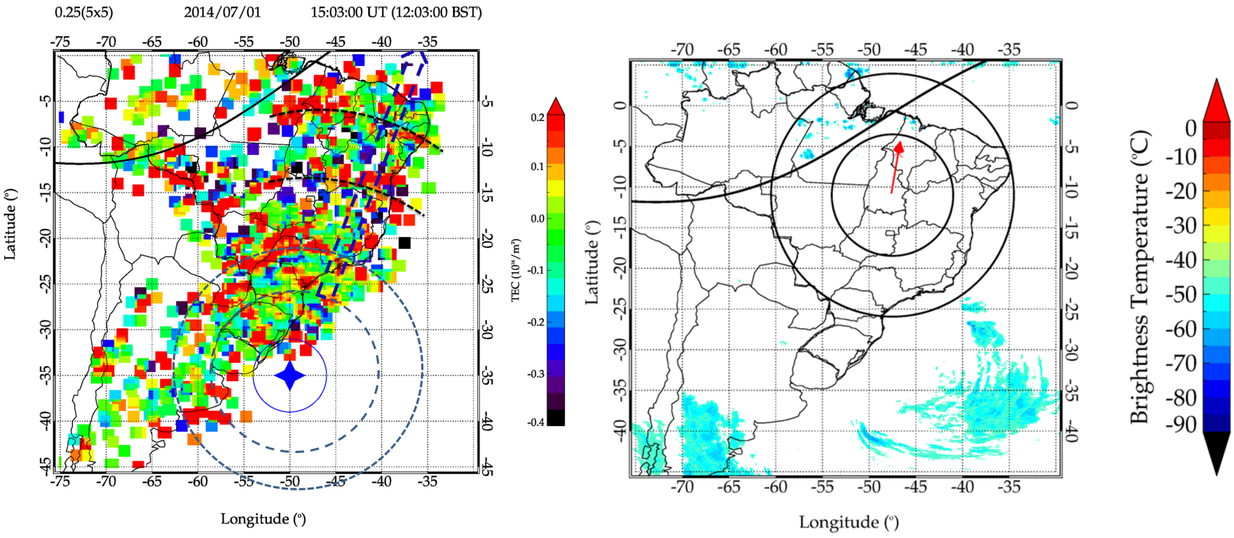

6.6 Summary of the Discussion II

Using the cloud top brightness temperature data from GOES 13 and 16 as a proxy for tropospheric deep convection, we have successfully located the possible primary sources and excitation mechanisms of the MSTIDs observed over the South American equatorial region between January 2014 to December 2019. The experiment was based on the correlation of the MSTIDs propagation directions pointing to meteorological sources that generated the likely gravity waves, which in turn excited the MSTIDs.

- Among others we found out that; on the 1st October, 2017, the MSTID propagated south-eastward and the possible source region is located around 7° to 12°S and 55° to 60° W over the Amazon region; on 30th June and 8th November, 2015, the possible source region of the MSTID which propagated north-northwestward located over the low latitude around 20° to 25° S and 50° to 60° W; and on 8th November 2015, the MSTID propagated north-northwestward the source region is located within the equatorial region around 10° to 15°S and 45° to 50° W.

- We investigated the seasonal variation of the sources regions of the observed equatorial MSTIDs. We realized that there are deep convective cells associated with cumulus nimbus clouds within the South American equatorial region in summer, spring and autumn/fall that are capable of generating gravity waves to excite the MSTIDs observed. However, some of the propagation directions of the observed MSTIDs did not correlate with the sources, which implies that those MSTIDs might have been excited by secondary or tertiary gravity waves. Moreover, in winter, convection clouds are located in the low latitude (around ∼20°) emanating from the midlatitude, which correlate well with the MSTIDs that propagated to north-northwestward and north-northwestward. We showed observational evidence of MSTID having concentric ring structure that were probably excited by medium- and large-scale secondary or tertiary gravity waves at the east of Southern Andes and propagated to the northeast of South American equatorial region on 1st July, 2014 at 15:03:00 UT (12:30:00 LT).

- Using the images from GOES 13 in the infrared (IR) and reanalysis data such as Outgoing Longwave Radiation (OLR), zonal(u (m/s)), meridional (v(m/s)) and the vertical (omega (Pa/s)) components of wind variables, we located the ITCZ position, the ascending humidity, vertical velocity and the divergence of the winds. The day-to-day variations of ITCZ as the possible source of equatorial MSTIDs have done; for instance, on; 5th of January 2016, 1st of January 2017 and 29th of January 2017, we also observed MSTID oscillations propagating to south-southeastward and correlating with the corresponding ITCZ positions.

- We found that in summer and fall/autumn, the average position of the ITCZ were located around latitude ∼0°, which is within the study area, hence, have more MSTID activities propagating to south-southeast direction, possibly as a result of the primary source location being located within the study area. Meanwhile, in winter, the ITCZ position was located around ∼5° and ∼10°N respectively, hence, we observed few MSTID events in these seasons propagating to the south-southeastward.

7 CONCLUSION

7.1 Conclusion

This chapter presents the outcome and summary of the present work and recommendation for the future research. The present work is the study on the MSTIDs over the South American equatorial region during solar cycle 24 (from January 2014 to December 2019) using GNSS (GPS and GLONASS specifically) TEC perturbation maps. First, we improve on the methodology of Figueiredo et al. (2018a) by including GLONASS data in order to develop detrending TEc maps and keograms to identify and characterize the day-to-day MSTID events. For the first time over South American region, we thoroughly studied the statistical analysis of the occurrence rate of MSTIDs during the solar maximum phase, descending phase and minimum phase as well as the long term seasonal variability of occurrence of the MSTIDs, their horizontal wavelengths, periods, phase velocities and propagation direction. The comparative study of the MSTID characteristics between the equatorial (present work) and low to mid latitude among others Figueiredo et al. (2018a), Otsuka et al. (2011), MacDougall et al. (2011) and Kotake et al. (2006) have also been discussed thoroughly. Finally, we investigated the possible source locations and generation mechanisms of the present equatorial MSTIDs for the first time.

- A total of 742 MSTIDs was observed from January 2014 to December 2019. Among them, 712 MSTIDs representing ∼96% were observed during geomagnetic quiet time when the Dst was less than 50 nT. The six-year observation of MSTIDs shows strong positive correlation with the solar activity. We observed 322, 251 and 171 MSTID events during solar maximum (2014-2015), descending (2016-2017) and minimum (2018-2019) which represent 43.3%, 33.7% and 23.0%. The positive correlation might have been caused by the variations of thermospheric temperature during the solar phases. We realized that gravity waves dissipate due to high viscosity in the thermosphere as a result of low thermospheric temperature which occur during solar minimum (VADAS, 2007): On the other hand, during solar maximum when the thermospheric temperature is high, the viscosity is low, hence occurred low dissipation of gravity waves.

- The seasonal statistics of the MSTID occurrence rate are 307, 106 and 329 events for equinoxes, summer, and winter respectively. The neutral wind velocity observed by Fisher et al. (2015) and Makela et al. (2013) are high in summer and low in winter. Consequently, there is high wind filtering in summer than winter which explains the seasonal variation of MSTIDs. This account for why the MSTIDs almost disappear in summer and mostly appear in winter. The summer mean horizontal wavelength, period and phase speed are larger than that of winter. This is might be due to the fact that, only MSTIDs events with long horizontal wavelength and fast phase speeds survived the critical level and dissipative filtering during summer.

- The present equatorial MSTIDs have long wavelengths, high velocities and period ranging from 300 - 1300 km, 100 - 700 m/s and 20 - 60 min with maximum peak at 500 and 800 km, 200 to 400 m/s and 30 to 45 min respectively, compare to the previous works conducted in low and midlatitude MSTIDs. Some of them might have likely been induced by the secondary or tertiary gravity waves created in the thermosphere from the dissipation of primary gravity waves that were excited from deep convection in the troposphere (VADAS; FRITTS, 2006; VADAS; CROWLEY, 2010; VADAS; BECKER, 2019). The mean horizontal wavelength for summer, equinoxes and winter are 719 ± 163 ,705 ± 120 and 628 ± 114 km respectively; the mean phase velocities 309 ± 78, 317 ± 85 and 291 ± 66 m/s, respectively; the mean periods for summer, equinoxes and winter are 37 ± 7 , 39 ± 7 and 34 ± 6 min respectively. The summer mean of all the characteristics of the present work is higher than that of winter, which was due to high dissipation and filtering rate in former than latter. Consequently, only MSTIDs events with long horizontal wavelength and fast phase speeds consequently survived dissipation and filtering process.

- We found out that the MSTIDs were highly dependence on the local time; the daytime and evening account for ∼70% and ∼28% of the total observation while the nighttime account for only ∼2%. The daytime MSTIDs occurred frequently in winter with the secondary peak in equinox, while the evening time MSTIDs occurred in summer and equinox. The dependency of the MSTIDs on the local time was attributed to the mechanisms generating them and the medium at which they propagated.

- There are three preferential propagation direction of the present MSTIDs; north-northeastward, north-northwestward and south-southeastward. Moreover, in equinox and summer evening time, a few MSTIDs propagating westward. The anisotropy of the propagation direction is due to the wind, dissipative filtering effects, ion drag effects that favors MSTIDs propagating equatorward along the magnetic field lines, the primary source region and the presence of the secondary or tertiary gravity waves in the thermosphere.

- There is strong link between the MSTIDs propagating to north-northeastward and north-northwestward of the Figueiredo et al. (2018a) and the present work especially, during winter and equinox. Also, MSTIDs observed by MacDougall et al. (2011) and the present have the same propagation directions. The present and the aforementioned works have high occurrence rate in winter daytime and secondary peak in equinox and a few events in summer. Among them, only the present work considered a detailed statistical analysis of MSTIDs and the solar cycle. Concerning the characteristics, the present equatorial MSTIDs have long wavelengths (300 - 1300 km m/s) and high phase velocities (100 - 700 m/s) compare to the former. They were likely induced by the secondary or tertiary gravity waves created in the thermosphere from the dissipation of primary gravity waves that were excited from deep convection in the troposphere (VADAS; CROWLEY, 2010).

- With regard to the sources region of the present equatorial MSTIDs, we used the cloud top brightness temperature data from GOES 13 and 16 as a proxy for tropospheric deep convection to locate the possible primary sources and excitation mechanisms. The experiment was based on the correlation of the MSTIDs propagation directions pointing to meteorological sources that generated the likely gravity waves, which in turn excited the MSTIDs. Among others, we found out that; on the 1st October, 2017, the MSTID propagated south-eastward and the possible source region is located around 7° to 12°S and 55° to 60° W over the Amazon region; on 30th June and 8th November, 2015, the possible source region of the MSTID which propagated north-northwestward located over the low latitude around 20° to 25° S and 50° to 60° W; and on 8th November 2015, the MSTID propagated north-northwestward the source region is located within the equatorial region around 10° to 15°S and 45° to 50° W.

- We also investigated the seasonal variation of the sources regions of the observed equatorial MSTIDs. We realized that there are deep convective cells associated with cumulus nimbus clouds within the South American equatorial region in summer, spring and autumn/fall that are capable of generating gravity waves to excite the MSTIDs observed. However, some of the propagation directions of the observed MSTIDs did not correlate with the source regions. This implies that those MSTIDs might have been excited by secondary or tertiary gravity waves. Moreover, in winter, convection clouds are located in the low to midlatitude (around ∼20°) emanating from the midlatitude, which correlate well with the MSTIDs that propagated to north-northeastward and north-northwestward. We showed observational evidence of MSTID having concentric ring structure that were probably excited by medium- and large-scale secondary or tertiary gravity waves at the east of Southern Andes and propagated to the northeast of South American equatorial region on 1st July, 2014 at 15:03:00 UT (12:30:00 LT).

- Using the images from GOES 13 in the infrared (IR) and reanalysis data such as Outgoing Longwave Radiation (OLR), zonal(u (m/s)), meridional (v(m/s)) and the vertical (omega (Pa/s)) components of wind variables, we located the ITCZ position, the ascending humidity, vertical velocity and the divergence of the winds. The day-to-day variations of ITCZ as the possible source of equatorial MSTIDs have done; for instance, on; 5th of January 2016, 1st of January 2017 and 29th of January 2017, we also observed MSTID oscillations propagating to south-southeastward and correlating with the corresponding ITCZ positions.
- We found that in summer and fall/autumn, the average position of the ITCZ were located around latitude ∼0°, which is within the study area, hence, have more MSTID activities propagating to south-southeast direction, possibly as a result of the primary source location being located within the study area. Meanwhile, in winter and the ITCZ position was located around ∼5° and ∼10°N respectively, hence, we observed few MSTID events in these seasons propagating to the south-southeastward.

7.2 Recommendation for the future work

With regard to future research on MSTIDs, we recommend that:

- The sources of the present equatorial MSTIDs traced to clear the discrepancies surrounding primary, secondary or tertiary gravity waves. In addition, the presence of secondary and tertiary gravity waves in the mesosphere and thermosphere should be investigated as well as the interaction between the excitation mechanisms of MSTIDs.

- The study of solar terminator as a regular source of wave-like atmospheric and ionosphere disturbances started in the early 1970s (CROMBIE, 1964). This solar terminator excited MSTIDs in question propagated eastward and westward during the passing of the sunrise and sunset terminator, which is common in the midlatitude (MACDOUGALL et al., 2011; KOTAKE et al., 2007). Meanwhile, in the present work, we could not see any perfect examples matching the above claim. Therefore, we recommend a thorough research into the solar terminator excited MSTID in the equatorial region.

- We also observed that during the equinox and summer, when the solar terminator is aligned with the magnetic equator, some MSTIDs became a seed for equatorial plasma bubbles Takahashi et al. (2018). We recommend for a future study on the seeding process between of the plasma bubbles by MSTIDs.

- Narayanan et al. (2014) reported that the nighttime MSTIDs disappearance was associated to the interaction with the EIA crest region. Since EIA is more pronounced during the daytime, we recommend for thorough statistical analysis between daytime EIA and MSTIDs.

- Last but not the least, we hope to extend the present study to the African continent for studying the conspicuous differences that exist between the ionospheres over the two continents. It is believing that this study will be able to unravel the effect of gravity waves and, MSTIDs in producing these differences.

REFERENCES

ABDU, M. A. Electrodynamics of ionospheric weather over low latitudes. **Geoscience Letters**, v. 3, n. 1, p. 11, 2016. 2

AFRAIMOVICH, E. L.; EDEMSKIY, I. K.; LEONOVICH, A. S.; LEONOVICH, L. A.; VOEYKOV, S. V.; YASYUKEVICH, Y. V. Mhd nature of night-time mstids excited by the solar terminator. **Geophysical Research Letters**, v. 36, n. 15, 2009. 108

AGGARWAL, M.; JOSHI, H.; IYER, K. Solar activity dependence of electron and ion temperatures using sross c2 rpa data and comparison with iri model. **Journal of Atmospheric and Solar-Terrestrial Physics**, v. 69, n. 7, p. 860–874, 2007. 116

AGGARWAL, M.; JOSHI, H.; IYER, K.; JIVANI, M. Studies of electron and ion temperatures at 500 km altitude during sunrise using indian sross c2 satellite. **Advances in Space Research**, v. 43, n. 2, p. 273–281, 2009. 116

ALEXANDER, M. J.; PFISTER, L. Gravity wave momentum flux in the lower stratosphere over convection. **Geophysical Research Letters**, v. 22, n. 15, p. 2029–2032, 1995. 15

ALEXANDER, M. J.; VINCENT, R. A. Gravity waves in the tropical lower stratosphere: a model study of seasonal and interannual variability. **Journal of Geophysical Research: Atmospheres**, v. 105, n. D14, p. 17983–17993, 2000. 121

AMORIM, D. C. M.; PIMENTA, A. A.; BITTENCOURT, J. A.; FAGUNDES, P. R. Long-term study of medium-scale traveling ionospheric disturbances using oi 630 nm all-sky imaging and ionosonde over brazilian low latitudes. **Journal of Geophysical Research: Space Physics**, v. 116, n. A6, 2011. 3, 24

ASTAFYEVA, E. Ionospheric detection of natural hazards. **Reviews of Geophysics**, v. 57, n. 4, p. 1265–1288, 2019. 119

BACMEISTER, J. T.; SCHOEBERL, M. R. Breakdown of vertically propagating two-dimensional gravity waves forced by orography. **Journal of the Atmospheric Sciences**, v. 46, n. 14, p. 2109–2134, 1989. 136

BALAN, N.; BAILEY, G. J.; ABDU, M. A.; OYAMA, K. I.; RICHARDS, P. G.; MACDOUGALL, J.; BATISTA, I. S. Equatorial plasma fountain and its effects over three locations: evidence for an additional layer, the f3 layer. **Journal of Geophysical Research: Space Physics**, v. 102, n. A2, p. 2047–2056, 1997. 13

BANKS, P.; KOCKARTS, G. **Aeronomy, Part B**. 1973. 175-186 p. 22

BANKS, P. M.; SCHUNK, R. W.; RAITT, W. J. No+ and o+ in the high latitude f-region. **Geophysical Research Letters**, v. 1, n. 6, p. 239–242, 1974. 9

BARROS, D.; TAKAHASHI, H.; WRASSE, C. M.; FIGUEIREDO, C. A. O. Characteristics of equatorial plasma bubbles observed by tec map based on ground-based gnss receivers over south america. **Annales Geophysicae**, v. 36, n. 1, p. 91–100, 2018. 99, 100

BASU, S. et al. Ionospheric effects of major magnetic storms during the international space weather period of september and october 1999:GPS observations,VHF/UHF scintillations, and in situ density structures at middle and equatorial latitudes. **Journal of Geophysical Research: Space Physics**, v. 106, n. A12, p. 30389–30413, 2001. 56

BATISTA, I. S.; ABDU, M. A.; MEDRANO, R. A. Magnetic activity effects on range type spread-f and vertical plasma drifts at fortaleza and huancayo as studied through ionosonde measurements and theoretical modelling. **Annales of Geophysicae**, v. 8, p. 357–364, 1990. 95

BEHNKE, R. F layer height bands in the nocturnal ionosphere over arecibo. **Journal of Geophysical Research: Space Physics**, v. 84, n. A3, p. 974–978, 1979. 24

BEVINGTON, P. R.; ROBINSON, D. K.; BLAIR, J. M.; MALLINCKRODT, A. J.; MCKAY, S. Data reduction and error analysis for the physical sciences. **Computers in Physics**, v. 7, n. 4, p. 415–416, 1993. 65

BOND, D. J.; CHRZANOWSKI, A.; KIM, D. **Bringing GPS into harsh environments for deformation monitoring**. [S.l.: s.n.], 2007. 49

BOOKER, J. R.; BRETHERTON, F. P. The critical layer for internal gravity waves in a shear flow. **Journal of Fluid Mechanics**, v. 27, n. 3, p. 513–539, 1967. 99

BOROVSKY, J. E.; SHPRITS, Y. Y. Is the dst index sufficient to define all geospace storms? **Journal of Geophysical Research: Space Physics**, v. 122, n. 11, p. 11–543, 2017. 83

BOSSERT, K.; KRUSE, C. G.; HEALE, C. J.; FRITTS, D. C.; WILLIAMS, B. P.; SNIVELY, J. B.; PAUTET, P.-D.; TAYLOR, M. J. Secondary gravity wave generation over new zealand during the deepwave campaign. **Journal of Geophysical Research: Atmospheres**, v. 122, n. 15, p. 7834–7850, 2017. 136

BOUCHER, C.; ALTAMIMI, Z. Itrs, pz-90 and wgs 84: current realizations and the related transformation parameters. **Journal of Geodesy**, Springer, v. 75, n. 11, p. 613–619, 2001. 54

BOWMAN, G. G. A review of some recent work on mid-latitude spread-f occurrence as detected by ionosondes. **Journal of Geomagnetism and Geoelectricity**, v. 42, n. 2, p. 109–138, 1990. 113

BRETHERTON, F. P. The propagation of groups of internal gravity waves in a shear flow. **Quarterly Journal of the Royal Meteorological Society**, v. 92, n. 394, p. 466–480, 1966. 108

BRISTOW, W. A.; GREENWALD, R. A. Multiradar observations of medium-scale acoustic gravity waves using the super dual auroral radar network. **Journal of Geophysical Research: Space Physics**, v. 101, n. A11, p. 24499–24511, 1996. 103, 110

CAI, C.; GAO, Y. A combined gps/glonass navigation algorithm for use with limited satellite visibility. **The Journal of Navigation**, v. 62, n. 4, p. 671–685, 2009. 54

CANDIDO, C. M. N.; PIMENTA, A. A.; BITTENCOURT, J. A.; BECKER-GUEDES, F. Statistical analysis of the occurrence of medium-scale traveling ionospheric disturbances over brazilian low latitudes using oi 630.0 nm emission all-sky images. **Geophysical Research Letters**, v. 35, n. 17, 2008. 3, 4, 24, 113

CHEN, G.; ZHOU, C.; LIU, Y.; ZHAO, J.; TANG, Q.; WANG, X.; ZHAO, Z. A statistical analysis of medium-scale traveling ionospheric disturbances during 2014-2017 using the hong kong cors network. **Earth, Planets and Space**, v. 71, n. 1, p. 1–14, 2019. 93, 103, 109

CHIMONAS, G. The equatorial electrojet as a source of long period travelling ionospheric disturbances. **Planetary and Space Science**, v. 18, n. 4, p. 583–589, 1970. 85

CHOU, M.-Y.; LIN, C. C.; HUBA, J. D.; LIEN, C.-P.; CHEN, C.-H.; YUE, J.; CHANG, L. C.; RAJESH, P. Numerical modeling of the concentric gravity wave seeding of low-latitude nighttime medium-scale traveling ionospheric disturbances. **Geophysical Research Letters**, v. 45, n. 13, p. 6390–6399, 2018. 3

CITEAU, J.; FINAUD, L.; CAMMAS, J.; GOURIOU, Y. Questions about the itcz migration over the tropical atlantic sea surface temperature in the gulf of guinea and the runoff of senegal river. Available from:
https://horizon.documentation.ird.fr/exl-
doc/pleins$_textes/pleins_textes_5/b_fdi_01/010016342.pdf$, 1986. 26

CLEMESHA, B.; MEDEIROS, A. D.; GOBBI, D.; TAKAHASHI, H.; BATISTA, P.; TAYLOR, M. J. Multiple wavelength optical observations of a long-lived meteor trail. **Geophysical Research Letters**, v. 28, n. 14, p. 2779–2782, 2001. 95

COLE, K. D.; HICKEY, M. P. Energy transfer by gravity wave dissipation. **Advances in Space Research**, v. 1, n. 12, p. 65–75, 1981. 100, 114

COUNTERMEASURES for [GPS. In: . [S.l.: s.n.]. 48

COWLING, D.; WEBB, H.; YEH, K. Group rays of internal gravity waves in a wind-stratified atmosphere. **Journal of Geophysical Research**, v. 76, n. 1, p. 213–220, 1971. 108

CROMBIE, D. Periodic folding of vlf signals received over long paths during sunrise ond sunset. **Journal of Research of the National Bureau of Standards: Mathematics and Mathematical Physics**, v. 68, p. 27, 1964. 145

CROWLEY, G.; AZEEM, I. Extreme ionospheric storms and their effects on gps systems. In: **Extreme events in geospace**. [S.l.: s.n.], 2018. p. 555–586. 4, 110, 113, 120, 121

CROWLEY, G.; JONES, T.; DUDENEY, J. Comparison of short period tid morphologies in antarctica during geomagnetically quiet and active intervals. **Journal of Atmospheric and Terrestrial Physics**, v. 49, n. 11-12, p. 1155–1162, 1987. 85, 99

DING, F.; WAN, W.; XU, G.; YU, T.; YANG, G.; WANG, J.-s. Climatology of medium-scale traveling ionospheric disturbances observed by a gps network in central china. **Journal of Geophysical Research: Space Physics**, v. 116, n. A9, 2011. 101

DROB, D. P. et al. An update to the horizontal wind model (hwm): the quiet time thermosphere. **Earth and Space Science**, v. 2, n. 7, p. 301–319, 2015. 99

EBEL, A. Contributions of gravity waves to the momentum, heat and turbulent energy budget of the upper mesosphere and lower thermosphere. **Journal of Atmospheric and Terrestrial Physics**, v. 46, n. 9, p. 727–737, 1984. 15

EHARD, B.; ACHTERT, P.; DÖRNBRACK, A.; GISINGER, S.; GUMBEL, J.; KHAPLANOV, M.; RAPP, M.; WAGNER, J. Combination of lidar and model data for studying deep gravity wave propagation. **Monthly Weather Review**, v. 144, n. 1, p. 77–98, 2016. 136

ESSIEN, P.; PAULINO, I.; WRASSE, C. M.; CAMPOS, J. A. V.; PAULINO, A. R.; MEDEIROS, A. F.; BURITI, R. A.; TAKAHASHI, H.; AGYEI-YEBOAH, E.; LINS, A. N. Seasonal characteristics of small-and medium-scale gravity waves in the mesosphere and lower thermosphere over the brazilian equatorial region. v. 36, n. 3, p. 899–914, 2018. 15, 58, 98, 99, 100, 113, 122

EVANS, J. V.; HOLT, J. M.; WAND, R. H. A differential-doppler study of traveling ionospheric disturbances from millstone hill. **Radio Science**, v. 18, n. 3, p. 435–451, 1983. 24

EVANS, J. V.; WAND, R. H. Traveling ionospheric disturbances detected by uhf angle-of-arrival measurements. **Journal of Atmospheric and Terrestrial Physics**, Elsevier, v. 45, n. 4, p. 255–265, 1983. 24

FIGUEIREDO, C.; TAKAHASHI, H.; WRASSE, C.; OTSUKA, Y.; SHIOKAWA, K.; BARROS, D. Medium-scale traveling ionospheric disturbances observed by detrended total electron content maps over brazil. **Journal of Geophysical Research: Space Physics**, v. 123, n. 3, p. 2215–2227, 2018. xviii, 3, 5, 6, 24, 32, 41, 55, 56, 58, 60, 87, 93, 96, 97, 98, 101, 102, 103, 107, 109, 118, 120, 122, 133, 137, 141, 143

FIGUEIREDO, C. A. O. B.; TAKAHASHI, H.; WRASSE, C. M.; OTSUKA, Y.; SHIOKAWA, K.; BARROS, D. Investigation of nighttime mstids observed by optical thermosphere imagers at low latitudes: Morphology, propagation direction, and wind filtering. **Journal of Geophysical Research: Space Physics**, 2018. 3

FIGUEIREDO, C. A. O. B.; WRASSE, C. M.; TAKAHASHI, H.; OTSUKA, Y.; SHIOKAWA, K.; BARROS, D. Large-scale traveling ionospheric disturbances observed by gps dtec maps over north and south america on saint patrick's day storm in 2015. **Journal of Geophysical Research: Space Physics**, v. 122, n. 4, p. 4755–4763, 2017. 14, 15, 24, 63, 86, 99, 100

FISHER, D. J.; MAKELA, J. J.; MERIWETHER, J. W.; BURITI, R. A.; BENKHALDOUN, Z.; KAAB, M.; LAGHERYEB, A. Climatologies of nighttime thermospheric winds and temperatures from fabry-perot interferometer measurements: from solar minimum to solar maximum. **Journal of Geophysical Research: Space Physics**, v. 120, n. 8, p. 6679–6693, 2015. 95, 99, 100, 110, 111, 112, 116, 117, 141

FORBES, J. M.; BRUINSMA, S. L.; MIYOSHI, Y.; FUJIWARA, H. A solar terminator wave in thermosphere neutral densities measured by the champ satellite. **Geophysical Research Letters**, v. 35, n. 14, 2008. 108

FRANCIS, S. H. A theory of medium-scale traveling ionospheric disturbances. **Journal of Geophysical Research**, v. 79, n. 34, p. 5245–5260, 1974. 85

______. Global propagation of atmospheric gravity waves: a review. **Journal of Atmospheric and Terrestrial Physics**, v. 37, n. 6-7, p. 1011IN91031–10301054, 1975. 15, 85

FREUND, J.; JACKA, F. Structure in the λ557. 7 nm [oi] airglow. **Journal of Atmospheric and Terrestrial Physics**, v. 41, n. 1, p. 25–31, 1979. 123

FRISSELL, N.; BAKER, J.; RUOHONIEMI, J.; GERRARD, A.; MILLER, E.; MARINI, J.; WEST, M.; BRISTOW, W. Climatology of medium-scale traveling ionospheric disturbances observed by the midlatitude blackstone superdarn radar. **Journal of Geophysical Research: Space Physics**, v. 119, n. 9, p. 7679–7697, 2014. 85

FRISSELL, N. A.; BAKER, J. B.; RUOHONIEMI, J. M.; GREENWALD, R. A.; GERRARD, A. J.; MILLER, E. S.; WEST, M. L. Sources and characteristics of medium-scale traveling ionospheric disturbances observed by high-frequency radars in the north american sector. **Journal of Geophysical Research: Space Physics**, v. 121, n. 4, p. 3722–3739, 2016. 85

FRITTS, D. C.; ALEXANDER, M. J. Gravity wave dynamics and effects in the middle atmosphere. **Reviews of Geophysics**, Wiley Online Library, v. 41, n. 1, 2003. 15, 16, 18, 121

FRITTS, D. C.; TSUDA, T.; VANZANDT, T. E.; SMITH, S. A.; SATO, T.; FUKAO, S.; KATO, S. Studies of velocity fluctuations in the lower atmosphere using the mu radar. part ii: momentum fluxes and energy densities. **Journal of the Atmospheric Sciences**, v. 47, n. 1, p. 51–66, 1990. 15

FUKUSHIMA, D.; SHIOKAWA, K.; OTSUKA, Y.; OGAWA, T. Observation of equatorial nighttime medium-scale traveling ionospheric disturbances in 630-nm airglow images over 7 years. **Journal of Geophysical Research: Space Physics**, v. 117, n. A10, 2012. 3, 122

GALUSHKO, V.; KASHCHEYEV, A.; KASHCHEYEV, S.; KOLOSKOV, A.; PIKULIK, I.; YAMPOLSKI, Y.; LITVINOV, V.; MILINEVSKY, G.; RAKUSA-SUSZCZEWSKI, S. Bistatic hf diagnostics of tids over the antarctic peninsula. **Journal of Atmospheric and Solar-Terrestrial Physics**, v. 69, n. 4-5, p. 403–410, 2007. 26

GARCIA, F.; KELLEY, M.; MAKELA, J.; HUANG, C.-S. Airglow observations of mesoscale low-velocity traveling ionospheric disturbances at midlatitudes. **Journal of Geophysical Research: Space Physics**, v. 105, n. A8, p. 18407–18415, 2000. 113

GARDNER, C. S. Introduction to aloha/anlc-93: The 1993 airborne lidar and observations of the hawaiian airglow/airborne noctilucent cloud campaigns. **Geophysical Research Letters**, v. 22, n. 20, p. 2789–2792, 1995. 132, 133

GENIO, A. D. D.; SCHUBERT, G.; STRAUS, J. M. Gravity wave propagation in a diffusively separated atmosphere with height-dependent collision frequencies. **Journal of Geophysical Research: Space Physics**, v. 84, n. A8, p. 4371–4378, 1979. 16

GEORGES, T. M.; HOOKE, W. H. Wave-induced fluctuations in ionospheric electron content: A model indicating some observational biases. **Journal of Geophysical Research**, v. 75, n. 31, p. 6295–6308, 1970. 120

GIRESSE, P. **Tropical and sub-tropical West Africa-marine and continental changes during the Late Quaternary**. [S.l.: s.n.], 2007. 126

GORAL, W.; SKORUPA, B. Determination of intermediate orbit and position of glonass satellites based on the generalized problem of two fixed centers. **Acta Geodynamica et Geromaterialia**, v. 9, n. 3, p. 283–291, 2012. 54

GOSSARD, E. E. Vertical flux of energy into the lower ionosphere from internal gravity waves generated in the troposphere. **Journal of Geophysical Research**, v. 67, n. 2, p. 745–757, 1962. 132

GOSSARD, E. E.; HOOKE, W. H. Waves in the atmosphere: atmospheric infrasound and gravity waves-their generation and propagation. **AtSc**, v. 2, 1975. 16, 17

GREENHOW, J. S. **Meteor trail measurements by radio echo detection means.** [S.l.: s.n.], 1958. 113

GREWAL, M. S.; WEILL, L. R.; ANDREWS, A. P. **Global positioning systems, inertial navigation, and integration**. [S.l.: s.n.], 2007. 48

GRIMSDELL, A. W.; ALEXANDER, M. J.; MAY, P. T.; HOFFMANN, L. Model study of waves generated by convection with direct validation via satellite. **Journal of the Atmospheric Sciences**, v. 67, n. 5, p. 1617–1631, 2010. 121

GROCOTT, A.; HOSOKAWA, K.; ISHIDA, T.; LESTER, M.; MILAN, S. E.; FREEMAN, M. P.; SATO, N.; YUKIMATU, A. S. Characteristics of medium-scale traveling ionospheric disturbances observed near the antarctic peninsula by hf radar. **Journal of Geophysical Research: Space Physics**, v. 118, n. 9, p. 5830–5841, 2013. 85

GUTMAN, G. J.; SCHWERDTFEGER, W. The role of latent and sensible heat for the development of a high pressure system over the subtropical andes. **Meteorologische Rundschau**, v. 18, n. 3, 1965. 129

HAGER, B. H.; KING, R. W.; MURRAY, M. H. Measurement of crustal deformation using the global positioning system. **Annual Review of Earth and Planetary Sciences**, v. 19, n. 1, p. 351–382, 1991. 49

HARGREAVES, J. K. **The solar-terrestrial environment: an introduction to geospace-the science of the terrestrial upper atmosphere, ionosphere, and magnetosphere**. [S.l.: s.n.], 1992. 9

HE, L. S.; DYSON, P.; PARKINSON, M.; WAN, W. Studies of medium scale travelling ionospheric disturbances using tiger superdarn radar sea echo observations. **Annales Geophysicae**, v. 22, p. 4077–4088, 2004. 85

HEALE, C.; BOSSERT, K.; SNIVELY, J. B.; FRITTS, D.; PAUTET, P.-D.; TAYLOR, M. J. Numerical modeling of a multiscale gravity wave event and its airglow signatures over mount cook, new zealand, during the deepwave campaign. **Journal of Geophysical Research: Atmospheres**, v. 122, n. 2, p. 846–860, 2017. 136

HEALE, C.; SNIVELY, J.; HICKEY, M.; ALI, C. Thermospheric dissipation of upward propagating gravity wave packets. **Journal of Geophysical Research: Space Physics**, v. 119, n. 5, p. 3857–3872, 2014. 16

HEALE, C. J.; BOSSERT, K.; VADAS, S.; HOFFMANN, L.; DÖRNBRACK, A.; STOBER, G.; SNIVELY, J.; JACOBI, C. Secondary gravity waves generated by breaking mountain waves over europe. **Journal of Geophysical Research: Atmospheres**, v. 125, n. 5, p. e2019JD031662, 2020. 126

HEELIS, R. Electrodynamics in the low and middle latitude ionosphere: a tutorial. **Journal of Atmospheric and Solar-Terrestrial Physics**, v. 66, n. 10, p. 825–838, 2004. 9, 10, 11

HEELIS, R. A.; KENDALL, P. C.; MOFFETT, R. J.; WINDLE, D. W.; RISHBETH, H. Electrical coupling of the e-and f-regions and its effect on f-region drifts and winds. **Planetary and Space Science**, v. 22, n. 5, p. 743–756, 1974. 12

HERNANDEZ-PAJARES, M.; JUAN, J. M.; SANZ, J. Medium-scale traveling ionospheric disturbances affecting gps measurements: Spatial and temporal analysis. **Journal of Geophysical Research: Space Physics**, v. 111, n. A7, 2006. 1

HERNANDEZ-PAJARES, M.; JUAN, J. M.; SANZ, J.; ARAGON-ANGEL, A. Propagation of medium-scale traveling ionospheric disturbances at different latitudes and solar cycle conditions. **Radio Science**, v. 47, n. 6, 2012. 112

HICKEY, M.; COLE, K. A numerical model for gravity wave dissipation in the thermosphere. **Journal of Atmospheric and Terrestrial Physics**, v. 50, n. 8, p. 689–697, 1988. 16

HINES, C. O. Internal atmospheric gravity waves at ionospheric heights. **Canadian Journal of Physics**, v. 38, n. 11, p. 1441–1481, 1960. 1, 13, 15, 16, 18, 98, 103, 113, 120, 121, 132

HINES, C. O.; REDDY, C. A. On the propagation of atmospheric gravity waves through regions of wind shear. **Journal of Geophysical Research**, Wiley Online Library, v. 72, n. 3, p. 1015–1034, 1967. 132

HOFFMANN, L.; XUE, X.; ALEXANDER, M. A global view of stratospheric gravity wave hotspots located with atmospheric infrared sounder observations. **Journal of Geophysical Research: Atmospheres**, v. 118, n. 2, p. 416–434, 2013. 126

HOFMANN-WELLENHOF, B.; LICHTENEGGER, H.; WASLE, E. **GNSS-global navigation satellite systems: GPS, GLONASS, Galileo, and more**. [S.l.]: Springer Science & Business Media, 2007. 49

HOOKE, W. H. Ionospheric irregularities produced by internal atmospheric gravity waves. **Journal of Atmospheric and Terrestrial Physics**, v. 30, n. 5, p. 795–823, 1968. 15, 98, 103, 120

______. The ionospheric response to internal gravity waves: 1. the f2 region response. **Journal of Geophysical Research**, v. 75, n. 28, p. 5535–5544, 1970. 107

HOREL, J. D.; HAHMANN, A. N.; GEISLER, J. E. An investigation of the annual cycle of convective activity over the tropical americas. **Journal of Climate**, v. 2, n. 11, p. 1388–1403, 1989. 130

HUANG, C.-S.; KELLEY, M. C. Nonlinear evolution of equatorial spread f: 1. on the role of plasma instabilities and spatial resonance associated with gravity wave seeding. **Journal of Geophysical Research: Space Physics**, v. 101, n. A1, p. 283–292, 1996. 41

HUMPHREYS, T. E.; LEDVINA, B. M.; PSIAKI, M. L.; O'HANLON, B. W.; KINTNER, P. M. Assessing the spoofing threat: Development of a portable GPS civilian spoofer. In: **RADIONAVIGATION LABORATORY CONFERENCE, 2008. Proceedings...** [S.l.: s.n.], 2008. 50

HUNSUCKER, R. D. Atmospheric gravity waves generated in the high-latitude ionosphere: a review. **Reviews of Geophysics**, v. 20, n. 2, p. 293–315, 1982. 13

HURSKAINEN, H.; LOHAN, E. S.; HU, X.; RAASAKKA, J.; NURMI, J. Multiple gate delay tracking structures for gnss signals and their evaluation with simulink, systemc, and vhdl. **International Journal of Navigation and Observation**, v. 2008, 2008. 50

HUSIN, A.; ABDULLAH, M.; MOMANI, M. Observation of medium-scale traveling ionospheric disturbances over peninsular malaysia based on ipp trajectories. **Radio Science**, v. 46, n. 02, p. 1–10, 2011. 3, 24, 28

INOUE, T.; SATOH, M.; MIURA, H.; MAPES, B. Characteristics of cloud size of deep convection simulated by a global cloud resolving model over the western tropical pacific. **Journal of the Meteorological Society of Japan. Ser. II**, v. 86, p. 1–15, 2008. 122

IVANOV-KHOLODNY, G. S.; MIKHAILOV, A. V. **The prediction of ionospheric conditions**. [S.l.: s.n.], 2012. 51

JACOBSON, A. R.; CARLOS, R. C.; MASSEY, R. S.; WU, G. Observations of traveling ionospheric disturbances with a satellite-beacon radio interferometer: Seasonal and local time behavior. **Journal of Geophysical Research: Space Physics**, v. 100, n. A2, p. 1653–1665, 1995. 24

JONAH, O. F.; KHERANI, E. A.; PAULA, E. R. D. Observation of tec perturbation associated with medium-scale traveling ionospheric disturbance and possible seeding mechanism of atmospheric gravity wave at a brazilian sector. **Journal of Geophysical Research: Space Physics**, v. 121, n. 3, p. 2531–2546, 2016. 3, 24, 68

______. Investigations of conjugate mstids over the brazilian sector during daytime. **Journal of Geophysical Research: Space Physics**, v. 122, n. 9, p. 9576–9587, 2017. 3, 24, 29

KAROLY, D.; ROFF, G.; REEDER, M. Gravity wave activity associated with tropical convection detected in toga coare sounding data. **Geophysical Research Letters**, v. 23, n. 3, p. 261–264, 1996. 121

KAWAMURA, S.; BALAN, N.; OTSUKA, Y.; FUKAO, S. Annual and semiannual variations of the midlatitude ionosphere under low solar activity. **Journal of Geophysical Research: Space Physics**, v. 107, n. A8, p. SIA–8, 2002. 116

KELLEY, M. C. **The Earth's ionosphere: plasma physics and electrodynamics**. [S.l.: s.n.], 2009. 12

KELLEY, M. C.; MAKELA, J. J.; SAITO, A.; APONTE, N.; SULZER, M.; GONZÁLEZ, S. A. On the electrical structure of airglow depletion/height layer bands over arecibo. **Geophysical Research Letters**, v. 27, n. 18, p. 2837–2840, 2000. 120, 121

KELLEY, M. C.; MILLER, C. A. Electrodynamics of midlatitude spread f 3. electrohydrodynamic waves? a new look at the role of electric fields in thermospheric wave dynamics. **Journal of Geophysical Research: Space Physics**, v. 102, n. A6, p. 11539–11547, 1997. 102, 103, 104

KELLY, M. C. The earth's ionosphere. **International Geophysics Series**, v. 43, p. 71, 1989. 9

KERTZ, W. Ring current variations during the igy. **Annual International Geophysical Year**, v. 35, 1964. 83

KIM, J.; MAHRT, L. Momentum transport by gravity waves. **Journal of the Atmospheric Sciences**, v. 49, n. 9, p. 735–748, 1992. 15

KINTNER, P. M.; LEDVINA, B. M.; PAULA, E. R. D. Gps and ionospheric scintillations. **Space Weather**, v. 5, n. 9, 2007. 4

KIRCHENGAST. **Keo Science ltd**, Available from :http://www.keoscientific.com/about.php. 2018. Access in: 21 Dec. 2017., p. 49–50. 21, 24

KLOSTERMEYER, J. Numerical calculation of gravity wave propagation in a realistic thermosphere. **Journal of Atmospheric and Terrestrial Physics**, v. 34, n. 5, p. 765–774, 1972. 21

KODAMA, Y. Large-scale common features of subtropical precipitation zones (the baiu frontal zone, the spcz, and the sacz) part i: characteristics of subtropical frontal zones. **Journal of the Meteorological Society of Japan. Ser. II**, v. 70, n. 4, p. 813–836, 1992. 130

KOMJATHY, A. **Global ionospheric total electron content mapping using the Global Positioning System**. Tese (Doutorado) — University of New Brunswick Fredericton, New Brunswick, Canada, 1997. 11, 49

KOTAKE, N.; OTSUKA, Y.; OGAWA, T.; TSUGAWA, T.; SAITO, A. Statistical study of medium-scale traveling ionospheric disturbances observed with the gps networks in southern california. **Earth, Planets and Space**, v. 59, n. 2, p. 95–102, 2007. 1, 56, 87, 93, 100, 101, 107, 108, 109, 120, 121, 145

KOTAKE, N.; OTSUKA, Y.; TSUGAWA, T.; OGAWA, T.; SAITO, A. Climatological study of gps total electron content variations caused by medium-scale traveling ionospheric disturbances. **Journal of Geophysical Research: Space Physics**, Wiley Online Library, v. 111, n. A4, 2006. 5, 6, 33, 38, 39, 54, 55, 103, 112, 141

KOUSKY, V. E. Pentad outgoing longwave radiation climatology for the south american sector. **Revista Brasileira de Meteorologia**, v. 3, n. 1, p. 217–231, 1988. 129

KRALL, J.; HUBA, J. D.; OSSAKOW, S. L.; JOYCE, G.; MAKELA, J. J.; MILLER, E. S.; KELLEY, M. C. Modeling of equatorial plasma bubbles triggered by non-equatorial traveling ionospheric disturbances. **Geophysical Research Letters**, v. 38, n. 8, 2011. 3

KUBOTA, M.; SHIOKAWA, K.; EJIRI, M.; OTSUKA, Y.; OGAWA, T.; SAKANOI, T.; FUKUNISHI, H.; YAMAMOTO, M.; FUKAO, S.; SAITO, A. Traveling ionospheric disturbances observed in the oi 630-nm nightglow images over japan by using a multipoint imager network during the front campaign. **Geophysical Research Letters**, v. 27, n. 24, p. 4037–4040, 2000. 2

LANGLEY, R. B. Propagation of the GPS signals. In: **TEUNISSEN, P. J. G.; KLEUSBERG, A. (Ed.). GPS for geodesy**. [S.l.: s.n.], 1996. p. 103–140. 49

LEE, Y. C. New concept for independent GPS integrity monitoring. **Navigation**, v. 35, n. 2, p. 239–254, 1988. 48

LENTERS, J. D.; COOK, K. H. On the origin of the bolivian high and related circulation features of the South American climate. **Journal of the Atmospheric Sciences**, v. 54, n. 5, p. 656–678, 1997. 129

LIU, H.; LÜHR, H.; WATANABE, S. A solar terminator wave in thermospheric wind and density simultaneously observed by CHAMP. **Geophysical Research Letters**, v. 36, n. 10, 2009. 108

LIU, Y.; LI, Z.; FU, L.; WANG, J.; ZHANG, C. Studying the ionospheric responses induced by a geomagnetic storm in september 2017 with multiple observations in America. **GPS Solutions**, Springer, v. 24, n. 1, p. 3, 2020. 120

MACDOUGALL, J.; ABDU, M. A.; BATISTA, I.; BURITI, R.; MEDEIROS, A. F.; JAYACHANDRAN, P. T.; BORBA, G. Spaced transmitter measurements of medium scale traveling ionospheric disturbances near the equator. **Geophysical Research Letters**, v. 38, n. 16, 2011. 2, 5, 6, 14, 24, 26, 27, 41, 68, 85, 94, 95, 96, 101, 107, 118, 120, 121, 122, 132, 133, 141, 143, 145

MACDOUGALL, J.; JAYACHANDRAN, P. Solar terminator and auroral sources for traveling ionospheric disturbances in the midlatitude f region. **Journal of**

Atmospheric and Solar-Terrestrial Physics, v. 73, n. 17-18, p. 2437–2443, 2011. 108

MACDOUGALL, J.; LI, G.; JAYACHANDRAN, P. T. Traveling ionospheric disturbances near London, Canada. **Journal of Atmospheric and Solar-Terrestrial Physics**, v. 71, n. 17-18, p. 2077–2084, 2009. 14, 24, 99

MACHADO, C. S. Estudo de distúrbios ionosféricos propagantes de média escala no hemisfério sul utilizando técnicas óticas, de rádio e simulações numéricas. **Instituto Nacional de Pesquisas Espaciais (INPE) PhD Thesis**, 2017. 3

MADDEN R. A, N. G. R. P. J. Z. F. E. **TROPICAL METEOROLOGY AND CLIMATE: intraseasonal Oscillation (Madden-Julian Oscillation)**. 2015. 132-136 p. 127

MAKELA, J. J.; FISHER, D. J.; MERIWETHER, J. W.; BURITI, R. A.; MEDEIROS, A. F. Near-continual ground-based nighttime observations of thermospheric neutral winds and temperatures over equatorial brazil from 2009 to 2012. **Journal of Atmospheric and Solar-Terrestrial Physics**, v. 103, p. 94–102, 2013. 95, 99, 100, 111, 112, 116, 117, 141

MAKELA, J. J.; MILLER, E. S.; TALAAT, E. R. Nighttime medium-scale traveling ionospheric disturbances at low geomagnetic latitudes. **Geophysical Research Letters**, v. 37, n. 24, 2010. 2, 15, 95

MALIN, S.; BARRACLOUGH, D. R. Humboldt and the earth's magnetic field. **Quarterly Journal of the Royal Astronomical Society**, v. 32, p. 279, 1991. 83

MANNUCCI, A. J.; WILSON, B. D.; YUAN, D. N.; HO, C. H.; LINDQWISTER, U. J.; RUNGE, T. F. A global mapping technique for GPS-derived ionospheric total electron content measurements. **Radio Science**, v. 33, n. 3, p. 565–582, 1998. 53

MARKOVIĆ, M. Determination of total electron content in the ionosphere using GPS technology. **Geonauka**, v. 2, n. 4, p. 1–9, 2014. 50, 51

MARKS, C. J.; ECKERMANN, S. D. A three-dimensional nonhydrostatic ray-tracing model for gravity waves: Formulation and preliminary results for the middle atmosphere. **Journal of the Atmospheric Sciences**, v. 52, n. 11, p. 1959–1984, 1995. 17

MAYAUD, P.-N. Derivation, meaning, and use of geomagnetic indices. **GMS**, v. 22, p. 607, 1980. 83

MEDVEDEV, A. S.; GONZÁLEZ-GALINDO, F.; YIĞIT, E.; FEOFILOV, A. G.; FORGET, F.; HARTOGH, P. Cooling of the martian thermosphere by CO2 radiation and gravity waves: an intercomparison study with two general circulation models. **Journal of Geophysical Research: Planets**, v. 120, n. 5, p. 913–927, 2015. 15

MEIRA, L. G. Rocket measurements of upper atmospheric nitric oxide and their consequences to the lower ionosphere. **Journal of Geophysical Research**, v. 76, n. 1, p. 202–212, 1971. 10

MILLER, C. A. Electrodynamics of midlatitude spread f 2. a new theory of gravity wave electric fields. **Journal of Geophysical Research: Space Physics**, v. 102, n. A6, p. 11533–11538, 1997. 4, 102

MIYOSHI, Y.; FUJIWARA, H.; JIN, H.; SHINAGAWA, H. A global view of gravity waves in the thermosphere simulated by a general circulation model. **Journal of Geophysical Research: Space Physics**, v. 119, n. 7, p. 5807–5820, 2014. 109

MORGAN, M. G.; CALDERON, C. H. J.; BALLARD, K. A. Techniques for the study of TIDs with multi-station rapid-run ionosondes. **Radio Science**, v. 13, n. 4, p. 729–741, 1978. 24

MUNRO, G. Short-period changes in the f region of the ionosphere. **Nature**, v. 162, n. 4127, p. 886–887, 1948. 113

______. Travelling disturbances in the ionosphere. v. 202, n. 1069, p. 208–223, 1950. 113

______. Travelling Ionospheric Disturbances in the f region. **Australian Journal of Physics**, v. 11, n. 1, p. 91–112, 1958. 113

NARAYANAN, V. L.; SHIOKAWA, K.; OTSUKA, Y.; SAITO, S. Airglow observations of nighttime medium-scale traveling ionospheric disturbances from yonaguni: Statistical characteristics and low-latitude limit. **Journal of Geophysical Research: Space Physics**, v. 119, n. 11, p. 9268–9282, 2014. 2, 58, 145

NEGALE, M. **Investigating the Climatology of Mesospheric and Thermospheric Gravity Waves at High Northern Latitudes**. Tese (Doutorado) — Thesis (PhD in Physics) -Utah Sate University, Logan, Utah, 2018. 40, 99

NICOLET, M.; AIKIN, A. The formation of the D region of the ionosphere. **Journal of Geophysical Research**, v. 65, n. 5, p. 1469–1483, 1960. 9

NICOLLS, M. J.; VADAS, S. L.; APONTE, N.; SULZER, M. P. Horizontal parameters of daytime thermospheric gravity waves and e region neutral winds over puerto rico. **Journal of Geophysical Research: Space Physics**, v. 119, n. 1, p. 575–600, 2014. 22, 23

OGAWA, T.; NISHITANI, N.; OTSUKA, Y.; SHIOKAWA, K.; TSUGAWA, T.; HOSOKAWA, K. Medium-scale traveling ionospheric disturbances observed with the SuperDARN Hokkaido radar, all-sky imager, andGPS network and their relation to concurrent sporadic E irregularities. **Journal of Geophysical Research: Space Physics**, v. 114, n. A3, 2009. 14

OTSUKA, Y.; KOTAKE, N.; SHIOKAWA, K.; OGAWA, T.; TSUGAWA, T.; SAITO, A. Statistical study of medium-scale traveling ionospheric disturbances observed with a GPS receiver network in Japan. In: **ABDU, M. A.; PANCHEVA, D. (Ed.). Aeronomy of the Earth's Atmosphere and Ionosphere**. [S.l.: s.n.], 2011. p. 291–299. 5, 6, 14, 93, 101, 103, 107, 108, 109, 120, 121, 141

OTSUKA, Y.; OGAWA, T.; SAITO, A.; TSUGAWA, T.; FUKAO, S.; MIYAZAKI, S. A new technique for mapping of total electron content using GPS network in Japan. **Earth, Planets and Space**, v. 54, n. 1, p. 63–70, 2002. 56

OTSUKA, Y.; SHIOKAWA, K.; OGAWA, T. Disappearance of equatorial plasma bubble after interaction with mid-latitude medium-scale traveling ionospheric disturbance. **Geophysical Research Letters**, v. 39, n. 14, 2012. 101, 103, 107

OTSUKA, Y.; SHIOKAWA, K.; OGAWA, T.; WILKINSON, P. Geomagnetic conjugate observations of medium-scale traveling ionospheric disturbances at midlatitude using all-sky airglow imagers. **Geophysical Research Letters**, v. 31, n. 15, 2004. 3

OTSUKA, Y.; SUZUKI, K.; NAKAGAWA, S.; NISHIOKA, M.; SHIOKAWA, K.; TSUGAWA, T. GPS observations of medium-scale traveling ionospheric disturbances over Europe. **Annales Geophysicae**, v. 31, n. 2, p. 163–172, 2013. 1, 3, 14, 15, 24, 33, 36, 37, 55, 56, 87, 103, 109, 120

PARAZZOLI, C. G.; GREEGOR, R. B.; LI, K.; KOLTENBAH, B. E. C.; TANIELIAN, M. Experimental verification and simulation of negative index of refraction using Snell's law. **Physical Review Letters**, v. 90, n. 10, p. 107401, 2003. 50

PAULINO, I. et al. Periodic waves in the lower thermosphere observed by oi630 nm airglow images. **Annales Geophysicae**, v. 34, n. 2, 2016. 3, 24, 30, 68, 94, 113, 120

_____. Intrinsic parameters of periodic waves observed in the oi6300 airglow layer over the Brazilian equatorial region. v. 36, n. 1, p. 265–273, 2018. 99

PAULINO, I.; TAKAHASHI, H.; GOBBI, D.; MEDEIROS, A.; BURITI, R.; WRASSE, C. Observações de ondas de gravidade de média escala na região equatorial do Brasil. In: SOCIETY OF EXPLORATION GEOPHYSICISTS AND BRAZILIAN GEOPHYSICAL SOCIETY. **12th International Congress of the Brazilian Geophysical Society & EXPOGEF, Rio de Janeiro, Brazil, 15-18 August 2011**. [S.l.], 2011. p. 2123–2126. 58, 64

PFISTER, L.; STARR, W.; CRAIG, R.; LOEWENSTEIN, M.; LEGG, M. Small-scale motions observed by aircraft in the tropical lower stratosphere: evidence for mixing and its relationship to large-scale flows. **Journal of the Atmospheric Sciences**, v. 43, n. 24, p. 3210–3225, 1986. 121

PIMENTA, A. A.; KELLEY, M. C.; SAHAI, Y.; BITTENCOURT, J. A.; FAGUNDES, P. R. Thermospheric dark band structures observed in all-sky oi 630 nm emission images over the Brazilian low-latitude sector. **Journal of Geophysical Research: Space Physics**, v. 113, n. A1, 2008. 3, 14, 15, 24, 31, 113

PITTEWAY, M. L. V.; HINES, C. O. The viscous damping of atmospheric gravity waves. **Canadian Journal of Physics**, v. 41, n. 12, p. 1935–1948, 1963. 16

PROL, F. d. S.; CAMARGO, P. d. O.; MUELLA, M. T. d. A. H. Comparative study of methods for calculating ionospheric points and describing the GNSS signal path. **Boletim de Ciências Geodésicas**, v. 23, n. 4, p. 669–683, 2017. 56

QIAN, J.; GU, Y. Y.; PAPEN, G. C.; GARDNER, C. S.; ESPY, P. J. Horizontal wave number spectra of density and temperature perturbations in the mesosphere measured during the 4 August flight of ANLC-93. **Geophysical Research Letters**, v. 22, n. 20, p. 2865–2868, 1995. 133

QUADRO, M. F. L. d. **Estudo de episódios de Zona de Convergência do Atlântico Sul (ZCAS) sobre a América do sul. 1994. 99p**. [S.l.]: Dissertação (Mestrado em Meteorologia)-Instituto Nacional de Pesquisas, Sção José dos Campos, 1994. 130

RAI, A. **Introduction to Global Positioning System**. [S.l.]: New Delhi: Indian Agricultural Statistics Research Institute. Available from: http://www. iasri. res. in/ebook/GIS TA/M3_4_INtoGPS. pdf, 2012. 48

REPP, J.; MEYER, G.; RIEDER, K.-H. Snell's law for surface electrons: refraction of an electron gas imaged in real space. **Physical Review Letters**, v. 92, n. 3, p. 036803, 2004. 50

RICHMOND, A. Gravity wave generation, propagation, and dissipation in the thermosphere. **Journal of Geophysical Research: Space Physics**, v. 83, n. A9, p. 4131–4145, 1978. 117

RICHMOND, A. D.; RIDLEY, E. C.; ROBLE, R. G. A thermosphere/ionosphere general circulation model with coupled electrodynamics. **Geophysical Research Letters**, v. 19, n. 6, p. 601–604, 1992. 9

RISHBETH, H. The f-layer dynamo. **Planetary and Space Science**, v. 19, n. 2, p. 263–267, 1971. 11

_____. Thermospheric winds and the f-region: a review. **Journal of Atmospheric and Terrestrial Physics**, v. 34, n. 1, p. 1–47, 1972. 115

RISHBETH, H.; GARRIOTT, O. K. Introduction to ionospheric physics. **IEEE Transactions on Image Processing**, 1969. 9, 10

RISHBETH, H.; MENDILLO, M.; WROTEN, J.; ROBLE, R. Day-by-day modelling of the ionospheric f2-layer for year 2002. **Journal of Atmospheric and Solar-Terrestrial Physics**, v. 71, n. 8-9, p. 848–856, 2009. 9

ROB. Royal observatory of Belgium using GNSS data. **Journal of Space Weather and Space Climate**, v. 4, p. A31, 2014. 53

RÖTTGER, J. Travelling disturbances in the equatorial ionosphere and their association with penetrative cumulus convection. **Journal of Atmospheric and**

Terrestrial Physics, v. 39, n. 9-10, p. 987–998, 1977. 2, 24, 25, 96, 100, 107, 120, 121, 132, 133

SAITO, A.; FUKAO, S.; MIYAZAKI, S. High resolution mapping of TEC perturbations with the GSI GPS network over Japan. **Geophysical Research Letters**, v. 25, n. 16, p. 3079–3082, 1998. 24, 33, 55

SAITO, A. et al. Traveling Ionospheric Disturbances detected in the FRONT campaign. **Geophysical Research Letters**, v. 28, n. 4, p. 689–692, 2001. 33, 34

SAITO, S.; YAMAMOTO, M.; HASHIGUCHI, H.; MAEGAWA, A.; SAITO, A. Observational evidence of coupling between quasi-periodic echoes and medium-scale traveling ionospheric disturbances. **Annales Geophysicae**, v. 25, n. 10, p. 2185–2194, 2007. 58

SHARMA, S.; GALAV, P.; DASHORA, N.; DABAS, R.; PANDEY, R. Study of ionospheric TEC during space weather event of 24 August 2005 at two different longitudes. **Journal of Atmospheric and Solar-Terrestrial Physics**, v. 75, p. 133–140, 2012. 116

SHIMIZU, A.; TSUDA, T. Characteristics of kelvin waves and gravity waves observed with radiosondes over Indonesia. **Journal of Geophysical Research: Atmospheres**, v. 102, n. D22, p. 26159–26171, 1997. 121

SHIOKAWA, K.; IHARA, C.; OTSUKA, Y.; OGAWA, T. Statistical study of nighttime medium-scale traveling ionospheric disturbances using midlatitude airglow images. **Journal of Geophysical Research: Space Physics**, v. 108, n. A1, 2003. 15, 113

SHIOKAWA, K.; OTSUKA, Y.; EJIRI, M. K.; SAHAI, Y.; KADOTA, T.; IHARA, C.; OGAWA, T.; IGARASHI, K.; MIYAZAKI, S.; SAITO, A. Imaging observations of the equatorward limit of midlatitude traveling ionospheric disturbances. **Earth, Planets and Space**, v. 54, n. 1, p. 57–62, 2002. 2

SHIOKAWA, K.; OTSUKA, Y.; OGAWA, T. Quasiperiodic southward moving waves in 630-nm airglow images in the equatorial thermosphere. **Journal of Geophysical Research: Space Physics**, v. 111, n. A6, 2006. 3

SIERADZKI, R.; PAZIEWSKI, J. Study on reliable GNSS positioning with intense TEC fluctuations at high latitudes. **GPS Solutions**, v. 20, n. 3, p. 553–563, 2016. 3

SOBRAL, J. H. A. et al. Thermospheric f-region travelling disturbances detected at low latitude by an oi 630 nm digital imager system. **Advances in Space Research**, v. 27, n. 6-7, p. 1201–1206, 2001. 24, 58

SQUAT, K.; SCHLEGEL, K. A review of atmospheric gravity waves and travelling ionospheric disturbances: 1982-1995. **Annales Geophysicae**, v. 14, n. 9, p. 917, 1996. 1, 21, 98

SU, S.-Y.; WU, C. L.; LIU, C. H. Correlation between the global occurrences of ionospheric irregularities and deep atmospheric convective clouds in the intertropical convergence zone (ITCZ). **Earth, Planets and Space**, v. 66, n. 1, p. 134, 2014. 41, 43, 44, 132

SUGIURA, M. Hourly values of equatorial dst for the igy. 1963. 83

SUGIURA, M.; CHAPMAN, S. **The average morphology of geomagnetic storms with sudden commencement**. [S.l.: s.n.], 1961. 84

TAKAHASHI, H.; WRASSE, C. M.; FIGUEIREDO, C. A. O. B.; BARROS, D.; ABDU, M. A.; OTSUKA, Y.; SHIOKAWA, K. Equatorial plasma bubble seeding by MSTIDs in the ionosphere. **Progress in Earth and Planetary Science**, v. 5, n. 1, p. 32, 2018. 4, 31, 123, 145

TAYLOR, M. Multiple wavelength optical observations of a long-lived meteor. **Geophysical Research Letters**, v. 28, n. 14, p. 2779–2782, 2001. 95

TAYLOR, M. J.; HAPGOOD, M. Identification of a thunderstorm as a source of short period gravity waves in the upper atmospheric nightglow emissions. **Planetary and Space Science**, v. 36, n. 10, p. 975–985, 1988. 123

TAYLOR, M. J.; PAUTET, P.-D.; MEDEIROS, A.; BURITI, R.; FECHINE, J.; FRITTS, D.; VADAS, S.; TAKAHASHI, H.; SABBAS, F. S. Characteristics of mesospheric gravity waves near the magnetic equator, brazil, during the SpreadFEx campaign. **Annales Geophysicae**, v. 27, n. 2, p. 461, 2009. 58, 113

TORRENCE, C.; COMPO, G. P. A practical guide to wavelet analysis. **Bulletin of the American Meteorological Society**, v. 79, n. 1, p. 61–78, 1998. 66, 67

TSUDA, T.; MURAYAMA, Y.; WIRYOSUMARTO, H.; HARIJONO, S. W. B.; KATO, S. Radiosonde observations of equatorial atmosphere dynamics over indonesia: characteristics of gravity waves. **Journal of Geophysical Research: Atmospheres**, v. 99, n. D5, p. 10507–10516, 1994. 121

TSUGAWA, T.; OTSUKA, Y.; COSTER, A. J.; SAITO, A. Medium-scale traveling ionospheric disturbances detected with dense and wide TEC maps over North America. **Geophysical Research Letters**, v. 34, n. 22, 2007. 1, 3, 14, 15, 24, 33, 34, 35, 36, 54, 55, 56, 87, 109

TSUGAWA, T.; SAITO, A.; OTSUKA, Y. A statistical study of large-scale traveling ionospheric disturbances using theGPS network in Japan. **Journal of Geophysical Research: Space Physics**, v. 109, n. A6, 2004. 3, 14

TSUNODA, R. T. On seeding equatorial spread f during solstices. **Geophysical Research Letters**, v. 37, n. 5, 2010. 26, 41, 132

VADAS, S. Compressible f-plane solutions to body forces, heatings, and coolings, and application to the primary and secondary gravity waves generated by a deep convective plume. **Journal of Geophysical Research: Space Physics**, v. 118, n. 5, p. 2377–2397, 2013. 18, 136

VADAS, S.; BECKER, E. The excitation of secondary gravity waves from body forces created by wave dissipation, and application to the Antartic winter. **EGUGA**, p. 5135, 2017. 16, 18, 21, 22, 98

VADAS, S.; NICOLLS, M. The phases and amplitudes of gravity waves propagating and dissipating in the thermosphere: theory. **Journal of Geophysical Research: Space Physics**, v. 117, n. A5, 2012. 18, 19

VADAS, S. L. Horizontal and vertical propagation and dissipation of gravity waves in the thermosphere from lower atmospheric and thermospheric sources. **Journal of Geophysical Research: Space Physics**, v. 112, n. A6, 2007. 16, 32, 95, 99, 121, 122, 123, 126, 141

VADAS, S. L.; BECKER, E. Numerical modeling of the generation of tertiary gravity waves in the mesosphere and thermosphere during strong mountain wave events over the Southern Andes. **Journal of Geophysical Research: Space Physics**, v. 124, n. 9, p. 7687–7718, 2019. 94, 98, 106, 107, 136, 137, 138, 142

VADAS, S. L.; CROWLEY, G. Sources of the traveling ionospheric disturbances observed by the ionospheric TIDDBIT sounder near wallops island on 30 October 2007. **Journal of Geophysical Research: Space Physics**, v. 115, n. A7, 2010. 32, 93, 98, 100, 110, 118, 142, 143

VADAS, S. L.; FRITTS, D. C. Thermospheric responses to gravity waves: influences of increasing viscosity and thermal diffusivity. **Journal of Geophysical Research: Atmospheres**, v. 110, n. D15, 2005. 17, 18, 19

______. Influence of solar variability on gravity wave structure and dissipation in the thermosphere from tropospheric convection. **Journal of Geophysical Research: Space Physics**, v. 111, n. A10, 2006. 93, 94, 112, 114, 136, 142

VADAS, S. L.; FRITTS, D. C.; ALEXANDER, M. J. Mechanism for the generation of secondary waves in wave breaking regions. **Journal of the Atmospheric Sciences**, v. 60, n. 1, p. 194–214, 2003. 136

VADAS, S. L.; NICOLLS, M. J. Temporal evolution of neutral, thermospheric winds and plasma response using PFISR measurements of gravity waves. **Journal of Atmospheric and Solar-Terrestrial Physics**, v. 71, n. 6-7, p. 744–770, 2009. 19, 20

VADAS, S. L.; TAYLOR, M. J.; PAUTET, P.-D.; STAMUS, P.; FRITTS, D. C.; LIU, H.-L.; SABBOS, F. S.; BATISTA, V.; TAKAHASHI, H.; RAMPINELLI, V. Convection: the likely source of the medium-scale gravity waves observed in the OH airglow layer near Brasilia, Brazil, during the SpreadFEx campaign. **Annales Geophysicae**, v. 27, p. 231, 2009. 113

VADAS, S. L.; ZHAO, J.; CHU, X.; BECKER, E. The excitation of secondary gravity waves from local body forces: theory and observation. **Journal of Geophysical Research: Atmospheres**, v. 123, n. 17, p. 9296–9325, 2018. 136

VINCENT, R. A. The dynamics of the mesosphere and lower thermosphere: a brief review. **Progress in Earth and Planetary Science**, v. 2, n. 1, p. 1–13, 2015. 113

VINCENT, R. A.; ALEXANDER, M. J. Gravity waves in the tropical lower stratosphere: an observational study of seasonal and interannual variability. **Journal of Geophysical Research: Atmospheres**, v. 105, n. D14, p. 17971–17982, 2000. 121

VIRJI, H. A preliminary study of summertime tropospheric circulation patterns over South America estimated from cloud winds. **Monthly Weather Review**, v. 109, n. 3, p. 599–610, 1981. 129

VUILLE, M. Atmospheric circulation over the Bolivian Altiplano during dry and wet periods and extreme phases of the southern oscillation. **International**

Journal of Climatology: A Journal of the Royal Meteorological Society, Wiley Online Library, v. 19, n. 14, p. 1579–1600, 1999. 129

WADA, K.; NITTA, T.; SATO, K. Equatorial inertia-gravity waves in the lower stratosphere revealed by TOGA-COARE TOP data. **Journal of the Meteorological Society of Japan. Ser. II**, v. 77, n. 3, p. 721–736, 1999. 121

WALDOCK, J.; JONES, T. The effects of neutral winds on the propagation of medium-scale atmospheric gravity waves at mid-latitudes. **Journal of Atmospheric and Terrestrial Physics**, v. 46, n. 3, p. 217–231, 1984. 99, 108

WALDOCK, J. A.; JONES, T. B. Source regions of medium scale travelling ionospheric disturbances observed at mid-latitudes. **Journal of Atmospheric and Terrestrial Physics**, v. 49, n. 2, p. 105–114, 1987. 121, 123

WALISER, D.; JIANG, X. Tropical meteorology and climate: intertropical convergence zone. 2015. 127

WALISER, D. E.; GAUTIER, C. A satellite-derived climatology of the ITCZ. **Journal of climate**, v. 6, n. 11, p. 2162–2174, 1993. 26, 42

WALTERSCHEID, R.; HICKEY, M. Group velocity and energy flux in the thermosphere: Limits on the validity of group velocity in a viscous atmosphere. **Journal of Geophysical Research: Atmospheres**, v. 116, n. D12, 2011. 16

WANG, S.; MIN, J.; YI, B. K. Location based services for mobiles: technologies and standards. In: **IEEE international conference on communication (ICC), 19., 2008. Proceedings...** [S.l.: s.n.], 2008. 48

WEBBER, W. The production of free electrons in the ionospheric d layer by solar and galactic cosmic rays and the resultant absorption of radio waves. **Journal of Geophysical Research**, v. 67, n. 13, p. 5091–5106, 1962. 9

WITCHAYANGKOON, B. **Elements of GPS precise point positioning**. [S.l.: s.n.], 2000. 49

YEH, K. C.; LIU, C. H. Acoustic-gravity waves in the upper atmosphere. **Reviews of Geophysics**, v. 12, n. 2, p. 193–216, 1974. 21

YU, Y.; WANG, W.; HICKEY, M. P. Ionospheric signatures of gravity waves produced by the 2004 sumatra and 2011 Tohoku tsunamis: a modeling study. **Journal of Geophysical Research: Space Physics**, v. 122, n. 1, p. 1146–1162, 2017. 22

ZHANG, F. Generation of mesoscale gravity waves in upper-tropospheric jet-front systems. **Journal of the Atmospheric Sciences**, v. 61, n. 4, p. 440–457, 2004. 126

ZVEREV, A. S. **Synoptic meteorology and numerical weather forecasting**. [S.l.]: Leningrad: Hydrometeoisdat, 1968. 129

PUBLICAÇÕES TÉCNICO-CIENTÍFICAS EDITADAS PELO INPE

Teses e Dissertações (TDI)

Teses e Dissertações apresentadas nos Cursos de Pós-Graduação do INPE.

Notas Técnico-Científicas (NTC)

Incluem resultados preliminares de pesquisa, descrição de equipamentos, descrição e ou documentação de programas de computador, descrição de sistemas e experimentos, apresentação de testes, dados, atlas, e documentação de projetos de engenharia.

Propostas e Relatórios de Projetos (PRP)

São propostas de projetos técnico-científicos e relatórios de acompanhamento de projetos, atividades e convênios.

Publicações Seriadas

São os seriados técnico-científicos: boletins, periódicos, anuários e anais de eventos (simpósios e congressos). Constam destas publicações o Internacional Standard Serial Number (ISSN), que é um código único e definitivo para identificação de títulos de seriados.

Pré-publicações (PRE)

Todos os artigos publicados em periódicos, anais e como capítulos de livros.

Manuais Técnicos (MAN)

São publicações de caráter técnico que incluem normas, procedimentos, instruções e orientações.

Relatórios de Pesquisa (RPQ)

Reportam resultados ou progressos de pesquisas tanto de natureza técnica quanto científica, cujo nível seja compatível com o de uma publicação em periódico nacional ou internacional.

Publicações Didáticas (PUD)

Incluem apostilas, notas de aula e manuais didáticos.

Programas de Computador (PDC)

São a seqüência de instruções ou códigos, expressos em uma linguagem de programação compilada ou interpretada, a ser executada por um computador para alcançar um determinado objetivo. Aceitam-se tanto programas fonte quanto os executáveis.